Modelling of dew point operating conditions in a rotary regenerative air heater

Warren Brandt
(Student number: 1968035)

School of Mechanical, Industrial and Aeronautical Engineering

University of the Witwatersrand

Johannesburg, South Africa.

Supervisors:
Prof W Schmitz
Prof T J Sheer

A research dissertation submitted to the Faculty of Engineering and the Built Environment, University of the Witwatersrand, in fulfilment of the requirements for the degree of Master of Science in Engineering.

2021/04/29

ABSTRACT
Regenerative rotary air heaters are usually one of the large contributors to the reduction of boiler efficiency, due to high leakage rates and insufficient heat transfer. Dew point related fouling of air heater element packs is one of the factors that causes insufficient heat transfer. Coal fired power station air heaters can experience excessive dew point related fouling, which commonly causes high pressure differences over the air heater steel matrix, increasing FD (Forced Draught) and ID (Induced Draught) fan loading, along with elevated air heater leakage rates. Additional consequences are premature failure of element packs, due to inflated fly ash erosion rates that occur on localised areas of the air heater steel matrix, air heater hoods, dampers and ducts. It also contributes to exaggerated levels of dust emissions due to an augmented flow and velocity of flue gas. Excessively fouled element packs can only be rectified by either applying frequent high pressure washing or replacement of element packs. Both of these are costly activities which can be avoided through applying the correct operating conditions and maintenance strategies.

Through modelling of dew point operating conditions of a rotary regenerative air heater, the onset of dew point related fouling was predicted. This modelling tool was developed using mass and energy balance methods applied to element volumes in the steel matrix to estimate the gas temperature, element surface metal temperature, and dew point temperatures (water, sulphuric acid and sulphurous acid) of the flue gas. The tool provides a platform to predict the temperature profiles and to identify where the onset of dew point related fouling exist. If the element surfaces and the flue gas experience temperatures less than the dew point temperatures, the onset of dew point related fouling is expected. The modelling tool was validated through plant experiments and historical test results from previous research projects. The plant experiments were conducted for three different load conditions, namely 99% MCR (Maximum Continuous Rating), 80% MCR and 68% MCR. The results indicated that the fouling region is located mostly in the cold end layer of packs, as predicted by the simulation model. The prediction of dew point related fouling regions correlated best for the full load condition, where the metal temperatures were below the 134˚C to 152˚C range (1% to 5% SO_2 to SO_3 conversion respectively) of sulphuric acid dew point temperatures. (Sulphurous acid and moisture dew point temperatures are mostly encountered during boiler shut-downs or light-ups, where transient states are experienced.) During sulphuric acid condensation in normal operation, ash particles start to adhere to each other and to the surrounding metal surfaces operating below the sulphuric acid temperature band mentioned above. For all three load conditions the simulated cold end metal temperatures compared quite well to the measured metal temperatures. The measured values were influenced by factors such as thermal inertia and contact resistance, which was caused by the selected method of installation.

The modelling tool was developed to equip system engineers with the means to improve operating conditions and maintenance strategies in order to prevent the onset of dew point related fouling. This study contributes to the possibility of increasing the life expectancy of air heater element packs and draught group components. It provides a platform to improve boiler efficiency, reduce maintenance costs and production losses.

ACKNOWLEDGEMENT

The author would like to acknowledge Professor Walter Schmitz and Professor Thomas John Sheer from the University of the Witwatersrand for their support and Mike Lander for his assistance as industrial supervisor. The author would also like to acknowledge the Research Testing & Development team (F Makananise, L Vilakazi, and J Mesolo) for their assistance with the planning and execution of the experiments for this research. The author would also like to acknowledge the station based Performance & Testing team (M Molo, P Masoba, H Nemakhavhani , K Ramalepe, M Moshatana, A Van Dyk, K Lebepe) for their assistance with the planning and execution of the experiments for this research. The author acknowledges ESKOM Power Plant Engineering Institute (EPPEI) for their financial support and providing the opportunity to carry out the project.

Table of Contents

List of Figures

List of Tables

Abbreviations

Nomenclature

a – Half of the thickness of the corrugated solid region
A – Suitable area for heat transfer
A_{cond} – Area of conduction at the given time interval
A_{conv} – Area of convection at the given time interval
AF_{stoich} – Stoichiometric Air Fuel Ratio
b – Half of the thickness of the undulated solid region
Ca_{sol} – Weight percentage of dilute-acid-soluble calcium in coal
C_b – concentration of the sulphuric acid vapour at the deposition surface
C_f – Heat capacity of the fluid
C'_{fa} – Unburnt Carbon in fly ash
C'_{fba} – Unburnt Carbon in bottom ash
C_i – concentration of the sulphuric acid vapour in the flue gas stream
C_s – Heat capacity of the solid material of the element pack
f_{ash} - Mass fraction of ash in coal
h - Overall heat transfer coefficient (Wm^2/K)
h_D – heat transfer coefficient
$h_{a,ambient,in}$ – Enthalpy of the ambient air
$h_{a,leak}$ – Enthalpy of the air leaking to the flue gas
$h_{a,sah,in}$ – Enthalpy of the secondary air entering the secondary air heater
h_c – Enthalpy of the coal entering the boiler
$h_{fg,pah,in}$ – Enthalpy of the flue gas entering the secondary air heater
$h_{fg,sah,in}$ – Enthalpy of the flue gas entering the secondary air heater
I – SI units of thermal inertia
k – is thermal conductivity
L – Length element pack (height of the element pack along the flow direction)
$LMTD$ – Log Mean Temperature difference
m – A constant depending on boiler combustion conditions
$\dot{m}_a$– Mass flow of the total air as determined from the coal analysis and O_2 at the boiler outlet
$\dot{m}_c$– Mass flow of coal
$\dot{m}_c$– Mass flow of coal
$\dot{m}_{fg,pah,in}$ – Mass flow of the flue gas entering the primary air heater
$\dot{m}_{fg,sah,in}$ – Mass flow of the flue gas entering the secondary air heater
$\widehat{m}_i$ – Mass of flue gas constituent
M_i – Molar mass of flue gas constituant
$\dot{m}_{ingress,a}$– Mass flow of ingress air
$\dot{m}_{leak}$ – Mass flow of the air leaking to the flue gas stream internal to the air heater
$\dot{m}_{pa,a}$– Mass flow of the primary air
$\dot{m}_{pa}$– Mass flow of primary air
M_s – Mass of the solid material of the element pack
$\dot{m}_{sa}$– Mass flow of secondary air
$\dot{m}_{sl,a}$– Mass flow of seal air
$\dot{m}_{tmp,a}$– Mass flow of tempering air
n_i – Number of moles
Na_{sol} – Weight percentage of dilute-acid-soluble calcium in coal
p – Is density, with unit $kg \cdot m^{-3}$

$P -$ Pressure of flue gas
q – Exchanger heat transfer (Watts)
$\dot{Q}_{C'} -$ Unburnt carbon energy loss
$\dot{Q}_{ba} -$ Heat energy lost due to sensible heat in bottom ash
$\dot{Q}_{fa} -$ Heat energy lost due to sensible heat in fly ash
$\dot{Q}_{fg} -$ Flue gas energy loss
$\dot{Q}_{loss} -$ Heat energy lost in the Boiler
$\dot{Q}_{rad} -$ Heat radiation energy lost to surroundings
S – Sulphur content in coal
T – Temperature for flue gas
T_{a1} – Temperature of air entering the air heater.
$T_{a2} -$ Temperature of air exiting the air heater
$T_{dp} -$ Dew point Temperature
$T_f -$ Fluid temperature
$T_f^* -$ Dimensionless fluid temperature
$T_{g1} -$ Air heater inlet gas temperature
T_{g2NL} – Undiluted flue gas exit temperature (temperature which excludes the influence of ingress air). This temperature accounts for temperature change due to leakage.
$T_{s1} -$ Corrugated solid temperature
$T_{s1}^* -$ Dimensionless corrugated solid temperature
$T_{s2} -$ Undulated solid temperature
$T_{s2}^* -$ Dimensionless undulated solid temperature
$^{v}/_{v}\, O_{2\ before\ AH} -$ The oxygen in the flue gas measured before the air heater
$V_i -$ Volume of flue gas constituent
W – Ash content of coal
x – A fraction of coal sulphur oxidized to sulphur trioxide
x – Length of the pack at a given time interval

1. INTRODUCTION

1.1. Purpose of the Study

South Africa predominantly relies on coal for electrical power generation. From as early as 1880 coal has dominated the energy supply sector in South Africa. In 2018, 77% of South Africa's primary energy needs were provided by means of coal. 224 Million tons of marketable coal was produced of which 25% was exported. The remainder of the coal production supplied various local industries of which 53% was used for electricity generation (Eskom, 2017). Eskom operates 23 power stations providing a nominal capacity of 42090MW. The power utility includes 15 coal fired stations contributing 85% of the total capacity (Eskom, 2017). Eskom claims that South Africa's coal reserves are estimated to be approximately 53 billion tons. With the current production rate the reserves can still provide coal for almost another 200 years (Laubscher, 2015).

This is a clear indication that coal powered stations will still be an important platform for power generation in the future of South African energy. Important considerations will be to maintain the coal-fired generation plants in a sustainable fashion, reducing expenditure, increasing the life expectancy, and reducing environmental pollution. This sustainable environment can only be created by utilizing innovative engineering solutions that provide safe and efficient operation of power plants.

Power Stations are designed to supply power according to design specifications. Certain factors influence the plant efficiency, which causes a reduction in the electrical output. This reduction in output is defined in Eskom terms as a partial load loss. Air heaters are usually one of the large contributors to partial load losses. These losses are incurred due to high leakage rates and insufficient heat transfer. The heat rejected in the boiler flue gas must be recovered to the combustion air supplied to the furnace, to enhance the boiler efficiency. Plant defects that influence the thermal properties of the boiler will cause a reduction in boiler efficiency. Load losses specifically related to this problem are usually associated with the following operating conditions (Kleynhans & Eganza, 2016):

- Occurrences of high differential pressure across the air heater steel matrix, resulting in excessive FD (Forced Draught) and ID (Induced Draught) fan loading (FD and ID fans incapable of supplying the required capacity). This process also increases air heater leakage rates due to a back pressure created by the fouled heating elements.
- Increased fly ash erosion rates occur on localised areas of the air heater steel matrix (Figure 11), air heater hoods, dampers and ducts up to the electrostatic precipitators or fabric filter plant inlet casing.
- Accelerated wear and premature failure of element packs on the steel matrix periphery. Failing elements result in a loss of heat transfer and can also cause unplanned load losses. This can be caused through falling element packs that get stuck preventing air heater rotation. An unplanned unit shutdown is required to rectify the problem (Figure 1.1).
- Exaggerated dust emission levels occur due to augmented flows and velocities caused by entrained air leakage to the flue gas stream. The flue gas velocity may be increased to a point that it exceeds the velocity which allows the ash particles to migrate towards and adhere to the precipitator screens of the electrostatic precipitator plant. This will influence the amount of ash particles captured by the precipitator screens. In the case of filter bags, the erosion will damage the bags reducing the life expectancy of the filter bags. In essence the particle count for the emissions will increase. If the air leakage to the flue gas stream increases, the gas flow becomes diluted and this will also increase the toxic gas emission count and ID fan loading.

These conditions are usually symptoms of excessive fouling of air heater element packs, which can only be rectified by either applying frequent high pressure washing or replacement of element packs. Both of these are costly activities, which can be avoided through applying the correct operating conditions and maintenance strategies.

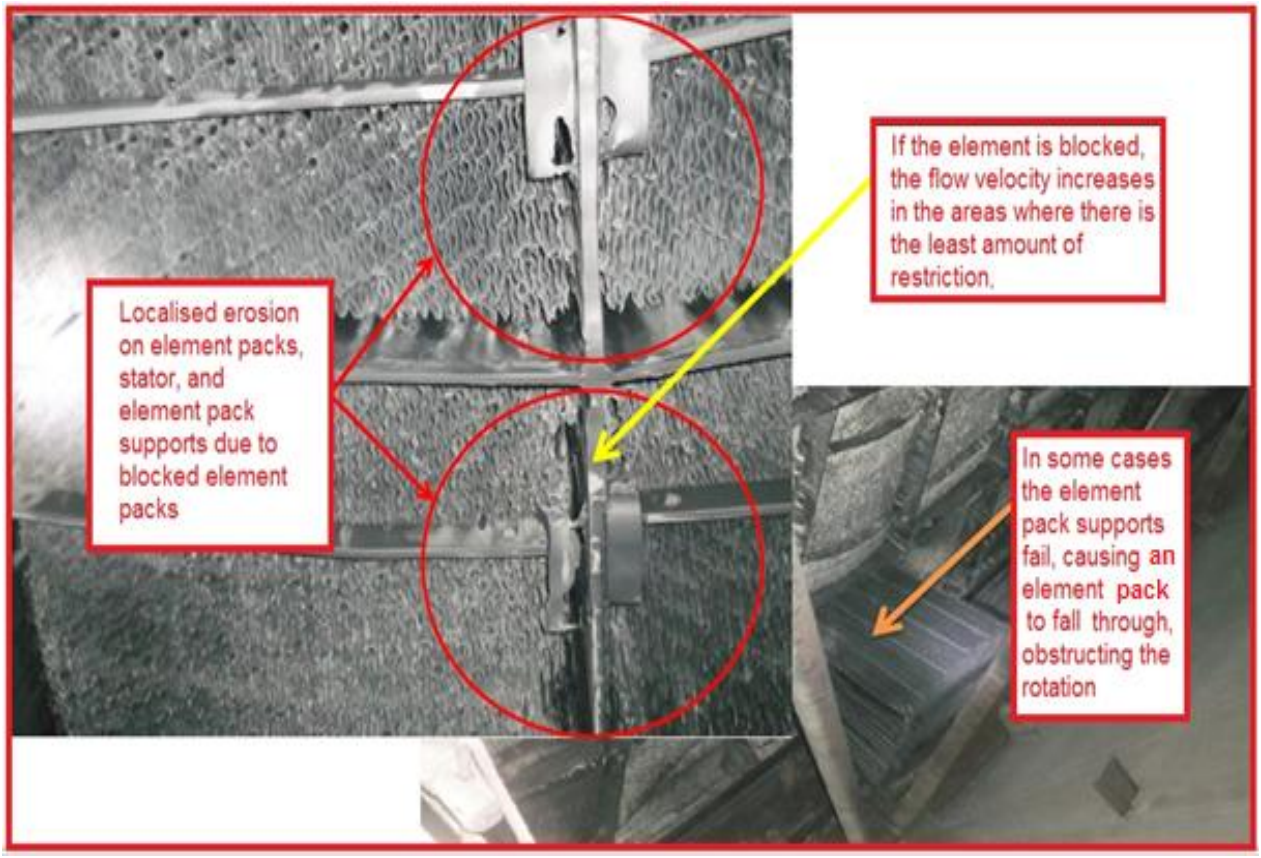

Figure 1.1: Element pack blockage, high erosion and failure of element packs experienced at Eskom coal fired power generation plants (Brandt, 2015).

The purpose of this study was to develop a methodology to improve the life expectancy and efficiency of air heaters, through prevention of dew point related fouling. A simulation tool had to be developed to predict onset of dew point related fouling in order to set critical parameters in place to prevent the condition from occurring. A modelling tool was required on an operational level to provide guidance to draught group system engineers to improve the condition of dew point related fouling. This tool therefore fulfils its purpose as a condition monitoring and performance analyses tool. The fouling prevention tool can be a guide to improve maintenance strategies, maintenance procedures, operating conditions and operating procedures that could increase the life expectancy of air heater elements.

1.2. Research Background/ Context

1.2.1 Air heater Thermal Performance

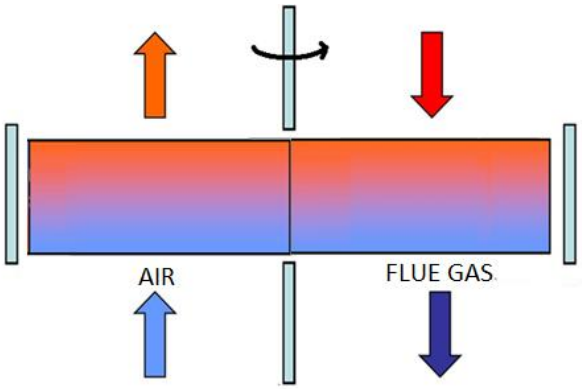

Figure 1.2: Basic air heater operation.

Air heaters are used to transfer the thermal energy contained in the flue gas to the combustion air entering the boiler (Figure 1.2). This process improves the boiler performance. If the thermal performance of an air heater deteriorate, a decrease in boiler performance can be expected. Therefore air heaters must at all times be maintained and operated in a way that extends its life expectancy and maintains its optimal thermal performance. There are three main modes of air heater element pack failures that influences air heater performance for rotary regenerative air heaters, namely erosion, corrosion and fouling. Figure 1.3 is an illustration of the three different modes of failure. Excessive levels of ash content in flue gas, conduce to increased element pack failures. In coal fired power generating stations, ash produced in boilers is deposited on the boiler walls and super-heater tubes. The deposited ash is then discharged as slag and clinker when boiler soot blowing is applied. A portion of the ash, along with the slag and clinker either gets caught up, or passes through the narrow passages of the air heater elements. The particles passing through collide with the steel surfaces, causing erosion on the surfaces. The entrained particles cause fouling if not removed by the air and flue gas passing through the elements or by means of air heater soot blowing. When these entrained ash particles are not removed it experiences dew point related operating conditions that cause blockage of these element packs.

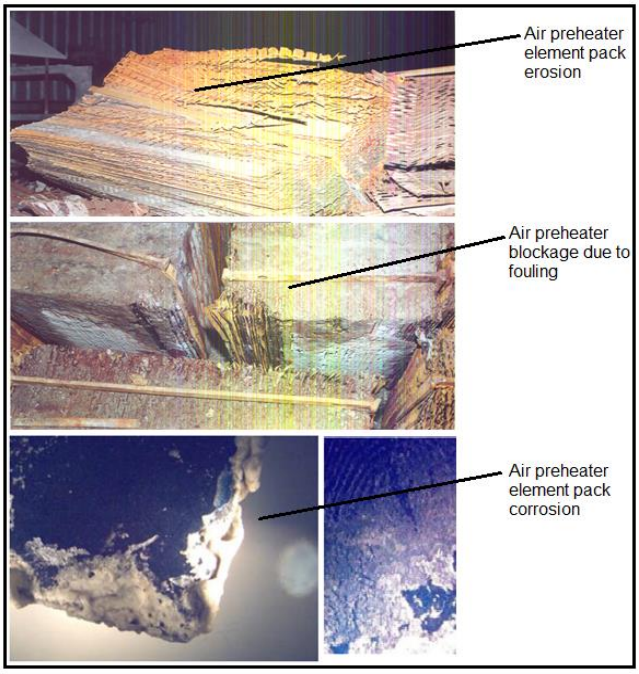

Figure 1.3: Three modes of failures for Air heater element packs (Brandt, 2018).

Erosion in air heaters is mainly caused through collision of fly ash particles with the steel surfaces. During these collisions the metal surfaces start to erode away. The components experiencing the highest reduction in operational life will be the element sheets, due to the fact that the sheets are not thick enough to withstand continuous collision of ash particles. Corrosion is damage caused to air heater components by means of a chemical reaction that occurs from the gases internal to the air heater. Corrosion is mostly caused and accelerated by condensation of sulphuric acid. Sulphur dioxide and sulphur trioxide are formed in the combustion process. When these two constituents combine with the moisture in the flue gas, sulphuric acid and sulphurous acid are formed. The acid then reacts with the alkaline ash, and with the mild steel plates of the air heater. Sulphuric acid is the most common corrosive chemical reaction in air heaters, especially in Europe due to the high sulphur content in the coal supplied in these countries along with the ambient conditions affecting the inlet air to the air heaters causing condensate formation. Based on these conditions important factors are the sulphur and moisture content in coal and the metal temperature of the element packs (Mabena, 2003). This research project mainly focused on addressing the third factor, namely regenerative air heater dew point related fouling. Corrosion formation correlates with dew point related fouling formation, but the only difference is that more ash particles are present in fouling, causing the particles to adhere to each other and to the metal surfaces operating below the dew point temperatures.

1.2.2 Regenerative Air heater fouling

Fouling is the accumulation of unwanted material on solid surfaces, affecting the functional operation of a system. In the case of heat exchangers, the actual energy exchange process is affected by deposit formations on the heating elements. Whether it is tubes, plates or any other form of conducting material, the heat transfer process will be affected by the unwanted deposits. Focusing on rotary regenerative air heaters, fouling occurs as a result of ash particles and other deposits that accumulate in the passages of the air heater elements. The overall heat transfer performance is degraded to the extent that boiler efficiency deteriorates. The Power Station used for testing has a history of frequent blockage of air heaters. With insufficient cleaning fouling occurs in the air heaters (Van Alphen, 2018). Fouling can usually occur in a chemical and a physical sense. After an investigation was done, it was assumed that sulphuric acid and anhydrite (gypsum) were present in the deposits that accumulated on the cold end elements. A Quantitative Evaluation of Minerals by Scanning Electron Microscopy (QEMSCAN) analysis of the samples indicated that the proportion of anhydrite was relatively low, but was present. It was lower than the proportion of "calcium reactive" fly ash particles. This would suggest that anhydrite conditions are not the main contribution to fouling of elements. There was however sulphur associated with fly ash particles in deposit samples that form on the surfaces of oxidised steel. This would suggest either sulphuric acid, hydrogen sulphide or some other form of sulphur is present. The main problem comes from operating below dew point conditions, associated with fly ash particles which deposit on the cold end element packs. Excessive fouling inside the cold end layer also allows accumulation of ash in the higher layers of the air heater element packs.

Physical fouling

Physical fouling is associated with plugging, also known as hot end fouling. Plugging is associated with incomplete combustion, and can also be caused by sintered and fused deposits, or loose light weight coarse ash which is transported by means of flue gas to the air heaters

(Mabena, 2003). During the cleaning process of boiler tubes, this material is dislodged into the flue gas stream carrying particles ranging from 1µm to 100 mm and in some cases even larger particles. Another cause of plugging is wet ash which is created by economiser leaks or defective soot blowers (Raask, 1985). If water vapour condenses it creates an environment where ash particles can adhere to each other, forming larger particles that are carried to the air heaters. Inconsistent grinding by the milling process can also produce coarse stone fragments, introducing rock fragments in the ash which also promotes plugging (Van Alphen, 2018). Figure 1.4 is an illustration of the different ash deposits found in air heaters. Figure 1.5 indicates how these deposits cause a plugging affect.

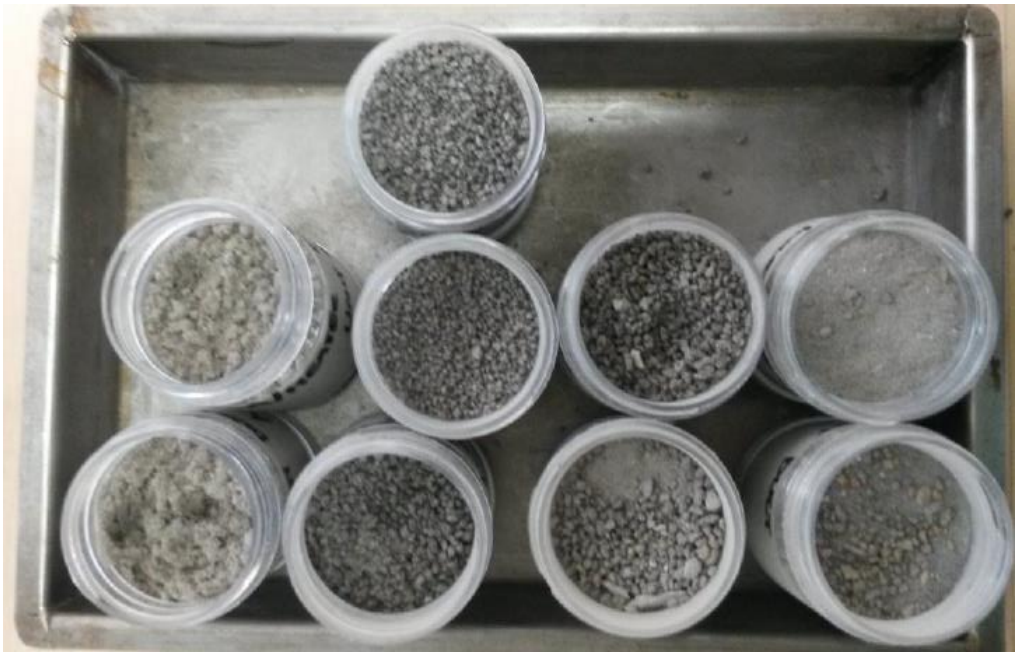

Figure 1.4: Visual features of the different air heater ash deposits. (Van Alphen, 2018)

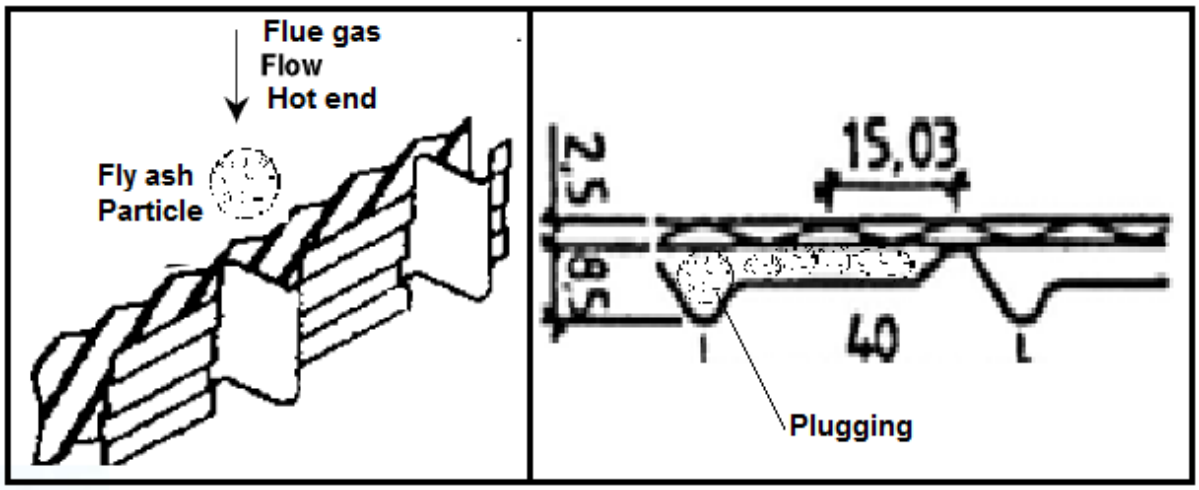

Figure 1.5: Effect of physical fouling of air heater elements

Dew point related fouling (Chemical fouling)

Chemical fouling is related to the accumulation of fly ash because of its chemical composition. When the fly ash particles start to adhere to each other and the element surfaces, a chemical

reaction occurs that changes the binding forces between ash particles. Sulphur dioxide and sulphur trioxide react with calcium rich fly ash to form anhydrite, and moisture. This occurs when sulphuric acid precipitates on the surface of the ash particles. These reactions are dependent on the temperature of the surroundings. The critical temperature is the dew point temperature. For instance, if the surrounding temperature is less than the acid dew point temperature, condensation of sulphuric acid, sulphurous acid and calcium sulphate will start to occur along with the formation of anhydrites. This temperature is not a fixed temperature, and varies according to the oxygen, sulphur dioxide, sulphur trioxide, and water vapour content in the flue gas. A reaction will occur according to the partial pressure of the sulphuric acid, sulphurous acid and water vapour (Van Alphen, 2018). Any alteration in the operating condition can change this temperature and pressure. Van der Hoven (1998) reports that in South Africa's coal fired power stations, the dew point is around 116-123°C. This estimate depends on the sulphur content in the coal, along with the moisture content in the flue gas. Sulphur trioxide already reacts with water vapour to form sulphuric acid but a condensate layer will exist on the surface elements when the metal temperature is less than the dew point as indicated in Figure 1.6.

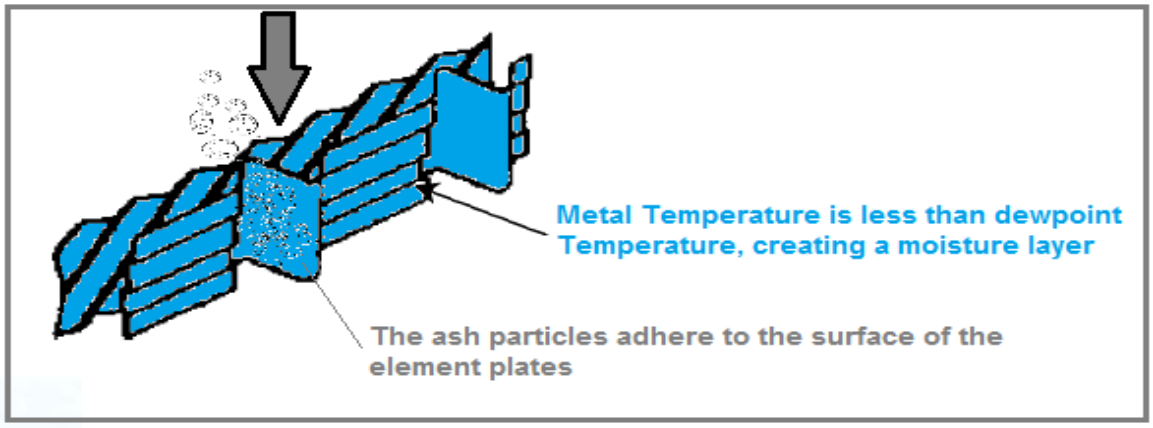

Figure 1.6: Effect of chemical fouling on air heater elements.

Moisture in coal plays a critical role as an impurity. From the inherent moisture and the surface moisture water vapour is released during combustion of coal. When this vapour is carried through to air heaters, condensation can occur causing fouling at the cold end of the air heater. Air heater fouling is stimulated by ineffective soot blowing. If the soot blowing system has any leaks, pressure losses will occur within the system. If the soot blower nozzle pressure is not maintained, the system will not produce enough energy to remove the deposits. Another problem that occurs is the fact that moisture is injected into the operating environment of the air heater. At the time of soot blowing dry steam is injected, but during periods after soot blowing, dry steam diffuses in to the perforated spaces of the element packs. This creates a change in the moisture content in the flue gas and also changes the partial pressure of water vapour along with the dew point temperature of the flue gas. Air at a temperature well below the dew point, enters the elements and condensation occurs on the element surfaces. This moisture layer then allows fly ash to adhere to the elements. Through applying high temperatures and drying air from the forced draught fans, the attached ash particles start to harden (can be seen in Figure 1.7). The soot blowing system is incapable of removing the hardened deposits. At this stage of fouling complete blocking of element packs is evident. This effect causes an increased pressure difference across the steel matrix.

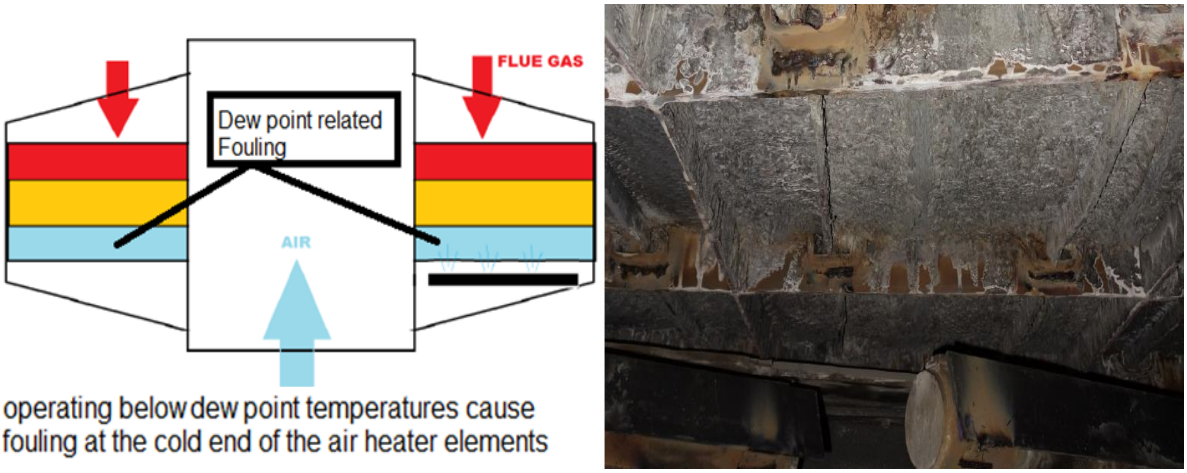

Figure 1.7: Blocked element packs due to ineffective soot blowing (Scheidegger, 2013)

1.2.3 Regenerative Air Heater model

The thermal analysis of air heaters is complex due to all the variables continuously influencing the dynamics of the system. The Regenerative Air Heater model, also known as the RAH model, was developed by Habbitts (1998) and De Klerk (2001) to provide detailed information on the thermal performance of these heat exchangers. This model is a simulation tool that accommodates both rotating-hood and rotating-matrix types of air heaters as explained in Chapter 2.2. It provides a platform to indicate what the effect of changes to variables will be such as flow rates, flow velocities, pressure rises and temperature excursions (De Klerk, et al., 2013). Another feature of the RAH model is to evaluate different packing arrangements of corrugated steel plates (element packs) with specified profiles and any given thicknesses and lengths. This model can be used to find the metal temperature profiles of the element packs, along with fluid temperature profiles. Input parameters such as rotational speeds, leakage, blockage and non-uniform inlet flow distribution, can also be simulated to illustrate what effect they will have on the thermal performance of the system. An additional feature is to evaluate the erosion rate on the elements caused by the fly ash particles (De Klerk, et al., 2013). The theoretical frame work of the RAH model is used in this project to develop a similar model in Excel Visual Basic Analysis format, where the factor of dew point related fouling is added to the capability of the simulation model. This simulation model is referred to here as VBA RAH model.

In the previous model the code was developed using Delphi. The Delphi format is not user friendly in terms of accessing and further altering and developing the code. This platform requires extensive training and measures to add different pack configurations and code alterations. The license to operate on Delphi is not freely accessible. The Visual Basic Analysis package exists within the freely accessible standard Excel platform and makes it easy to access and alter code to optimize a program. Therefore it was decided to redevelop the RAH model using VBA Excel. This also makes it easier to access the detailed calculations and to track any discrepancies in the calculation process. Any system engineer using Excel can now therefore use the VBA RAH model freely.

1.3. Research Motivation and Objectives

The aim of the project was to develop a rotary regenerative air heater simulation model to predict the onset of dew point related fouling. The simulation model should equip system engineers with the knowledge to enhance operating conditions and maintenance strategies, in order to prevent the onset of dew point related fouling. The study will also contribute to the possibility of increasing the life expectancy of air heater element packs and draught group components such as ducting, dampers and supple joints. The study also provides a platform to improve boiler efficiency, reduce maintenance costs and production losses, which will contribute to improved and sustainable operating of coal fired power generation plants. The current maintenance approach is reactive; creating preventative maintenance measures will be beneficial to Eskom.

The objectives of this research were defined by the following:

1) Identify dew point related fouling parameters with regard to coal composition, flue gas composition and process parameters
2) Carry out modelling of dew point related fouling conditions of a rotary regenerative air heater using the new VBA RAH model.
3) Verify the fouling conditions and simulated results by means of plant experiments to prove the accuracy of the model. The plant experiments were to include:
    - air heater fluid temperature measurements,
    - air heater metal temperature measurements,
    - air heater dew point temperature estimations,
    - coal analysis to give coal composition,
    - Flue gas analysis.

1.4. Research Methodology

Figure 1.8 is a schematic diagram illustrating the research methodology for this project.

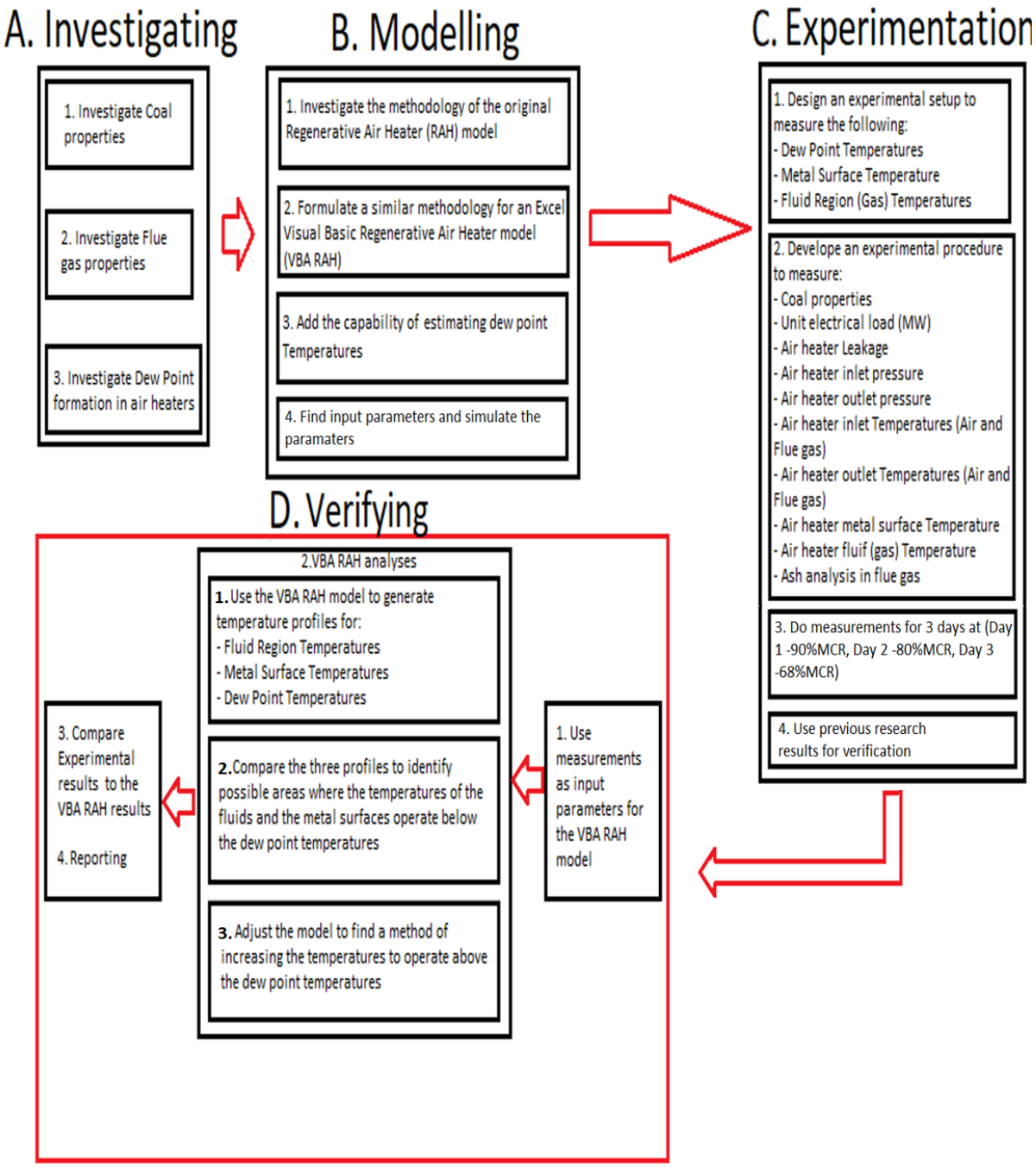

Figure 1.8: Research Methodology flow diagram

The method followed is divided into four sections. Section A is the Investigating phase, where coal properties are analysed to find the fouling parameters with regard to the chemical reactions that accompany fouling conditions. The coal composition also contributes to the second component which relates to the flue gas properties. The flue gas properties are found through the application of a mass balance. The chemical reactions formed during combustion, and in the downstream conditions, are analysed to find the reactions that cause dew point related air

heater fouling in the air heaters. These results are then used in Section B, where the dew point related fouling factors are incorporated into the VBA RAH model.

In Section B, the VBA RAH program was developed, based on the previous RAH program, to simulate temperature profiles for the regenerative air heater element pack metal surfaces, and the fluid temperatures. The model then also considers dew point related fouling through calculating the dew point temperatures for the identified critical parameters and comparing them to the metal surface temperatures of the elements. Chapter 3 elaborates on the theoretical basis used for the VBA RAH development.

Section C focuses on an experimental programme to verify the accuracy of the VBA RAH simulation model. The experimental design includes measuring of dew point temperatures, metal surface temperatures, and fluid temperatures. The method of installation is explained in Chapter 4. An important consideration is the procedure required to perform the experiment. To evaluate the accuracy of the model, all the input parameters had to be verified as accurately as possible.

Section D covers the method followed to verify the accuracy of the VBA RAH model. The gathered data were used as input parameters to the VBA RAH simulation tool. The fluid, metal surface and dew point temperatures were generated, giving graphical representations of the temperature profiles for the metal surfaces and fluids. An average dew point temperature was calculated and plotted with the metal surface temperature profiles. When the metal surface operates below the dew point temperature, condensation is expected to occur. The plant measurements were compared to the simulation results, and this information was used to indicate whether the model can be an acceptable method to predict the onset of dew point related fouling. Furthermore, methods of altering design configurations and operating parameters were identified and analysed to find a method of reducing dew point related fouling. (Discussed in Chapter 5)

2. LITERATURE REVIEW

2.1 Function of Air Heaters

Figure 2.1 is a schematic representation of the operation of the boiler in a coal fired power station. Coal is supplied to a milling plant, which pulverises the coal to a specified combustible size. A Primary Air fan generates a draught to dry and transport the pulverised coal to the burners of the combustion chamber. The FD (Forced Draught) fan supplies secondary air to the burners for complete combustion of coal. Both the primary and secondary air are first heated by means of a recuperative or a regenerative air heater. During combustion a large portion of the generated heat will be transferred to the boiler steam pipes and walls, to generate steam. The remainder of the gases, also known as flue gas, will be extracted by means of an induced draught (ID) fan. The heat from the flue gas is transferred downstream in the regenerative and recuperative air heaters to increase the primary and secondary air temperatures for optimal efficiency. To maintain the optimal boiler performance, most of the rejected heat exiting the system must be recovered effectively to increase boiler efficiency.

If the boiler efficiency is not maintained, higher volumes of fuel and air are required to maintain the required electrical load. As a result the FD fans need to supply increased volumes of air and the ID fans need to extract greater volumes of flue gas. Due to the fact that these volumes pass through the air heaters (Figure 2.1), it is required that flow is not restricted to the extent where the fans are incapable of supplying, or extracting these volumes. If the restriction in flow increases to an extent that the fans cannot maintain the required capacity, it is required to reduce the generated electrical load to allow safe operation. Air is supplied in excess to promote complete combustion and safe operation. As per the Fossil Fuel Firing Regulation requirement (ESKOM, 2018), the excess air must at all times be adequately higher than stoichiometric conditions, to prevent an increase of carbon monoxide levels. Carbon monoxide is generated during the combustion process. High levels of carbon monoxide after combustion usually indicate that the air supplied is less than the required stoichiometric quantity. This occurrence promotes boiler explosive and implosive conditions. Therefore excess air must always be maintained above the design quantity for each power station (ESKOM, 2018). This calculated excess air consists of a safe oxygen percentage which allows the boiler to run above stoichiometric conditions. This oxygen value is compared to a measured oxygen reading taken at the air heater flue gas inlet duct.

The critical air for combustion is supplied through primary and secondary air. If air heaters have high leakage rates and fouled element packs, a risk becomes evident that the flow of the secondary air and flue gas are restricted. During this occurrence the safe excess air condition may not be maintained, which then leads to a required reduction in load to ensure that the FD fans supply enough air for safe operation and the ID fans maintain the furnace pressure with adequate capacity to extract the flue gas. This is a common occurrence at Eskom coal fired power plants, and this research aims to reduce the restrictions caused by air heater blockages.

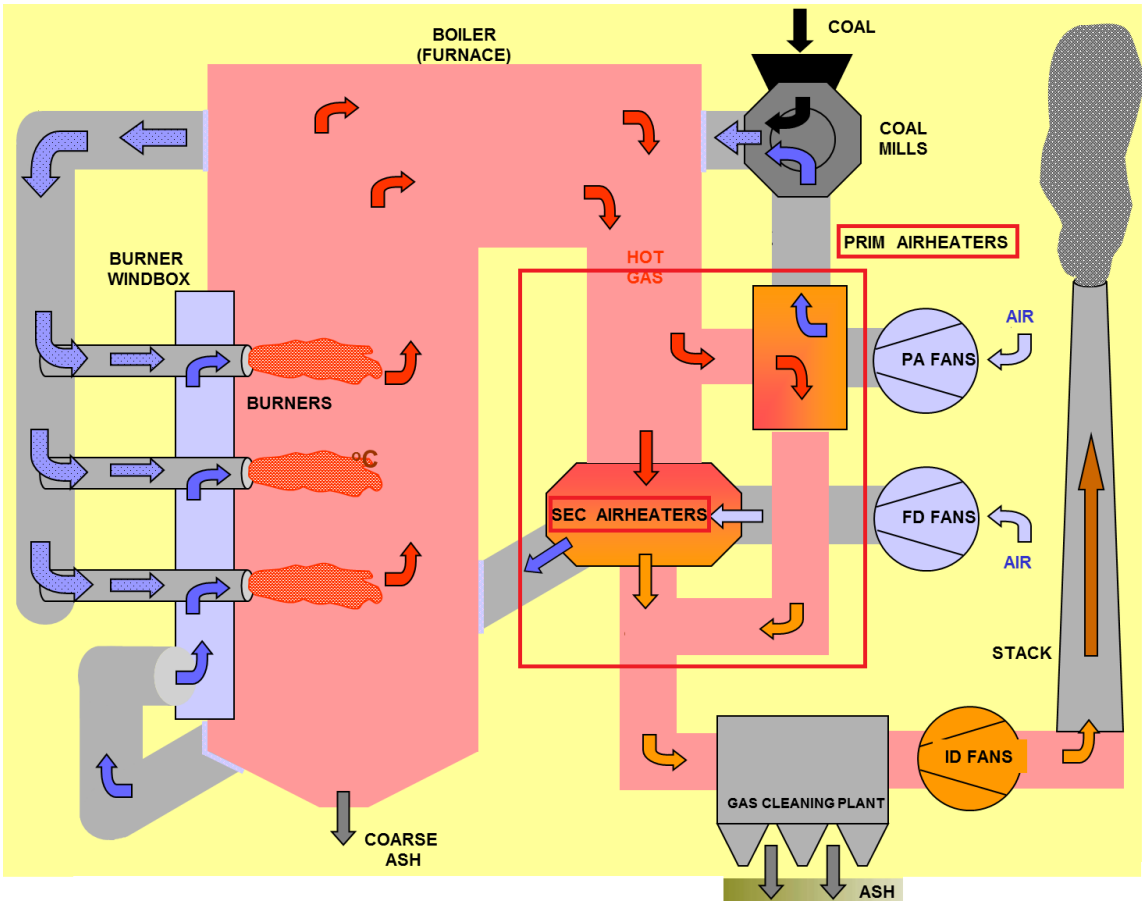

Figure 2.1: Boiler Plant with a recuperative- and regenerative air heater.

Air heaters are the medium for the exchange of thermal energy between the flue gas and the cold air supplied for combustion. Power stations may either have the two air heaters (regenerative and recuperative) combined or separated (Figure 2.2). The combined design incorporates both primary and secondary air into one air heater, exchanging heat with the extracted flue gas. These designs allow flue gas to enter a steel matrix and pass through stacked element plates, where the heat from the flue gas is transferred to the plates. Both primary and secondary air then pass through the stacked element packs which allow the heat from the plates to be transferred to the air passing through.

In the case of separated air heaters, usually the primary air will be preheated by means of a recuperative (tubular) air heater and the secondary air with a regenerative (rotating hood or rotating matrix) type of air heater. A recuperative air heater consists of a bundle of tubes containing the extracted flue gas, transferring heat to the primary air, which is forced by means of cross flow through the passages between the tubes. Therefore the two streams are designed to be completely isolated to avoid leakage from the air stream to the flue gas stream. The secondary air will be heated using a rotary regenerative air heater, also using flue gas that is forced through a steel matrix of stacked plates to transfer heat to the secondary air that is forced, in counter flow, through the heated plates. For this research the focus will be on rotary regenerative air heaters of both the rotating hood and rotating matrix types. Recuperative air heaters do not promote high blockage and leakage rates in comparison with the rotary regenerative air heaters and are therefore excluded from the study.

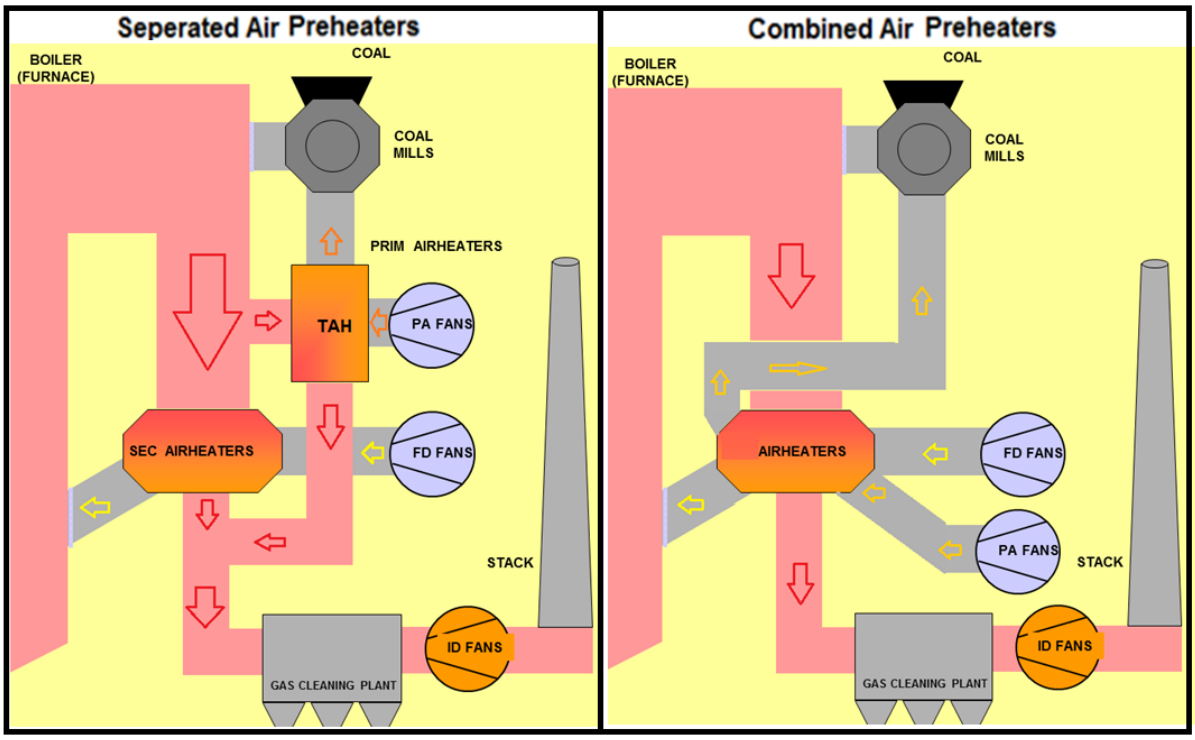

Figure 2.2: Air heater types for a split air preheating setup for primary and secondary air (Spot, 2016; Mathebula, 2014).

2.2 Air Heater Types

There are two types of rotary regenerative air heaters, namely rotating hood and rotating matrix types (traditionally known as Rothemühle and Rothemühle/Ljungström respectively). The distinguishing factor between the two types is the design of the steel matrix assembly.

2.2.1 Rotating Matrix Type

These air heaters are rotary, counter-flow, steel plated matrix regenerative air heaters. They are used with either a vertical or horizontal axis of rotation. The vertical axis installation is preferable because it is easier to be maintained (De Klerk, 2001). Most power stations have two 50% duty air heaters. The rotational speed of the rotor is between 0.5 and 3 revolutions per minute, depending on the required heat exchange and flow properties of the air and flue gas (Chojnowski, 1981). There are three types of rotating matrix air heaters, as shown in Figure 2.3. The first type is a Tri-sector, containing one flue gas passage, a primary air passage and a secondary air passage. The Bi-sector type has one passage for secondary air and one passage for flue gas. The Quad-sector consists of two secondary air passages that are divided by a primary air passage, along with one flue gas passage on the opposite end.

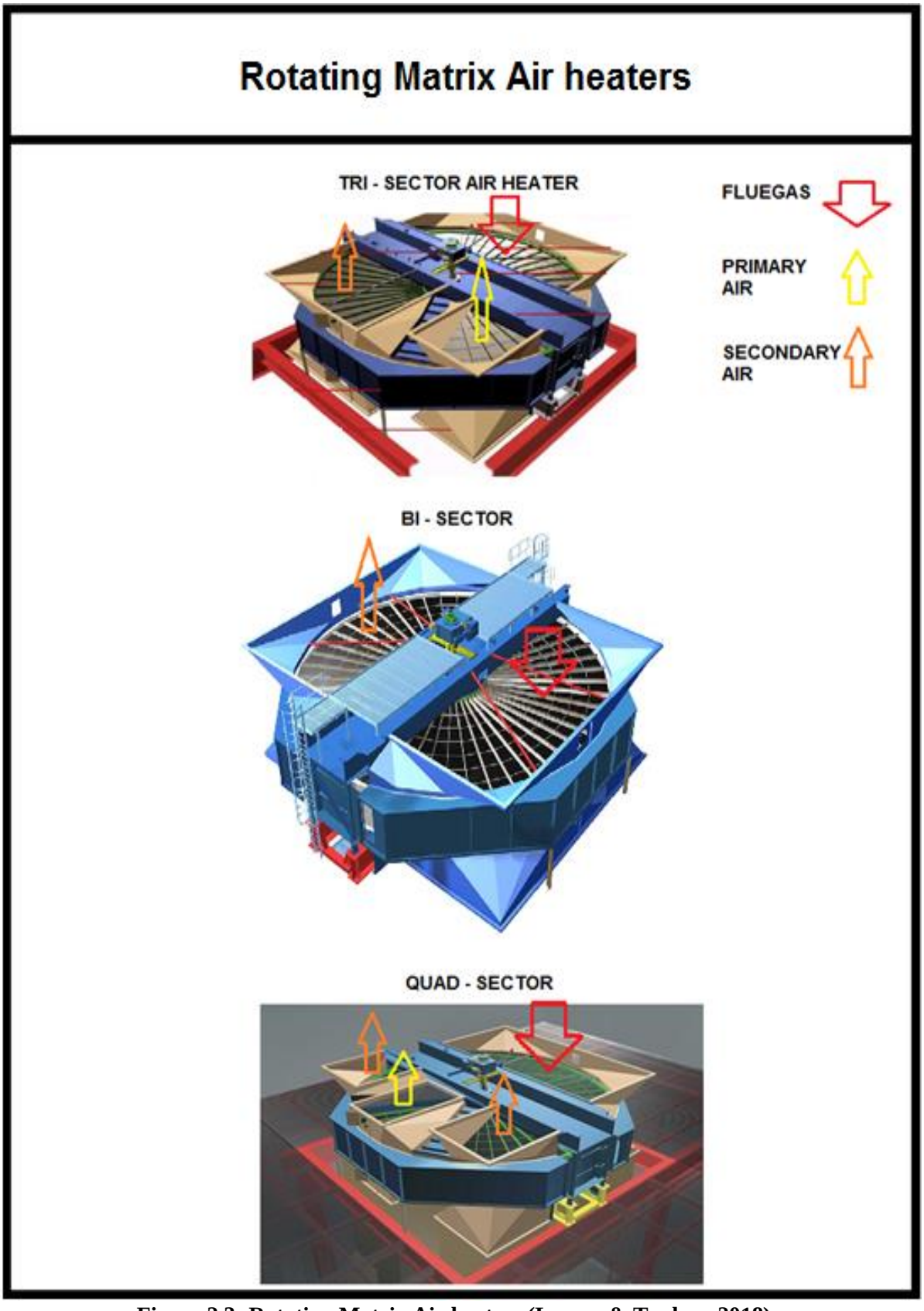

Figure 2.3: Rotating Matrix Air heaters (Larsen & Toubro, 2018).

2.2.2 Rotating Hood Type

The rotating hood air heater operates with similar heat transfer principles to the rotating matrix air heater, but the rotary part is the hood and the steel matrix is stationary (stator). The hoods are designed to provide the air passages, and the open areas between are the passages for the counter flowing flue gas. There are two types of rotating hood air heaters, which are illustrated in Figure 2.4. The two types are the single flow and dual flow air heaters. The single flow has a bottom and top hood which guide the secondary air through the steel matrix. The flue gas passes through the open areas. The dual flow type has an inner and outer hood and provides for heating of the secondary air. The inner hoods are located in the centre of the rotor. The outer hoods are located in the outer shell as shown in Figure 2.4.

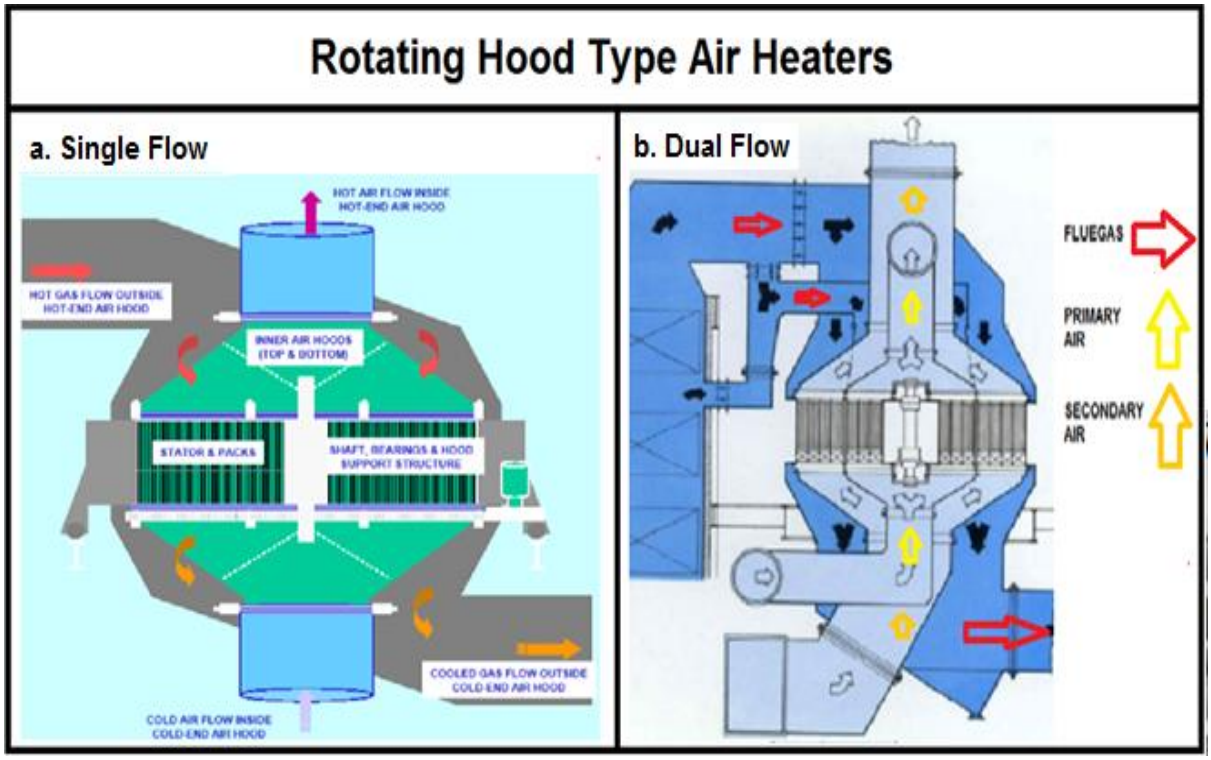

Figure 2.4: Rotating hood Air heater types (Kleynhans, 2015)

2.2.3 Air Heater Steel Matrix Layout

Each boiler design requires a calculated quantity of heat to be gained by the inlet air utilizing the air heaters. To achieve the design value of the required heat gain, there are certain design aspects of the air heaters that can be altered to enhance the heat transfer in the air heater. One of the design aspects is the layout of the steel matrix. The layout can change in terms of the layer quantity and the element pack heights. Layers are the vertical stacking of the element packs. Most Eskom power stations use two, three or four layer setups. Figure 2.5, is a representation of the three different layer setups. The steel matrix is constructed with radial and circumferential braces. These braces form pockets, also known as sockets, for the element packs to be inserted. In Figure 2.5 the blue blocks can be seen as the element packs and the grey area is the steel matrix. The elements are closely packed corrugated metal sheets, formed

according to a specific profile. The Hot End is the side where the flue gas enters, and therefore these element packs are exposed to higher temperatures.

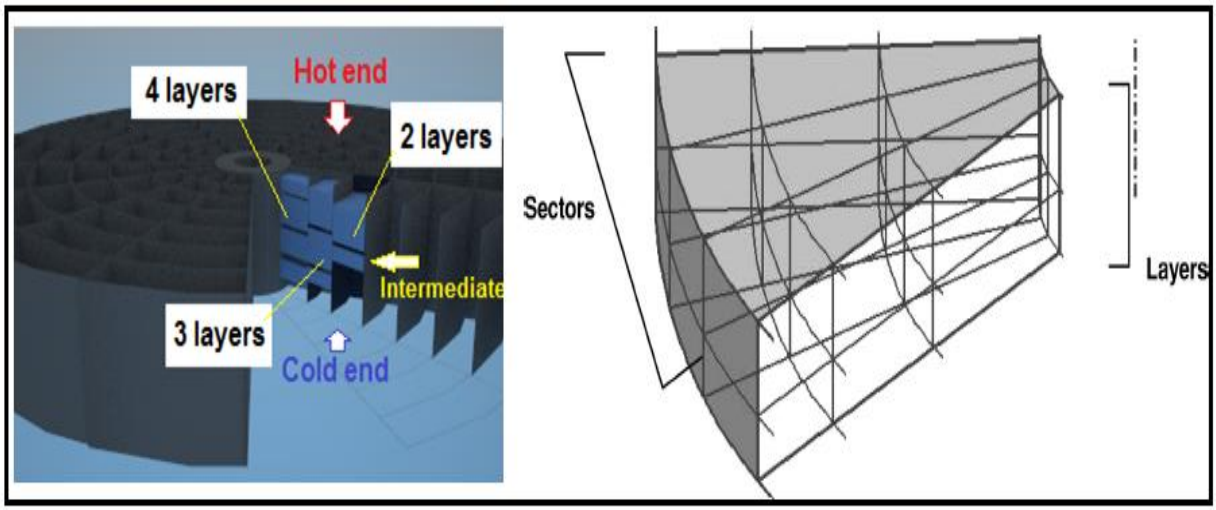

Figure 2.5: Different layer setups of the element packs in the steel matrix (De Klerk, et al., 2013).

At the Cold End all the element packs are exposed to the incoming air, which is at a lower temperature at the bottom of the steel matrix. The intermediate area is the set of element packs in between the hot end and cold end element packs. Blockage tends to start at the cold end of the steel matrix due to the fact that the metal temperature at times could operate below the dew point, causing components in the flue gas to condense, which then creates acid deposition and also increases the adhesiveness of the fly ash particles to the corrugated plates. It is critical to maintain the metal temperature above the dew point temperature to avoid blockage of the element packs (Figure 1.7 section 1.2.2).

Air heater element packs are metal sheets packed closely together to ensure that the heat transfer area is increased. The plates are thin steel sheets. The close stacking of the plates allows enough resistance in the flow to increase the time of the exposure to the heat source for optimal heat transfer to occur. To ensure that efficient heat transfer occurs, the profile of the plates becomes an important property to consider during the designing of an air heater. The packs are usually packed with many pairs of plates, with each plate having a different geometry. One of the plates will have gas flowing in line with the corrugation, while the other plate will have the gas flowing at an angle to the corrugation. The plate with a profile allowing corrugation to be in line with the flow is known as the notched plate. The plate that allows flow at a specified angle is known as the undulated plate. In some cases plates are also packed with double undulated plates. The element packs are supplied in different packing configurations. They can be supplied with a frame keeping all the plates together as one cased pack, or a basket can be used for each pack of elements. During installation, the packs without casings may be trimmed unevenly to fit into the steel matrix, causing high erosive areas due to increased flow areas. Erosion rates are increased to the extent that the element pack supports are eroded away. Figure 1.1(Section 1.1) also illustrates this effect, where the erosion tends to be higher in the areas with large gaps between the steel matrix and the element pack. Figure 2.6 is an illustration of the different types of packing methods as explained above.

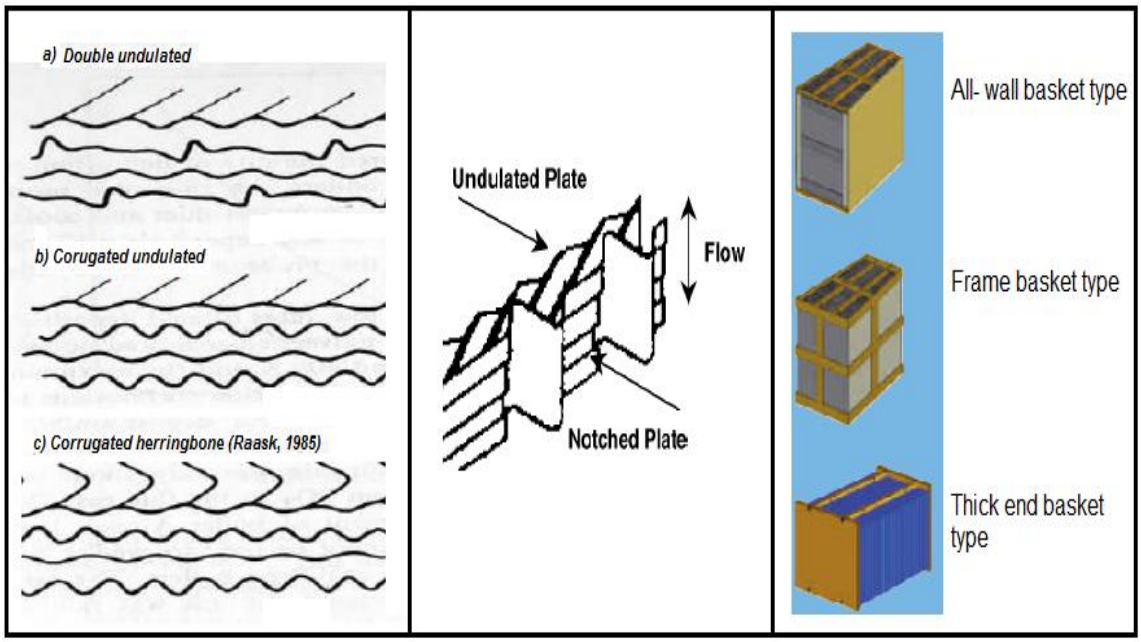

Figure 2.6: Element plate packing types (De Klerk, et al., 2013)

The profile of the plates depends on the design criteria for the application, which was investigated by Gruen (Gruen, 1998). Air heater elements can generally be evaluated according to their pressure drop, thermal properties, fouling, and corrosion and erosion performance. Figure 2.7 illustrates various design profiles, which affect the thermal performance of the air heater as well as the other criteria. Important design considerations are the material, geometry and the thickness. A high performance in one aspect can result in poor performance in another aspect. If the profiles restrict flow more, the possibility of fouling will increase, due to expected lower outlet temperatures for the flue gas. If the thermal performance is high, the flue gas outlet temperature can be affected to the extent that the metal temperature will be below the acid dew point at the cold end, also promoting fouling. The required system efficiency and coal characteristics will establish what the desired performance will be, which will provide guidance to choose the correct profile. By selecting the correct profile, the life expectancy will be maximized and maintenance costs will be minimized.

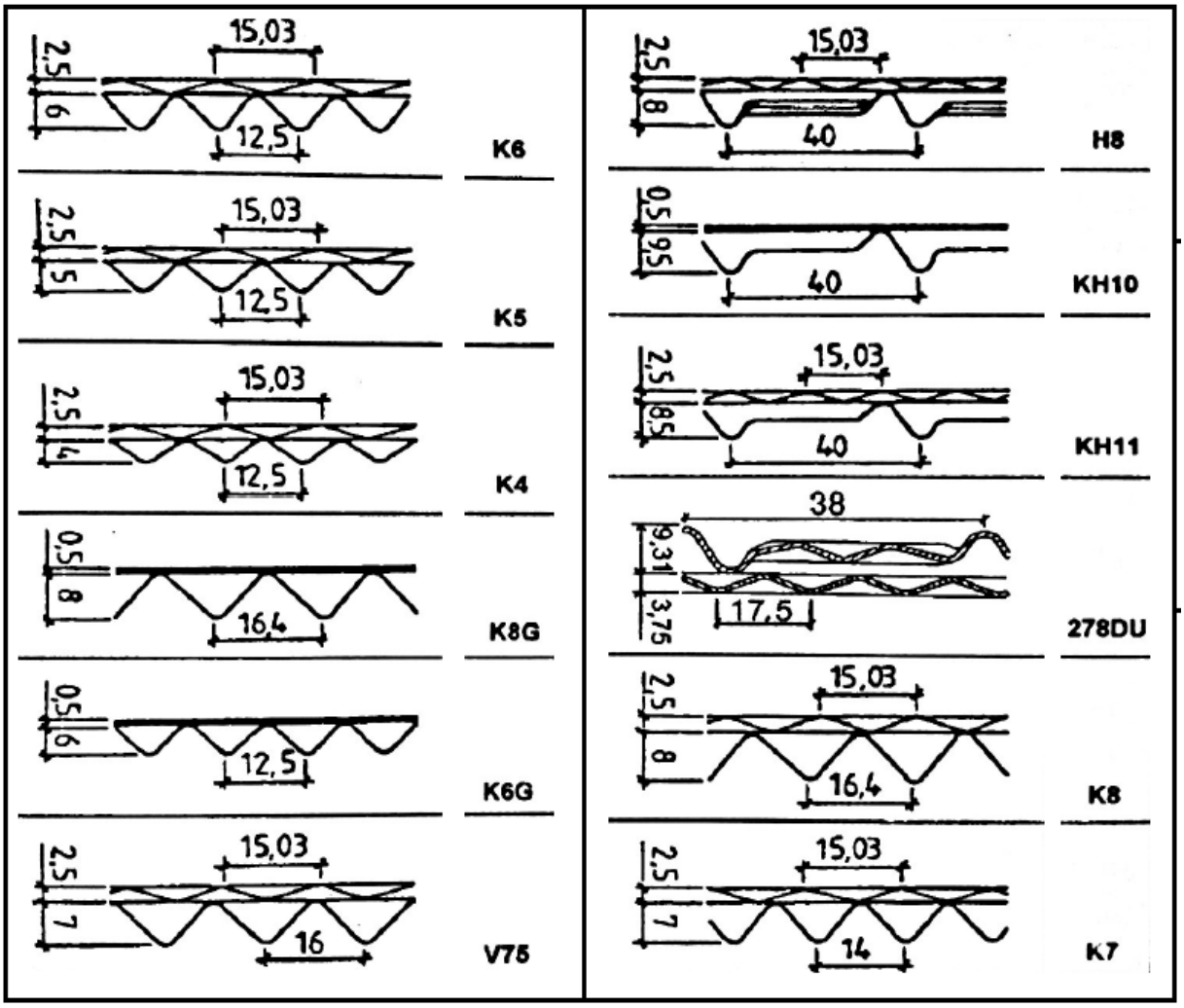

Figure 2.7: Various profiles of heat transfer elements (Gruen, 1998)

The thermal performance of rotary regenerative air heaters has been researched in a collaborative effort by Eskom's Technology Services International and the School of Mechanical, Industrial and Aeronautical Engineering at the University of the Witwatersrand. This research activity established a sound platform to provide sufficient knowledge to optimise the design and operation of rotary regenerative air heaters. Part of this knowledge was the development of a computer simulation program by Habbitts (1998). This program simulates the air heater thermal performance, allowing the flue gas stream outlet temperatures to be generated. The program further estimates pressure drop across the steel matrix and the surface metal temperature of the steel elements. The program was later enhanced by De Klerk (2001) through adding the capability of having non-uniform inlet flow velocity and also the option to alternate the plate thicknesses of the element sheets. Research with regard to erosion wear was investigated by Crookes (2000), to establish the erosion experienced on various geometries of steel elements. Fouling was later investigated by Mabena (2003), to identify and rank factors causing fouling in boiler regenerative heat exchangers. The correlation of fouling rates with respect to the operating conditions for various coal fired power generation stations were investigated, along with the comparison of fouling problems specific to each station. This information was researched to establish a set of guidelines to reduce fouling. Further investigations were done to establish composition of flue gas entering the air heater along with formation of corrosive conditions generated downstream. The classification of the fouling mechanisms in a regenerative rotary air heater was investigated by Mathebula (2014).

2.3 Research related to Regenerative Air Heater Modelling

An experimental investigation of heat transfer in regenerative air heaters was done by Caby (1996) with the objective to build and commission an experimental facility (Figure 2.8), suitable for high performance regenerative heat exchanger surfaces.

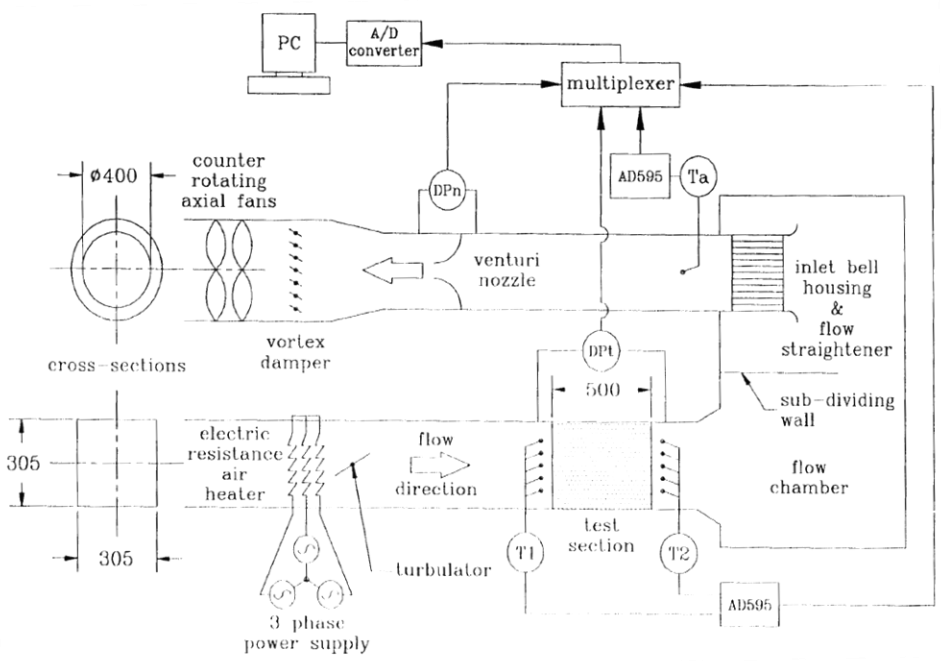

Figure 2.8: Schematic view of the test rig used by Caby (1996).

A computational procedure was developed to determine the heat transfer performance and flow friction characteristics of these surfaces. Mullison and Loerhke (1986) developed a numerical technique using a finite difference method, which was the basis of the numerical procedure for heat transfer performance developed by Caby. The fluid region and wall region are divided into a network of nodes using an implicit formulation equation that was converted to a finite difference equation as explained in chapter 3. This research contributed to the development of a computer simulation of power station rotary regenerative heat exchangers by Habbitts (1998). The technique considers an elemental volume, which consists of half of the fluid thickness and half of the plate thickness with an incremental length Δx. This element is extracted from a series of parallel flat plates (Figure 2.9).

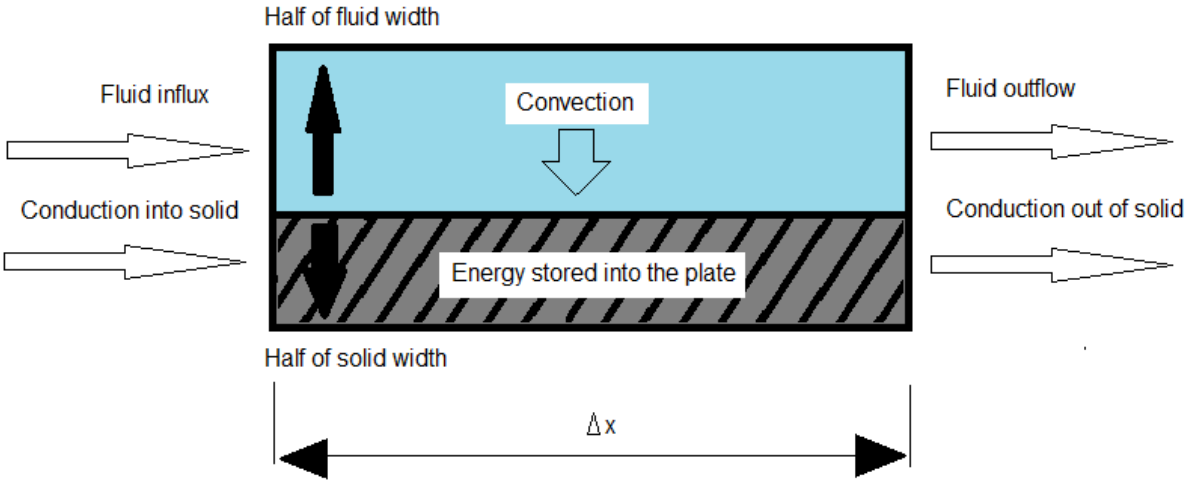

Figure 2.9: Basic element on which the model is based with the relevant heat transfer.

The heat transfer across a finite area is analysed, and by using numerical methods the complete temperature profile of the surface temperature and gas temperature are established. Kumar (1998) researched the heat transfer characteristics of air heater elements. The various geometries of the commercially available element profiles were considered to evaluate the effect each type has with regard to the heat transfer characteristics and heat transfer coefficients of the elements. Kumar used the test rig, commissioned by Caby, to evaluate the performance of various air heater packs used in Eskom power plants. A computer based data acquisition reduction program was used to find the heat transfer coefficients. A comparison, by means of the direct curve matching method, was done between the theoretical exit fluid temperatures, estimated through the finite difference analysis method, and the measured values. The heat transfer coefficient of each element pack type was obtained along with an equation illustrating the relationships between the Colburn j factor and Reynolds number, and the Fanning friction factor and Reynolds number. These relationships provided a theoretical method of calculating heat transfer coefficients and pressure drops across the packs respectively. The method is elaborated in Chapter 3, sections 3.2.2 and 3.2.3.

The Fanning friction factor relationship was used by Gruen (1998) to establish the pressure loss for the commercially available element packs. Gruen compared the hydraulic and thermal performance of these elements, and tested eroded packs using the same procedure in comparison with a new set of element plates. Twelve different non-eroded element pack profiles were tested along with one eroded element pack. A Rothemühle H8 type test pack was tested to verify the accuracy and reliability of the test facility in comparison with the results found from the Rothemühle test facility in Germany. The results showed that the test facilities provided closely-correlating results.

The measurements also confirmed the theoretical expectation of an inversely proportional relationship between the heat transfer coefficient and the hydraulic diameter, and differential pressure and hydraulic diameter. A lower heat transfer coefficient was found with profiles consisting of a flat counter plate than profiles with an undulated counter plate. The eroded pack was tested three times, with a 20% mass loss during the first test, a 30% mass loss during the second test and a 40% mass loss for the third test. The test results were compared to one non-eroded element pack. This test concluded that irrespective of the extent of erosion, the results yielded a 15% lower pressure drop for the eroded plates with no significant change in the heat transfer coefficient.

Caby (1996) and Gruen (1998) used a multiple plate model to determine the heat transfer and pressure drop correlations of a complete pack. These correlations were later used in the model of Habbitts (1998). The pack type, inlet conditions, and geometry can be selected to analyse the thermal performance for each section for every point in time, until a full rotation is complete. This model was used to simulate a rotating hood (Rothemühle) air heater located at an Eskom Power Station. For this station, Unit 5 was selected as it was instrumented for monitoring the change in thermal conditions as part of the basket modification to the element packs (As indicated in Figure 2.6). According to Habbitts various factors affecting the real plant were not considered in the simulation model, which influence the results for the model. These factors were the following:

- Non-uniform velocity distributions across the faces of the matrix exposed to a particular stream.
- Heat transfer to the surroundings.
- Fouling.
- The mass of the basket support framework.
- Thermal conduction in directions other than parallel to the direction of flow.
- The effect of the gaps that exist between the layers.
- Heating or cooling of the plates under the seals.
- Radial temperature variations.

Comparing the measurements with the simulation model results of Habbitts, an adequate result was yielded with regard to thermal performance. The pressure drop from the simulation was still a concern, with an error of 30%, which was a result of external factors such as the effect of leakage on pressure drop and fouling of elements, not considered in the model. In addition the model also had the capability to generate an economical forecast of the air heater. It could be used to predict the increase or decrease in cost due to a particular change made to the input data of the thermal performance calculation.

De Klerk (2001) improved the simulation model by extending the model with the option of using alternating thicknesses of plates, simulating the effect of non-uniform velocities, and determining the effect of misdistribution of flow. De Klerk also implemented a numerical procedure developed by Gruen to accommodate perforated packing. The model was verified through plant experiments. The economic model developed by Habbitts was enhanced through basing the improved model on the net present value of costs.

2.4 Research Related to Dew Point Related Fouling

Eskom power plant air heaters experience conditions of fouling, which initiated research to analyse fouling. In 2003 Mabena researched fouling in regenerative air heaters, with the objective to identify and rank factors causing fouling. Previous research and Eskom power station information were used to complete the objectives of the research. Fouling rates were correlated with relevant operating conditions, along with a comparison of regenerative air heater fouling problems between Eskom power plants. These results were used to create a set of guidelines for boiler operation and maintenance of regenerative air heaters, to prevent the occurrence of fouling. The results concluded that fouling improvement for a particular air heater cannot be a general solution due to the amount of variables influencing the occurrence of fouling. These variables are the type of fuel used during combustion, heat transfer surface

geometries, soot blowing conditions and operating conditions. Fourteen guiding points for draught plant engineers were proposed to reduce the occurrence of fouling.

1. The excess oxygen after combustion, measured at the air heater inlet should be maintained between 3% and 3.5%. According to Mabena (2003) the SO_3 production is lowered which also reduces the deposition rate of sulphuric acid. This can reduce the risk of fouling.

2. It is recommended that the air inlet temperature of the air heater should be above 45 ºC to ensure that the cold end element surfaces do not operate below the acid dew point set point temperature of 90ºC.

3. The flue gas flow rate must preferably be high to provide higher velocities, without exceeding the allowable pressure drop. The air heater performance is increased with higher velocities (RAH model to be used for optimisation).

4. The acid deposition rates are reduced when the rotational speed is high. Ideally small air heaters should operate at a speed of 1.6 rev/min and larger air heaters should operate at 0.9 rev/min (RAH model to be used for optimisation).

5. The total layer height should be chosen according to the selected plate profiles during routine pack replacements. This would ensure enhanced air heater performance, which will not promote fouling (RAH model to be used for optimisation).

6. To avoid high pressure drops across the air heaters, the number of layers should be 2 or 3 layers. When the number of layers exceeds this range, the change in thermal performance becomes negligible, although the pressure drop will be increased. High pressure drop across the air heater is not an ideal practice, due to the fact that the fans would operate at a higher capacity to overcome the resistance from the element packs in the steel matrix.

7. During a pack installation it is required that the cold end elements are installed at a height of 150 mm from the soot blowing nozzle to ensure all the deposits are removed.

8. Mild steel sheets are the correct material and not Corten, to reduce the capital costs by 20%. The material properties are similar and therefore the performance will remain the same.

9. For draught plants having ash hoppers at the economiser, careful consideration should be given to the method of emptying the ash hoppers, to prevent coarse ash and debris from reaching the hot end heating elements.

10. Soot blowing must be applied according the required time intervals. For stations experiencing fouling of air heaters, soot blowing must be done every 8 hours. It must be noted that soot blowing is installed to avoid ash deposition and not to remove previous build-up ash deposits.

11. Leaking economiser tubes and fire system tubes must be detected to limit the occurrence of fouling. Water causes a sticky ash deposit that adheres to the element surfaces causing blockage of elements. Soot blowers do not remove these deposits effectively. The pressure at the nozzle must be checked to ensure that adequate pressure is supplied to remove deposits. The soot blower drainage system must be used effectively to ensure the use of dry steam for soot blowing at all times.

12. The soot blower nozzles can be fouled when fly ash, from the flue gas, erodes the nozzles to the extent where ash accumulates inside the system causing insufficient soot blowing of heating elements. The nozzles need to be inspected on a regular basis, specifically the nozzles located on the flue gas outlet side.

13. Low pressure washing is required immediately after economiser tube leaks or fire system leaks. This will avoid drying and hardening of deposits in the element packs. The air heater rotational speed must be reduced to enhance the washing process.

14. According to research done by Bailey (1999), higher fouling rates are found on fouled surfaces. Therefore, during high pressure washing, it is important to thoroughly clean the element packs to their original condition to avoid higher rates of fouling.

Mabena also concluded that the deposition rate was directly affected by the amount of CaO in the ash. High CaO level in the ash would usually be associated with low acid deposition, and low CaO would result in high ash deposition, although it will contribute to the hardening of fouled deposits. Figure 2.10 is an illustration of the variation in temperatures within a heat storing matrix of a rotary regenerative air heater (Raask, 1985). In this figure, van der Hoven (1998) also illustrated that at the cold end sections of the element packs, temperature below the acid dew point temperature is experienced. During the phase where cooled segments of the heat exchanger leave the air stream and enter the flue gas stream, the temperatures of the elements increase rapidly at first, but then change to a slow increase in temperature. In this period T_1 and T_2 in Figure 2.10 shows the change in temperature and also indicate in which region condensation will occur due to the surface temperature operating below sulphuric acid dew point conditions.

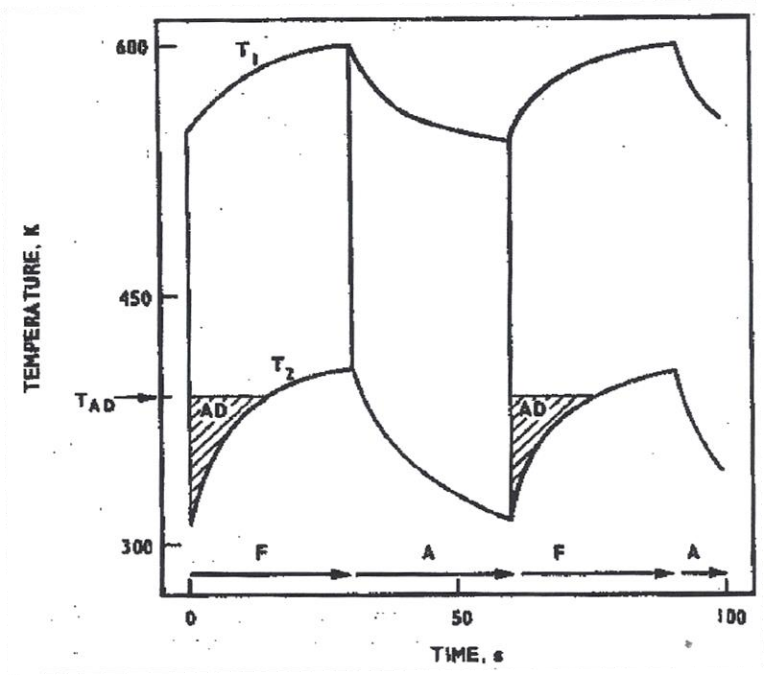

Figure 2.10: Dew point and metal temperature of rotary regenerative air heaters: T_1 - Heat exchanger inlet temperature, T_2 - heat exchanger outlet temperature, T_{AD} - acid dew point temperature, AD - Acid deposition, F - heating phase of air, A - cooling phase of flue gas (Raask, 1985).

The typical curves for high and low rates of acid deposition on a cooled probe inserted into an air heater of a coal fired boiler can be seen in Figure 2.11. A test was conducted by Raask (1985) and Peterson (1991), where air cooled probes were used to measure the rate of sulphuric acid deposition. Curve "A" shows that the dew point temperature is approximately 405 K and the deposition rate is 4.0 mg/m^{2}s. This rate corresponds to about 10 ppm (parts per million) of SO_3 in the flue gas. Another test was conducted on a different coal fired boiler, and the maximum deposition rate was only about 0.8 mg/m^{2}s, as show in Figure 2.11 curve "B". This is equivalent to about 1 ppm of SO_3 in the flue gas. The sulphur content of the coal used in test "B" was 1.5% versus 0.9% for test "A". According to Raask (1985), the sulphur content of fuel itself cannot be used as the only factor of prediction of the rate of acid deposition. The rate of acid deposition was low with coal "B" due to the high calcium content in the coal and a large quantity of SO_3, formed in the combustion flame, reacted with the calcium oxide to form sulphate (Mabena, 2003).

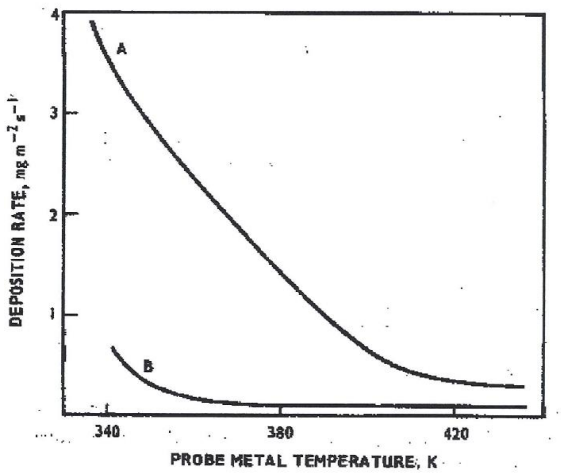

Figure 2.11: The effect of ash composition on acid deposition in pulverised coal fired power boiler air heaters: A - low calcium ash and 0.9% sulphur in coal, B - high calcium ash and 1.5% sulphur in coal (Raask, 1985).

The results presented by Raask (1985) yielded that deposition was also affected by the alkalinity of ash, mainly calcium oxide content. Therefore, not only sulphur must be considered when calculating the deposition rate. The following equation is an illustration of the deposition rate for a system consisting of flue gas and ash (Raask, 1985):

$$R = m\left\{\frac{xS-[(0.8Ca_{sol}+0.7Na_{sol})(1-kW^{2/3})]}{S}\right\}^{3/4} \quad \text{(mg/m}^2\text{s)} \tag{2.1}$$

m – A constant depending on boiler combustion conditions
x – A fraction of coal sulphur oxidized to sulphur trioxide
S – Sulphur content in coal
Ca_{sol} – Weight percentage of dilute-acid-soluble calcium in coal
Na_{sol} – Weight percentage of dilute-acid-soluble calcium in coal
$(1 - kW^{2/3})$ – Represents the fraction of calcium and sodium captured by fused ash at high temperature and sulphur not available for reactions with SO_3
k – Constant
W – Ash content of coal

The above equation can be used together with Table 2.1 to estimate the deposition rate of sulphuric acid. This table was generated by using an excess oxygen percentage of 4%.

Table 2.1:SO3 concentration, dew point temperature, and acid deposition in coal fired boilers (Raask, 1985).

Type of coal	Sulphur in coal (%)	CaO in ash(%)	SO_3 in flue gas (ppm)	Dewpoint temperature (K)	Max. acid deposition rate ($mg.m^{-2}.s^{-1}$)
High sulphur, low calcium	>2.5	2-5	10-25	400-410	5-10
Medium sulphur, low calcium	1-2.5	2-5	5-10	295-400	2.5-5
Medium sulphur, medium calcium	1-2.5	5-10	1-5	285-295	1-2.5
Low sulphur, high calcium	<1	>10	<1	<285	<1

A deposition sampler was mounted in the economiser exit gas duct to determine the relationship between boiler operating parameters and acid condensation rates. The test was conducted by D'Agostini et al (1989a), where a gold plated deposition surface was kept at a constant temperature below the acid dew point. Operating conditions were varied to evaluate the effect on acid deposition. When the operating parameters were kept constant and the excess air was increased the acid deposition rate increased, and the rate decreased at lower excess air. 1%, 2% , 4% and 5% of excess oxygen were used during this test. The results found by D'Agostini correlated with the results found by Raask. Figure 2.12 is an illustration of the experimental setup used by D'Agostini, and Figure 2.13 is a graphical representation of the results from the research done by Raask (1985).

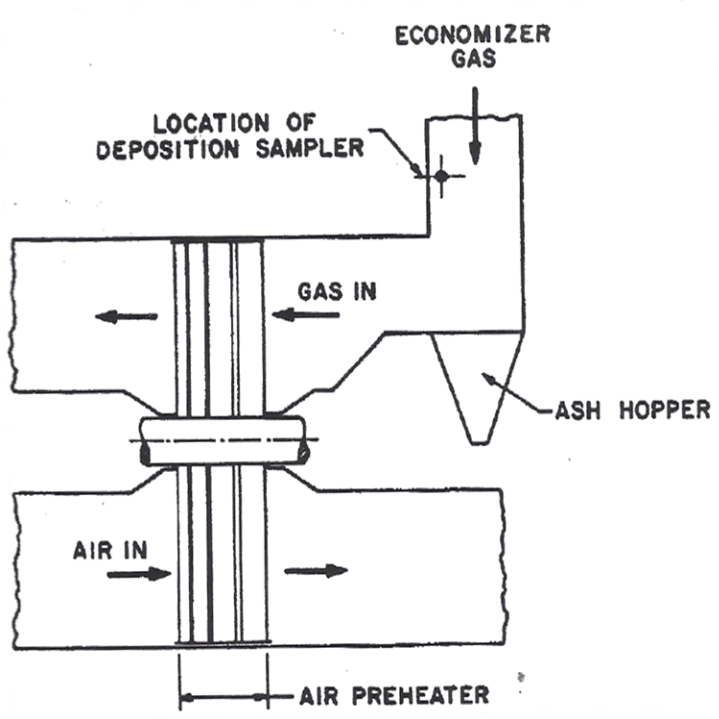

Figure 2.12: Location of the deposition sampler installed at the economiser exit duct (D'Agostini, et al., 1989).

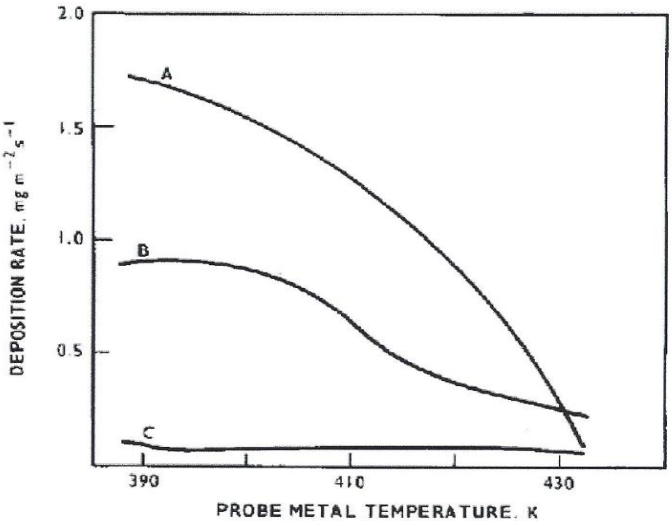

Figure 2.13: The effect of flue gas oxygen on acid deposition in pulverised coal fired boiler air heaters: A = 3.9% oxygen, B= 3.1% oxygen, C = 2.1% oxygen (Raask, 1985).

The effect of variations in flue gas flow rate was tested by varying the unit load from 300 MW to 585 MW, while all the other control parameters were kept constant. The condensation rate was found to be higher at higher loads and lower at lower loads. A study done by Jones (1993) came to an opposite conclusion. Jones stated that increasing the flow rate caused a reduction in residence time, therefore less time is available for acid deposition. This contradiction revealed that the position of the sampler plate is important. The mass of sulphuric acid and the partial flue gas composition in the duct varies at different positions, which could influence the deposition rate accordingly. Figure 2.14 shows the results found from the tests conducted by changing the load (Raask, 1985).

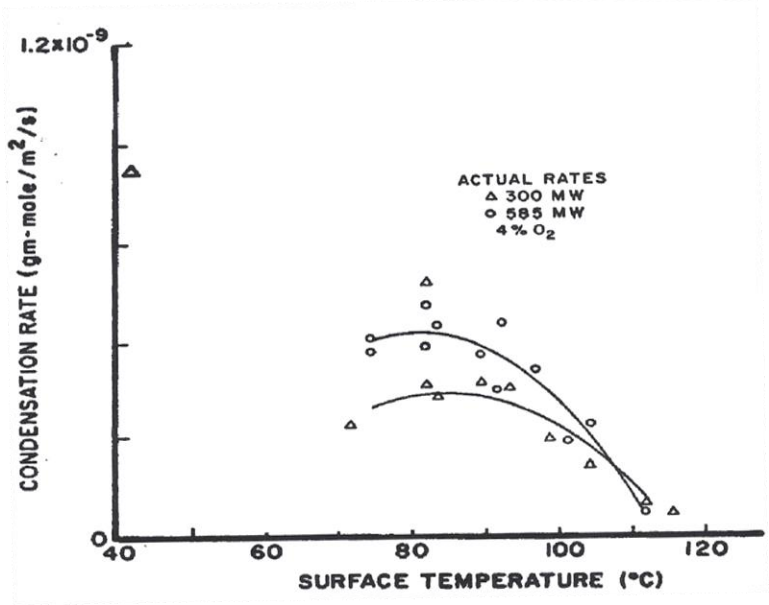

Figure 2.14: Acid condensation rates when load variation of 300MW and 585MW were applied, while the excess O_2 was fixed at 4%.

The rate of condensation of sulphuric acid in a turbulent gas stream can be written in the form of equation 2.2. The results from the model developed using equation 2.2 (Mabena, 2003) showed that a portion of the condensed sulphuric acid evaporated into the incoming air stream. The results further showed that the rate of evaporation strongly depends on the moisture of the incoming air. The fact that evaporation occured, indicated that the mass transfer rate becomes negative. D'Agostini further demonstrated the effect of moisture in the incoming air into the air heater, which showed that for dry inlet air, the net acid deposition was less. Therefore dry air causes more evaporation to occur. The rate of fouling is determined by rate, quantity and mechanism of acid condensation and deposition.

$$R = h_D(C_b - C_i) \tag{2.2}$$

C_b – concentration of the sulphuric acid vapour at the deposition surface
C_i – concentration of the sulphuric acid vapour in the flue gas stream
h_D – heat transfer coefficient

The classification of the fouling mechanisms in a regenerative rotary air heater was investigated by Mathebula (2014). The objective of the research was to identify the mechanisms and extent of fouling, observe the distribution of the fouling across the steel matrix, and verify the velocity profile of the fluids entering the air heater. The velocity profile was required to estimate the influence it has on the temperature distribution of the element packs and fluids passing through the air heater. A QEMSCAN surficial and cross sectional analysis was done to indicate the phases of fouling of ash deposits from Eskom Power Plants. These phases were anhydrite, AlSi-sulphate, Si(Al)-sulphate, iron sulphate and sulphur. These phases are formed due to a reaction between sulphuric acid and fly ash components, and some are also formed from a reaction between sulphuric acid and fuel oil catalysts. The surficial analyses indicated that the four most dominating phases are AlSi-sulphite, aluminosilicate, cenospheres and Al(Si)-sulphate. The cross sectional analysis revealed a similar trend but included a fith dominating mineral being quartz. In samples two, three and four, ALSi-Sulphate was found to be more than 25% in both surficial and cross sectional analyses. In samples three and four specifically, Al(Si)-sulphate was the highest volume percentage of the constituents for both tests. Spherical, cooled molten slag particles, also known as cenospheres, usually form from pulverised fuel exceeding the fusion temperature of the coal in the combustion zone. This results in a physical fouling form also known as plugging due to the formation of increased ash particles. In the first and second samples the surficial analysis showed a volume percentage of more than 20% cenospheres (Mathebula, 2014).

Considering the dew point temperature calculation for sulphurous acid (H_2SO_3), the main contributor to variations is the partial pressure of moisture (H_2O). The dew point temperature calculation for sulphuric acid (H_2SO_4) mainly experiences variations due to changes in the partial pressure of moisture (H_2O) and sulphur trioxide (SO_3). The results also showed that a 0.2% volume increase in sulphur from the coal supplied, will only influence the sulphuric acid dew point temperature by 2ºC and has almost no effect to the sulphurous acid dew point temperature. The change in hydrogen and moisture also showed a similar result, which shows that the dew point temperatures are not sensitive to changes in hydrogen, moisture and sulphur in coal. If high volumes of moisture would leak into the flue gas stream, due to tube leaks or defective soot blowers, the partial pressure of moisture will change enough to influence the acid dew point temperatures (Mathebula, 2014).

A Power Station operates with a dual rotary regenerative air heater that consists of a inner primary air duct and an outer secondary air duct as shown in Figure 2.4b. A dual rotary hood air heater was simulated with the RAH model by Mathebula (2014) to analyse the velocities and performance of the air heater. The model indicated that higher velocities are experienced in the primary air duct when compared to the secondary air section (as seen in Figure 2.15). This also affects the element surface temperature causing a higher average element surface temperature for the secondary air side, than for the primary air side. The RAH results indicated the simulated metal temperatures never operated below the dew point temperature of H_2O and H_2SO_3. Therefore condensation of moisture and sulphurous acid will only occur when the surface temperature operates below 40 ºC (H_2O dewpoint) and 36 ºC to 38 ºC (H_2SO_3 dew point). The dew point temperature for sulphuric acid (H_2SO_4) was reached and the result showed that 34% of the steel matrix volume experienced metal temperatures below the sulphuric acid dew point temperature (133 ºC to 149 ºC).

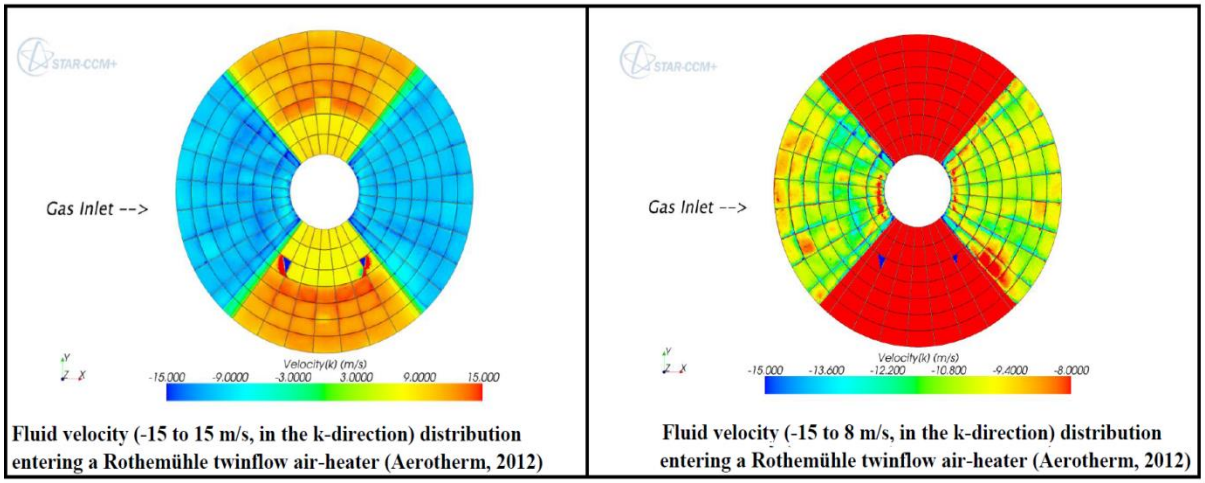

Fluid velocity (-15 to 15 m/s, in the k-direction) distribution entering a Rothemühle twinflow air-heater (Aerotherm, 2012)

Fluid velocity (-15 to 8 m/s, in the k-direction) distribution entering a Rothemühle twinflow air-heater (Aerotherm, 2012)

	Mass flow rate (kg/s)	Density (kg/m³)	Flow area (m²)	Average velocity (m/s)
Primary air	81	1.05	8.65	8.92
Secondary air	265.6	0.97	42.89	6.38

Figure 2.15: Flow distribution results for an Eskom Power Station duel flow regenerative air heater (Mathebula, 2014).

The investigation also concluded that fly ash may adhere to the sulphuric acid that condenses onto the air heater plates, along with the fly ash particles adhering to each other when the gas temperature reduces below the sulphuric acid dew point temperature. The phase formation indicated that sulphuric acid reacts with fly ash components and fuel oil char. When the plate temperature heats up the condensate and fly ash mixture experiences a baking effect. This hardens the mixture to create severe fouling that requires either high pressure washing or a complete element pack replacement. The presence of lime in the fly ash contributes to the hardening process. Lime forms when calcium monoxide combines with oxygen and sulphur dioxide to form calcium sulphate. The amount of lime is usually less than 5 %; therefore it is not severely influential. Another factor that that plays a role in hardening of the ash deposits, is minerals such as quartz with a Moh hardness of 7. As indicated in the QEMSCAN results, the cenospheres present also contribute to hardening of ash deposits. The critical parameters for dew point related fouling include coal and flue gas properties. Therefore the coal composition and flue gas composition need to be considered in this research.

There are two frequently used methods for predicting acid dew point of flue gas, namely direct measurement by special instruments and calculation by empirical formulas and charts. The special instruments for direct measurement of acid dew point are based on the main resistance method, current method, and acid deposition quantity method. The measuring results are preferential according to the different principles of measurement apparatuses. Factors such as sensitivities of determination parameters, probe setups, measuring steps affect the measuring accuracy. Even with continuously measured acid dew points under the same operating condition, inconsistencies exist because of the complexity and instantaneity of actual flue gas. The following table shows the different empirical formulas for predicting acid dew point of flue gas reported in previous studies.

Table 2.2 Prediction models on acid dew point in previous studies (Qin K F, 1994; Müller, 1959; Haase R, 1963; Verhoff F H, 1974; Okkes A G, 1987; Halstead W D, n.d.; Feng J F, 2003; Wei W, 2017).

Müller	$t_{ADP} = 116.5515 + 16.06329lgV_{SO_3} + 1.05377(lgV_{SO_3})^2$
Soviet Union calculation standard 73	$t_{ADP} = t_{WDP} + \frac{125(S_{ar})^{1/3}}{1.05^{\alpha_{fh}} A_{ar}}$
Soviet Union calculation standard 98	$t_{ADP} = t_{WDP} + \frac{200(S_{ar})^{1/3}}{1.05^{\alpha_{fh}} A_{ar}}$
Junkai Feng	$t_{ADP} = t_{WDP} + \frac{\beta(0.42S_{ar})^{1/3}}{1.05^{0.42\alpha_{fh}} A_{ar}}$
Japan Institute of Electric Power Industry	$t_{ADP} = 20lgV_{SO_3} + a$
И. А. Варанов	$t_{ADP} = 186 + 20lgV_{H_2O} + 26lgV_{SO_3}$
A.G.Okkes-A	$t_{ADP} = 10.8809 + 27.6lgP_{H_2O} + 10.83lgP_{SO_3} + 1.06(lgP_{SO_3} + 2.9943)^{2.19}$
A.G.Okkes-B	$t_{ADP} = 203.25 + 27.6lgP_{H_2O} + 10.83lgP_{SO_3} + 1.06(lgP_{SO_3} + 8)^{2.19}$
A.G.Okkes-C	$t_{ADP} = 365.6905 + 11.9864lgP_{H_2O} + 4.70336lgP_{SO_3} + (0.446lgP_{SO_3} + 5.2572)^{2.19}$
Halstead	$t_{ADP} = 113.0219 + 15.0777lgV_{H_2SO_4} + 2.0975(lgV_{H_2SO_4})^2$
Verhoff & Branchero-A	$1000/(t_{ADP} + 273.15) = 2.9882 - 0.13761lgP_{H_2O} - 0.2674lgP_{SO_3} + 0.03287lgP_{H_2O}lgP_{SO_3}$
Verhoff & Branchero-B	$1000/(t_{ADP} + 273.15) = 1.7842 + 0.0269lgP_{H_2O} - 0.1029lgP_{SO_3} + 0.0329lgP_{H_2O}lgP_{SO_3}$
Verhoff & Branchero-C	$1000/(t_{ADP} + 273.15) = 2.276 - 0.0294lnP_{H_2O} - 0.0858lnP_{H_2SO_4} + 0.0062lnP_{H_2O}lnP_{H_2SO_4}$
Haase & Borgmann	$t_{ADP} = 255 + 18.7lgP_{H_2O} + 27.6lgP_{SO_3}$
Correlation contained experimental constants	$t_{ADP} = t_{WDP} + B(P_{H_2SO_4})^n$

Note: (1) S_{ar}: sulfur content as received coal, %; A_{ar}: ash content as received coal, %; a_{fh}: the coefficient of fly ash, %.

(2) V_{SO_3}, $V_{H_2SO_4}$: volume fraction of SO_3, H_2SO_4, %; V_{H_2O}: volume fraction of H_2O, %.

(3) P_{SO_3}, $P_{H_2SO_4}$: the partial pressure of SO_3, H_2SO_4; P_{H_2O}: the partial pressure of H_2O; for A. G. Okkes-A, Verhoff & Branchero-A, Pa; for A. G. Okkes-B, Verhoff & Branchero-B, Haase & Borgmann, Correlation contained experimental constants, atm; for A. G. Okkes-C、 Verhoff & Branchero-C, mmHg.

(4) Japan Institute of Electric Power Industry: V_{H_2O} = 5%, a = 184; V_{H_2O} = 10%, a = 194; V_{H_2O} = 15%, a = 201.

(5) Dew point: $t_{WDP} = 6.715 + 13.787lnV_{H_2O} + 1.357(lnV_{H_2O})^2$, °C.

The calculating formulas are divided into two categories according to whether considering sulphur content and ash content in coal. The formula results calculated under the same parameters are shown in Figure 2.16. From these results the largest temperature difference is up to 40 °C. The researches indicated that there are certain differences between the calculated data and experimental values with the various contents of acid vapour and water vapour. Consequently, the applicability of the empirical formula is strictly limited, and the predicted values are generally not so perfect under the unit operation conditions.

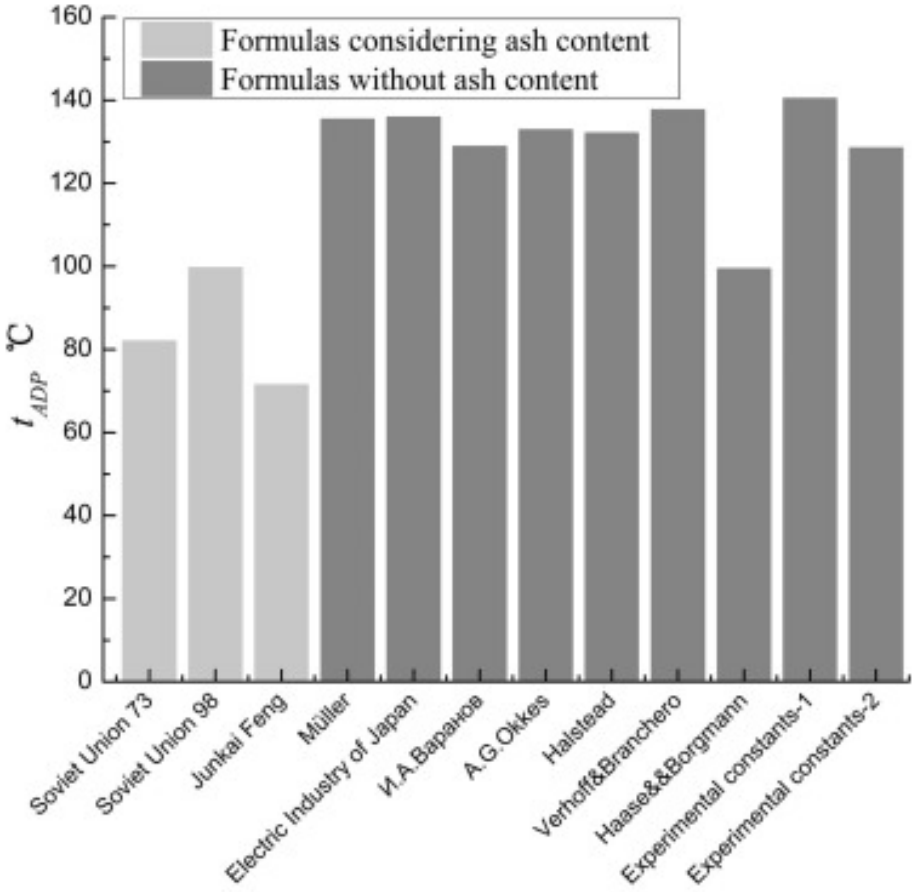

Figure 2.16: Prediction models on acid dew point (Wei W, 2017).

ZareNezhad and Aminian (2010) presented a multi-layer feed forward artificial neural network for predicting acid dew point temperatures of the flue gas. Xiang (2014, 2015, and 2016) tested the acid dew point of flue gas by using the plug-measuring device and the extraction-measuring device respectively. From this an improved thermodynamic correlation formula between acid dew point and its influencing factors was derived. A semi-empirical prediction model of acid dew point was proposed and Wang (2016) numerically calculated the acid dew point on a heat transfer fin surface by considering both the gas-liquid equilibrium effect and multi-component diffusion effect. Influential factors such as the wall temperature, velocity of flue gas and fin parameters were identified. But there was no new calculation method of acid dew point. In conclusion, the above-mentioned prediction methods of acid dew point are strictly limited, and in general the predicted values were not consistent.

Abel (1947) initially derived the method of calculating the pressure of water vapour and sulphuric acid vapour based on the fugacity equation at the gas-liquid interface. Wilson (1989) further fixed the fugacity equation of ideal gas to obtain the real vapour partial pressure at interface by importing the apparent fugacity coefficient. Hodge (1994) studied the calculation

of sulphuric acid condensation rate and He (2015) carried out the numerical simulations of the sulphuric acid condensation. The numerical model considered both the gas-liquid equilibrium effect and multi-component diffusion effect. Sulphuric acid condensation influence factors such as the wall temperature, flue speed and fin parameters etc. were analysed. It was found that it would be feasible to study the sulphuric acid condensation by using the fugacity equations of water and sulphuric acid at the gas-liquid interface considering both the gas-liquid equilibrium effect and multi-component diffusion effect. The air heater flue gas exhaust temperature affects the low temperature corrosion. And the low temperature corrosions on the low-temperature sections of the equipment are more severe than those of the high-temperature sections. Thus it can be seen that the surface temperature of heat exchangers is crucial to the low temperature corrosion and also contribute to fouling.

Based on the fugacity equations of water and sulphuric acid at the gas-liquid interface, the thermodynamic iterative calculation method is put forward for the prediction of sulphuric acid. The impact of temperature, acid vapour content and water vapour content on the acid condensation are obtained via single-factor and orthogonal calculations. Besides, the safe operating temperature of the heat exchanger is put forward on account of the analysis of corrosion mechanism and acid condensation calculation results.

Kunze (2000) proposed the acid dew point concept based on the gas-liquid equilibrium. This method showed that the acid dew point can be defined as the temperature of gas-liquid equilibrium interface when the apparent partial pressures of sulphuric acid vapour and water vapour at the interface equal to those in the flue gas. The accuracy calculates the apparent partial pressures of sulphuric acid vapour and water vapour at the gas-liquid equilibrium interface.

Wei (2017) compared the experimental data from previous methods to the predicted values using empirical formulas (Müller, 1959; Haase R, 1963; Verhoff F H, 1974; Okkes A G, 1987; Halstead W D, n.d.; Feng J F, 2003) and an iterative calculation model. The following assumptions and simplifications were made by Wei (2017) to perform the condensation calculation and iterative computations.

- The flue gas is assumed to be an ideal gas mixture with a variety of gas compositions
- The content of SO_3 completely transforms to H_2SO_4.
- The condensation system is simplified to the binary systems of H_2SO_4-H_2O
- Gases such as CO_2, NO_2, SO_2 in the flue gas are assumed for inert gas and not soluble in sulphuric acid solution, which only have the effect of formation of total pressure.
- In order to simplify the calculation of the effective diffusivity of component i $D_{i,m}$, other gases are assumed to air in the calculation
- The condensation of water vapour and sulphuric acid vapour is computed only on the gas-liquid equilibrium interface.

Small deviations between the calculation results and experimental data were noted except for the studies of Haase & Borgmann and experimental constants-1. The results of Haase & Borgmann were abnormally low while the results of experimental constants-1 showed a large-span increase, and the greatest deviation was around 41 °C. Müller ignored the influence of the content of water vapour on acid dew point. Halstead took the content of water vapour into consideration, but the results did not concur with the experiment data. The predictions of Verhoff & Branchero agree well with the experimental data, the same as the results shown in the previous study. Verhoff & Branchero were the lowest compared with other deviations between other formula results and experimental data. Therefore, the prediction of Verhoff & Branchero is of great accuracy and has wide range of application (Kiang Y H, 1981).

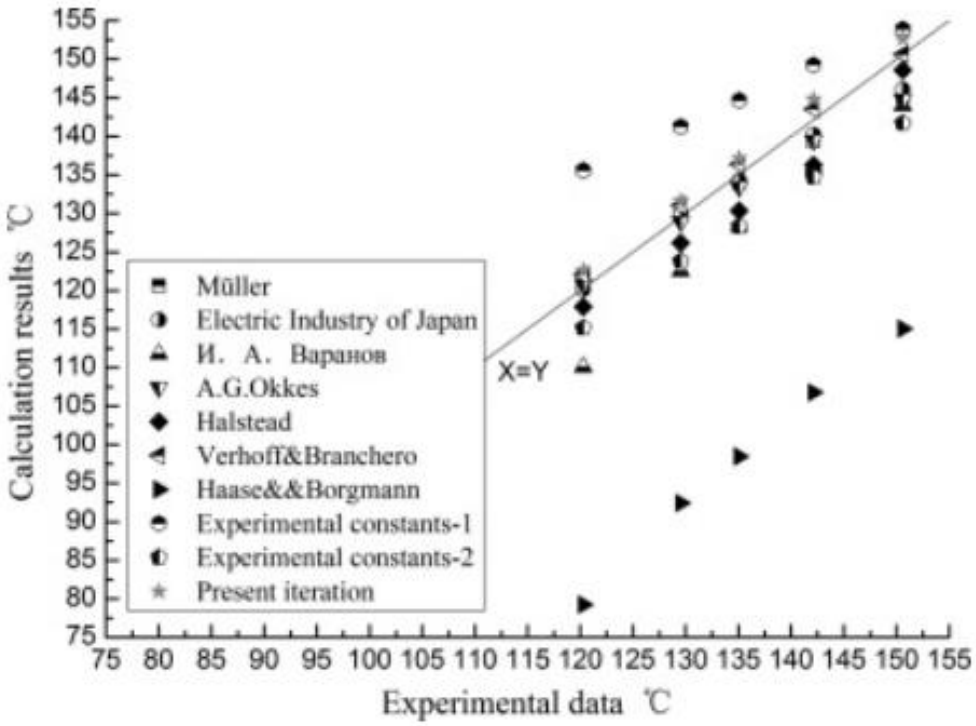

Figure 2.17 Comparison between the predicted values in this work and experimental data in previous research (Wei W, 2017).

2.4.1 Coal Composition

Coal is classified into three major types, namely anthracite, bituminous, and lignite (Figure 2.18). The types are classified further as semi-anthracite, semi-bituminous and sub-bituminous. The oldest coal is known as anthracite, which is a hard type of coal mainly consisting of carbon with low volatile content and no moisture. Lignite is known to be the youngest type of coal in terms of a geological perspective. The coal is usually soft and consists mostly of volatile matter and moisture with low quantities of fixed carbon. The phrase "fixed carbon" refers to carbon in its free state which is not combined with other elements. The volatile matter is all the constituents that vaporize during heating of coal. Bituminous coal, also known as black coal, is a relatively soft coal containing a tarlike substance called bitumen or asphalt. It is a higher quality coal compared to lignite coal, but of poorer quality than anthracite. During the formation phase of coal it was the result of high pressure being exerted on lignite. Semi-bituminous is an intermediate between bituminous coal and anthracite and averaging from 10 to 20 percent of volatile matter. Sub-bituminous coal has properties that range from those of lignite to those of bituminous coal and is used primarily as fuel for steam-electric power generation. Another coal intermediate between anthracite and bituminous coal is known as semi-anthracite. Semi-anthracite is coal approaching anthracite in non-volatile character. The following table is an illustration of the types of coal (Williams, et al., 2018). This composition becomes important when the constituents in the flue gas are determined to find the reactions causing dew point related fouling.

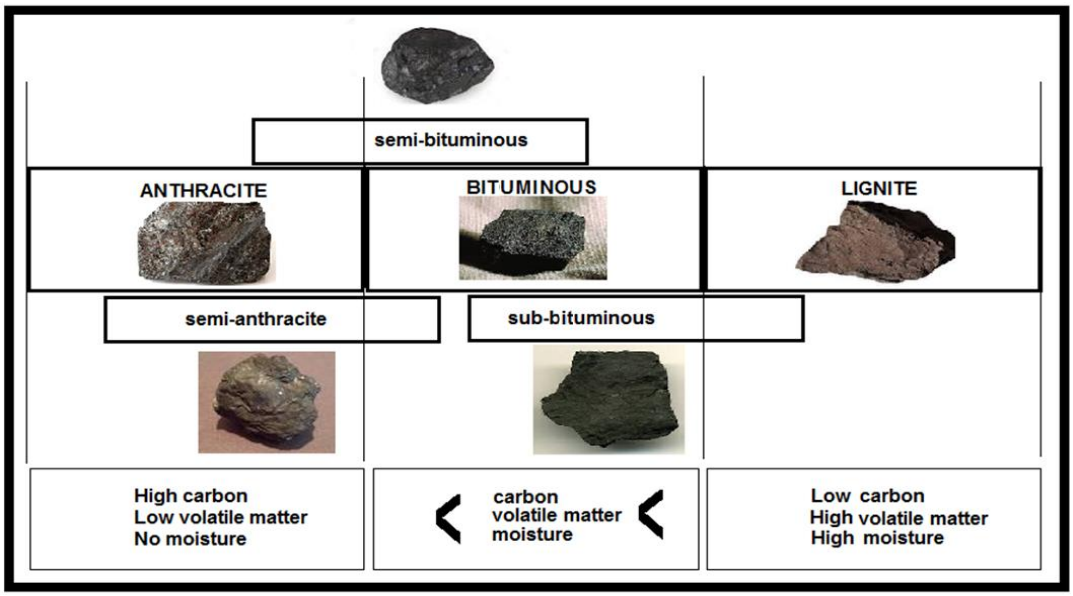

Figure 2.18: Classification of coal.

When coal is received it is analysed according to its chemical composition. The analysis is done by considering three main groups of composites (Figure 2.18). The first group is the pure coal composite. The coal composite consists of the portion of volatile matter, volatile organic matter and fixed carbon. The second composite group is mineral matter that consists of ash, volatile mineral matter and the remaining portion of volatile matter. The third group is the total moisture of the coal. This portion looks at the quantity of inherent and surface moisture. To fully understand the flue gas composition the coal composition must be analysed to know what chemical reactions will occur during combustion. Figure 2.19 shows the variations of coal analyses.

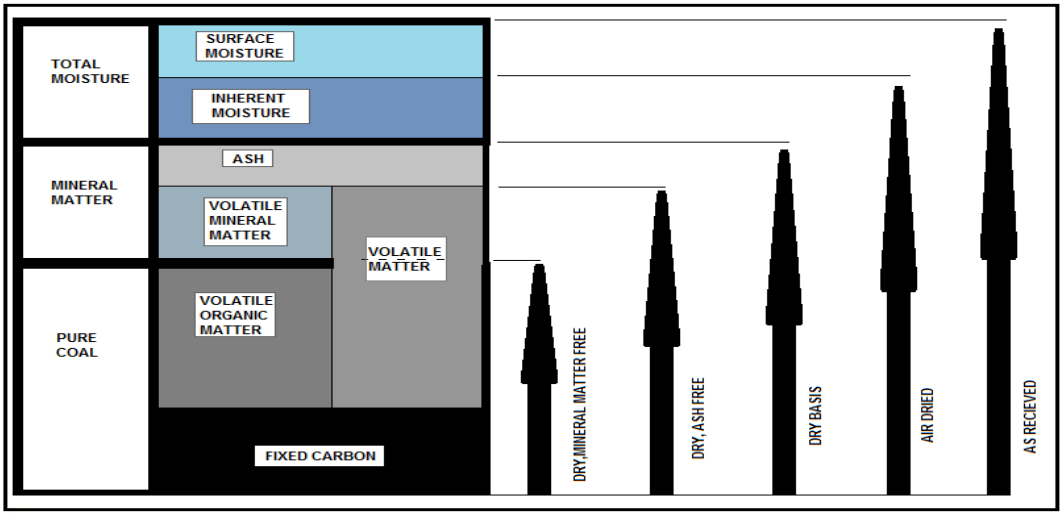

Figure 2.19: Composition of coal (Van Wyk, 2010).

Two methods are used to analyse coal, namely ultimate analysis and proximate analysis. The ultimate analysis considers all the coal component elements, solid or gaseous. The proximate analysis only indicates fixed carbon, volatile matter, moisture and ash content of the coal. The ultimate analysis will be used to find the coal composition in order to establish the flue gas composition by means of a mass balance calculation. Moisture plays a critical role with regard to fouling. The amount of moisture largely contributes to the dew point temperature of the flue gas. To measure moisture content, powdered raw coal of a size of 200 microns is placed in an

uncovered crucible in an oven at 108 +/-2 °C. The sample is then cooled down to room temperature and weighed again to show what the weight lost is. The weight loss is the representation of the moisture content. This measurement is used to estimate the amount of moisture to be present in the flue gas. The partial pressure of moisture is calculated accordingly. The ash content is an indication of the impurities that will not burn and typically ranges between 5 to 40%. Ash reduces the handling and burning capacity and affects the combustion and boiler efficiency. This is also the constituent causing slagging and clinkering in the furnace. It promotes higher deposition rates along with increased hardening when the deposits are combined with moisture and heating in the air heater elements.

2.4.2 Flue gas composition

Eskom power stations use three sources for combustion. These three sources are fuel oil, propane gas and pulverised coal. The propane gas is used to ignite the fuel oil, and the fuel oil provides support for the ignition of pulverised fuel. During light-ups, de-loading or loading of units, all three fuel sources are used. Each also generates a specific type of composition in the flue gas, which is also transported to the air heaters during extraction of flue gases. Due to the fact that the amount of propane gas, in relation to the rest of the fuel supplied, is relatively small its effect can be neglected. The assumption of a steady state condition only considers when the system has stabilized and all the fuel oil support is removed. Therefore fuel oil combustion and composition is not considered for this research. Pulverised fuel is assumed to be the main source of fuel and therefore the coal analyses are used to determine the flue gas composition. Pulverised fuel mainly consists of combustibles such as carbon, hydrogen, oxygen and sulphur. The following equations represent the oxidation process of the combustibles in the coal.

$$C + O_2 \rightarrow CO_2$$
$$H_2 + \frac{1}{2}O_2 \rightarrow H_2O$$
$$S + O_2 \rightarrow SO_2$$
$$2N_2 + 2O_2 \rightarrow 2NO_2 + N_2$$

A study done by Sathyanathan and Mohammed (2004) stated that 80-90% of the total ash produced from pulverised fuel is fly ash. For this study the assumption of 90% for fly ash and 10% boiler bottom ash will be used.

2.5 Literature Survey Summary

The onset of dew point related fouling in rotary regenerative air heaters was not included in the previous regenerative air heater (RAH) model. A finite difference technique, to analyse the heat transfer for transient tests by Mullison and Loerhke (1986), was used by Habbitts (1998) to develop a heat transfer simulation model. This model was further developed by De Klerk (2001), to estimate the gas temperatures, element surface metal temperatures and differential pressure across the steel matrix. The recently developed VBA RAH simulation model is based on the study done by Ganapathy (1989) and Mathebula (2014), which is explained in section 3.3.3, to calculate dew point temperatures (water, sulphuric acid and sulphurous acid) of the flue gas, utilizing the partial pressures of the flue gas. If the element surfaces and the flue gas experience temperatures less than the dew point temperatures, the onset of dew point related fouling is expected.

3. THEORETICAL ANALYSIS

3.1 Boiler Performance

Coal fired power generation plants are diverse with regard to the design of each plant, but the basis of energy conservation remains the same. Figure 3.1 shows the heat sources entering and leaving the control volume. Taking the conservation of energy into consideration, the relationship of the boiler efficiency and heat gained from the air heater can be expressed. The boiler efficiency is a relationship between the difference in heat energy entering the boiler and the heat energy exiting the boiler, divided by the product of the mass flow rate of coal and net calorific value of the coal (Equation 3.1 and Figure 3.1). Equation 3.1 is a representation of the boiler efficiency based on the Lower Heating Value or Net CV (Calorific Value). From equation 3.2, the relationship of heat losses in the boiler indicates, that there is a direct influence on the boiler efficiency, when the energy lost is not recuperated or regenerated in the downstream conditions, to heat up combustion air (Van Wyk, 2010). Equation 3.2 shows all the energy losses. The flue gas energy loss is directly related to the heat transferred in the air heater, which is illustrated in equation 3.3 and Figure 3.1.

$$\boldsymbol{n_{LHV}} = \frac{\dot{Q}_{in} - \dot{Q}_{loss}}{\dot{m}_c \, CV_{LHV}} \tag{3.1}$$

Where $\dot{Q}_{in}$ is the heat energy input from the coal to the boiler along with the energy input from the fan and the motors to the boiler in the form of $\dot{m}_c \, CV_{LHV} + \dot{Q}_{credits}$.

$$\dot{\boldsymbol{Q}}_{\boldsymbol{loss}} = \dot{\boldsymbol{Q}}_{\boldsymbol{fg}} + \dot{\boldsymbol{Q}}_{\boldsymbol{C'}} + \dot{\boldsymbol{Q}}_{\boldsymbol{rad}} + \dot{\boldsymbol{Q}}_{\boldsymbol{ba}} + \dot{\boldsymbol{Q}}_{\boldsymbol{fa}} \tag{3.2}$$

$$\dot{\boldsymbol{Q}}_{\boldsymbol{fg}} = \left[\left(\dot{\boldsymbol{m}}_{\boldsymbol{fg,sah,in}} \boldsymbol{h}_{\boldsymbol{fg,sah,in}} \right) + \left(\dot{\boldsymbol{m}}_{\boldsymbol{fg,pah,in}} \boldsymbol{h}_{\boldsymbol{fg,pah,in}} \right) + \left(\dot{\boldsymbol{m}}_{\boldsymbol{leak}} \boldsymbol{h}_{\boldsymbol{a,leak}} \right) \right] - \left[\left(\left(\dot{\boldsymbol{m}}_{\boldsymbol{a}} - \dot{\boldsymbol{m}}_{\boldsymbol{tmp,a}} - \dot{\boldsymbol{m}}_{\boldsymbol{sl,a}} - \dot{\boldsymbol{m}}_{\boldsymbol{pa,a}} - \dot{\boldsymbol{m}}_{\boldsymbol{ingress,a}} \right) \boldsymbol{h}_{\boldsymbol{a,sah,in}} \right) + \left(\dot{\boldsymbol{m}}_{\boldsymbol{tmp,a}} \boldsymbol{h}_{\boldsymbol{a,sah,in}} \right) + \left(\dot{\boldsymbol{m}}_{\boldsymbol{sl,a}} \boldsymbol{h}_{\boldsymbol{a,sah,in}} \right) + \left(\dot{\boldsymbol{m}}_{\boldsymbol{pa,a}} \boldsymbol{h}_{\boldsymbol{a,sah,in}} \right) + \left(\dot{\boldsymbol{m}}_{\boldsymbol{ingress,a}} \boldsymbol{h}_{\boldsymbol{a,ambient}} \right) + \left(\dot{\boldsymbol{m}}_{\boldsymbol{c}} \boldsymbol{h}_{\boldsymbol{c}} \right) \right] \tag{3.3}$$

$\dot{Q}_{loss}$ – Heat energy lost in the Boiler
$\dot{Q}_{fg}$ – Flue gas energy loss
$\dot{Q}_{C'}$ – Unburnt carbon energy loss
$\dot{Q}_{rad}$ – Heat radiation energy lost to surroundings
$\dot{Q}_{ba}$ – Heat energy lost due to sensible heat in bottom ash
$\dot{Q}_{fa}$ – Heat energy lost due to sensible heat in fly ash
$\dot{m}_{fg,sah,in}$ – Mass flow of the flue gas entering the secondary air heater
$\dot{m}_{fg,pah,in}$ – Mass flow of the flue gas entering the primary air heater
$\dot{m}_{leak}$ – Mass flow of the air leaking to the flue gas stream internal to the air heater
$\dot{m}_a$ – Mass flow of the total air as determined from the coal analysis and O_2 at the boiler outlet
$\dot{m}_{tmp,a}$ – Mass flow of tempering air
$\dot{m}_{sl,a}$ – Mass flow of seal air
$\dot{m}_{pa,a}$ – Mass flow of the primary air
$\dot{m}_{ingress,a}$ – Mass flow of ingress air
$\dot{m}_c$ – Mass flow of coal
$h_{fg,sah,in}$ – Enthalpy of the flue gas entering the secondary air heater
$h_{fg,pah,in}$ – Enthalpy of the flue gas entering the secondary air heater

$h_{a,leak}$ – Enthalpy of the air leaking to the flue gas
$h_{a,sah,in}$ – Enthalpy of the secondary air entering the secondary air heater
$h_{a,ambient,in}$ – Enthalpy of the ambient air
h_c – Enthalpy of the coal entering the boiler

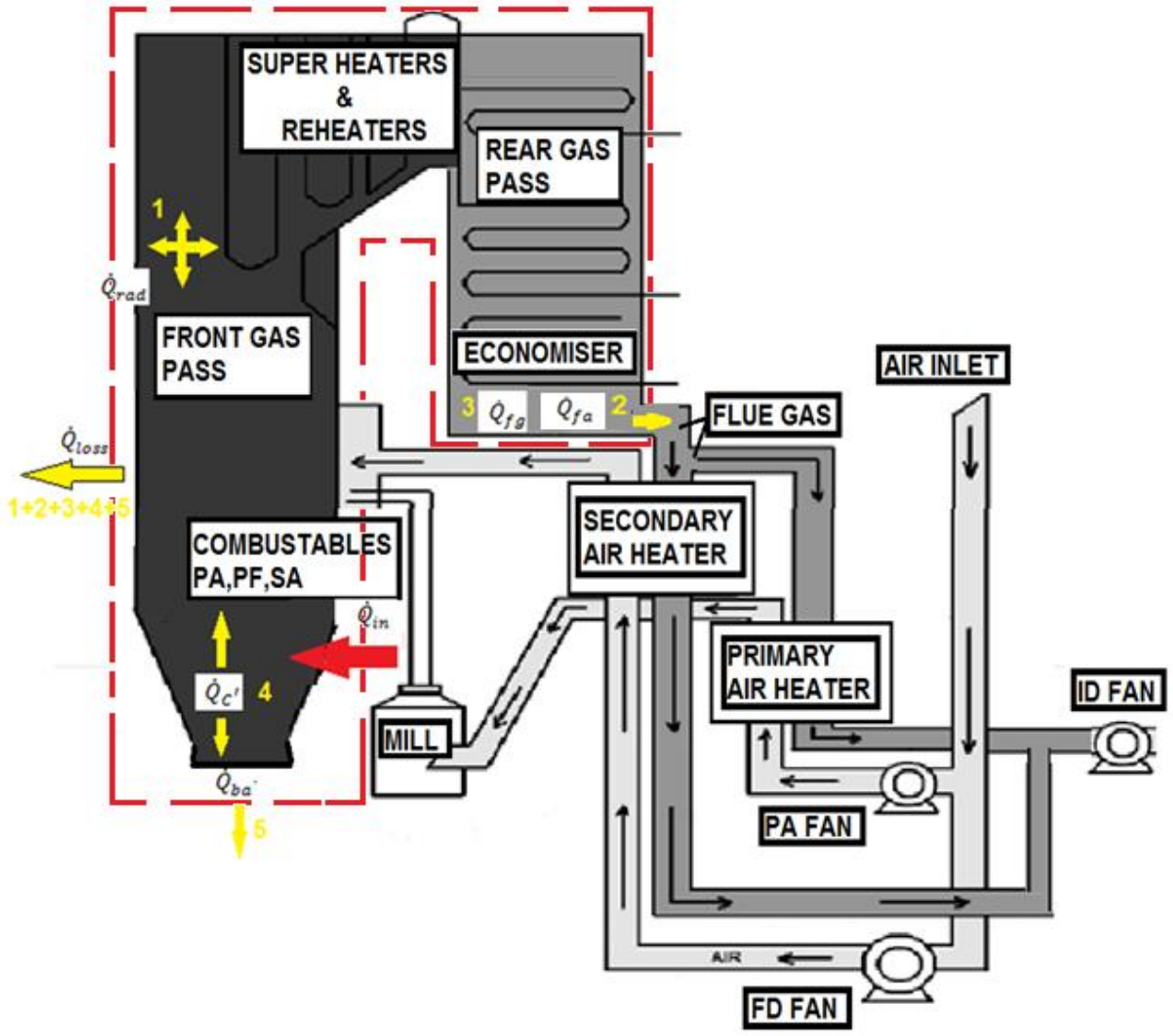

Figure 3.1: Heat energy gained and lost during the operation of a boiler.

The simulation model developed for this research has an option of simulating the air heater performance according to the design input parameters of the boiler. A mass and energy balance across the boiler calculates the boiler efficiency and performance. It is then used to identify what the effect of changes to the air heater input parameters will have on the performance of the boiler. The change in coal flow is identified along with the variation in boiler efficiency, steam flow and air flow. Therefore, heat entering and leaving the system are used to determine the required air flow and flue gas flow, which become input parameters to the simulation model to generate a temperature profile for both air and flue gas along with the surface metal temperatures. The coal properties of the coal for the specified design are used to estimate the flue gas composition. The flue gas composition provides a platform to determine what the dew point temperatures in the air heater will be based on the partial pressure of sulphur trioxide,

sulphur dioxide and moisture in the flue gas. Based on these results, the possibility of fouling can be evaluated.

3.2 Air Heater Performance

The efficiency of a coal fired power station is typically 35%. This efficiency is the ratio of the energy extracted and used, from the fuel, to the total heat energy available in the fuel. Approximately 45% of the energy is lost in the condenser, 10% is lost in the turbo-generator and an additional 10% is lost in the boiler (Kumar, 1998). The air heater takes up about 60% of the energy contained in the flue gas. There are two main sources of loss in air heaters, namely air leakage to the flue gas stream and poor heat recovery. The standard conventional method of calculating air heater efficiency relies on the following (Mallikarjuna, et al., 2014; Maskew, et al., 1998):

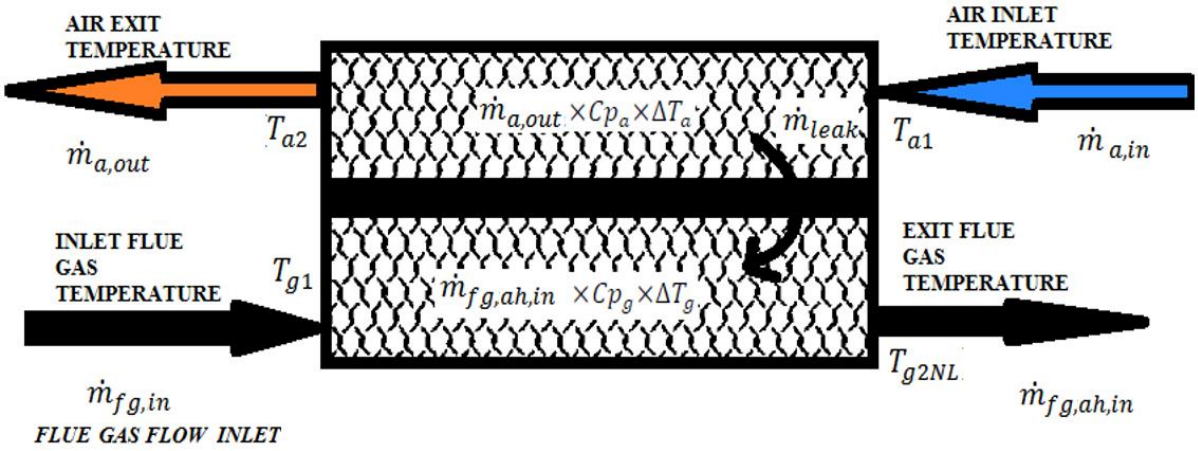

Figure 3.2: Air heater heat exchange model (Maskew, et al., 1998).

- ***flue gas temperature drop***
  This temperature is the difference between the inlet- and outlet-flue gas temperatures. This difference also shows what the expected heat transfer from the flue gas to the air will be. The flue gas temperature drop is used as part of the estimation of the heat energy extracted from the flue gas.

$$\Delta T_g = T_{g1} - T_{g2NL} \tag{3.4}$$

- ***Air side temperature rise***
  The air side temperature rise is defined as the difference between the air temperature leaving the air heater and the air temperature entering the air heater. The change in temperature is caused by the dissipated heat from the flue gas flow through the elements. The air side temperature rise is used as part of the estimation of the heat energy absorbed from the flue gas.

$$\Delta T_a = T_{a2} - T_{a1} \tag{3.5}$$

- ***X – ratio***
  The X-ratio is a measure of the operating conditions. This ratio is defined by the flue gas temperature drop, taking leakage into account, divided by the air side temperature rise. The ratio does provide a measure of thermal performance, but is mostly used to measure operating conditions. A low X-ratio (X_R) either indicates that excessive gas volumes pass through the air heater, or that air is either leaking or bypassing the air

heater. This ratio can be affected by moisture in coal, air infiltration, air and gas mass flow rates, leakage from seal setting and specific heats from air and flue gas.

$$X_R = (T_{g1} - T_{g2NL})/(T_{a2} - T_{a1}) \quad (3.6)$$

T_{g1} - Air heater inlet gas temperature
T_{g2NL} – Undiluted flue gas exit temperature (temperature which excludes the influence of ingress air). This temperature accounts for temperature change due to leakage.
T_{a2} - Temperature of air exiting the air heater
T_{a1} – Temperature of air entering the air heater.

- ***Air in - leakage***

Due to the fact that a rotary regenerative air heater has a rotational component (either a rotating hood or a rotating matrix), the risk of leakage will always be evident. The flue gas is extracted by means of an induced draught fan. This draught is a suction pressure usually maintaining the furnace pressure at approximately -0.24 kPa gauge pressure. The air supplied to the air heater is a forced draught, which implies that it will have a positive operating pressure. When a system has high pressure and low pressure zone, the fluid will always tend to flow to the low pressure area. In the case of air heater operation, the air will tend to dissipate through the seals to the flue gas stream. Air heater leakage can be calculated by using air heater mass balance principles (Van Wyk, 2010).

$$\dot{m}_{leak} = \dot{m}_{a,out} - \dot{m}_{a,in} \quad (3.7)$$

$$\%Air\ leakage = (\dot{m}_{\ leak} / \dot{m}_{a,in}) \times 100 \quad (3.8)$$

$\dot{m}_{leak}$– Mass flow of the air leaking to the flue gas stream internal to the air heater
$\dot{m}_{a,in}$– Mass flow of the air entering the air heaters
$\dot{m}_{a,out}$– Mass flow of the air exiting the air heaters
$\dot{m}_{fg,sah,in}$ – Mass flow of the flue gas entering the secondary air heater
$\dot{m}_{fg,sah,out}$– Mass flow of the flue gas exiting the secondary air heater

Using the derivation as indicated in Appendix A4, the mass fraction of O_2 is used to predict leakage, assuming that no flue gas leaks into the air stream and that the mass fraction of O_2 at both the inlet- and outlet-airstreams is 23%:

$$\%\ Air\ leakage = \left[\frac{(O_{2\,fg,sah,out} - O_{2\,fg,sah,in})}{(0.23 - O_{2\,fg,sah,out})}\right] \times \frac{\dot{m}_{fg,sah,in}}{\dot{m}_{a,in}} \times 100 \quad (3.9)$$

In the case where volume fractions for O_2 are used:

$$\%\ Air\ leakage = \left[\frac{(0.21 - O_{2\,fg,sah,in}\,v/v)}{(0.21 - O_{2\,fg,sah,out}\,v/v)}\right] \times \frac{\dot{m}_{fg,sah,in}}{\dot{m}_{a,in}} \times 100 \quad (3.10)$$

$O_{2\,fg,sah,in}v/v$ – Volume fraction of the oxygen in the flue gas entering the secondary air heater

$O_{2\,fg,sah,out}v/v$– Volume fraction of the oxygen in the flue gas exiting the secondary air heater

In the case where air leakage is defined as the air to gas ratio per kilogram of flue gas entering the air heater, the following equation is used (volume fraction of measured O_2):

$$\%\ Air\ leakage = \left[\frac{(O_{2\,fg,sah,out}v/v - O_{2\,fg,sah,in}v/v)}{(20.9 - O_{2\,fg,sah,out}v/v)}\right] \quad (3.11)$$

When the flue gas is sampled on a dry basis for certain analysers a dryness factor must be taken into account. The readings taken at the flue gas inlet duct of the air heater are measured with a portable analyser which requires a dryness factor when the leakage is calculated. For the permanent analysers, a zirconia cell analyser is used, which samples flue gas on a wet basis and therefore does not require a dryness factor. The dryness factor can be calculated by:

$$Factor = \left(\frac{1.28701}{\rho_g} - 1.6011 \times k\right) \times 99 \quad (3.12)$$

k - % mass moisture in the flue gas entering the air heater

The final leakage calculation for dry basis measuring equipment is:

$$\%\ Air\ leakage(AL) = \left[\frac{(O_{2\,fg,sah,out} - O_{2\,fg,sah,in})}{(20.9 - O_{2\,fg,sah,out})}\right] \times Factor \quad (3.13)$$

- ***Undiluted gas exit temperature***

If no leakage occurs the flue gas outlet temperature would slightly change. This temperature can be calculated by:

$$T_{g2NL} = AL \times (T_{g2} - T_{a1}) + T_{g2} \quad (3.14)$$

The undiluted temperature estimated by the VBA RAH model is used to estimate the mixed flue gas temperature, which includes the leaked air to the flue gas stream exiting the air heater.

- ***Gas side efficiency/effectiveness (η_g)***

The gas side efficiency is the ratio of the gas temperature drop, to the difference between the air inlet temperature and the gas inlet temperature.

$$\eta_g = \frac{T_{g1} - T_{g2NL}}{T_{g1} - T_{a1}} \times 100 \quad (3.15)$$

- ***Air side efficiency/effectiveness (η_a)***

Air side effectiveness is the ratio of the air temperature drop, to the difference between the air inlet and the gas inlet temperature:

$$\eta_a = \frac{T_{a1} - T_{a2}}{T_{g1} - T_{a1}} \times 100 \quad (3.16)$$

- ***Differential pressure across the steel matrix***

Section 3.2.3 elaborates on the effect and measurement of pressure drop across the steel matrix. If the excess air is greater than expected, the pressure drop will be greater. If the element packs are fouled a differential pressure rise can be expected. The variations in pressures are directly related to the change in temperatures of the fluids passing through the air heaters, due to fluctuations in density. These changes are incorporated by calculating the average temperature for each layer at every time step by using the outlet temperature from the previous time step and the inlet temperature at the current time step. This average temperature becomes an input parameter to calculate density and fluid properties for each time step. The fluid properties are used as input parameters to the Fanning friction factor calculation to estimate the pressure drop for each layer at every time step.

The air heater performance relies on the effectiveness of the heat transfer process. This process is based on the mass and energy balance across the air heater, leakage rates, and differential pressure across the steel matrix. The mathematical model takes these calculations into consideration to formulate a method to estimate the temperatures for the fluid and solid regions. The heat transfer process also requires the heat transfer coefficient, and the pressure drop is required to find the partial pressure at the cold end of the air heater. The heat transfer coefficient is calculated using the Colburn j factor and the pressure drop estimation use the Fanning friction factor. Both values are obtained from tests of plate elements of the various geometries, as mentioned in section 3.2.2.

3.2.1 Heat transfer model

For the simulation model the rotational speed is used to calculate a time step and a size step, also known as the angle step (Figure 3.3). The entire heat exchanger is modelled by dividing the steel matrix into sectors depending on the time step specified by the user. The solid temperature calculation is time dependent, in the sense that the temperatures change during every time step and length step.

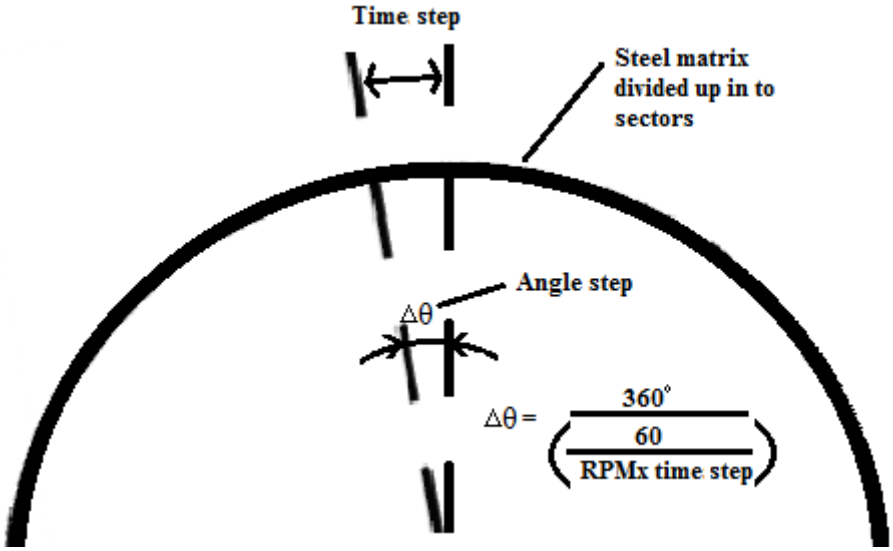

Figure 3.3: Steel matrix divided up into sectors according to the time step and angle step

The following assumptions were made by Habbits, and were reviewed by De Klerk (2001), which were used for the development of the VBA RAH model:

- Steady flow conditions are experienced flowing into and out of the air heater.

- The width and number of plates are sufficient to essentially reduce the problem to a one dimensional setup, with one-directional flow in each block.
- Finite thermal conduction occurs in the solid parallel to the direction of flow, with no traverse temperature gradients. Thus the boundary conditions for the side walls of the elements are adiabatic. (as indicated in Figure 3.4 below along the top and bottom plate centre lines)

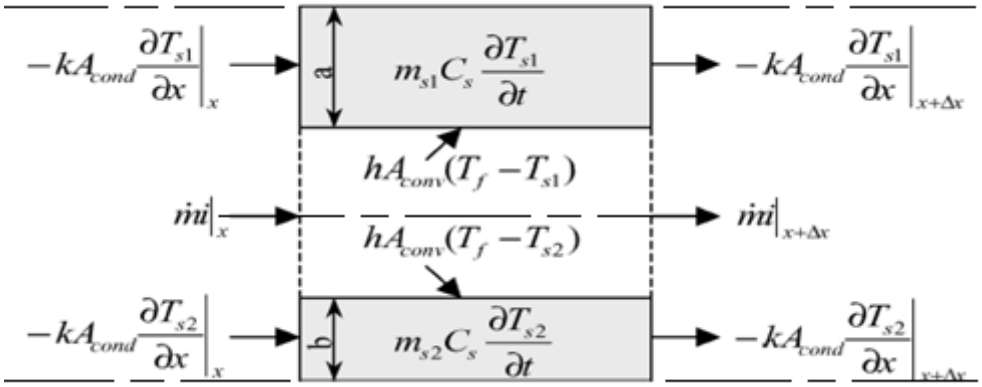

Figure 3.4: Basic plate/channel element. (De Klerk, et al., 2013)

- Convection heat transfer occurs at the solid surface interfaces within the element, the magnitude of which is determined by a heat transfer coefficient h (temperature dependent). A single h value is assumed to apply throughout a particular block of plates at a particular instant in time. This is a space averaged convective heat transfer coefficient assumed to be applied across a series of parallel plates for a particular flow rate.
- The plates are made from the same material.
- The fluid thermal capacity is negligible in comparison with the solid thermal capacity.
- The effect of heat transfer by radiation is neglected due to its small contribution to the temperature difference between plate regions. The symmetrical gas molecules do not participate in radiation, and the concentration of water vapour in air is too small. Therefore radiation from the air stream can be neglected. Radiation from the flue gas to the plates can be significant owing to temperatures differences of up to 40°C between gas and the plates. This effect is ignored due to this temperature difference occurring only over small regions at the hot end of the matrix. Once a temperature drop is experienced, the effect of radiation decreases rapidly.
- The fluid flowing into and out of the control volume is considered to be at a steady state. This assumption is used for the formulation of the energy balance of the volume in Figure 3.4 above. The energy exchanges across the boundaries of each region are assumed to be represented by conduction in the solid parallel to the direction of flow, (this is known as longitudinal conduction), convection between the solid and fluid region, and enthalpy flux into and out of the fluid region. Energy is stored within the solid regions and is proportional to thermal capacity of the solid.
- The mass flow rate for each block of plates for a specific fluid stream is constant, but the temperatures along with densities and velocities do change with time.

The enhanced model for energy balance for the fluid region can be expressed in the following way (De Klerk, 2001):

$$\frac{\partial T_f}{\partial x} + \frac{h \cdot W}{\dot{m}_{fluid} \cdot C_f}\left(2T_f - T_{s1} - T_{s2}\right) = 0 \quad (3.17)$$

Each solid region will be formulated using:

Solid 1

$$\frac{\partial T_{s1}}{\partial t} = \frac{k}{\rho_s C_s}\frac{\partial^2 T_{s1}}{\partial x^2} + \frac{h}{\rho_s C_s a}\left(T_f - T_{s1}\right) \quad (3.18)$$

Solid 2

$$\frac{\partial T_{s2}}{\partial t} = \frac{k}{\rho_s C_s}\frac{\partial^2 T_{s2}}{\partial x^2} + \frac{h}{\rho_s C_s a}\left(T_f - T_{s2}\right) \quad (3.19)$$

Dimensionless parameters are used as part of the numerical method. T^* is the dimensionless temperature and can be calculated using the following equation:

$$T^* = (T - T_{cold\ inlet})/(T_{hot\ inlet} - T_{cold\ inlet}) \quad (3.20)$$

The following equations are used to convert the heat transfer parameters to non-dimensional parameters:

b. Dimensionless time, $\theta = \frac{\dot{m}C_f}{M_s C_s}$ (3.21)

c. Conduction Parameter, $\lambda = \frac{kA_{cond}}{\dot{m}C_f L}$ (3.22)

d. Dimensionless length, z= $\frac{x}{L}$ (3.23)

e. Number of transfer units, $NTU = \frac{hA_{conv}}{\dot{m}C_f}$ (3.24)

f. Thickness Ratio, $\beta = \frac{a}{b}$ (3.25)

$\dot{m}$ – Mass flow of fluid
C_f – Heat capacity of the fluid
M_s – Mass of the solid material of the element pack
C_s – Heat capacity of the solid material of the element pack
k – Conductivity of the solid material of the element pack
L – Length element pack (height of the element pack along the flow direction)
x – Length of the pack at a given time interval
a – Half of the thickness of the corrugated solid region
b – Half of the thickness of the undulated solid region
A_{conv} – Area of convection at the given time interval
A_{cond} – Area of conduction at the given time interval
h – Average heat transfer coefficient

Dimensionless Temperatures must be calculated for both solid regions and the fluid region:

$$T_f^* = (T_f - T_{cold\ inlet})/(T_{hot\ inlet} - T_{cold\ inlet}) \quad (3.26)$$

$$T_{s1}^* = (T_{s1} - T_{cold\ inlet})/(T_{hot\ inlet} - T_{cold\ inlet}) \quad (3.27)$$

$$T_{s2}^* = (T_{s2} - T_{cold\ inlet})/(T_{hot\ inlet} - T_{cold\ inlet}) \quad (3.28)$$

Therefore rewriting the equations 3.17 to 3.19 by substituting in the non-dimensional parameters

$$\frac{\partial T_f^*}{\partial z} + NTU\left(T_f^* - \frac{T_{s1}^* - T_{s2}^*}{2}\right) = 0 \quad (3.29)$$

Solid 1

$$\frac{\partial T_{s1}^*}{\partial \theta} = \lambda \frac{\partial^2 T_{s1}^*}{\partial z^2} + \frac{NTU}{2}\left(1 + \frac{1}{\beta}\right)\left(T_f^* - T_{s1}^*\right) \quad (3.30)$$

Solid 2

$$\frac{\partial T_{s2}^*}{\partial \theta} = \lambda \frac{\partial^2 T_{s2}^*}{\partial z^2} + \frac{NTU}{2}(1 + \beta)\left(T_f^* - T_{s2}^*\right) \quad (3.31)$$

Where:

T_f - Fluid temperature

T_{s1} - Corrugated solid temperature

T_{s2} - Undulated solid temperature

T_f^* - Dimensionless fluid temperature

T_{s1}^* - Dimensionless corrugated solid temperature

T_{s2}^* - Dimensionless undulated solid temperature

The above-mentioned equations are solved using the standard difference approximations and the Crank-Nicholson implicit method. These three equations (equations 3.29 to 3.31) are used to calculate the surface metal temperatures for both solid regions and the fluid region along the elements at any point in time. The ends of the plates in a pack were taken into account by modifying these equations. This requires that the conduction term at the free end of the element must be replaced with a convection term and then rederiving the equations (De Klerk, 2001). Figures 3.5 are an illustration of the descretization of a flat double- and single-plated region into finite difference elements respectively.

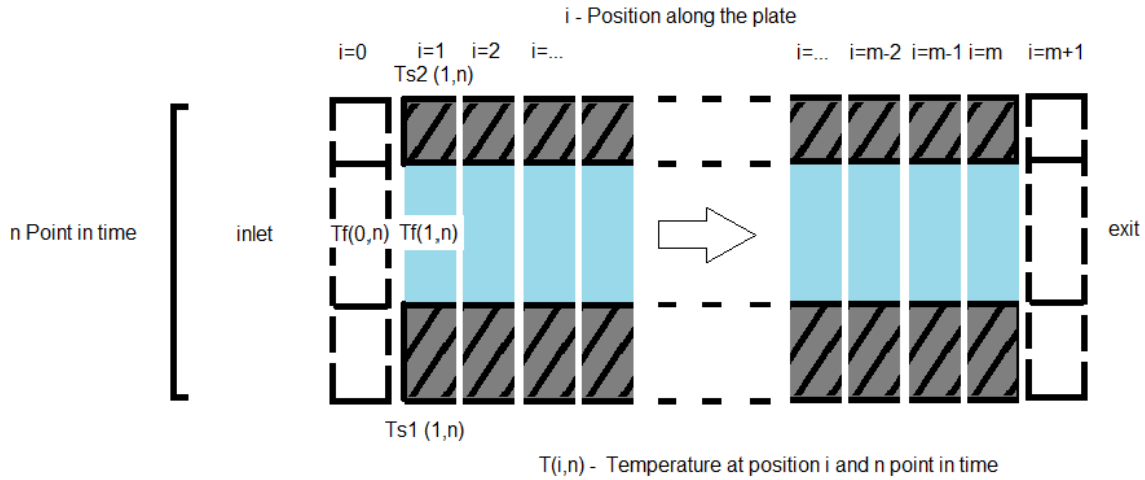

Figure 3.5: Discretization of a flat double plated region into finite difference elements

A system of equations can now be formulated in a matrix form. These equations are used in a finite difference scheme in the following way:

$$\frac{T_f^*(i,n) - T_f^*(i,n)}{\Delta z} + NTU\left(T_f^*(i,n) - \frac{T_{s1}^*(i,n) - T_{s2}^*(i,n)}{2}\right) = 0 \quad (3.32)$$

Solid 1

$$\frac{T_{s1}^*(i,n+1) - T_{s1}^*(i,n)}{\Delta \theta} = \lambda(X + Y) + \frac{NTU}{2}\left(1 + \frac{1}{\beta}\right)\left(T_f^*(i,n) - T_{s1}^*(i,n)\right) \quad (3.33)$$

Solid 2

$$\frac{T_{s2}^{*}(i,n+1)-T_{s2}^{*}(i,n)}{\Delta\theta}=\lambda(X+Y)+\frac{NTU}{2}\left(1+\frac{1}{\beta}\right)\left(T_{f}^{*}(i,n)-T_{s2}^{*}(i,n)\right) \quad (3.34)$$

X and Y can be substituted with:

Solid 1

$$X=\frac{T_{s1}^{*}(i+1,n+1)-2T_{s1}^{*}(i,n+1)+T_{s1}^{*}(i-1,n+1)}{2\Delta z^{2}} \quad (3.35)$$

$$Y=\frac{T_{s1}^{*}(i+1,n)-2T_{s1}^{*}(i,n)+T_{s1}^{*}(i-1,n)}{2\Delta z^{2}} \quad (3.36)$$

Solid 2

$$X=\frac{T_{s2}^{*}(i+1,n+1)-2T_{s2}^{*}(i,n+1)+T_{s2}^{*}(i-1,n+1)}{2\Delta z^{2}} \quad (3.37)$$

$$Y=\frac{T_{s2}^{*}(i+1,n)-2T_{s2}^{*}(i,n)+T_{s2}^{*}(i-1,n)}{2\Delta z^{2}} \quad (3.38)$$

The assumption of an insulated end is applied here. To satisfy the condition of zero heat transfer from ends of the plates elements are added to the ends as indicated in Figure 3.5. The following assumptions are made (De Klerk, 2001):

$$T_{s1}^{*}(0,n)=T_{s1}^{*}(1,n) \quad (3.39)$$

$$T_{s1}^{*}(m+1,n)=T_{s1}^{*}(m,n) \quad (3.40)$$

$$T_{s2}^{*}(0,n)=T_{s2}^{*}(1,n) \quad (3.41)$$

$$T_{s2}^{*}(m+1,n)=T_{s2}^{*}(m,n) \quad (3.42)$$

Equation 3.43 can be substituted into 3.33 and 3.34:

$$\gamma=\lambda\Delta\theta/2\Delta z^{2} \quad (3.43)$$

Rewriting equations 3.33 and 3.34 as a system of equations in matrix form the matrices A, B and D can now be generated to exemplify the system of equations:

Matrix A is the m × m matrix that will form part of the augmented matrix to solve matrix B. Matrix B is the solid temperature matrix for the next time step. Matrix D can be calculated for each time step. To solve Matrix B either the inverse method can be used or Gaussian elimination method can be used.

$$\text{A}=\begin{bmatrix}1+\gamma & -\gamma & 0 & 0 & 0 & 0\\ -\gamma & 1+2\gamma & -\gamma & 0 & 0 & 0\\ 0 & \dots & \dots & \dots & 0 & 0\\ 0 & 0 & -\gamma & 1+2\gamma & -\gamma & 0\\ 0 & 0 & 0 & \dots & \dots & -\gamma\\ 0 & 0 & 0 & 0 & -\gamma & 1+\gamma\end{bmatrix} \quad (3.44)$$

$$B=\begin{bmatrix} T^*_{s1/s2}(1,n+1) \\ T^*_{s1/s2}(2,n+1) \\ \dots \\ T^*_{s1/s2}(i,n+1) \\ \dots \\ T^*_{s1/s2}(m,n+1) \end{bmatrix} \quad (3.45)$$

$$D=\begin{bmatrix} D(1) \\ D(2) \\ \dots \\ D(i) \\ \dots \\ D(m) \end{bmatrix} \quad (3.46)$$

The augmented matrix form:

$A \times B = D$ (3.47)

Using the inverse method equation 3.48 is found:

$B = A^{-1}D$ (3.48)

In the simulation model the following boundary conditions are used to calculate the Matrix D.

For i=1:

$$D_{s1}(1) = \gamma T^*_{s1}(2,n) + (1-\gamma-\frac{NTU}{2}(1+\frac{1}{\beta})\Delta\theta)T^*_{s1}(1,n) + \frac{NTU}{2}(1+\frac{1}{\beta})\Delta\theta T^*_f(1,n) \quad (3.49)$$

$$D_{s2}(1) = \gamma T^*_{s1}(2,n) + (1-\gamma-\frac{NTU}{2}(1+\beta)\Delta\theta)T^*_{s1}(1,n) + \frac{NTU}{2}(1+\beta)\Delta\theta T^*_f(1,n) \quad (3.50)$$

For 2≤i≤m-1:

$$D_{s1}\ (i) = \gamma T^*_{s1}(i+1,n) + \left(1-2\gamma-\frac{NTU}{2}\left(1+\frac{1}{\beta}\right)\Delta\theta\right)T^*_{s1}(i,n) + \gamma T^*_{s1}(i-1,n) + \frac{NTU}{2}(1+\frac{1}{\beta})\Delta\theta T^*_f(i,n) \quad (3.51)$$

$$D_{s2}\ (i) = \gamma T^*_{s2}(i+1,n) + \left(1-2\gamma-\frac{NTU}{2}(1+\beta)\Delta\theta\right)T^*_{s2}(i,n) + \gamma T^*_{s2}(i-1,n) + \frac{NTU}{2}(1+\beta)\Delta\theta T^*_f(i,n) \quad (3.52)$$

For i=m:

$$D_{s1}(m) = \gamma T^*_{s1}(m-1,n) + (1-\gamma-\frac{NTU}{2}(1+\beta)\Delta\theta)T^*_{s1}(m,n) + \frac{NTU}{2}(1+\beta)\Delta\theta T^*_f(1,n) \quad (3.53)$$

$$D_{s2}(\mathrm{m}) = \gamma T^*_{s2}(m-1,n) + (1-\gamma-\frac{NTU}{2}(1+\beta)\Delta\theta)T^*_{s2}(m,n) + \frac{NTU}{2}(1+\beta)\Delta\theta T^*_f(1,n) \quad (3.54)$$

Through solving equations 3.32, 3.33 and 3.34 iteratively in the form of matrices A, B and D the fluid and solid region temperatures can be predicted.

3.2.2 Calculation of the heat transfer coefficient

As described in Chapter 2, a thermal test facility was built by Caby (1996) to measure the heat transfer coefficient and pressure drop of a sample pack. The facility was built to test all the available element packs, but packs with equal thickness plates were only considered. Gruen's research indicated how significantly the thermal properties change when different thicknesses are used. The heat transfer model from Habbitts (1998) did not take this aspect into account. De Klerk (2001) reviewed the simulation code to add the capability of simulating alternating thicknesses of the element plates. Table A1 in Appendix A is a representation of the results from the above mentioned tests, showing the constants for calculating both the Colburn j factor and the Fanning friction factor in relation to the Reynolds number. Area of conduction, area of convection, mass and plate thickness are included. This information is used to calculate the thermal properties to estimate the gas and metal temperatures of the air heaters. The change of the heat transfer coefficient is calculated at every time step for each layer. The calculation process is explained in detail in Appendix A, section A2.

3.2.3 Calculation of the pressure drop

The results of the pressure drop tests were formulated in terms of the Fanning friction factor versus the Reynolds number. For an air heater element pack the Reynolds number can be calculated using the hydraulic diameter multiplied with the fraction of the average velocity (m/s) of flow in the pack divided by the kinematic viscosity (m^2/s). Habbitts used the mass velocity (kg/ m^2s) and the dynamic viscosity (kg/ms) as indicated in Appendix A3. This calculation takes into consideration the entrance and exit factors to isolate the losses associated with the fluid flowing through the pack. The Fanning friction factor relationship is explained in detail in Appendix A. section A3.

3.3 Analysis of Dew Point Related Air Heater Fouling

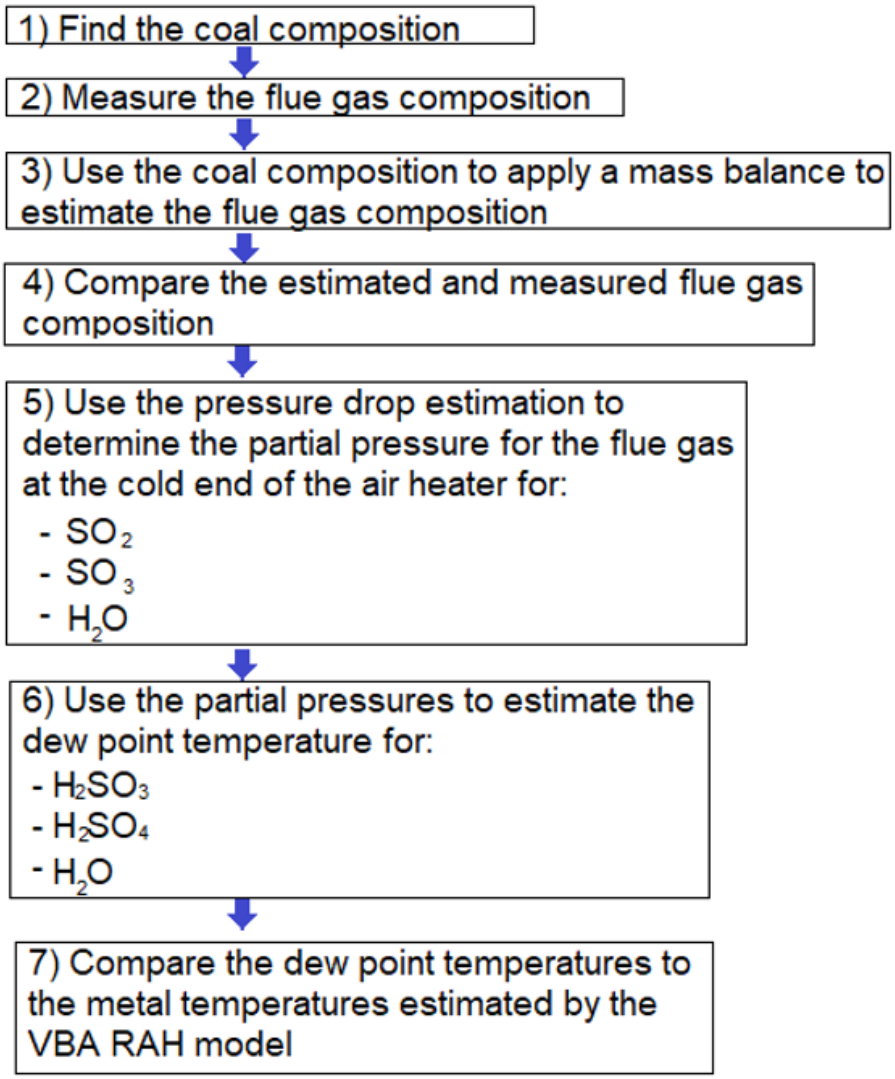

Figure 3.6: Schematic illustration of the dew point temperature estimation process.

Figure 3.6 is an illustration of the simplified methodology used to estimate the dew point temperature. The process is followed for each time step of the mathematical model. For this calculation process the coal composition, flue gas composition and flue gas partial pressure estimation is done using the following:

3.3.1 Coal composition

The simulation model uses the coal composition as input parameters, to estimate the fluid properties for flue gas. The theoretical process starts with estimating the amount of unburnt carbon using equation 3.55:

$$C' = \%Ash\ in\ coal\ \times [(\%C'_{fa}\ \times \%fly\ ash) + (\%C'_{ba}\ \times \%bottom\ ash)] \quad (3.55)$$

C'_{fa}- Unburnt Carbon in fly ash

C'_{fba}- Unburnt Carbon in bottom ash

There is an amount of carbonite (carbon dioxide) in the coal that must also be taken into consideration to find the final carbon content in the flue gas (equation 3.56):

$$C = \frac{\%C}{100} - C' + \frac{12}{44}CO_2 \quad (3.56)$$

C - Carbon in coal

CO_2 - Carbon dioxide in coal

If insufficient combustion occurs it would be a result of insufficient combustion air supplied causing sub-stoichiometric conditions. Stoichiometric air refers to the theoretical amount of air required for full combustion to occur. In the case of sub-stoichiometric conditions there is simply not enough oxygen and therefore a highly explosive gas accumulates during combustion namely carbon monoxide (CO). To avoid this, the required air is calculated along with an amount of excess air to maintain a safe operation. These forms part of the basis of the mass balance that occurs during combustion. The following process shows how the air requirements are calculated:

Theoretical Air required

$$TAR = AF_{stoich} = \frac{1}{0.23}\left[\frac{32}{12}(C - C') + \frac{32}{32}(S) + 8(H) + 0.3\frac{32}{14}(N) - (O)\right] \quad (3.57)$$

AF_{stoich}- Stoichiometric Air Fuel Ratio
S - Sulphur in coal
H - Hydrogen in coal
O - Oxygen in coal
N - Nitrogen in coal

Excess Air

$$EA_{\,after\ AH} = \left[\frac{TAR + 1 - \%\ Ash}{TAR}\right] \times \left[\frac{{}^{v}/_{v}O_{2\ before\ AH}}{21 - {}^{v}/_{v}O_{2\ before\ AH}}\right] \times 100\% \quad (3.58)$$

${}^{v}/_{v}\,O_{2\ before\ AH}$ - The oxygen in the flue gas measured before the air heater

Dry Air required

$$DAR = TAR \times (1 + EA_{\,after\ AH}) \quad (3.59)$$

a) ***Humid Air required***

$$HAR = DAR \times (1 + \omega) \quad (3.60)$$

ω – *Air humidity ratio*

b) *Composition of flue gas by means of mass balance*

Considering the basic principles of mass balance:

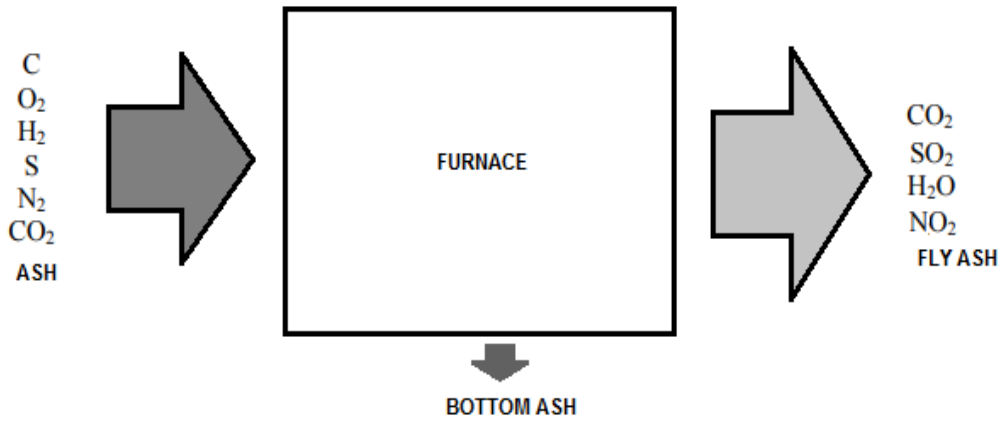

Figure 3.7: Mass balance of the coal combustion process (Van Wyk, 2010).

Mass ratio of flue gas per kilogram coal

$$\hat{m}_{FG} = (1 - \%Ash\ in\ coal) - C' + HAR \quad (3.61)$$

Mass ratio of CO_2 per kilogram coal

$$\hat{m}_{CO_2} = \frac{44}{12} \times (C - C') \quad (3.62)$$

Mass ratio of SO_2 per kilogram coal

$$\hat{m}_{SO_2} = \frac{64}{32} \times (S) \quad (3.63)$$

Mass ratio of N_2 per kilogram coal

$$\hat{m}_{N_2} = 0.77 \times DAR + (\%F \times \frac{1}{2}(N)) \quad (3.64)$$

Where; F- Nitrogen conversion factor

Mass ratio of H_2O per kilogram coal

$$\hat{m}_{H_2O} = H_2O_{coal} + (\omega \times DAR) + \frac{18}{2} H \quad (3.65)$$

Mass ratio of NO_2 per kilogram coal

$$\hat{m}_{NO_2} = \frac{46}{14} \times (N) \times (100 - \%Remainder\ of\ Nitrogen) \quad (3.66)$$

Mass ratio of O_2 per kilogram coal

$$\hat{m}_{FG} = \hat{m}_{CO_2} + \hat{m}_{SO_2} + \hat{m}_{N_2} + \hat{m}_{H_2O} + \hat{m}_{NO_2} + \hat{m}_{O_2} \quad (3.67)$$

Rewriting equation3.78:

$$\hat{m}_{O_2} = \hat{m}_{FG} - \hat{m}_{SO_2} - \hat{m}_{N_2}\ \hat{m}_{H_2O} - \hat{m}_{NO_2} - \hat{m}_{CO_2} \quad (3.68)$$

The flue gas constituents can now be established by using the constituent masses per kg of coal and dividing each constituent by the flue gas ratio per kg of coal. The following equation is a general expression of this conversion:

$$^{m}/_{m}\ i_{x,flue\ gas} = \frac{\hat{m}c_{x,fluegas}}{\hat{m}_{FG}} \quad (3.69)$$

The volume percentage can also be determined by using Amagat's law of additive volumes for a gas mixture. The assumption made is that all components are at the same temperature for the flue gas mixture. The gas mixture volume should then be the sum of all the individual volumes. This effect was illustrated in a study done by Rathore (2010). The ideal gas law can be used to derive the volume for each constituent.

$$PV_i = n_i RT = \frac{\hat{m}_i}{M_i} RT \quad (3.70)$$

$$V_i = \frac{\hat{m}_i RT}{PM_i} \quad (3.71)$$

Where:
V_i – Volume of flue gas constituent
$\hat{m}_i$ – Mass of flue gas constituent
n_i – Number of moles
P – Pressure of flue gas
R – Gas constant for flue gas
T – Temperature for flue gas
M_i – Molar mass of flue gas constituant

The volume per kilogram of coal can be determined and the volume percentage can be used by dividing each constituent volume per kilogram coal, by the total volume of flue gas per kilogram coal.

3.3.2 Critical Parameters for dew point related fouling

There are certain operating parameters that play a critical role in the formation of deposits in air heaters. Firstly the correct atmospheric pressure must be taken into consideration when estimating the absolute pressure of flue gas. This requires a correct value for the altitude at which the power station is operating. Secondly acid dew point temperature of the flue gas plays a role as it relies on the sulphur dioxide, sulphur trioxide, water vapour and oxygen in the flue gas. The third critical parameter is the air heater flue gas inlet temperature to ensure that the correct initial flue gas temperature is used for the estimation of the fourth parameter, namely the air heater element metal surface temperature, estimated by using the regenerative air heater simulation model. This temperature will establish where fouling can be expected in element packs. The fifth parameter is the air inlet temperature, which forms an integral part in ensuring that the cold end of the air heater operates at gas- and metal temperatures higher than the dew point temperature. The sixth parameter is the air heater leakage, as it also adds air that contains some moisture to the flue gas mixture, which increases the rate at which fouling will occur. As mentioned before the final condensed sulphuric acid equation is the following:

$$SO_2 + H_2O \rightarrow H_2SO_3$$

$$SO_3 + H_2O \rightarrow H_2SO_4$$

Absolute pressure of flue gas

To determine the flue gas absolute pressure, the correct atmospheric pressure will be required; based on the altitude this can be calculated by using an equation 3.72:

$$P = P_0(1 - \frac{Bz}{T_0})^{\frac{g}{RB}} \quad (3.72)$$

P_0- 101.325 kPa
T_0- 288.16 °K
z- Altitude in metres
B- 0.0065 °K/m
$\frac{g}{RB}$ – 5.26 (for air)

Dew point temperature

Sulphur is the critical parameter for fouling and corrosion. This constituent affects the tendencies of clinkering and slagging. It promotes corrosion and dew point related fouling in the downstream conditions or any areas where the surfaces operate below the acid dew point temperatures. The chemical formation after combustion is the following (Ganapathy, 1989):

- 1% to 5% of the SO_2 in the flue gas will be converted to SO_3:
  $SO_2 + O_2 \rightarrow SO_3$ (in the flame)

- Low temperature zone between 602 ºC to 752 ºC:
  SO_2 + Catalyst (Vanadium pentoxide and iron oxide) → SO_3 + catalyst product
  Vanadium pentoxide (V_2O_5) is generated from burning of fuel oil, and Iron oxide exposure comes from the boiler materials and fuel ash.
  The SO_3 further reacts with moisture to form sulphuric acid vapour
  $SO_3 + H_2O \rightarrow H_2SO_4$ (below 350 °C)

- Condensation of the water vapour in the flue gas takes place at temperatures below the water dew point:
  $SO_2 + H_2O \rightarrow H_2SO_{3\ liquid}$
  $SO_3 + H_2O \rightarrow H_2SO_{4\ liquid}$

Raask (1985) stated that the concentrated solution of H_2SO_4 would combine with alkaline ash and a reaction would occur with the air-heater element surface. These reactions are the critical chemical reactions that cause dew point related fouling. A mass balance from the coal to the flue gas state is required to find the partial concentration of SO_2, SO_3 and H_2O in flue gas.

These results determine the dew point temperatures for sulphurous acid, sulphuric acid and moisture. This process is shown in Figure 3.8. During condensation of the water vapour in the flue gas, sulphurous and sulphuric acids are formed. The dew point temperature is therefore one of the critical parameters to ensure that limits are identified in terms of the metal temperature control. If the metal temperature is kept above the acid dew point temperature, deposition can be avoided. The three critical dew point temperatures to be taken into consideration are the dew point temperature of water vapour, sulphurous acid and sulphuric acid. The critical common factor is the partial pressure of the water vapour. Sulphur dioxide partial pressure also plays a role in the dew point temperature calculation for sulphurous acid. For sulphuric acid the partial pressure of sulphur trioxide becomes a critical parameter. The following figure illustrates the formation of the flue gas in relation to the critical reactions regarding dew point temperatures (Mathebula, 2014).

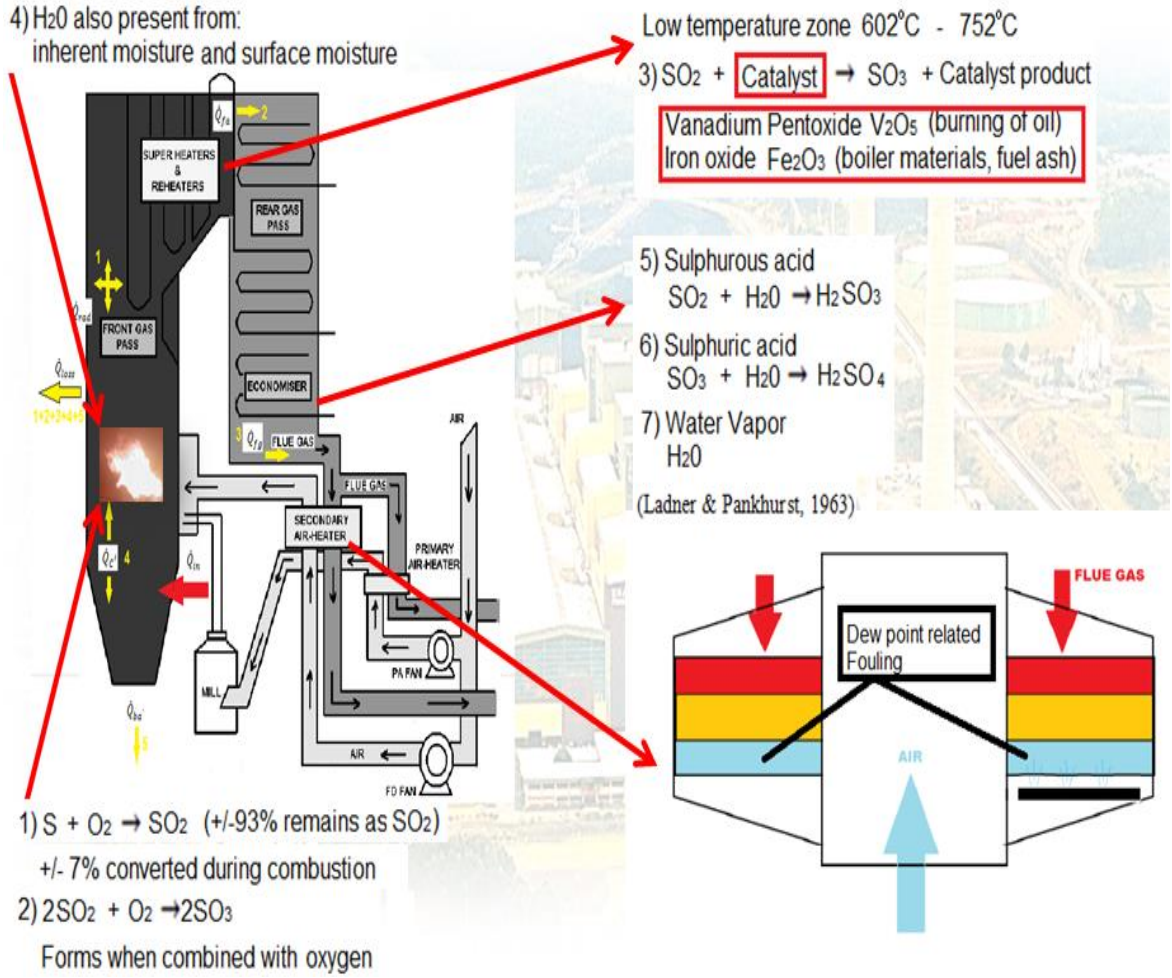

Figure 3.8: Sulphurous acid and sulphurous acid formation in Air heaters.

The developed VBA RAH simulation model estimates the dew point temperatures, which also makes it possible to change some parameters to keep condensation in air heater elements to the minimum. The correct partial pressure is required to ensure accurate results are obtained to reduce condensation. This pressure can be determined by using the inlet pressure to the air heater. The Dalton model indicates that the sum of the partial pressures of the individual gases forms the flue gas pressure. To use the Dalton model, the flue gas must first be proven to be an ideal gas mixture. This condition was verified by Mathebula (2014). Kunz (2011) determined

the compressibility factor (Z) of the air, which was used to determine the compressibility factor of each flue gas constituent. From these results water vapour was the only gas not acting according to an ideal gas at 300°K. But for higher temperatures water vapour reacted accordingly. Considering the fact that water vapour only forms 10% of the flue gas, the concern of this effect is minimized. Given the fact that Eskom air heaters usually have a flue gas exit temperature of about 400°K, the compressibility factor for water vapour would be close enough to one. Therefore the flue gas may be modelled as an ideal gas. The compressibility factors for the flue gases can be seen in the table in Appendix A5, along with the method followed to find the compressibility factor

Equation 3.75 can be used to calculate the partial pressure ($Þ_i$) of the flue gas components. The partial pressure for sulphur trioxide would be the percentage conversion initially assumed for the formation of sulphur trioxide.

$$Þ_i = \left(\frac{\%\, mole\ fraction}{100}\right) \times P \tag{3.75}$$

Using the partial pressure for water vapour the steam tables can be used to find the saturation temperature of water vapour. This will then be the dew point temperature for water vapour.

$$Þ_{H_2O} = \left(\frac{\%H_2O}{100}\right) \times P \quad ;\ Find\ T_{H_2O}\ from\ the\ steam\ tables \tag{3.76}$$

For the sulphurous acid dew point a different approach is used. Ganapathy (1989) illustrated that equation 3.77 (Verhoff & Branchero –C method) could be used to determine the dew point temperature for H_2SO_3. The partial pressures for water vapour and sulphur dioxide will be used in equation 3.78 and 3.79 for the variables "a" and "b" in equation 3.77.

$$\frac{1000}{T_{dp}} = 3.9526 - (0.1863\ \times a) + (0.000867\ \times B) - (0.000913\ \times a \times b) \tag{3.77}$$

$$a = \ln(Þ_{H_2O}) \tag{3.78}$$

$$b = \ln(Þ_{SO_2}) \tag{3.79}$$

For the sulphuric acid dew point, equation 3.80 may be used to determine the dew point temperature for H_2SO_4. The partial pressures for water vapour and sulphur trioxide will be used in equation 3.81 and 3.82 for the variables c and d in equation 3.80.

$$\frac{1000}{T_{dp}} = 2.276 - (0.0294\ \times c) - (0.0858\ \times d) + (0.0062\ \times c \times d) \tag{3.80}$$

$$c = \ln(Þ_{H_2O}) \tag{3.81}$$

$$d = \ln(Þ_{SO_3}) \tag{3.82}$$

Mass flow rate of coal, flue gas, air

For the dew point related fouling simulation model, the option of using the mass and energy balance (MEB) model developed by Govindsamy (2014) is included. The MEB model considers both energy and mass transfer for the boiler, and the flows can be selected as input parameters to the dew point related fouling simulation model. This provides an additional capability of the model, to consider design changes to the boiler, which influences the flow rates of coal, air and steam. The effect of these changes can then be quantified in terms of the change in air heater performance (Govendsamy, 2014). The detail pertaining the boiler mass energy balance can be seen from section 3.1.

Mass flow rate of coal (kg/s)

$$\dot{m}_{coal} = \frac{\dot{Q}_{out} - Q_{credits}}{CV_c\left[1 - C''' - \frac{0.8}{100}\right] + h_c + HAR(h_{sa,ah,in} - (\%leak \times h_{leak})) - \hat{m}_{fg} h_{fg}} + \frac{\dot{Q}_{out} - Q_{credits}}{-[\%Ash \times \%\ BA]h_{ba} - [\%Ash \times \%\ FA]h_{fa} - \left(\%H_2O \times h^{v}_{H_2O}\right))}$$

(3.84)

Mass flow rate of flue gas (kg/s)

$$\dot{m}_{fg} = \hat{m}_{fg} \times \dot{m}_{coal} \quad (3.85)$$

Mass flow rate of Air (kg/s)

$$\dot{m}_{air} = HAR \times \dot{m}_{coal} \quad (3.86)$$

3.4 Dew Point Related Fouling Simulation Model Methodology

The theoretical background from sections 3.1 to 3.3 was integrated into a VBA format to generate a graphical representation of the onset of dew point related fouling. Figure 3.9 is a schematic representation of the steps followed within the model interface to generate this graphical representation.

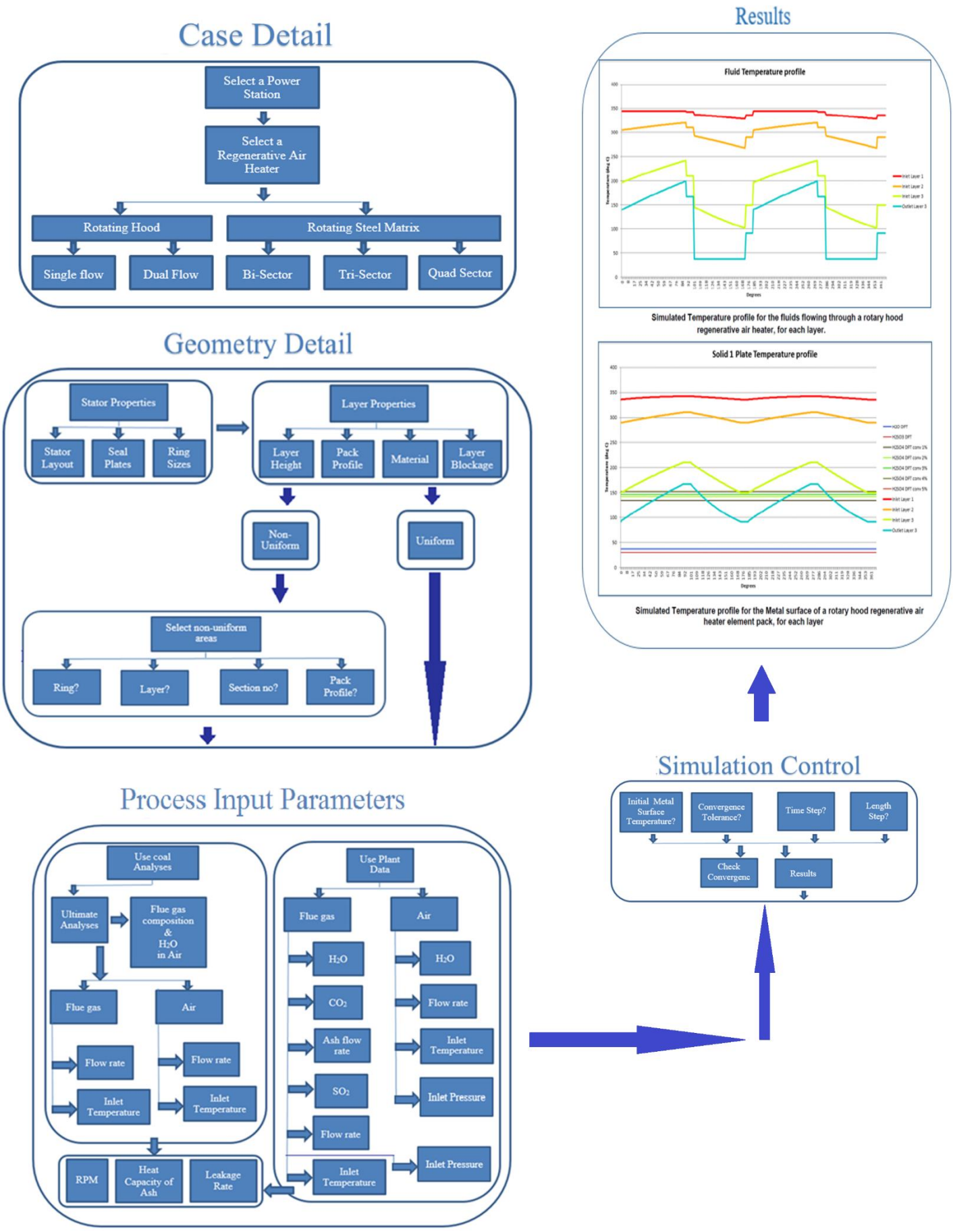

Figure 3.9: Flow diagram for the VBA RAH model interface.

The method of calculating the temperature profiles starts with the case detail. From this first step a power station is selected, which is shown in Figure 3.10 and the applicable unit where the case study is conducted. The type of air heater shown here as an example is a rotating hood, single flow air heater. The selection options for the rotating hood are a single flow type or a dual flow type. For the rotating matrix three types can be selected, a bi-sector, tri-sector or a quad sector. Figure 3.10 is an illustration of the interface display in the program. Figure 3.10 is the selection flow diagrams for section A – Case detail.

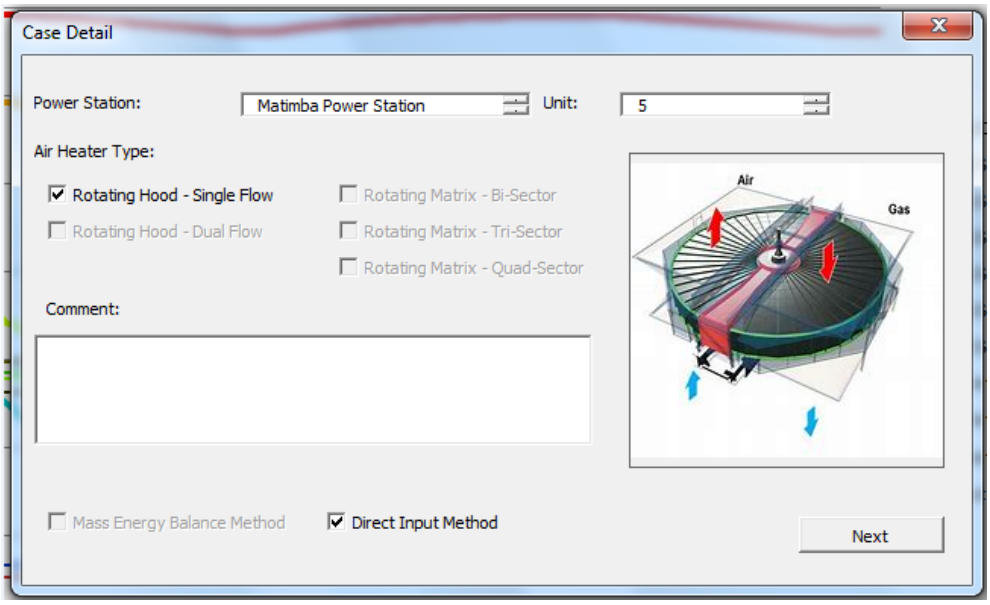

Figure 3.10: Case detail RAH VBA – Interface

The case detail interface also consists of a selection between Mass Energy Balance or Direct input methods. The mass energy balance method consists of a path to analyse a boiler according to its mass and energy balance properties. The energy input to the boiler is compared to the energy outputs to calculate the flow rates for coal, air, flue gas and steam. This method also considers the coal properties through applying a mass balance across the combustion process to find the flue gas composition, which then contributes to the calculation procedure of the theoretical air required for combustion and the above mentioned flow calculations. This option provides a platform to consider a boiler design and then selecting an appropriate air heater for the application. The direct method uses plant measurements as input parameters. In both options temperature profiles are generated for the fluids and the metal surfaces of each ring, including the average dew point temperatures for sulphuric acid, sulphurous acid and water vapour.

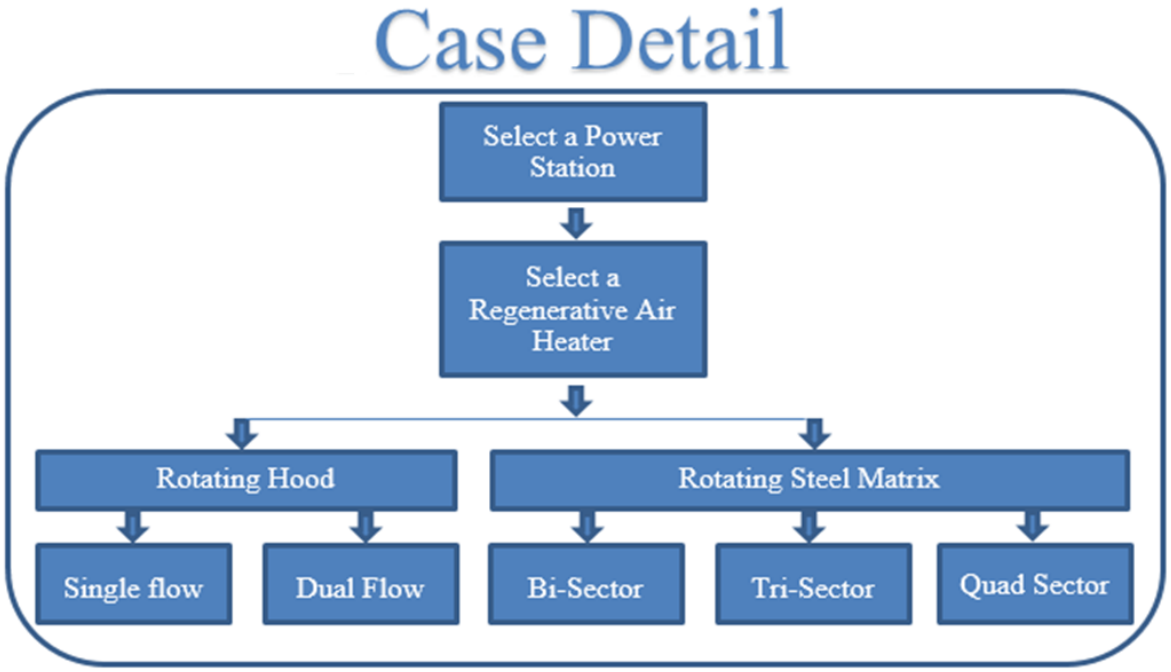

Figure 3.11: VBA RAH - Case detail flow diagram.

After the Case detail is completed the geometry detail is required, which is captured into the model using the interface shown in Figures 3.12 and 3.13. The detail consists of two main groups of input parameters, namely steel matrix properties and layer properties. For the steel matrix properties the layout of the steel matrix is configured. The steel matrix configuration consists of the number of rings, the number of circumferential and radial divisions, the width of the grease lubrication channel and the thickness of all the plates. The information is used to establish the amount of area available for flow. The total area per stream is calculated according to the area available for flow. The next interface for input parameters is the sector angles to ensure that the flow areas are calculated according to the streams passing through the air heater. Figure 3.12 illustrates where the sector angles must be inserted to calculate the flow areas. The steel matrix properties referred to in Figure 3.13 include the seal plates.

Figure 3.12: Sector angle and area calculation – Interface

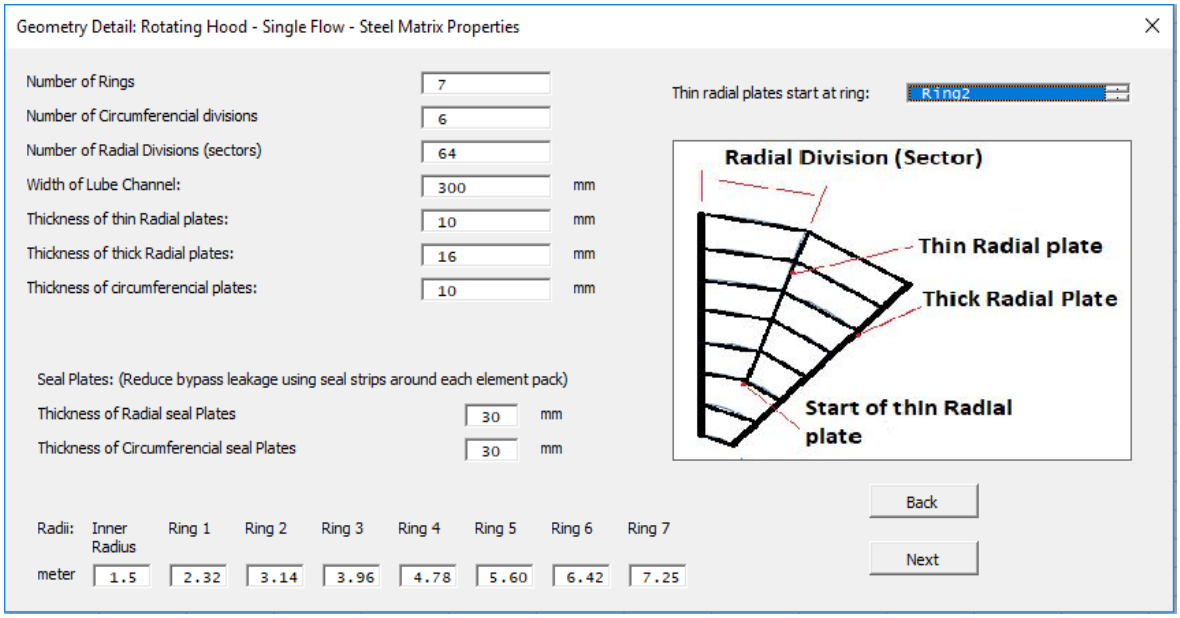

Figure 3.13: Geometry detail – Steel matrix properties – flow area – Interface

Figure 3.14 shows the interface for the VBA RAH model to insert all the steel matrix properties into the model. The layer height, pack type, material and blockage per layer are selected.

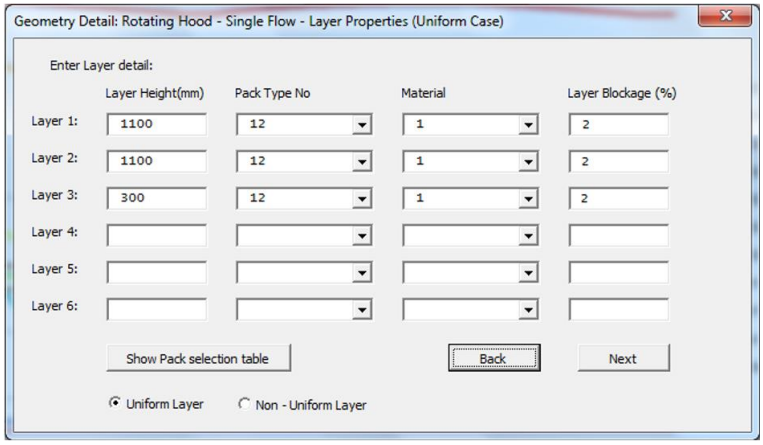

Figure 3.14: Layer Properties – Interface

If the uniform option is selected the layer properties for that section are copied to all the remaining sections. If the non-uniform option is selected Figure 3.15 will appear as an interface for a non-uniform pack selection. In this section the ring number is selected along with the layer in which a different pack is installed. The section where the pack is installed is selected and the pack profile used in this section is selected. The input parameters are then submitted until all the different packs are inserted into the model. Figure 3.16 is a flow diagram explaining the latter.

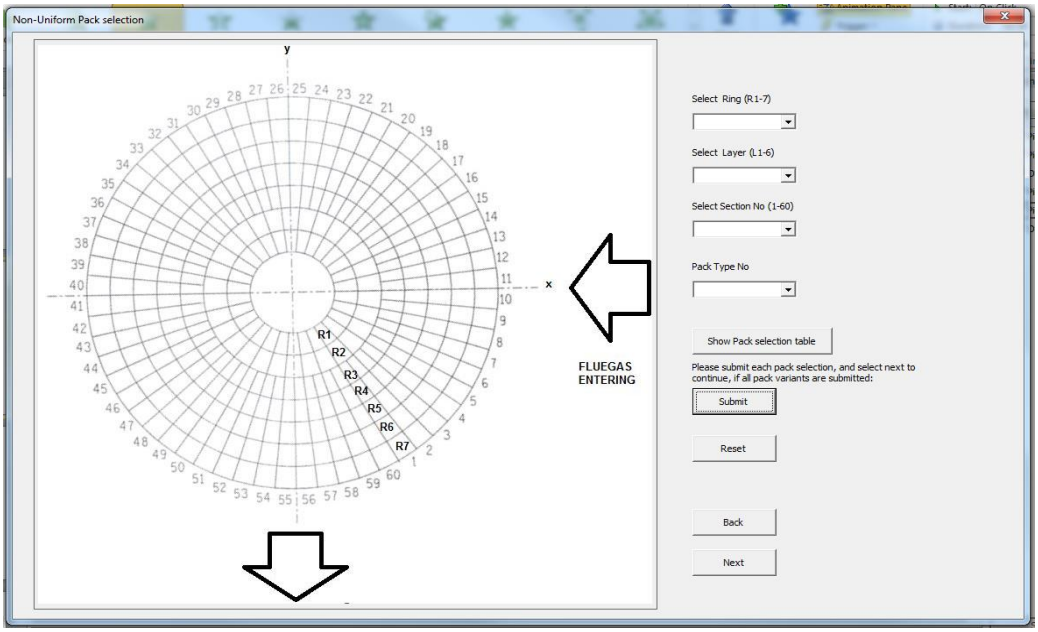

Figure 3.15: Non-uniform pack selection – Interface

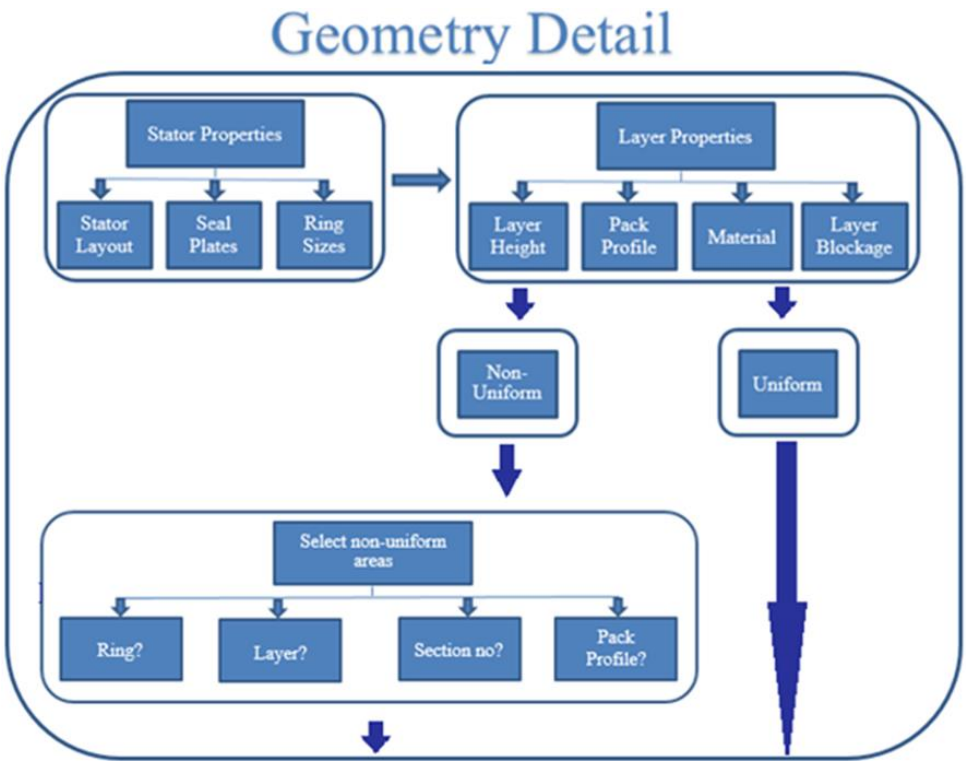

Figure 3.16: VBA RAH - Geometry detail flow diagram.

After all the geometrical detail is captured the user will be required to insert the process parameters. In the case of a direct input method, the coal ultimate analysis is required to include the coal composition into the model. This method will still allow the calculation to apply a mass balance to estimate the flue gas composition. If the option of plant data is used, the measured flue gas and air properties will be required as indicated in Figure 3.17. These parameters are used to calculate the fluid properties for each time interval. For each layer, the inlet temperature and pressure for each time interval are added to the outlet temperature and

pressure from the previous time interval and then divided by 2 to find an average temperature and pressure per time interval. The pressure and temperature are then used to calculate the density, viscosity, thermal conductivity and heat capacity for each time interval. These fluid properties are then used to calculate the fluid temperature and metal surface temperature for each length step until the outlet temperatures for the full pack height is reached. The outlet conditions are then used as the inlet condition to the next layer and the same process is followed to calculate the outlet conditions per layer. Figure 3.17 is an illustration of the interface used to capture the process parameters into the model.

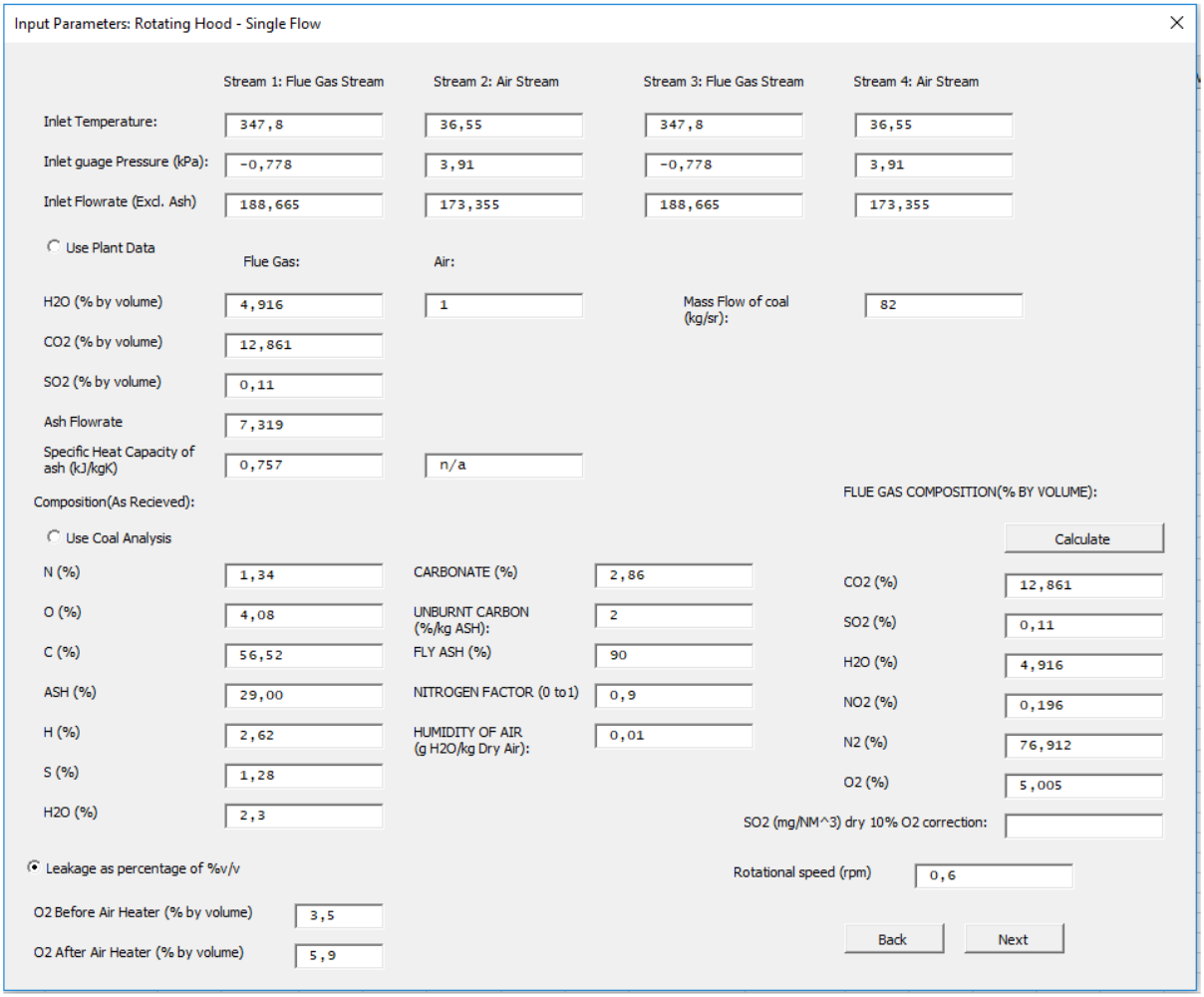

Figure 3.17: Process Input parameters – Interface

The VBA RAH model has one method of capturing air heater leakage. The volumetric percentage of oxygen measured at the inlet of the air heater and the volumetric percentage of oxygen measured at the outlet of the air heater are entered into the model where the percentage leakage is then calculated. This percentage is then used to amend the air flow entering the air heater. The temperatures of the flue gas and air mixture are also calculated using the leakage rates. There are three forms of leakages in a rotary regenerative air heater namely, direct leakage, entrained leakage and bypass leakage (as shown in Figure 3.18):

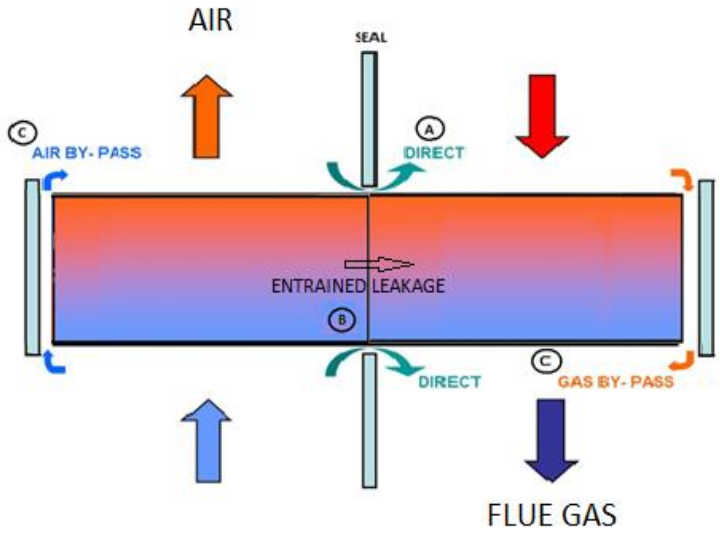

Figure 3.18: Various Air heater leakage types

A. Direct leakage

The direct leakage is the amount of air directly leaking to the flue gas stream due to insufficient sealing from the air heater seals. The method explained in section 3.2 calculates the total air heater leakage and therefore this portion of leaked air is included into this calculation. Direct leakage is considered to occur on the cold end of the air heater. This is caused by the thermal expansion of the air heater creating high leakage areas at the periphery of the steel matrix. The inlet air flow is reduced, but the flue gas stream flow leaving the air heater is increased by the amount of leaked air.

B. Entrained leakage

Entrained leakage occurs as a result of the rotation effect of the air heater. As the steel matrix rotates, a portion of the fluid is trapped in the element packs passing through the seal area. The fluid portion is therefore lost by the one stream, but added to the other stream. For the VBA RAH model entrained leakage is ignored until the outlet temperatures have been calculated. Equation 3.87 is then used to calculate the mass flow of the entrained portion. This formula is derived by considering the product of the average density of the stream and the volume per second of the section underneath the seals.

$$\dot{m}_{entrained} = \rho . \pi . (r_{outer}^2 - r_{inner}^2) . L . n \tag{3.87}$$

The temperature of the entrained flow is assumed to be the outlet temperature of the stream that it came from. This temperature is then used to calculate the density for the entrained leakage stream. The mixed fluid stream temperature takes the latter into consideration in the results interface.

C. Bypass Leakage

Rotary regenerative air heaters experience bypass leakage when a rotating matrix has a gap on the periphery that allows the fluid to bypass the steel matrix. This is caused due to gaps around the circumference of the heat exchanger or due to gaps in the steel matrix itself. For the rotating hood type of regenerative air heater, the steel matrix is stationary and therefore no flow passes through the circumferential sections of the steel matrix. This is a common

leakage for a rotating matrix type of air heater. To accurately incorporate this leakage into the simulation model is impossible, therefore an estimate of bypass leakage is used which is then accounted for in the mixed stream temperature calculated at the outlet of the air heater.

Another process input parameter that is required for the calculation is the specific heat capacity of the ash in flue gas, along with the flow rate of the ash. The ash present in the flue gas stream increases the net thermal capacitance of the stream. As the ash passes through the heat exchanger thermal energy is exchanged. The heat energy provided by the ash is taken into account in the simulation model by using the mass flow rate of ash and the thermal heat capacity to calculate the amount of thermal energy added to the stream through the ash content. The present model uses a default value of 757.2 J/kgK for the specific heat capacity of ash. This value is accurate for ash with a composition of 60% silicon dioxide and 40% aluminium oxide by mass. For this calculation it is assumed that the temperature of the ash particles is the same as the surrounding flue gas temperature at all times. According to Wilson (1998), the typical size for ash particles is 45µm, and the approximation of the above mentioned is therefore accurate for this ash particle size (Wilson, et al., 1998). Figure 3.19 is an illustration of the flow diagram for the process input parameters required for the calculation procedure.

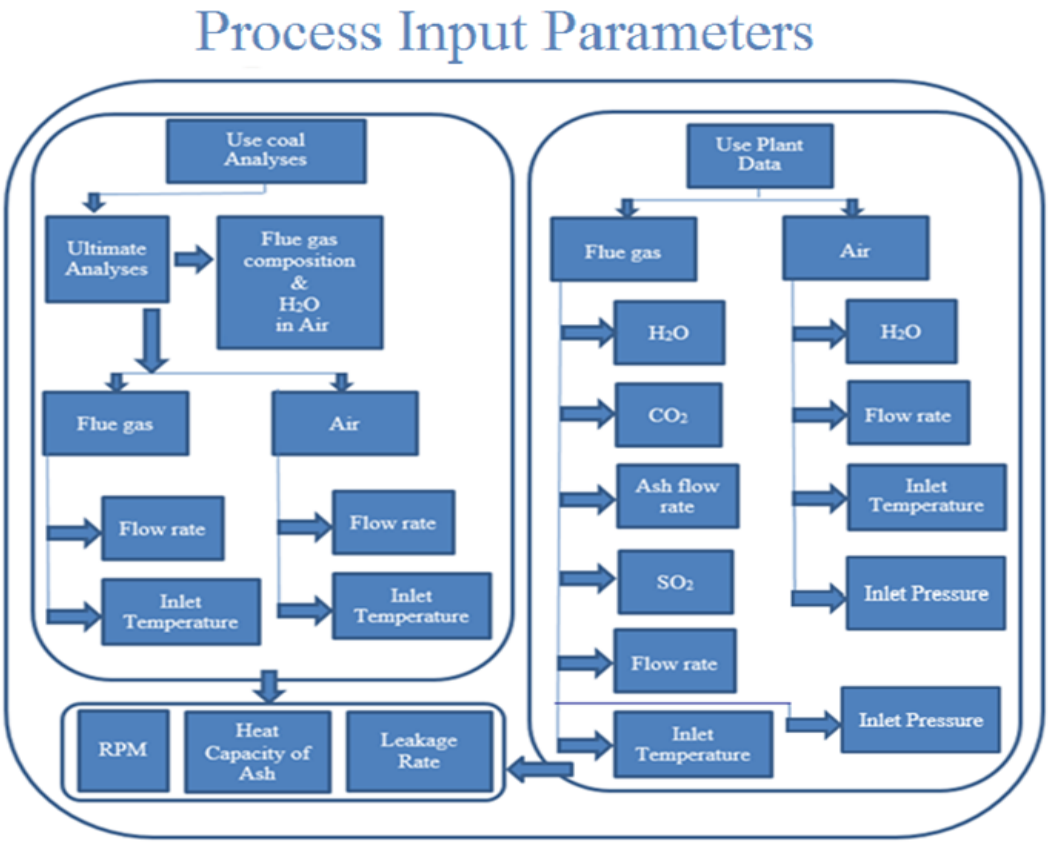

Figure 3.19: Process input parameters flow diagram.

The next interface, illustrated in Figures 3.20 and 3.21, assists in adjusting the simulation controls. Four main inputs are required to initiate an iterative calculation procedure. The simulation model uses a default value which is the average between the inlet temperature of the flue gas and the inlet temperature of air. The simulation will then recalculate the

temperature until the two streams fully converge. The convergence tolerance is selected as a guide to find an accurate temperature profile.

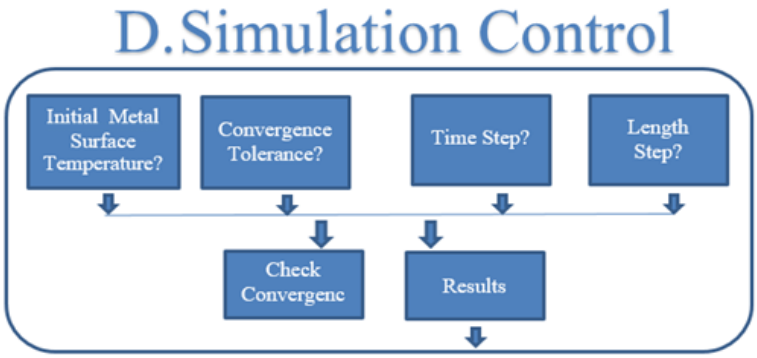

Figure 3.20: Simulation control flow diagram.

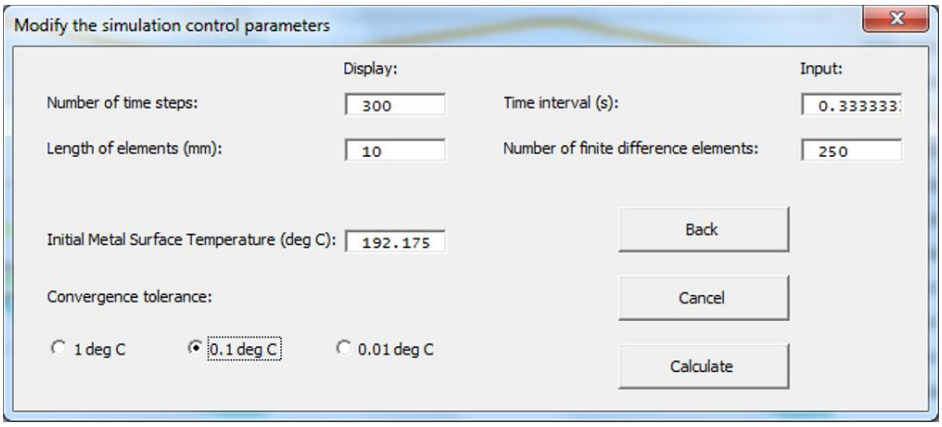

Figure 3.21: Simulation properties – Interface

There are two types of convergence effects. The one type of convergence is for a uniform case, and the other is for a non-uniform case. When different element packs are selected in a layer, the case becomes non-uniform. A cycling effect of temperatures is caused by thermal performance of the varying layers. Therefore to check for convergence in a non-uniform case study, two full revolutions must be completed. The difference between the corresponding temperatures per time step of the two revolutions must be less than the convergence tolerance. For the uniform case the outlet temperature of the current time step is compared to the outlet temperature of the previous time step. For convergence, the difference between the outlet temperatures must be less than the converging temperatures.

The next input parameter is the time step, which is linked to the number of radial divisions according to the rotational speed. The length step is equal to the distance of each finite element length used per time step. The length step also determines the amount of elements used per layer height for elemental analysis. Based on previous research results from De Klerk (2001), 0.333 seconds is the ideal time step which is used as a default setting in the simulation model along with a length step of 10 mm.

From Figure 3.20 the calculation button is selected to initiate the calculation to provide results. The simulation starts by considering ring one. In this ring, layer one is then considered where the inlet flue gas temperature is used at the initial time step to calculate the temperature change for the flue gas and the metal surface temperature at every length step until the complete height

of the layer is reached. The outlet temperature of the layer one becomes the inlet temperature for layer two at the same time step. The same calculation is followed to calculate the outlet temperature for this layer. This process continues until the final layer outlet temperature is calculated. During this calculation the solid temperatures for the next time step for each length step is calculated and stored in a matrix. In the next time step the outlet temperature of the previous time step is added to the inlet temperature of the current time step and divided by two, to find an average temperature for the time step. This temperature is then used to find the fluid properties for the calculation. The following fluid properties are calculated:

3.4.1 The specific heat capacity

The specific heat capacity for both air and flue gas use the same calculation procedure. Nitrogen, oxygen, argon, carbon dioxide, water vapour and ash are the main components for flue gas. Carbon monoxide and oxides from nitrogen and sulphur are ignored due to their small concentrations. The volume fraction and the molar mass of each constituent are required to find the heat capacity of the fluid. Another requirement is the specific heat capacity per constituent, which is found using linear interpolation of a constant pressure specific heat capacity table against the temperature. This method predicts the specific heat of each constituent at a specified temperature. This specified temperature is the average temperature per time step as explained previously. The mixture of the specific heat capacity of the fluid is calculated according to the sum of the proportion of each component according to its mass as explained in equation 3.88.

$$c_{p\ flue\ gas} = \frac{(VMc_p)_{N_2}+(VMc_p)_{O_2}+(VMc_p)_{Ar}+(VMc_p)_{CO_2}+(VMc_p)_{H_2O}}{(VM)_{N_2}+(VM)_{O_2}+(VM)_{Ar}+(VM)_{CO_2}+(VM)_{H_2O}} \quad (3.88)$$

V - Volume fractions
M – Molar mass (kg/kmol)

To include the effect of the thermal energy from the ash, the ratio of flow rates is used to calculate the mixture of ash and flue gas heat capacity as indicated in equation 3.89.

$$c_{p\ mix} = \frac{c_{p\ flue\ gas}\cdot\dot{m}_{gas}+c_{p\ Ash}\cdot\dot{m}_{Ash}}{\dot{m}_{gas}+\dot{m}_{Ash}} \quad (3.89)$$

For the specific heat of air calculation, the volume percentage of carbon dioxide and the mass flow rate of ash are set to zero.

$$c_{p\ Air} = \frac{(VMc_p)_{N_2}+(VMc_p)_{O_2}+(VMc_p)_{Ar}+(VMc_p)_{H_2O}}{(VM)_{N_2}+(VM)_{O_2}+(VM)_{Ar}+(VM)_{H_2O}} \quad (3.90)$$

3.4.2 Viscosity

The viscosity of the fluid is calculated using a derivative of a kinetic theory approach ignoring second order effects, which is a method developed by Wilke (Reid, et al., 1986). This method is valid for a mixture of gases at a low pressure and is illustrated in equations 3.91and 3.92.

$$\mu_m = \sum_{i=1}^{n} \frac{y_i\cdot\mu_i}{\sum_{j=1}^{n} y_j\cdot\varphi_{ij}} \quad (3.91)$$

Where

$$\varphi_{ij} = \frac{\left[1+\left(\frac{\mu_i}{\mu_j}\right)^{0.5}\cdot\left(\frac{M_j}{M_i}\right)^{0.25}\right]^2}{\left[8\cdot\left(1+\frac{M_i}{M_j}\right)\right]^2} \quad (3.92)$$

The constituents assumed for the fluid are dry air, carbon dioxide and water vapour. The viscosity of each constituent is tabled at various temperatures. Linear interpolation is used to find the viscosity of each constituent. The flue gas mixture viscosity is then estimated using equations 3.91 and 3.92. The effect of ash in the flue gas is neglected for this calculation. For the viscosity of air calculation, the volume percentage of carbon dioxide is set to zero.

3.4.3 Thermal conductivity

A method to calculate the conductivity for a mixture of gases was developed by Wassiljewa, which was modified by Mason and Saxena (Reid, et al., 1986). This method is used for the estimation of the thermal conductivity of the fluid, which is similar to the equations used for the viscosity. The only difference is that the viscosity variable is replaced with the conductivity variable as shown in equations 3.93 and 3.94.

$$\kappa_m = \sum_{i=1}^{n} \frac{y_i \cdot \kappa_i}{\sum_{j=1}^{n} y_j \cdot \varphi_{ij}} \quad (3.93)$$

Where

$$\varphi_{ij} = \frac{\left[1+\left(\frac{\kappa_i}{\kappa_j}\right)^{0.5}\cdot\left(\frac{M_j}{M_i}\right)^{0.25}\right]^2}{\left[8\cdot\left(1+\frac{M_i}{M_j}\right)\right]^2} \quad (3.94)$$

The constituents assumed for the fluid are dry air, carbon dioxide and water vapour. The conductivity of each constituent is tabled at various temperatures, and the same method of linear interpolation is used to find the conductivity of each constituent as seen from the method to calculate the viscosity. The flue gas mixture conductivity is then estimated using equations 3.93 and 3.94. The effect of ash in the flue gas is neglected for this calculation. For the conductivity of air calculation, the volume percentage of carbon dioxide is set to zero.

3.4.4 Density

The ideal gas law is used to find the density of the fluids which consist of air, water vapour and carbon dioxide. Equation 3.95 is an illustration of this relationship, where the complete equation is used for the estimation of the flue gas mixture density. For the air the carbon dioxide volume percentage is set to zero.

$$\rho_{mix} = +\left(\frac{PMV}{RT}\right)_{Dry\ Air} + \left(\frac{PMV}{RT}\right)_{CO_2} + \left(\frac{PMV}{RT}\right)_{H_2O} \quad (3.95)$$

After the above mentioned properties are calculated the calculation procedure completes the total time for each stream until one full revolution is completed. The calculation procedure then moves to next stream applying the exact same procedure until the outlet temperatures for all the rings have been calculated. The same process follows for the pressure calculation; each pressure drop is calculated for each layer and ring. In the case of a non-uniform matrix the final temperatures will be copied to the rings that have the same element packs installed, but for the sections where different packs are installed the temperatures and pressures will then be

calculated for these sections. Once all the pressure differences are calculated the values are stored in matrix used later to find the dew point temperatures of sulphurous acid, sulphuric acid and the water dew point. A final temperature and pressure per stream will then be calculated using equations 3.96 and 3.97 respectively.

$$T_{f\ out} = \frac{1}{M}\sum_{n=1}^{M}(T_f(i)) \tag{3.96}$$

$$P_{f\ out} = \frac{1}{M}\sum_{n=1}^{M}(P_f(i)) \tag{3.97}$$

The final interface will be the results sheet. In this sheet a summary of the air heater performance is given. The temperature profiles for the metal surfaces for each ring and section can be selected and displayed. The summary gives an average inlet temperature, outlet temperature, inlet pressure and outlet pressure, various leakages, inlet specific heat capacity, outlet specific heat capacity, inlet velocity, outlet velocity, inlet density, outlet density, and the amount of energy exchanged per stream. The dew point temperature for sulphurous acid and water are also calculated per layer. Based on the percentage of sulphur dioxide that converted to sulphur trioxide the sulphuric acid dew point is calculated. An average sulphuric acid dew point temperature is calculated for 1% to 5% conversion per layer. Figure 3.22 is a representation of the result sheet interface.

For a non-uniform case the section where different pack configurations are used can be selected and the temperature profiles for these specified regions can be viewed in selection options as shown in Figure 3.22. If the mass energy balance method was followed the option of viewing the MEB results can be selected to view the two different cases. The important results regarding this comparison are the dry flue gas loss, boiler efficiency and the change in coal flow rate, which is seen in Figure 3.23 after two cases have been compared. These changes will indicate whether the change in operating conditions is ideal or not. This capability is important when the design configuration of the air heater is changed. The effect on the efficiency and coal usage can be quantified, providing a platform to do feasibility studies. Chapter 6 is an example of a feasibility study done using this tool to improve the condition of dew point related fouling by removing the third layer of the air heater element packs.

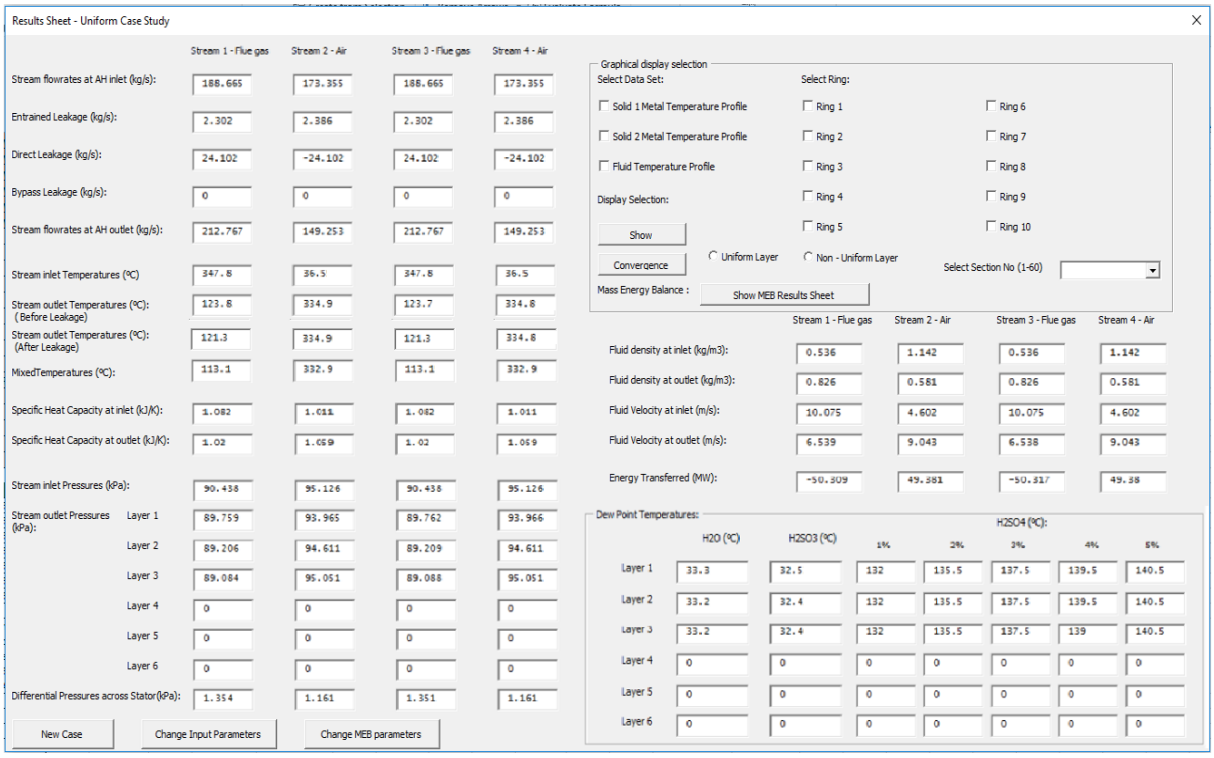

Figure 3.22: Result Sheet interface.

Figure 3.23: Mass Energy Balance Results Comparison Sheet.

4. EXPERIMENTAL METHODOLOGY

4.1 Background

Through focusing on energy conservation methods, the VBA RAH dew point related fouling prediction tool has been developed to provide a platform for failure prevention and efficient operation of regenerative air heaters. The modelling tool is used to avoid operating the regenerative air heaters in dew point conditions that promote fouling. To ensure accuracy of this VBA RAH simulation tool, the VBA RAH model was verified by means of a plant experiment. There were measuring points which were installed and were used in the (DCS) Digital Control System, which are also linked to Visual Automation (VA) system. The Digital Control System is used as an interface for operating control parameters for plant operators to operate the plant. Some of these signals are connected to the VA system used by system engineers for condition monitoring signals for the operating plant. This system stores a history of data which can be used for this research project. The data were collected for three days (Day 1- 90% maximum continuous rating (MCR), Day 2 – 80% MCR and Day 3 – 68% MCR) and then analysed for the verification test. Due to the risk of a 60 day life expectancy of measuring equipment installed inside the air heater, a pre-test was done for the same load conditions that were taken during the allocated testing period. The available VA readings were used along with the installed measuring thermocouples for comparison to the actual test data, which could only be done three months after the installation. The experiment conducted consisted of the following:

a) Coal sampling to measure coal composition.
b) Continuous flue gas composition measurement using HORIBA analyser (measuring CO_2, CO, NO_x, O_2, SO_2 and H_2O measured with a moisture analyser).
c) Measure pressures at the air heater inlet and outlet.
d) Measure the metal surface temperatures of the elements (Ring 2 and Ring 6)
e) Measure the fluid temperatures of the fluids flowing through the elements (Ring 2 and Ring 6).
f) Estimate the dew point temperatures for the measured flue gas composition considering moisture, oxygen, and sulphur dioxide and an assumption of 1% to 5% of sulphur trioxide formation.

This data was analysed to conclude whether it will be possible to prevent dew point related fouling through ensuring an operating environment where the metal temperature exceeds the dew point temperature.

4.2 Experimental design

The simulation model is formulated to consider a full steel matrix of a regenerative air heater. Therefore, each layer is considered in the iterative calculation process along with each segment. A temperature profile can be varied in any ring to verify the temperature changes when different element pack profiles are used. The simulation model was applied to a rotating hood air heater for the verification process. Test points for measuring the metal surface temperature and fluid temperature were installed at Ring 2 and Ring 6. The dew point temperature was estimated measuring the pressure at the outlet of layer 3, and then determining the partial pressure for each gas constituent according to theory explained in section 3.3.3. Figure 4.1 is an illustration of the location of test points that were installed for the verification test. The complete experimental design drawings with the drawing register for working drawings are illustrated in Appendix B.

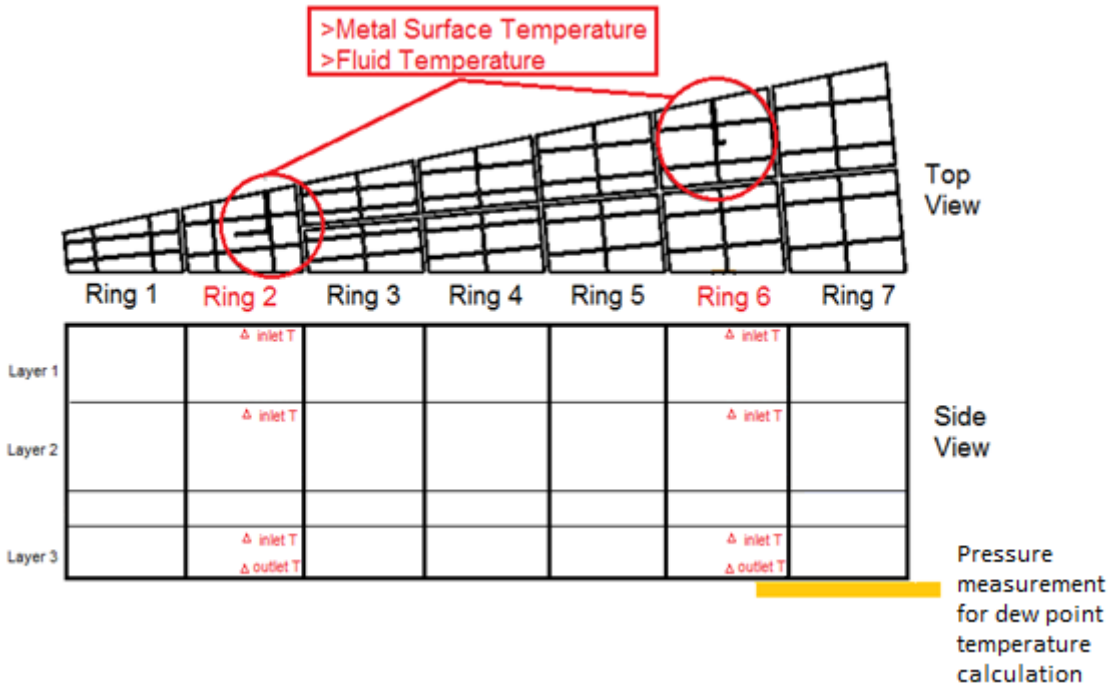

Figure 4.1: Location of test points installed at the Eskom Power Station

The operating parameters were collected along with the test data for a three day period (from 00:00 until 04:00) at three different load conditions namely 670 MW, 544 MW and 465 MW. The gathered data were used as input parameters for the model, which generated temperature profiles for the air heater. The experimental setup and execution preparation are discussed in Appendix B2 – Experimental Preparation & Execution.

4.2.1 Fluid and Metal Surface Temperature Measuring

The left hand air heater was used for the verification test. From this area a sector was selected and test points were installed in Ring 6 and Ring 2 as shown in Figure 4.2 and 4.3.

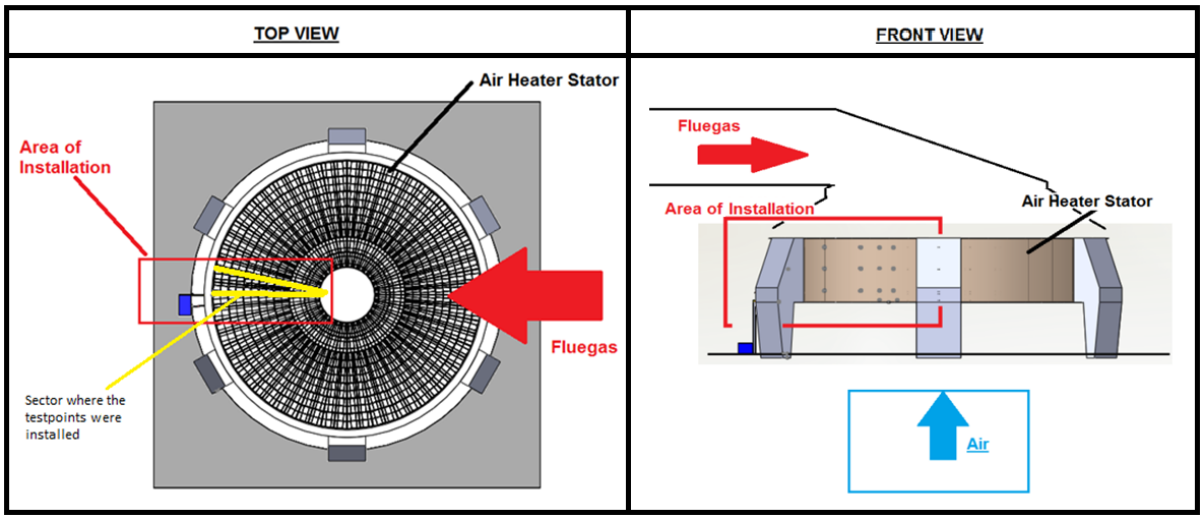

Figure 4.2: Location of test points in the steel matrix

The selected section was equipped with vertical cable channels routing the compensating cables for the thermocouples from the data logging cabinet to each thermocouple. For layer one, Ring 2 and Ring 6 had type K thermocouples installed at the hot end inlet of the element pack. A type K thermocouple was also mounted onto the metal surface of the inlet of the hot end element pack. This gave a temperature reading for both the solid and the fluid region at the inlet of layer one. Layer two, Rings 2 and 6, had type K thermocouples installed at the intermediate inlet of the element pack, for both the fluid region and the metal surface temperatures. Layer three, Rings 2 and 6, had type K thermocouples installed at the cold end inlet and outlet of the element pack for both the fluid region and the metal surface temperatures.

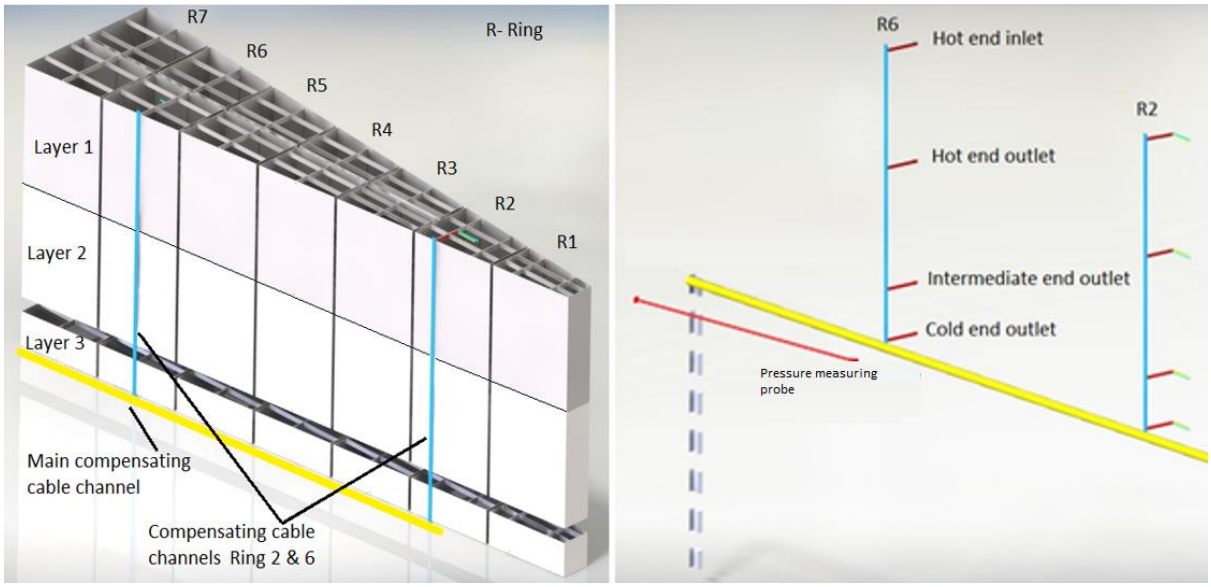

Figure 4.3: Location of test point in the element packs located inside the steel matrix

Figure 4.4 is an illustration of the physical installation on the thermocouples for both the fluid and the metal surface regions. Type K thermocouples were press fitted and insulated to measure the metal temperature. The compensating cables were routed to the middle of the element sheet using mild steel channelling. These steps are illustrated in Figure 4.4 from A to D. Section E and F is an illustration of the type K thermocouple and erosion protection installation to measure the fluid temperature passing through the element sheets. The cables were then routed vertically in Rings 6 and 2 to the logging cabinet mounted outside the air heater. A Madincos MPR5000S universal colour paperless recorder was installed as a data logging system, which had 16 recording channels. Figure 4.4 - G is an illustration of the logging system used for these measurements.

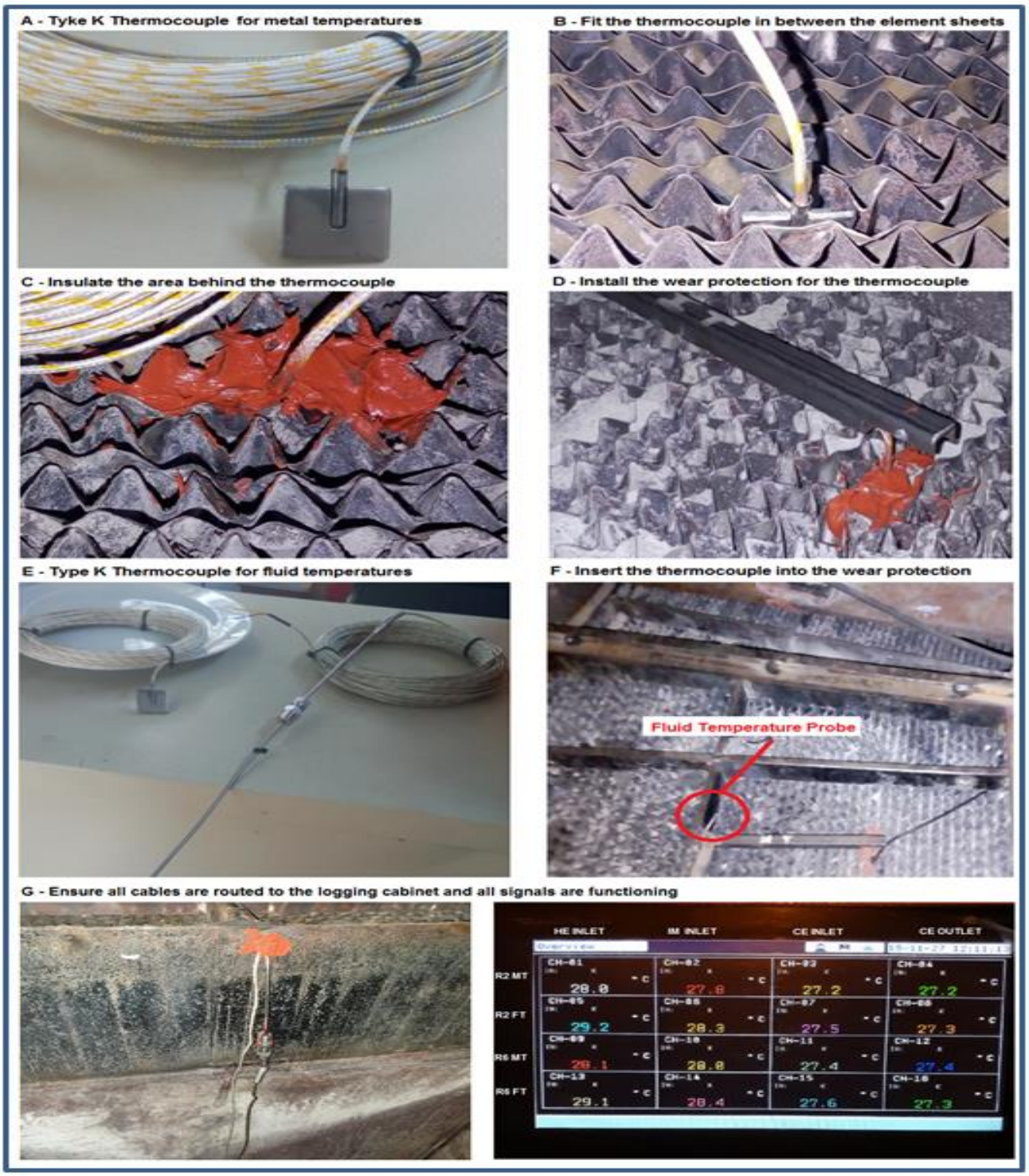

Figure 4.4: Installation of the air heater thermocouples.

The effectiveness of the use of a type K thermocouple, for the surface metal temperature measurements, was tested beforehand. A method of first attaching the thermocouple to the metal surface, with a thermal conduction adhesive, and then to thermally insulate the area to prevent any thermal convection to affect the readings, were tested. The tests were conducted on a small scale element surface. A thermal scanner was used to verify the surface temperature

to the reading from the type K thermocouple. The following experimental setup was used for this test.

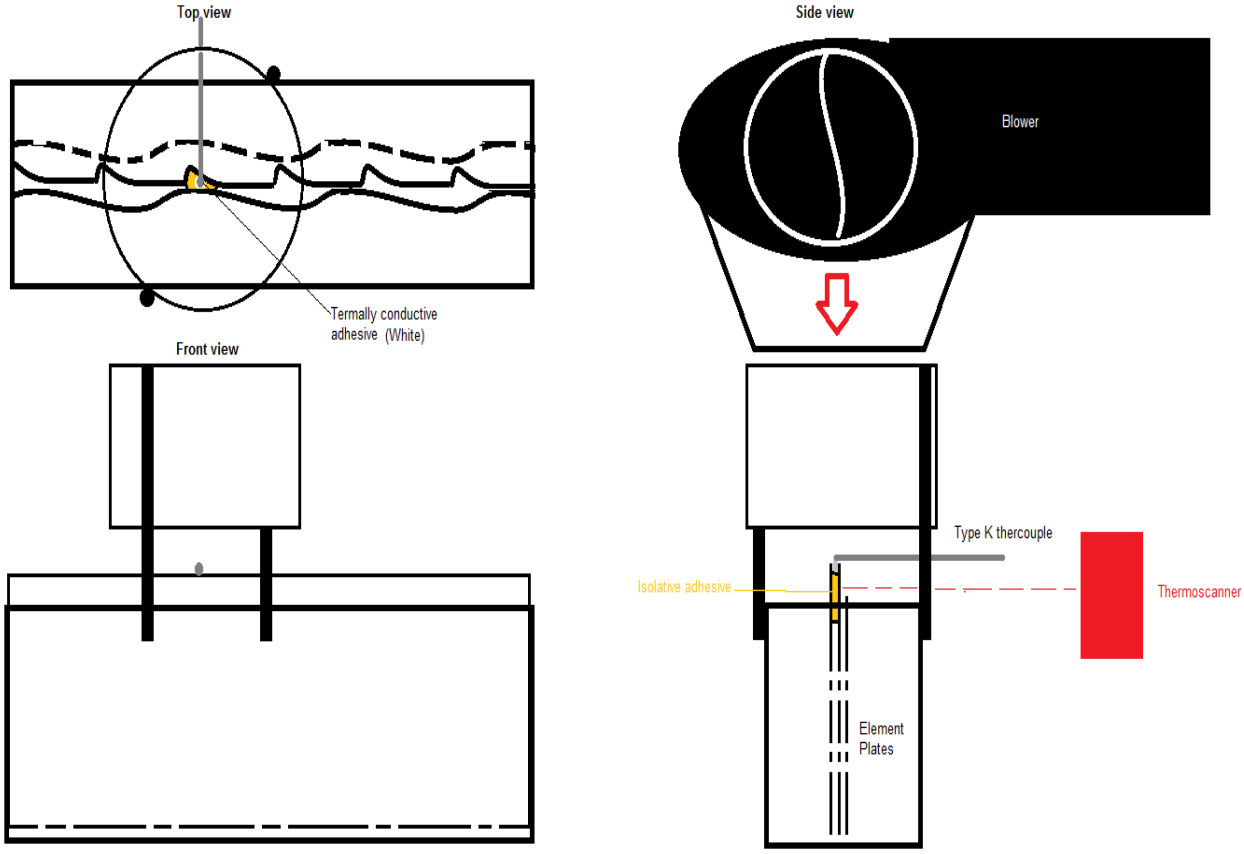

Figure 4.5: Experimental setup to verify the accuracy of the use of a type K thermocouple as a metal surface temperature measurement.

The blower heated the air up to a temperature of 85ºC. The heated air was forced through a sample of three stacked element plates. A type K thermocouple was initially mounted onto the surface of one plate to measure the meatal surface temperature. The plate was heated until a plate temperature of 80ºC was reached from the type K thermocouple reading. The plates were then allowed to cool down for 120 seconds. During this period the surface temperature was measured by a thermal scanner and the attached type K thermocouple. The three data sets were compared and the results are illustrated in the following graphs.

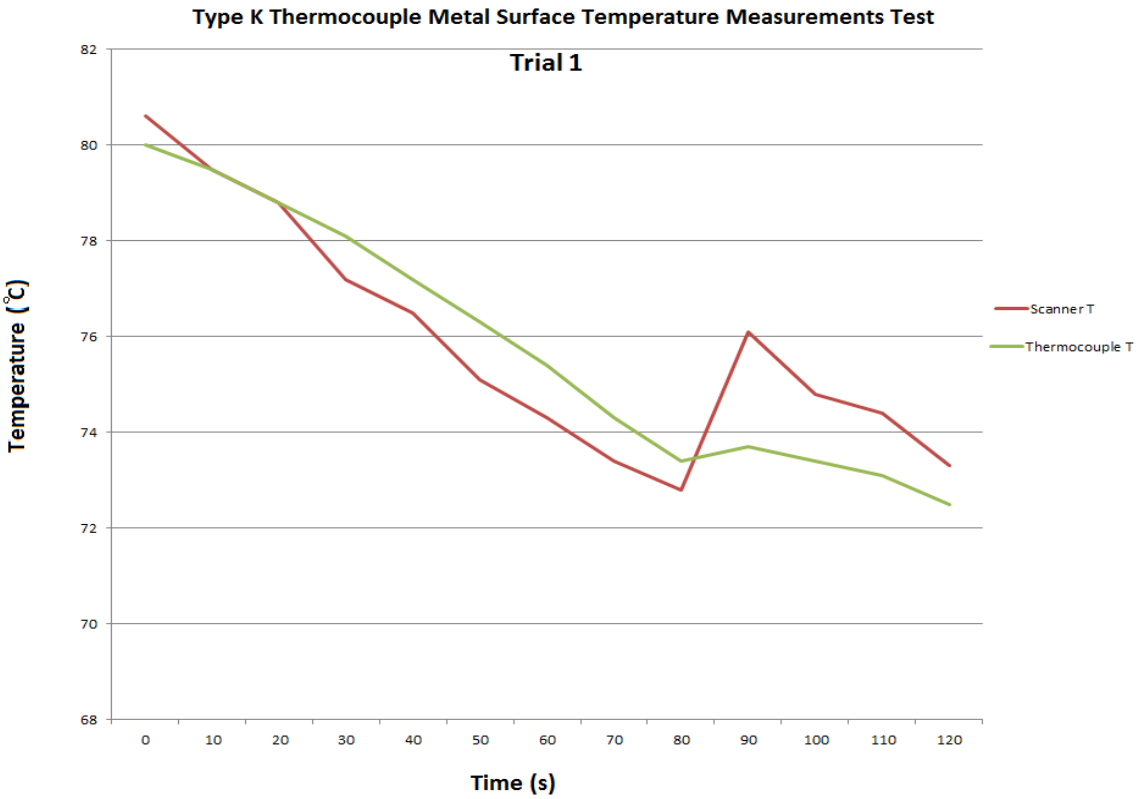

Figure 4.6: Trial 1 results from the type K thermocouple verification tests.

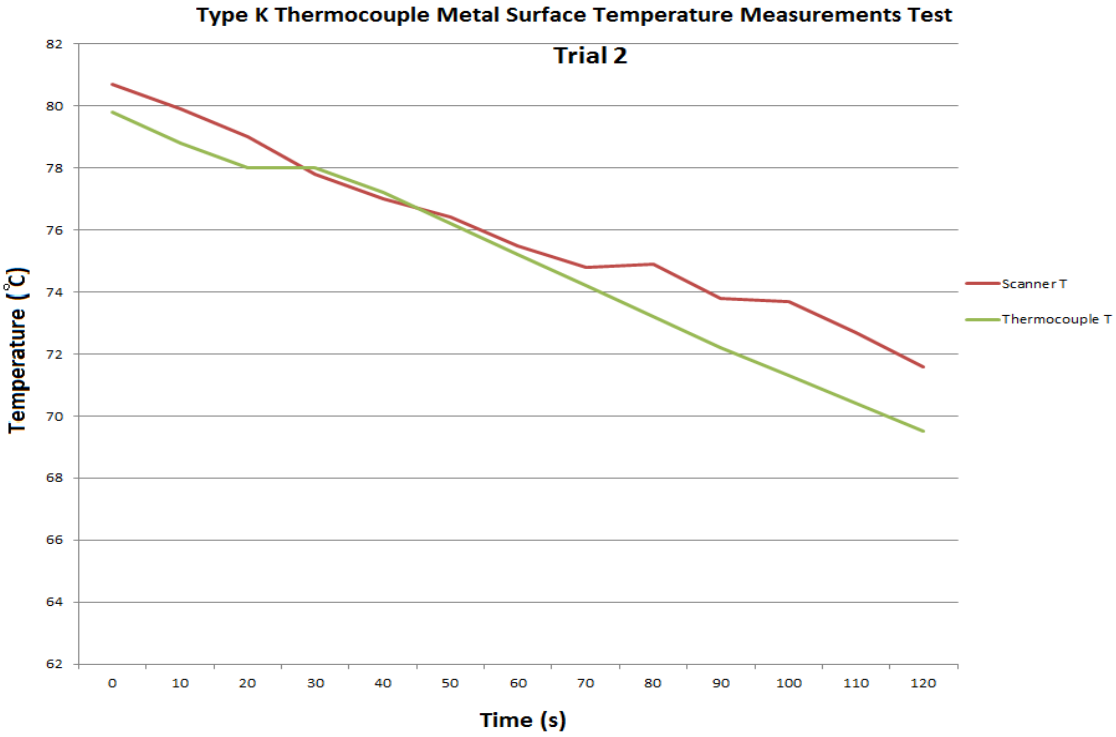

Figure 4.7: Trial 2 results from the type K thermocouple verification tests.

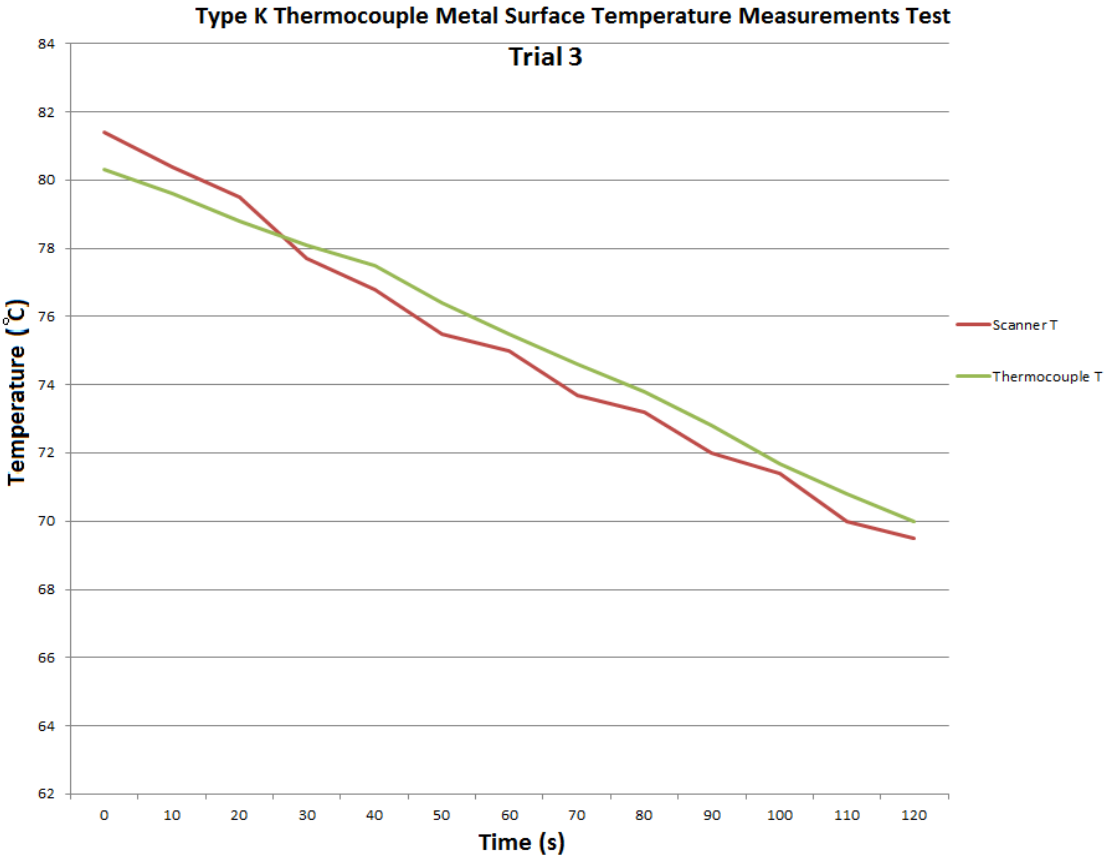

Figure 4.8: Trial 3 results from the type K thermocouple verification tests.

For the first trial the results yielded from the thermal scanner indicated an inconsistent reading with a large variation in temperature. The scanner was held by hand during these trials and it introduced a form of human error to the results due to the change in the focus point when the scanner changed position. During the second trial the positioning was steadier, which resulted in an improved set of data, and indicated a temperature difference of about 1.5ºC. During the third trial the results indicated that the temperature differences between the two readings were 0.5 ºC to 1 ºC. This result provided guidance to find a standard temperature offset when type K thermocouples are used to measure the metal surface temperature.

For the experimental setup used for the verification of the VBA RAH model, careful consideration had to be taken with regard to the installation process of the thermocouple. The thermocouple was exposed to highly erosive conditions. Therefore, each thermocouple was protected with a protection channel. For a gas measuring thermocouple, a high temperature silicone was injected into the protection channel to protect and keep the thermocouple out of contact with the surfaces of the protection channel and surrounding fly ash. Figure 4.9 is an illustration of the protection channel used for the thermocouple.

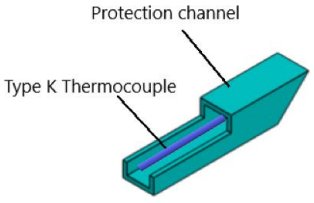

Figure 4.9: Thermocouple protection channel.

4.2.2 Dew Point Temperature Measuring

To verify the dew point temperatures, a probe was installed at the outlet of layer three to measure the flue gas pressure at this point. The flue gas composition was measured before the air heater inlet, which was used to find the partial pressure of each constituent in the flue gas at the cold end outlet of layer three. This technique had to be used due to the high ash content in the flue gas that fouls the sensors of analyser probes for a sensor type technique of acid dew point temperature measurement. One of these techniques were considered, but the option of using a LANCOM 200 system was rejected based on the amount of ash in the flue gas, exceeding the required amount for operation. Other methods such as the Isopropyl Alcohol Method (IPA) and Controlled Condensation Method (CCD) tests were also considered but these options exceeded the allocated budget for the research project.

The dew point related fouling simulation tool was used to determine in which region condensate would be expected. Eskom Power Station specific input parameters were used for the simulation which generated fluid, solid and dew point temperature profiles. The combination of these three profiles for one rotation of the air heater in Figure 4.10 indicated that 42% of the time for one rotation, the cold end metal surface and flue gas temperatures operate below the sulphuric acid dew point. The experimentation described in Chapter 5 aimed to measure the metal temperature and accordingly measure the operating pressure in this region to calculate the dew point temperatures for verification of the results from the VBA RAH model.

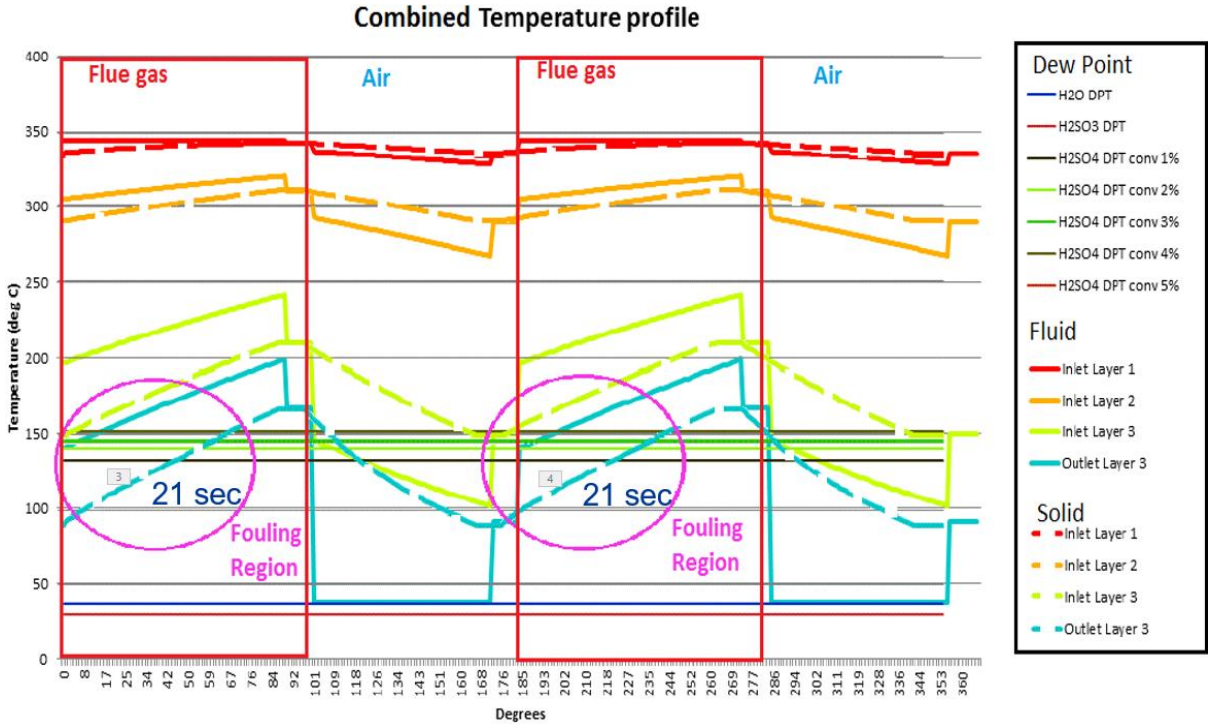

Figure 4.10: A combined graphical representation of the simulated metal surface, fluid and dew point temperatures for all three layers in an air heater.

4.2.3 Coal Analyses

Two methods are used to analyse coal namely ultimate analysis and proximate analysis. The ultimate analysis method was used to find the coal composition in order to establish the flue gas composition by means of a mass balance calculation. This analysis incorporates constituents such as carbon, hydrogen, oxygen, and sulphur. It becomes useful in the process of obtaining the quantity of air that is required for combustion, along with the volume and composition of the combustion gases. Coal samples were taken every 30 minutes, for four hours, for the three tests to create a history of coal composition for the duration of the plant experiment conducted to verify the operation of the simulation model (as per Table B1 in Appendix B). The samples were collected at the feeders of the mills. These samples were sent for proximate and elemental analyses to establish the following constituents:

- Proximate Analysis (excluding surface moisture)
    - Gross Calorific Value
    - Inherent moisture
    - Volatile matter
    - Fixed Carbon
    - Ash

- Elemental analysis
  Carbon
  Hydrogen
  Oxygen (determined by difference)
  Nitrogen
  Sulphur
  Ash
  Carbonates (as CO_2)
  Ash Elemental Analysis

The simulation model has the capability to use the coal analyses to predict the flue gas composition by means of a mass balance. An ultimate analysis is therefore required as input parameters to the VBA RAH model. The analyses also provide a platform to estimate the acid deposition rates based on the method investigated by Raask 1985 (as explained in Table A5 – Appendix A).

5. RESULTS AND DISCUSSION

This chapter elaborates on the collective results from this research project. Figure 5.1 is a road map showing how the results were collected, interpreted and analysed to verify whether the VBA RAH model is a suitable tool to identify the onset of dew point related fouling. Section 5.1 classifies the importance of parameters and shows which parameters must be correct to ensure reliable results.

Section 5.2 summarises the operating conditions taken into account during the collection of Data Set 1 (Pre-testing phase). Data set 1 is the phase where pre-testing was done to identify the accuracy and functionality of the experimental setup and results. Three load conditions were measured that correlated with Data set 2 operating parameters. The results can be found in Appendix C3. The experimental results were compromised due to failure of thermocouples and the unavailability of calibration gas to calibrate the analysers used for flue gas composition measurement, therefore a data set had to be collected from the first 30 days of operation of the installed equipment (Data set 1). The calibrated analysers were only available three months after the installation. Therefore a pre-testing phase was selected which is called Data Set 1. Factors such as functionality of the installed measuring equipment, air heater leakage, air heater differential pressures and plant operating conditions were considered for the Data set 1 results. In this section possible challenges from the experimental design were identified to show where errors were expected to occur during the experimental phases of the research project. In this section only measured data was considered.

The correlation between the simulated and measured results for three identified periods where a 99% MCR, 80% MCR, and 68% MCR load condition was set, was recorded and discussed. This results is shared in Appendix C3. The data collected from Data Set 1(from the three identified load conditions), were used as input parameters to the VBA RAH and de Klerk RAH models to compare and evaluate the air heater performance using these models(generating simulated results) and the available experimental data(generating measured results). Data Set 1 only considered the measurements taken from the DCS and the installed thermocouples; the coal analysis and flue gas analysis were not done.

Section 5.3 shows the VBA RAH model correlation with the Data Set 2 results from a 68% MCR and 99% MCR load condition (The 80%MCR load condition is discussed in Appendix C4). The correlation between measured flue gas composition and simulated flue gas composition (using the measured coal composition as input parameters to simulate the flue gas composition results) was also considered. The flue gas and coal analysis were completed during the second set of experiments (Data Set 2). Data Set 2 was taken three months after the installation was done when the gas analysers were available. Due to the erosion experienced in three months, only the cold end thermocouples remained available for verification of the VBA RAH model for the actual testing phase.

Section 5.4 shows the correlation between the performance of the HC11 elements packs and the 2.78DU element packs. This correlation was done by simulation from the OEM model to indicate that the thermal performance is the same, but the results were further compared to the VBA RAH model and RAH model to show the deviation between the models.

Section 5.5 further verifies the VBA RAH model through using the input parameters from the research conducted by Habbitts in 1995, and then comparing the VBA RAH results to the RAH model results generated in the research conducted by Habbitts . This comparison was required

to also show the validity of the VBA RAH model when compared to more accurate measured data sets. A numbers of factors influenced the measurements and therefore further verification was required.

Section 5.6 focuses on the capability of the VBA RAH model in terms of how the model can be used to find a solution to reduce dew point related fouling, and how these changes affect the overall air heater and boiler performance.

Section 5.7 considers how an error in flue gas flow measurements influenced the results. A method was also identified to show what the ideal flow should be. The impact of this error was analysed to indicate how the outcome would have affected the results when using the correct flue gas flow.

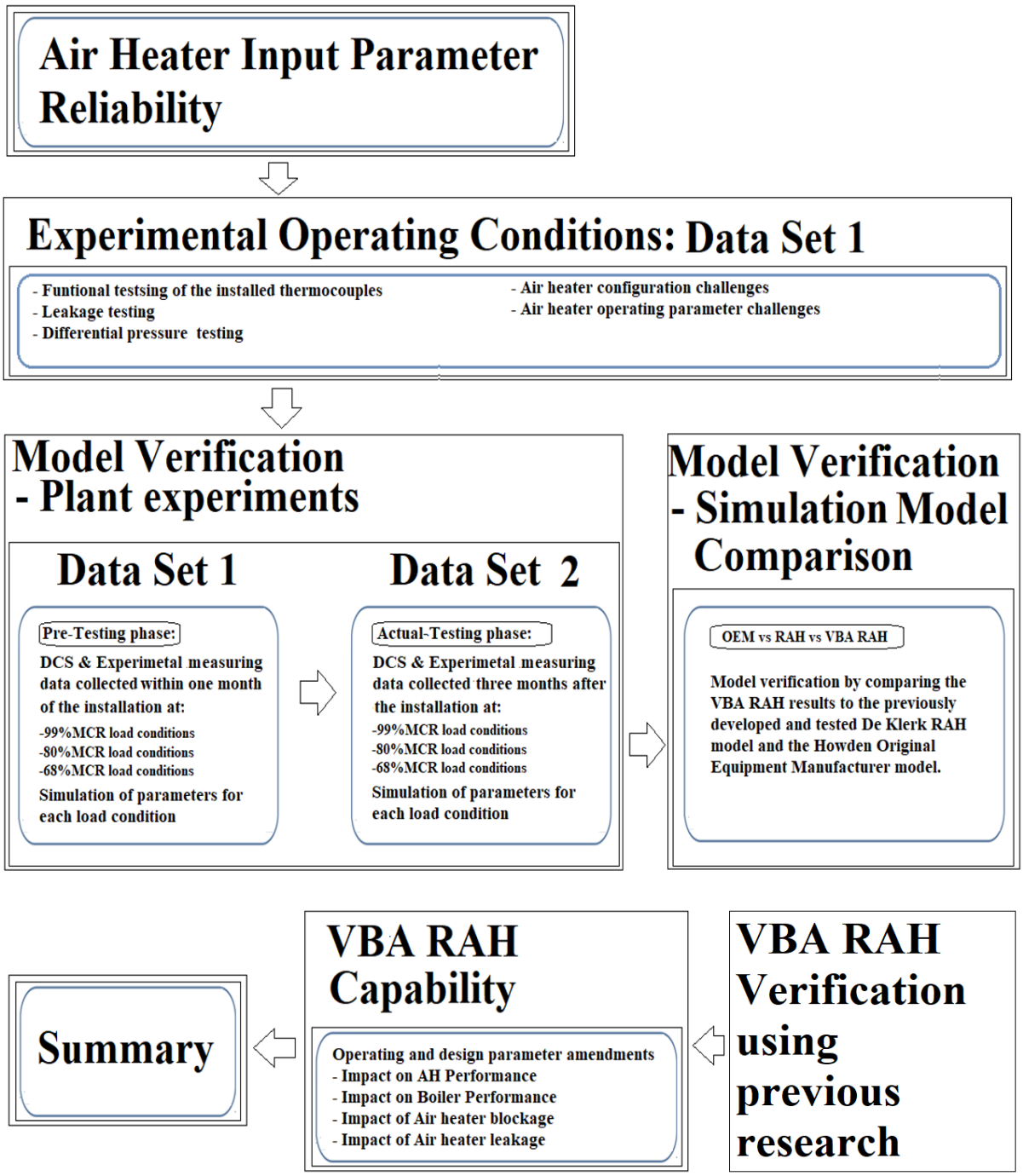

Figure 5.1: Results and discussion road map.

5.1 Air Heater Input Parameter Reliability

An important consideration for the experimental results is the quality of the input parameters. If a simulation model is verified the measured data must be accurate to ensure that the model generates reliable data. Unreliable data leads to unreliable decision making regarding plant design optimisation which leads to wasteful cost expenditure. Most of the data used for the experimental results were taken from the DCS measurements, which can sometimes be inacurate. A sensitivity table regarding input parameters was created by De Klerk (2001). The same approach was used for the test simulations done with DCS input parameters. The following table shows the sensitivity of the input parameter, based on the importance of the

parameters measured. This table shows which signals require high accuracy to generate reliable results, and which signals are less important. A sensitivity of 1 indicates that a good accuracy is required. A sensitivity of 2 has a noticeable effect, and a sensitivity of 3 shows that standard values are sufficient.

Table 5.1: Input data sensitivity table

Geometry:		**Sensitivity:**
Flow area of inner and outer radii (Measured)	m	1
Stream and seal sector angles	Degrees	1
Direction of flow of each stream	Hot end to Cold end or Cold end to Hot end	1
Layer Heights	m	1
Pack types and plate thickness (As per installed design)	Profile type HC11(similar to 2.78 DU) and plate thickness of 0.5	1
Operating Data:		
Rotational speed (As per design)	Rev/min	2
Flue gas inlet temperature (Measured from installed thermocouples)	ºC	1
Flue gas pressure at inlet (gauge) (From DCS)	kPa	3
Flue gas inlet flow rate (Excluding ash) (Measured)	kg/s	1
Flue gas CO_2 content (Measure)	%v/%v	3
Flue gas H_2O content (Measure)	%v/%v	3
Ash Flow rate (As per design data)	kg/s	2
Secondary air inlet temperature (Measured)	ºC	1
Secondary Air inlet pressure (Measured from DCS)	kPa	3
Secondary air inlet flow rate (Measured from DCS)	kg/s	1
Secondary air H_2O content (As per design data)	%v/%v	3
Change in flue gas O_2 content (Measured)	%v/%v	1

The rate of energy transferred from the flue gas to the air stream can be expected to be about 50 MW per air heater (100% MCR) for a power unit with a generating capacity greater than 500 MW. During the simulation this energy exchange is calculated and used as an indication that the data are reasonably accurate. A similar approach can be used with the data collected from the experimental results. A method of identifying good accuracy was used by de Klerk,

where the difference between the input and output thermal energy should always be less than 1 MW. If the difference is less than 1MW, the data can be seen to be reasonable. The following equation is used to calculate the difference in energy exchange rates of the two streams ($\Delta\dot{Q}$), and the results are displayed in the result sheet as shown in Figure 3.22 in Chapter 3.

$$\Delta\dot{Q} = ((\dot{m} - \dot{m}_{leak})c_p(T_{out} - T_{in}))_{air} + ((\dot{m}_{fg} - \dot{m}_{ash})c_p(T_{out} - T_{in}))_{fg} + \dot{m}_{leak}c_p(T_{fg\_out} - T_{air\_in}) \quad (5.1)$$

The flue gas flow rate was not measured using the DCS system, therefore a different method was used to determine the flue gas flow. This method consisted of measuring the differential duct pressure, which was then used to calculate the velocity in the flue gas duct. The density was also measured. With the flue gas duct geometry known the area could also be calculated. Once the area, velocity and density was known the flue gas mass flow rate was estimated. A mass balance calculation can be done to find the flue gas flow rate through the air heater (equation 5.2). This calculation is applicable to steady state conditions (De Klerk, 2001).

$$\dot{m}_{fg} = \dot{m}_{pa} + \dot{m}_{sa} + \dot{m}_c(1 - f_{ash} * r_{ash}) \quad (5.2)$$

Where
f_{ash} - Mass fraction of ash in coal
r_{ash} - Ratio of coarse ash to fly ash
$\dot{m}_{pa}$– Mass flow of primary air
$\dot{m}_{sa}$– Mass flow of secondary air
$\dot{m}_c$– Mass flow of coal

5.2 Operating Conditions for the Pre-Testing Phase (Data Set 1)

During the installation of thermocouples, the plan was to do the first set of tests after thirty days, but the tests were delayed due to the calibration gas not being available in time for the HORIBA analyser which was used to measure flue gas composition. The thermocouples installed in the plant had a life expectancy of sixty days taking the abrasive environment of the air heater during operation into consideration. After eleven days, the Ring 2 cold end metal temperature thermocouples started showing signs of failure, and seven days later the hot end fluid temperature thermocouple at Ring 6 failed. The data for each thermocouple was captured prior to these component failures (for the pre-testing phase-Data Set 1). Using DCS load history, three load conditions were identified and used to compare the results to the results gathered during the actual tests (Data Set 2) following the availability of the flue gas analyser calibration gas. The Data Set 1 results can be found in appendix C3. Section 5.2 is a summary of the data collected during the first phase of testing, which is termed as the "pre-testing phase – Data Set 1". This section identifies what challenges affected the results and how they would influence the validity assumption of the VBA RAH model.

5.2.1 Effect of air heater leakage and differential pressure

For Data set 1 it was found that the temperature profile for one cycle of Ring 6 had a greater rate of change in temperature in comparison to the temperature profiles generated from Ring

2. This effect is due to the fact that the single-flow rotary regenerative air heater has a tendency of augmented leakage air to the flue gas path on the cold end periphery of the air heater steel matrix as explained in Figure 5.2. During thermal expansion the air heater steel matrix will be forced to expand upward into the hot end hood seals at the centre, which is also known as capping of the steel matrix. When seal setting is applied to the air heater, the thermal expansion of the air heater is taken into consideration. The periphery gap between the seals and the steel matrix has a pre-set value of 25mm. Therefore, if the air heater experiences lower temperatures at low loads, higher leakage rates are expected. But at high load conditions the flue gas temperature increases, which then leads to increased thermal expansion of the steel matrix. The gap between the steel matrix and periphery seals decreases, causing more effective sealing to occur at the periphery as shown in Figure 5.2.

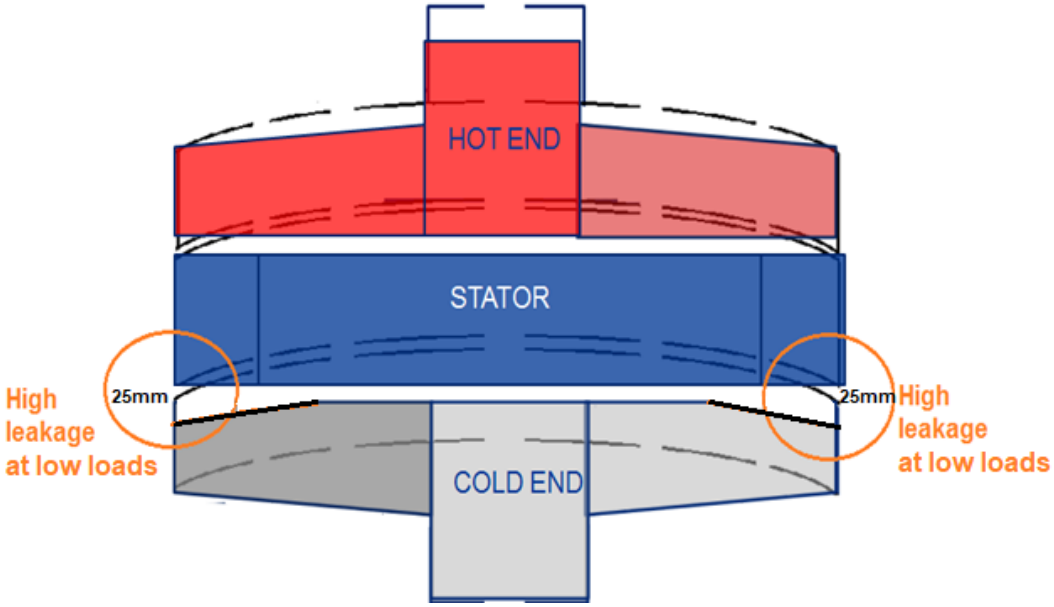

Figure 5.2: High leakage on the cold end of the steel matrix peripheries.

For the pre-test (Data Set 1) simulation, leakage was assumed to be constant due to the fact that leakage tests was conducted after an outage in January 2020 at a load of 678MW (maximum generated load). The results for the Data Set 1 (pre-test) did not take the leakage into account for each load condition (83%MCR, 80% MCR and 99%MCR). But due to the fact that the pre-test results were taken in December 2019 it is safe to say that the leakage would not deteriorate much from December 2019 to January 2020, therefore the 99% MCR Data Set 1 results should be more accurate than the lower load results. The leakage trend for the air heaters can be seen from Figure 5.3. This trend shows that the leakage improved after the outage when the installation of the testing equipment was done. The result also shows that the leakage deteriorated from January 2020 to May 2020. For Data Set 2 the leakage was measured for each load condition. As explained in section 5.3.

Air heater leakage is measured using a probe with three suction pipes each cut at a different length. The Longest suction pipe takes the bottom level of the duct oxygen reading, the shortest pipe takes the oxygen reading from the top level of the duct and the middle length pipe measures the oxygen content of the middle layer. This probe is then inserted into three different measuring ports located on the right hand, middle and left hand of the cross sectional area of the duct. This traverse measurement then gives a 3x3 matrix of measuring point. The average of this matrix is then calculated. The process is followed for the measurements taken at both the inlet and the outlet of the flue gas ducts of the air heater. The average inlet and outlet oxygen

measurements are then inserted into equation 3.13 to estimate the amount of air that leaked to the flue gas stream.

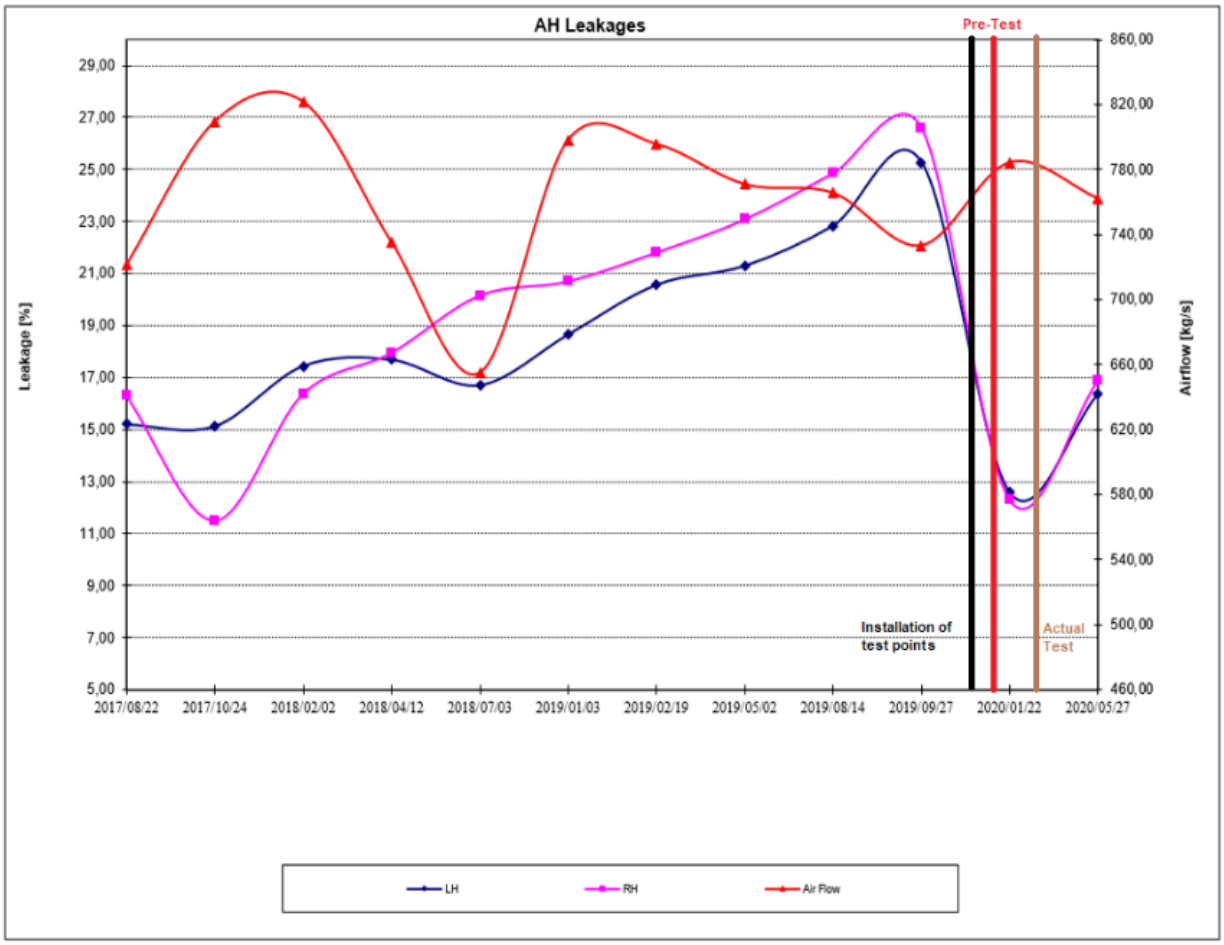

Figure 5.3: Air heater leakage test results for unit 5 before and after the pre-test phase for the Data set 1 results.

Figure 5.4 is an illustration of the history for the differential pressures for both the flue gas and air side of the air heater. This shows that the air differential pressure improved after the outage but the flue gas differential pressure remained the same. The flue gas differential pressure is also influenced by the Tubular air heater condition, due to the fact the induced draught for the flue gas stream flows through both the secondary and the tubular (Primary) air heaters. If the tube bundles consist of leaking pipes it influences the suction pressure from the ID fans. The secondary air only receives air from the forced draught fan and stays in an isolated flow path, and the tubular air hater receives primary air from the PA fan in an isolated stream. So a difference in performance can be expected from the two differential pressures for air and for flue gas measurements. The differential pressure (Figure 5.4) showed that there were signs of deterioration in the fouling condition from December 2019 until May 2020. This is an indication that the third layer could have experienced fouling in the third layer by the time the actual tests for Data Set 2 were conducted. The simulation model does allow the option of including a blockage factor per layer. This effect was taken into consideration for the results shown in section 5.6. It is expected that when the third layer pack is fouled the differential pressure should increase along with increased flue gas exit temperatures.

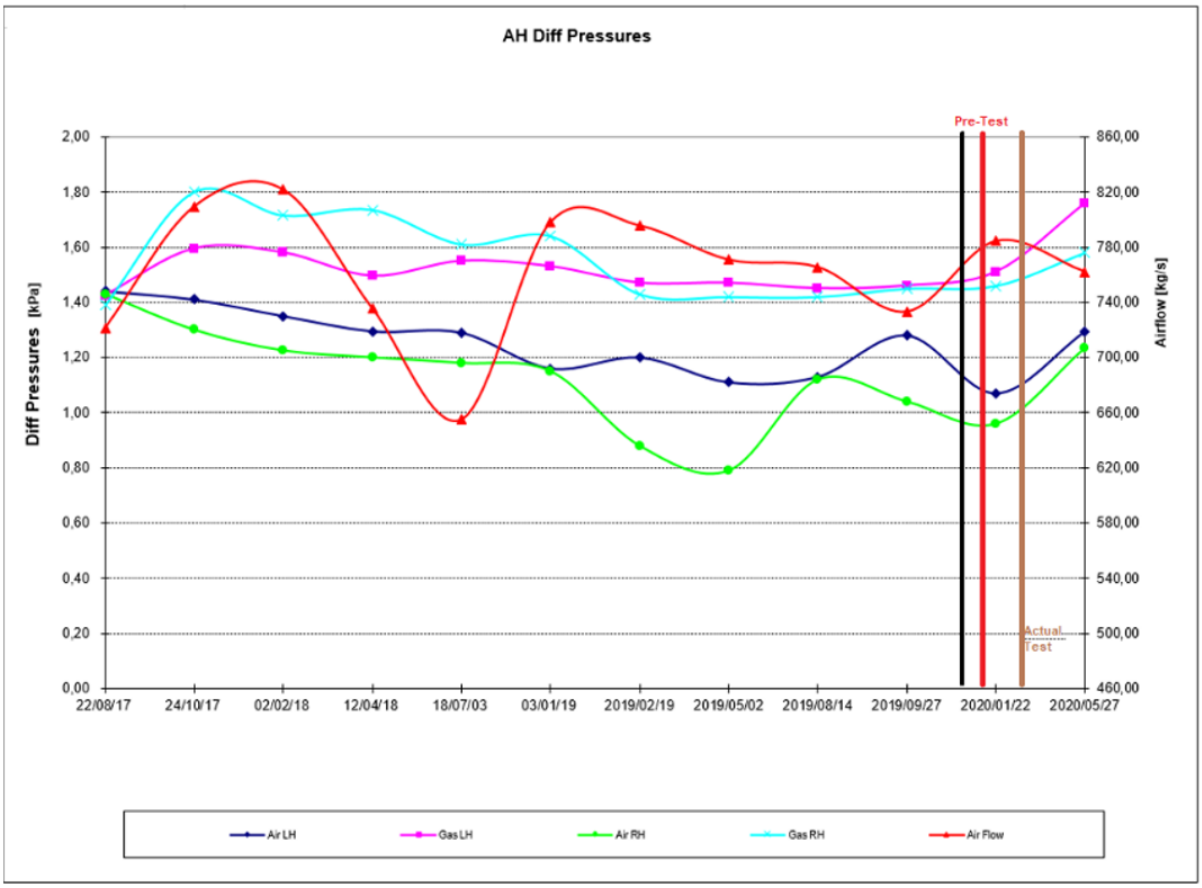

Figure 5.4: Air heater differential pressure test results for unit 5 before and after the pre-test and actual test.

5.2.2 Air heater performance differences between Ring 2 and Ring 6 for Data set 1

The effect of the difference in the rate of change in temperature due to leakage can be seen in the graphical representation of the temperature profiles for Ring 2 and Ring 6 illustrated in Figures 5.5 and 5.6. The average cold end metal temperature for Ring 2 was found to be 7.02% higher than the cold end metal temperature for Ring 6. The average cold end fluid temperature for Ring 2 was 5.09% higher than the hot end fluid temperature for Ring 6. The slight difference in temperature between the two rings is assumed to occur due to the leakage being higher closer to the periphery. This shows that the periphery rings could experience more dew point related fouling at the cold end due to the reduced operating temperatures at the periphery. The average temperature refers to the average of the measured temperatures as indicated in the red blocks from the two figures below. This data represents a 100 seconds of measurements collected on the 23 of December 2019, to see verify which signal was still working and what the typical behaviour were of the two rings.

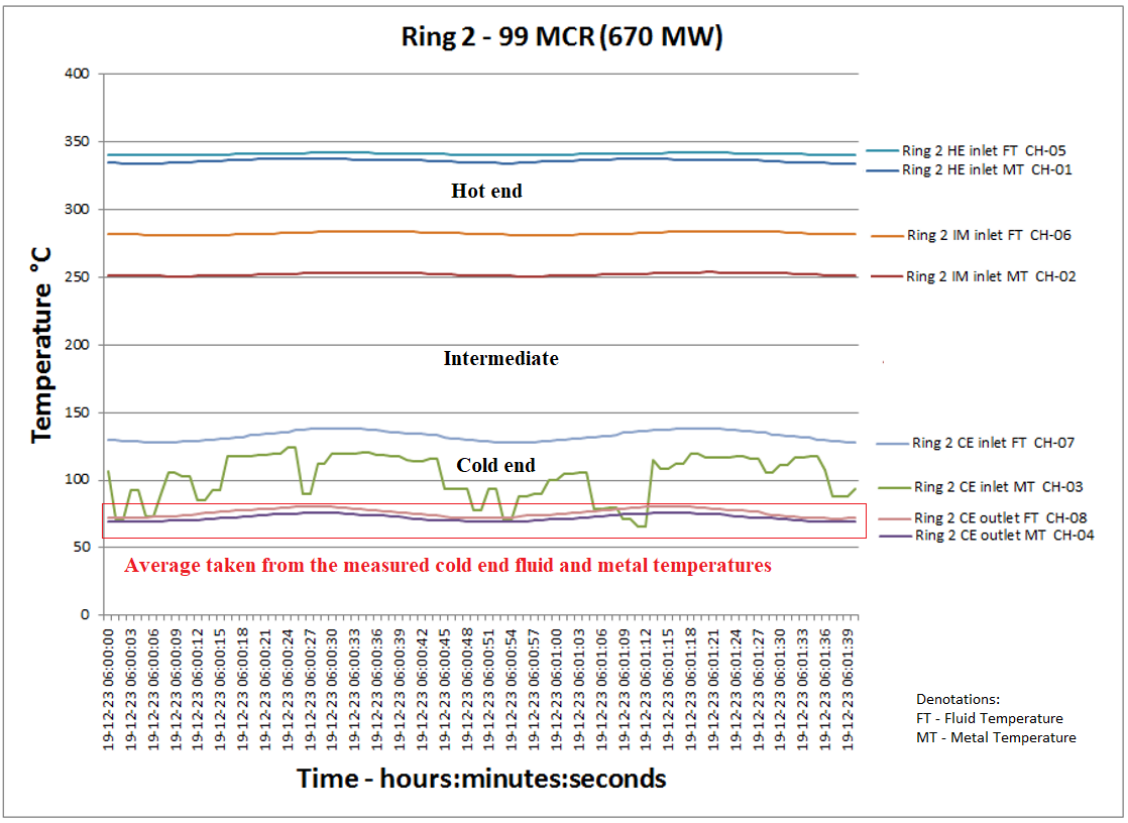

Figure 5.5: Ring 2 Temperature profile for the air heater fluid and metal temperatures at 99% MCR

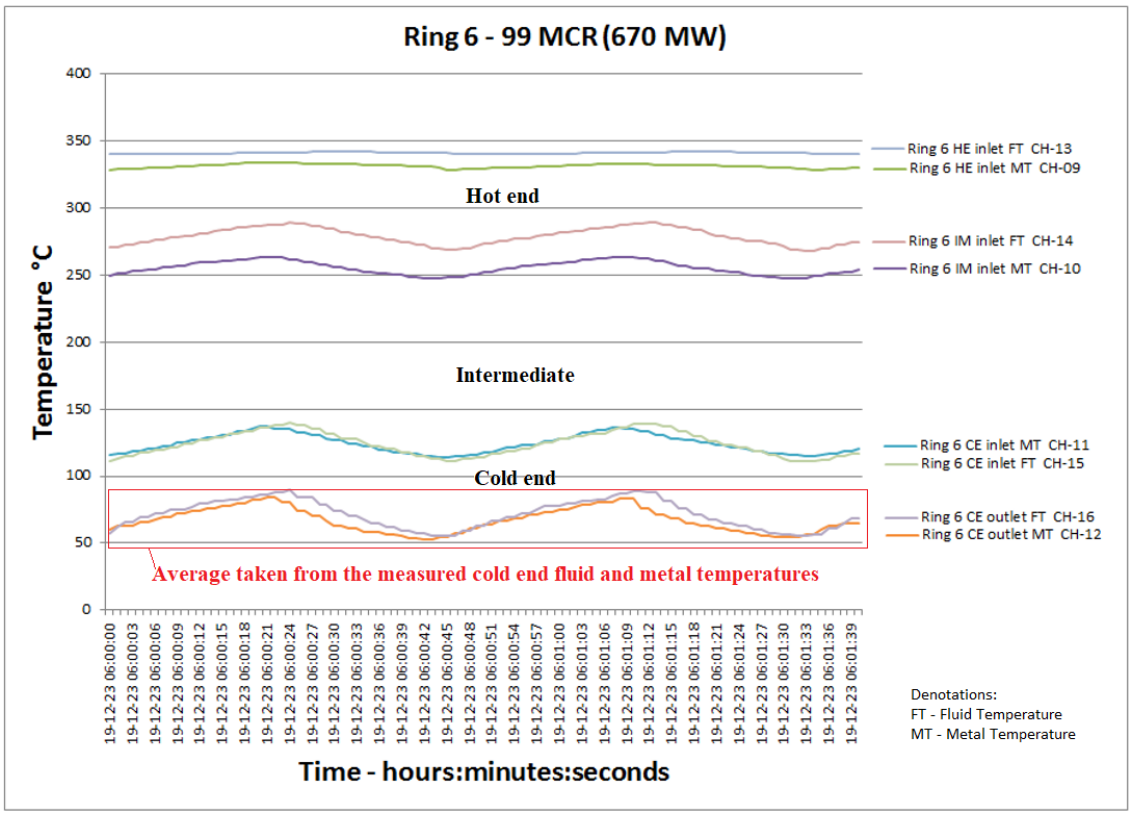

Figure 5.6: Ring 6 Temperature profile for the air heater fluid and metal temperatures 99% MCR

There is a clear difference between the temperature fluctuation at the hot end and the cold end. This difference between the hot end and cold end, is due to the average difference in temperatures for the inlet and outlet temperatures of the fluids at each end. The hot end experiences an incoming flue gas temperature of 315ºC-340ºC with an air temperature of 295ºC-315ºC which gives an average temperature difference of 20ºC-25 ºC. Therefore, the fluctuation in temperature is expected to be within this region of 20ºC-25 ºC. For the cold end the inlet temperature of air is 35ºC-60ºC, and the flue gas outlet temperature 105ºC-130ºC. An average temperature difference of 70ºC can be expected, which is why the rate of temperature change decreases at the higher layers in steel matrix. Figure 5.5 and 5.6 is a clear indication of this effect. These figures shows the temperatures recorded for +/-100 seconds of 1 rotation for the metal and fluid temperatures from the hot end to the cold end for ring 2 and ring 6 at 99%MCR conditions.(HE- Hot end, IM – Intermediate, CE – Cold end, FT – Fluid temperature, MT – Metal Temperature)

The average cold end metal outlet temperature for Ring 2 was 72.6ºC, and Ring 6 was 67.8ºC, which is well below the sulphuric acid dew point temperature range. Therefore, the formation of sulphuric acid can be expected in the third layer. The temperature was above the normal sulphurous acid and moisture dew point temperature, but during a light-up or shut-down the metal and flue gas temperatures will pass through these temperature ranges causing further dew point related fouling. Other factors such as accumulation of ash on the thermocouple and the wear protection of the thermocouple could also affect the reading. The ash has a heat capacity and stores heat, and reduce heat transfer for longer periods and this effect influences the measurements taken in the open space and on the surface of the element packs. The accumulated ash in the open spaces of the element packs can also obstruct flow through the perforated area, which has a negative impact on the fluctuation in temperature.

5.2.3 Effects of dew point related fouling during shutdown

Figure 5.7 is a representation of the temperature profiles of an air heater during a shutdown of the unit used for the experiment on 01/01/2020. The figure shows how the metal and fluid (flue gas and air) react when a generating unit is taken out of service. For both the light up and the shutdown periods the air heaters pass through a transient state where the operating temperature of the air heater pass the sulphurous acid, moisture and sulphuric acid dew point temperatures. These periods become critical fouling periods. From this data set it is clear that during the draught group (PA, FD and ID fans) rundown period the air heater elements and fluid temperatures operate below the dew point temperature ranges. It is expected that during this phase, entrained ash captured in the elements experiences temperatures that allow condensation of surface moisture on the entrained ash surfaces to occur for the periods where the flue gas passes through the areas of accumulated ash. This causes the formation of anhydrite (calcium monoxide in ash reacting with sulphuric acid forming a cement type of paste) and excessive fouling is experienced during this period. Soot blowing is applied to remove the deposits, but this exercise is not always successful. In some cases, where the reaction was followed by drying and hardening, only high pressure washing can remove the deposits. A possible solution for this problem is to run the forced draught fan for a longer period before fuel is admitted (light up conditions) to the furnace or after fuel supply is stopped (during shut down conditions), with the pre-steam air heater in service allowing air to enter the air heater above 50 ºC (above the

dew point temperature for moisture and sulphurous acid). Pre- steam air heaters are recuperative heat exchangers using auxiliary steam (installed before the air heater) to allow pre heating of air before it enters the air heater. This system serves as protection to avoid operating the air heaters in dew point conditions. Ideally this system must heat the inlet air to heat up the elements until the flue gas and most of the ash is removed from the air heater. The effectiveness of this method must be investigated and will be a recommendation for future operation.

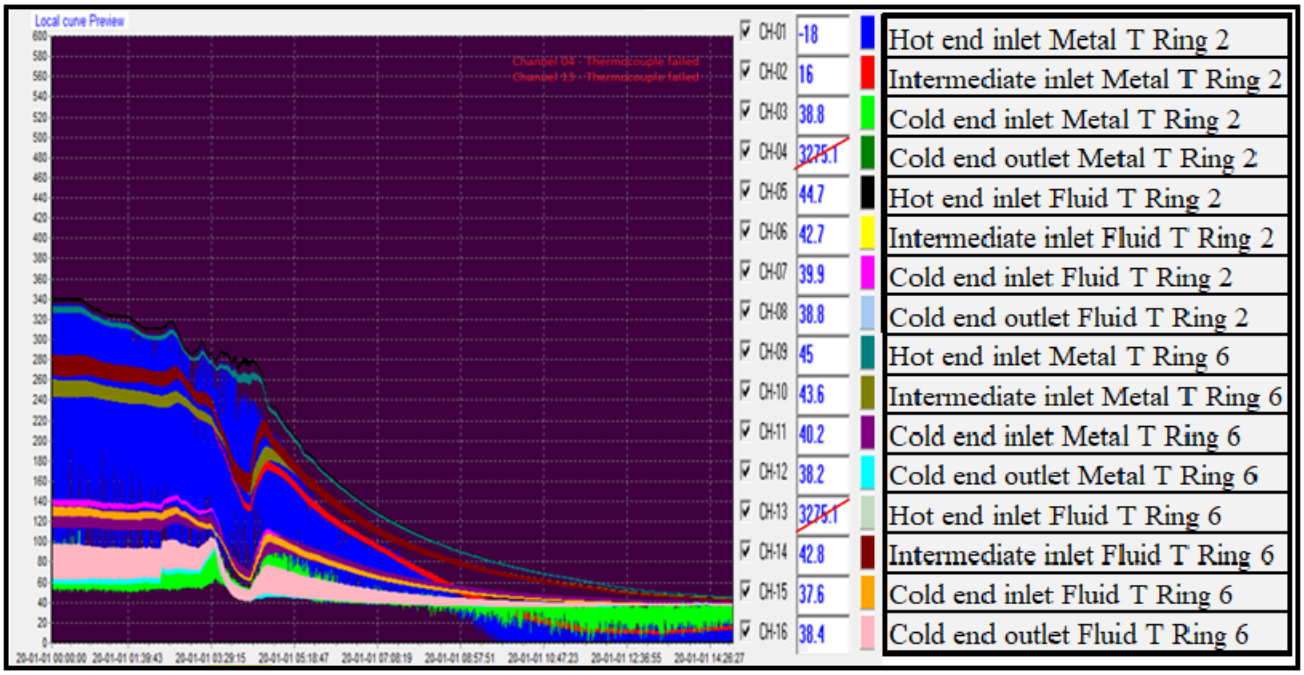

Figure 5.7: Air Heater Temperatures during a shut down

An initial comparison was done to calculate a range of dew point temperatures with fluctuation in sulphur content of coal. Table 5.2 is a representation of the as-received coal composition data that were used to calculate the dew point temperature, to see how the temperature varies with fluctuation in sulphur content. Table 5.3 shows how the change in sulphur content influences the dew point temperatures. This result indicates that during shut-down periods the entrained ash will be exposed to moisture and sulphurous acid condensate formation on ash particles and metal surfaces.

Table 5.2: Coal properties for pre-determining of dew point temperature fluctuation due to sulphur changes

As Received		
Coal content		unit
C	51.29	v%/v%
H	3.27	v%/v%
O	4.24	v%/v%
N	1.34	v%/v%
S	*x*	v%/v%
Ash	*36.5-(2-x)*	v%/v%
H20	1.5	v%/v%
TOTAL	**100**	
UBC	2	kg unburnt carbon/kg coal, measured from ash
BA	0.1	Bottom ash ratio
FA	0.9	Fly ash ratio
Factor F	0.3	Fuel Nitrogen conversion Factor
O_2 in flue gas	3.6	v%/v%
humidity air	10	g H20/kg DA

Table 5.3: Dew point temperature change due to changes in sulphur content of coal

Moisture Dew Point °C	**Sulphurous Acid Dew Point Temperature °C**	**Sulphuric Acid Dew Point (1% conversion SO3) Temperature °C**	**Sulphuric Acid Dew Point (5% conversion SO3) Temperature °C**	**Sulphur in coal *(x%)***	**Moisture in coal % (v/v)**
40.3	36.3	126.5	142.5	0.5	1.5
40.3	36.5	134.8	151.9	1.2	1.5
40.3	36.5	135.6	152.9	1.3	1.5
40.3	36.5	136.3	153.7	1.4	1.5
40.3	36.5	137.1	154.3	1.5	1.5
40.3	36.5	137.7	155.2	1.6	1.5
40.3	36.5	138.4	155.8	1.7	1.5
40.3	36.5	138.9	156.5	1.8	1.5
40.3	36.6	139.5	157.1	1.9	1.5
40.3	36.6	140.1	157.6	2	1.5

For the verification process for both the Data Set 1 and Data Set 2 the RAH VBA results were compared to the plant data and to the RAH model from De Klerk (2001). The results are shown in Appendix C - Tables C2, C3 and C4 which are explained in section 5.3.4.

The temperature differences between Ring 2 and Ring 6 were evaluated for the pre-testing phase at 80% MCR. The average cold end metal temperature for Ring 2 was 7.4% higher than the cold end metal temperature for Ring 6. The average cold end fluid temperature for Ring 2 was 9.4% higher than the hot end fluid temperature for Ring 6. These results again correlate with the fact that lower temperatures are experienced at the cold end periphery due to the cold air stream leaking to the flue gas stream. The results indicated that during a 544 MW (80 MCR) load the cold end metal temperature was +/-10ºC higher than the 670 MW operating cold end metal temperature for Rings 2 and 6. This shows that the periphery rings are expected to experience more dew point related fouling at the cold end due to the reduced operating temperatures at the periphery, and that the possibility of dew point related fouling would be higher for air heaters operating at full load conditions.

The same conclusion was found for the 68% MCR operating condition. The average cold end metal temperature for Ring 2 was 6.3% higher than the cold end metal temperature for Ring 6. The average cold end fluid temperature for Ring 2 was 7.7% higher than the hot end fluid temperature for Ring 6. The difference in temperature between the two rings is once again assumed to occur due to the leakage being higher closer to the periphery. The results also showed that during a 465 MW (68% MCR) load the cold end metal temperature was +/-16 ºC higher than the 670 MW cold end metal temperature for Rings 2 and 6. For the fluid temperatures the same occurred. During a 465 MW (68% MCR) load the average cold end flue gas and air temperatures were 15.0 ºC higher for Ring 2, and 10.1 ºC higher for Ring 6 in comparison to the 670 MW cold end fluid and metal temperatures. This again correlates with the previous indication that the periphery rings could experience more dew point related fouling at the cold end due to the reduced operating temperatures at the periphery, and that the possibility of dew point related fouling would be higher for air heaters operating at full load conditions.

5.2.4 Effect of the difference in simulation and operating pack profiles

For the simulation results of Data Set 1 it was initially assumed that all three layers had no blockage. With no fouling the pressure drop for the air side across the air heater should be 0.720 kPa and for the gas side 0.778 kPa according to the design specification. Simulating the original selection of packs (Figure 5.8), the differential pressure was 0.638 kPa for the air side and 0.696 kPa for the gas side, which gives an 11% error on the air side and a 10% error on the gas side.

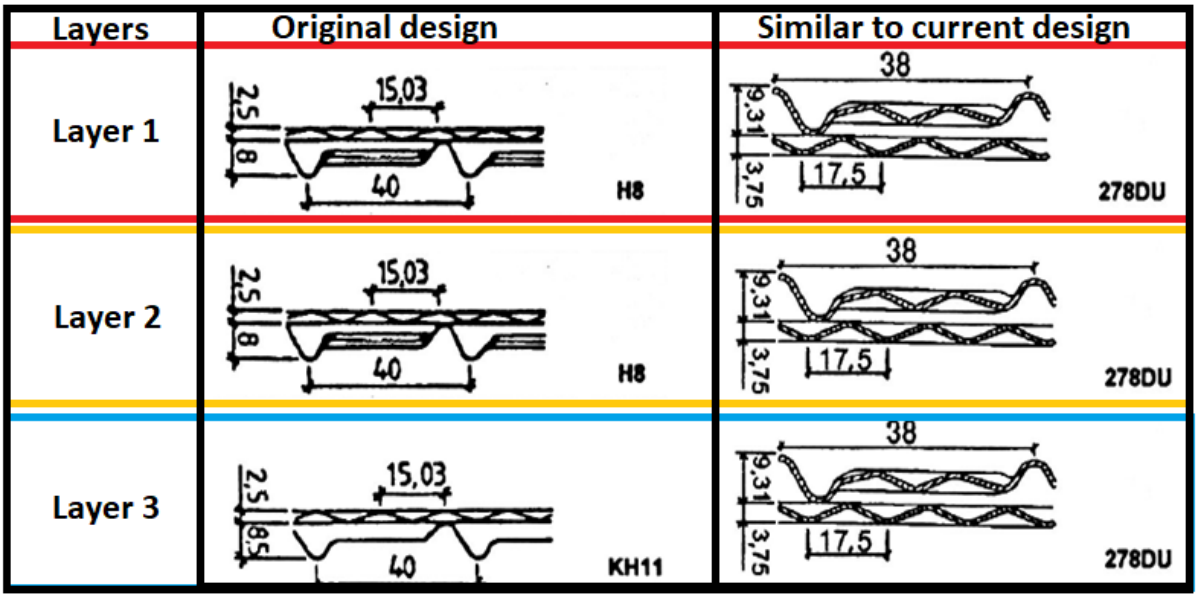

Figure 5.8: Element pack configuration

Figure 5.9 is a representation of the fouling seen from each pack where the thermocouples were installed. The same amounts of fouling were seen in Ring 2 and Ring 6. High pressure washing was done after the installation to remove most of the fouled deposits.

Figure 5.9: Blockage of each layer of the element packs where thermocouples were installed

Considering the cold end image from Figure 5.9 severe fouling can be seen which motivated for an assumption of 2% blockage for the hot end, 5% for the intermediate layer and 10% for the cold end. The pressure drop from the simulation result was 1.036 kPa for the gas side and 0.958 kPa for the air side. This simulation was done using the packs that have the same thermal properties as the currently installed HC11 packs. Different packs had to be selected for the simulation because the HC11 design specification is not available to Eskom. The 2.78DU element profile was proven to have similar thermal performance as the HC11 packs, according to the original equipment manufacturer. The possibility of introducing a form of error exists when a different type of simulation pack profile is compared to a different profile used in the plant. There was a clear difference in the measured differential pressure comparison between the two pack profiles. In the past the 2.78DU packs were used, but were replaced with the HC11 profile by the recommendation of the OEM. The HC11 packs were installed to allow more effective cleaning from the installed soot blowing system. Another factor to consider is that the HC11 element packs were never part of the test packs used during previous studies.

The original equipment manufacturer designed the packs according to the properties of the 2.78DU packs, to ensure the thermal performance is maintained. The comparison data was not shared due to restriction in sharing of intellectual property. Therefore the pressure drop component of the HC 11 packs are an unknown. Section 5.4 elaborates on the effect of the pack differences. The original design had the following element pack configuration:

Hot end: H8 – 0.5 mm
Intermediate: H8 – 0.5 mm
Cold end: KH11 – 0.8 mm

The difference between the gas side simulated and measured values was 0,474 kPa. For the air side the difference was found to be 0,034kPa. For Data Set 2 these measurements were taken again for further verification at the three different load conditions. The high differential pressure is affected by the fouling of the element packs. During the installation of the thermocouples excessive fouling was evident in the cold end layer. High pressure washing was applied to the element packs after the installation to ensure that the fouling condition was improved. Table 5.4 shows what the differential pressures were during the measurement in January 2020 before the Actual tests Data Set 2 was collected.

Table 5.4: Air heater differential pressure and leakage results

LH Air heater			
Leakage	12.59%		Air Flow Total
Date	Air LH	Gas LH	
22/01/20	1.07kPa	1.51kPa	784.40 kg/s

5.2.5 Effect of location of measuring points

A large error existed between the flue gas outlet temperature leaving the air heater (measured after the air heater outlet isolating dampers – DCS measurement) and the temperature measured at the outlet of the third layer of the steel matrix(directly at the outlet of the cold end element pack). When comparing the DCS measured value of 129.3˚C to the VBA RAH result of 90.7˚C an error of 30% exists, this error was related to an incorrect flue gas flow measurement, which is addressed in section 5.7. The cold end outlet gas temperature measured at the outlet of the third layer for Ring 2 (B in Figure 5.10) and Ring 6 (A in Figure 5.10) was 73˚C. This shows that for both readings A and B the actual gas temperature leaving the third layer is low in comparison with the measurement taken at point C further downstream in the flue gas path after the outlet dampers as shown in Figure 5.10.

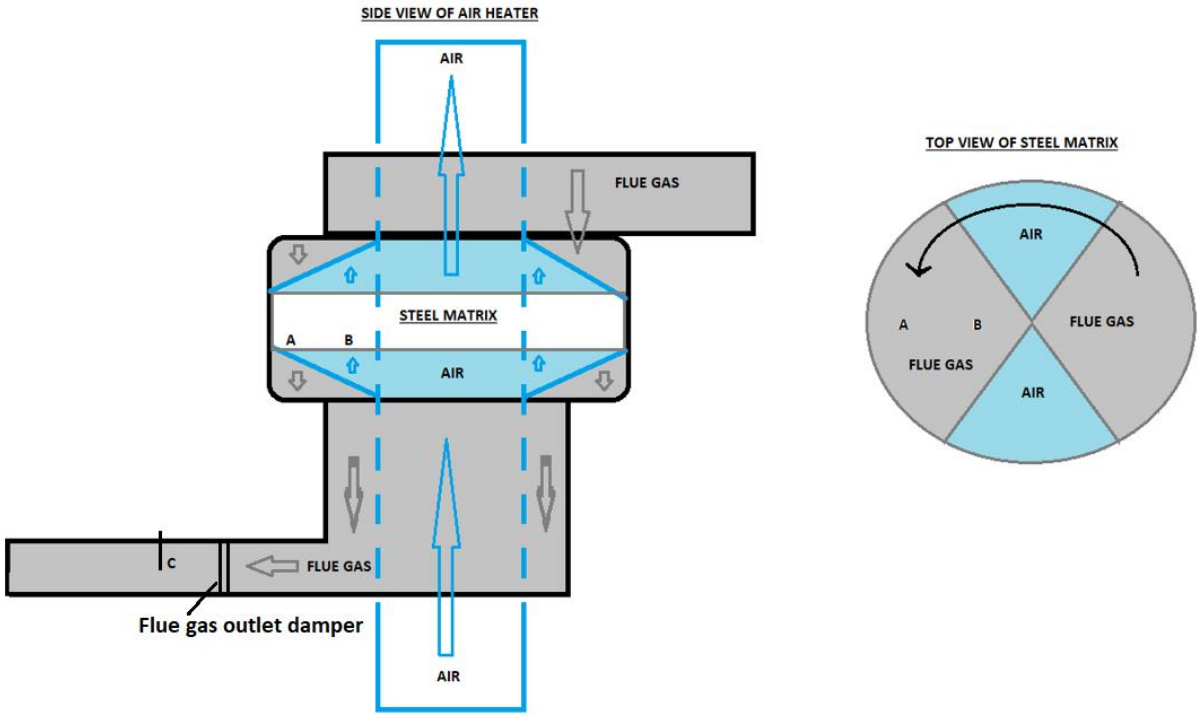

Figure 5.10: A – Ring 6 test point, B – Ring 2 test point, C – DCS measuring point for flue gas.

This measuring point is located at the secondary air heater flue gas outlet duct after the flue gas outlet damper. Point C experiences a continuous stream of flue gas. The points A and B in this figure experience a flue gas stream for period of +/-24 seconds and then a cold stream for +/-20 seconds. Therefore, a difference in temperature between points A and B compared to C can be expected. The local heat flux density for the two thermocouples is different. The heat flux density is illustrated in equation 5.3:

$$q = -k\nabla T \ \ (\mathrm{W/(m°}K)) \tag{5.3}$$

$q -$ Local heat flux density

$k -$ Material conductivity

$\nabla T -$Temperature gradient

The heat flux density is a measure of the flow of energy per unit of area of time. Considering the fact that the material conductivity is the same for the thermocouples, but the temperature change that the thermocouples experience for the two locations (A or B, and C) are different. “A” and “B” have a greater difference in temperature due to the fact that these thermocouples experience the cold air stream and the hot flue gas stream within each air heater rotation. Thermocouple C is located in an area that is isolated from the cold air stream, therefore the change in temperature is less. Based on this fact a type K thermocouple was actually not the ideal instrument, although it was the only type that could withstand the abrasive conditions inside the air heater due to the high ash content in the flue gas, within the project budget estimate. This effect can be expected for all the results.

The flue gas outlet duct in Figure 5.10 mostly experiences fluid temperatures well above the measured temperature at the element pack outlet. Considering the simulated mixed flue gas

stream outlet temperature of 117, 5 ˚C, this temperature is reached within 24 seconds of one revolution. Therefore it is possible that the physical structure at point C in Figure 5.10 with dampers, ducting and the surrounding material will experience higher temperatures when it is continuously exposed to the flue gas outlet temperature. The fact that the measured value at point A and B does not reach the measured value at point C of 129, 3 ˚C, shows that the thermocouple is not exposed to the flue gas stream long enough to reach the actual maximum flue gas outlet temperature. The ideal method for measuring would have been to measure an instantaneous temperature and not an average temperature. Equipment able to measure to such a level of accuracy will unfortunately not be able to withstand the air heater operating conditions.

5.2.6 Errors in the simulation results

As mentioned previously the collected input parameters from Data Set 1 were simulated for the RAH model and the VBA RAH model. The results of the comparison can be found in Appendix C1. Based on this it does seem that the simulation models tend to overestimate the outlet temperature at higher loads. In the time and length step calculations for the simulation models the values are rounded off to 1 decimal place in order to simplify and improve the calculation time of the model. This process introduces a form of overestimation of final outlet fluid and metal temperatures due to the fact that in some iterations it adds an additional iteration to the length and to the time step in order to complete the calculation.

As mentioned previously the flue gas flow is also a variable that is calculated based on combustion air and coal flow. Therefore some error can also be introduced if one of these parameters are incorrect. The combustion air consists of total primary and secondary air along with excess air, which can be found from the readings produced by the DCS. These readings can be influenced by errors introduced in the measurement of primary air and secondary air flows. The coal flow on the other hand must be converted from MJ/s to kg/s using the calorific value of coal. A coal analysis was not done for these first tests (Data Set 1), therefore historic data were used to find an average calorific value for coal to estimate the coal flow in order to calculate the flue gas flow. Section 5.7 elaborates on the effect of the error in flue gas estimation, where a 17.7 % deviation in flow was found due to incorrect measurements from the plant.

5.2.7 Summary of Data Set 1 Results

There is always a risk of various forms of error that are introduced in an experiment that is not set up for ideal conditions. With this in mind, the verified RAH model developed by De Klerk (2001) was also used to compare and verify the VBA RAH simulation results. Tables C3, C4 and C5 in Appendix C are the summarised set of input and output parameters for the measured data, VBA RAH simulation data and the RAH (GB de Klerk) data. The results were then used to estimate an error between VBA RAH results and the measured data from the DCS and the installed thermocouples. As mentioned previously there were a number of thermocouples that failed earlier than expected. The unit was shut down for three days from 1st of January 2020, during this time the thermocouples for the hot end and cold end were inspected. This inspection showed that the thermocouple insulation was already worn off and the hot end thermocouple

compensating cables were eroded off completely. During the actual tests no thermocouples were functioning for the hot end, but ring 6 cold end inlet and outlet temperatures were still functioning. As explained before the cold end layer is where fouling usually occurs, and therefore for the Data set 2 results could still be collected, due to the availability of these thermocouples.

Due to the fact that no coal samples were taken for the coal composition during the pre-testing phase, the dew point estimations were not included in the results. These results are included in the actual test results for Data set 2. Comparing the three different load conditions all three test results showed reliable results for the verification of the metal temperatures. The fluid temperatures could at least be used to see whether the fluid regions correlate for the simulated fluid temperatures and the measured fluid temperatures but for the accuracy of simulated results the measured values could not be used as reliable data

The large contributors for errors were assessed to be contact resistance, unaccounted-for thermal inertia, ash build, incorrect flue gas flow estimation and the use of incorrect measuring techniques for the application. Figure 5.11 is an illustration of these effects. During high pressure washing, fouled deposits could have caused localised accumulation of deposits around the thermocouples, influencing the flow through the area, and in turn also affecting the heat transfer to an extent where the results were compromised. Another problem is the thermal insulation that only lasted for a short period. Therefore, the measured values actually measured an average temperature of the metal surface and the fluid passing through. The ideal condition would have been to also measure temperature after a complete element pack replacement to avoid the possibility of uneven distribution of flow due to fouling in various localised areas, which was not removed by the high pressure washing (as shown in Figure 5.11). Although the method of installation was not ideal, it still provided guidance in terms of indicating what the possible temperature ranges could be for operating under different loads. This information is valuable and provides a platform to see whether the element packs could experience dew point related fouling.

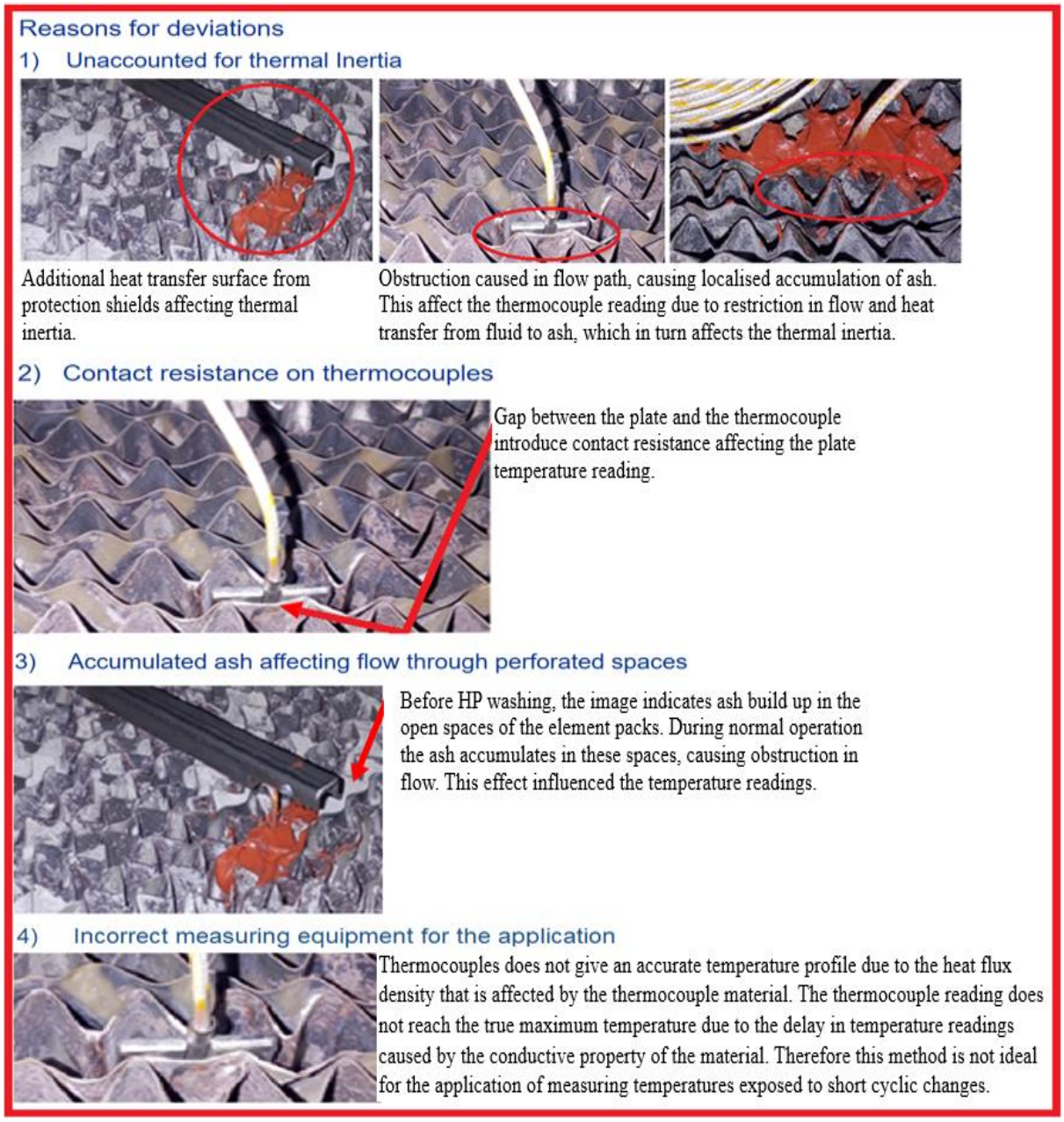

Figure 5.11: Factors influencing the experimental results.

5.3 Comparison of Measured Results and Simulation Results: Data Set 2

The next set of tests was carried out from 24 to 26 February 2020. Initially the plan consisted of only doing plant measurements once, but there was a delay to conduct the tests due to the availability of the calibration gas for the Horiba flue gas analyser. This analyser was used to measure the flue gas composition to determine the amount of carbon dioxide and sulphur dioxide in the flue gas. As mentioned previously, thermocouples were damaged prior to the test. The important fact was that the metal temperature probes for the third layer in Rings 2 and 6 were still available, where dew point related fouling is expected. The same method of leakage measurement was used as explained in section 5.2.1, to measure leakage for each test at the specific load and the results for the leakage test can be seen in Figure 5.12. The fact that the

leakage decreases as load increases shows that the articulation of the seal frames operated correctly (Figure 5.2). This information is critical in terms of understanding the impact on air heater performance at various loads.

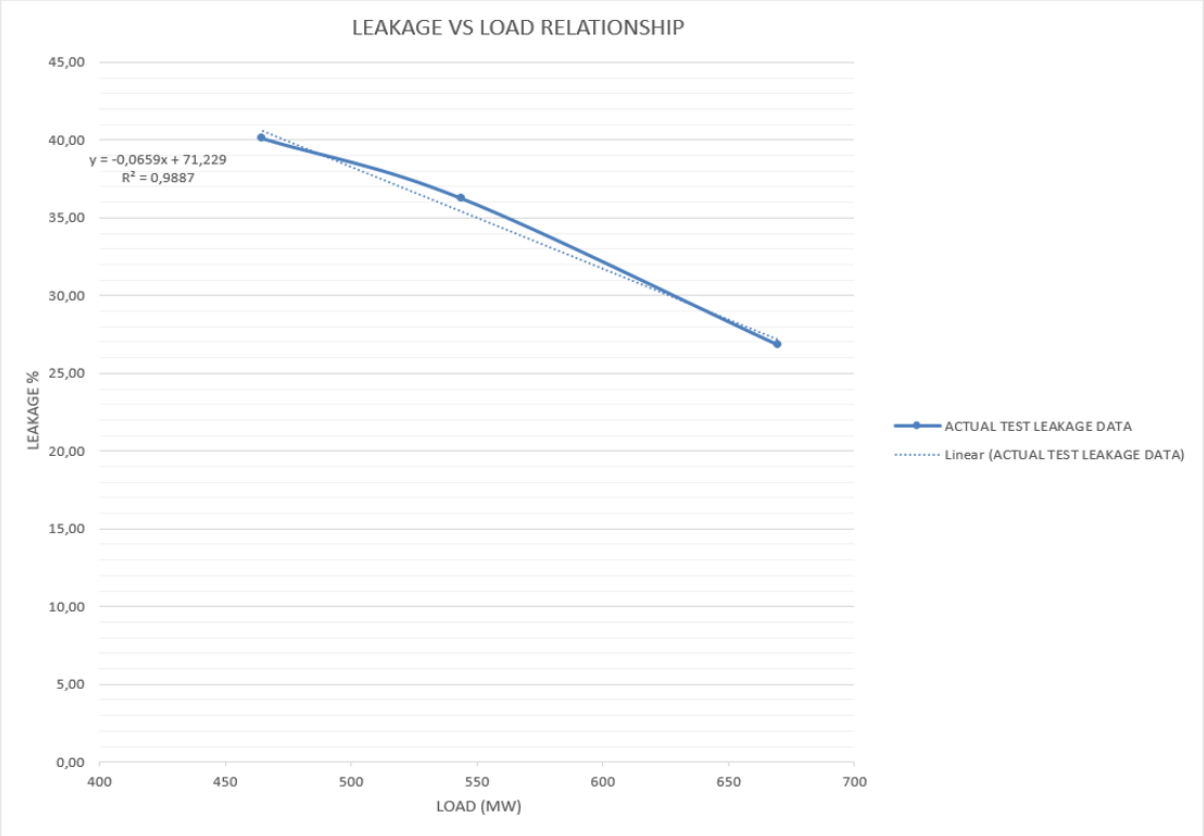

Figure 5.12: Air Heater Leakage Test results for Data Set 2 tests performed in February 2020.

In Data set 2 the simulation results for all three loads were compared to the measurements taken from the plant and the DCS. The simulation results were also compared to the simulated results from De Klerk's (2001) RAH model. An error deviation was estimated between the VBA RAH simulated results and the plant data, along with an error estimation of the VBA RAH model in comparison to De Klerk's RAH model. Tables C7, C8 and C9 in Appendix C (C2: Data Set 2 Results) contain the comparison results for the respective load conditions during the actual tests. The same approach was used as Data set 1 for the allocation of the tag names in the graphs. Table 5.5 illustrates the allocated tag names for the measured and simulated data points. The table also includes the estimated dew point temperatures for sulphurous acid, sulphuric acid and moisture. The 1% to 5% for the sulphuric acid dew point temperature is based on the assumption amount of sulphur dioxide that converts to sulphur trioxide post-combustion. This provides a range of dew point temperatures, which shows where fouling can possibly occur in the steel matrix.

Table 5.5: Tag names for each temperature profile for Data Set 2.

Tag name	Description
SIMFITHE	Simulation Fluid Inlet Temperature Hot End
SIMIFIT	Simulation Intermediate Fluid Inlet Temperature
SIMCEIFT	Simulation Cold End Inlet Fluid Temperature

SIMCEOFT	Simulation Cold End Outlet Fluid Temperature
SIMHEIMT	Simulation Hot End Inlet Metal Temperature
SIMIMIMT	Simulation Intermediate Inlet Metal Temperature
SIMCEIMT	Simulation Cold End Inlet Metal Temperature
SIMCEOMT	Simulation Cold End Outlet Metal Temperature
HEIMTR6	Measured Hot End Inlet Metal Temperature Ring 6
IMMITR6	Measured Intermediate Inlet Metal Temperature Ring 6
CEIMTR6	Measured Cold End Inlet Metal Temperature Ring 6
CEMTOR6	Measured Cold End Outlet Metal Temperature Ring 6
CEOFTR6	Measured Cold End Outlet Fluid Temperature Ring 6
CEIFTR6	Measured Cold End Inlet Fluid Temperature Ring 6
IMFITR6	Measured Intermediate Fluid Inlet Temperature Ring 6
HEFIR6	Measured Hot End Fluid Inlet Temperature Ring 6
HEFIR6	Measured Hot End Fluid Inlet Temperature Ring 6
H2SO4 DP 1%	Sulphuric Acid Dew Point with 1% of SO_2 converted to SO_3
H2SO4 DP 2%	Sulphuric Acid Dew Point with 2% of SO_2 converted to SO_3
H2SO4 DP 3%	Sulphuric Acid Dew Point with 3% of SO_2 converted to SO_3
H2SO4 DP 4%	Sulphuric Acid Dew Point with 4% of SO_2 converted to SO_3
H2SO4 DP 5%	Sulphuric Acid Dew Point with 5% of SO_2 converted to SO_3
H2SO3 DP	Sulphurous Acid Dew Point
H20 DP	Moisture Dew Point

During Data Set 2 tests, coal composition was measured for each test condition and the flue gas composition was also measured for the period of four hours during each test. The loads were kept constant to reduce variations in the measured input parameters. During the Data Set 1 tests the error in flue gas outlet temperatures was identified; due to this the DCS values for the gas outlet temperatures were not used, but were rather measured during each test of Data Set 2.

5.3.1 Air heater performance results vs. VBA RAH simulated results at 670 MW (99% MCR):

During these tests the inlet temperatures for the fluid (Flue gas and air stream) and metal temperatures were not available due to the failure of the hot end thermocouples. The signals from the cold end element packs were still available for identifying possible dew point related fouling. The measured readings and the simulated values were combined for the metal and fluid temperatures to show that they operate in the same regions as expected. Figure C5 in Appendix C shows this comparison.

No measured data points were available for Ring 2, all the thermocouples were out of service, and therefore the readings from Ring 6 were used for the metal temperatures. The intermediate layer inlet metal temperature thermocouple showed erratic behaviour, but for the times it was in operation the corresponding simulated temperature fell in the same region. The simulation once again indicated a higher rate of temperature change in comparison to the measured values. The same argument holds that the effects explained in Figure 5.11 affected the results from the measured data. Thermal inertia in reality changes the rate of heat transfer due to the various

sources that absorb and store heat for longer periods, causing reduced fluctuation in temperature. This condition could have deteriorated further due to excessive wear, increasing the contact resistance between the thermocouples and the metal surface.

Figure 5.13 shows the metal temperature profiles that were simulated in comparison with the measured metal temperatures at the inlet and outlet of the third layer. The metal temperatures showed good correlation and also indicated that the third layer would experience sulphuric acid dew-point related fouling during normal operation. Figure 5.14 illustrates the results for the simulated and measured fluid (flue gas and air stream) temperatures. The results show that at a high load, as expected, dew point related fouling would increase. This condition will occur due to an increase in heat transfer that occurs with higher flows, which causes lower flue gas outlet temperatures to occur. Although the leakage is less at higher loads, the actual metal temperature at the outlet of the cold end is expected to be less than at lower load conditions. In Figure 5.13 the dew point temperature is also estimated for sulphuric acid, sulphurous acid and moisture. The results show that the third layer operates in sulphuric acid dew point conditions. Figure 5.13 also shows the measured and simulated metal temperatures for each layer, where the solid lines indicates the simulated profiles and the dashed lines illustrates the profile for the measured temperatures.

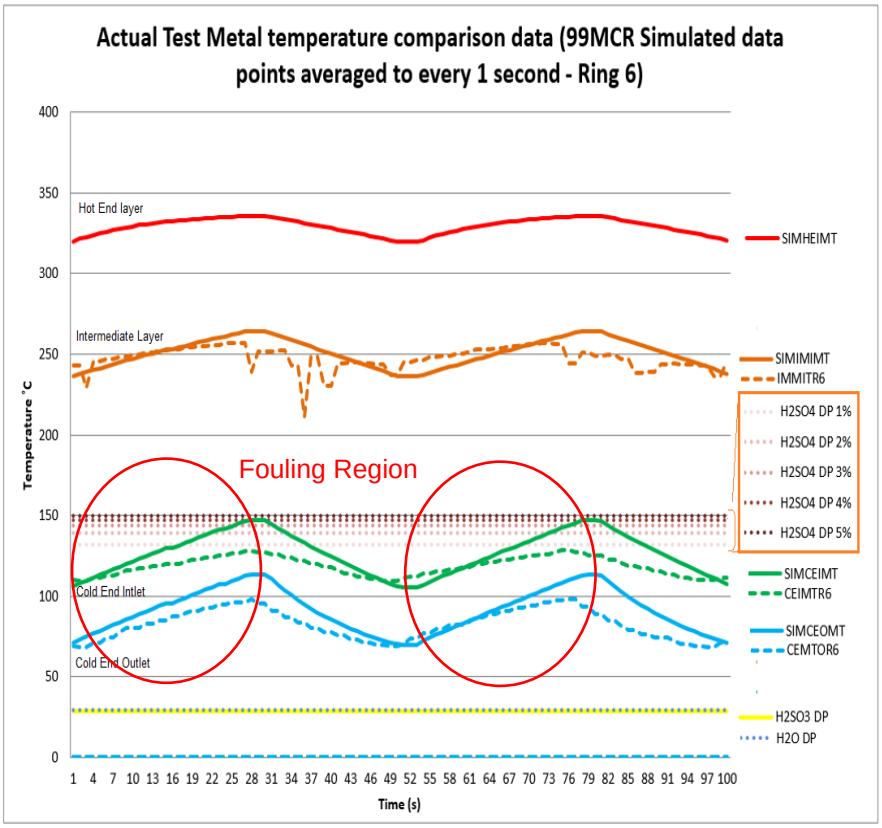

Tag name	Description
SIMFITHE	Simulation Fluid Inlet Temperature Hot End
SIMIFIT	Simulation Intermediate Fluid Inlet Temperature
SIMCEIFT	Simulation Cold End Inlet Fluid Temperature
SIMCEOFT	Simulation Cold End Outlet Fluid Temperature
SIMHEIMT	Simulation Hot End Inlet Metal Temperature
SIMIMIMT	Simulation Intermediate Inlet Metal Temperature
SIMCEIMT	Simulation Cold End Inlet Metal Temperature
SIMCEOMT	Simulation Cold End Outlet Metal Temperature
HEIMTR6	Measured Hot End Inlet Metal Temperature Ring 6
IMMITR6	Measured Intermediate Inlet Metal Temperature Ring 6
CEIMTR6	Measured Cold End Inlet Metal Temperature Ring 6
CEMTOR6	Measured Cold End Outlet Metal Temperature Ring 6
CEOFTR6	Measured Cold End Outlet Fluid Temperature Ring 6
CEIFTR6	Measured Cold End Inlet Fluid Temperature Ring 6
IMFITR6	Measured Intermediate Fluid Inlet Temperature Ring 6
HEFIR6	Measured Hot End Fluid Inlet Temperature Ring 6
HEFIR6	Measured Hot End Fluid Inlet Temperature Ring 6
H2SO4 DP 1%	Sulphuric Acid Dew Point with 1% of SO_2 converted to SO_3
H2SO4 DP 2%	Sulphuric Acid Dew Point with 2% of SO_2 converted to SO_3
H2SO4 DP 3%	Sulphuric Acid Dew Point with 3% of SO_2 converted to SO_3
H2SO4 DP 4%	Sulphuric Acid Dew Point with 4% of SO_2 converted to SO_3
H2SO4 DP 5%	Sulphuric Acid Dew Point with 5% of SO_2 converted to SO_3
H2SO3 DP	Sulphurous Acid Dew Point
H20 DP	Moisture Dew Point

Figure 5.13: Data comparison for Ring 6 Metal temperatures for the 99% MCR Data Set 2.

The fluid temperatures showed poor correlation, but the measured fluid temperatures showed better correlation with the measured metal temperas. This is a definite sign of thermal inertial affects that influenced the measurements, which was also evident for the cases of the 80% MCR load condition (Discussed in Appendix C4) and for 68%MCR condition(discussed in section 5.3.2. Figure 5.14 is an illustration of the measured and simulated fluid temperatures, where the solid lines indicates the measured profiles and the dashed lines illustrates the profile for the simulated temperatures.

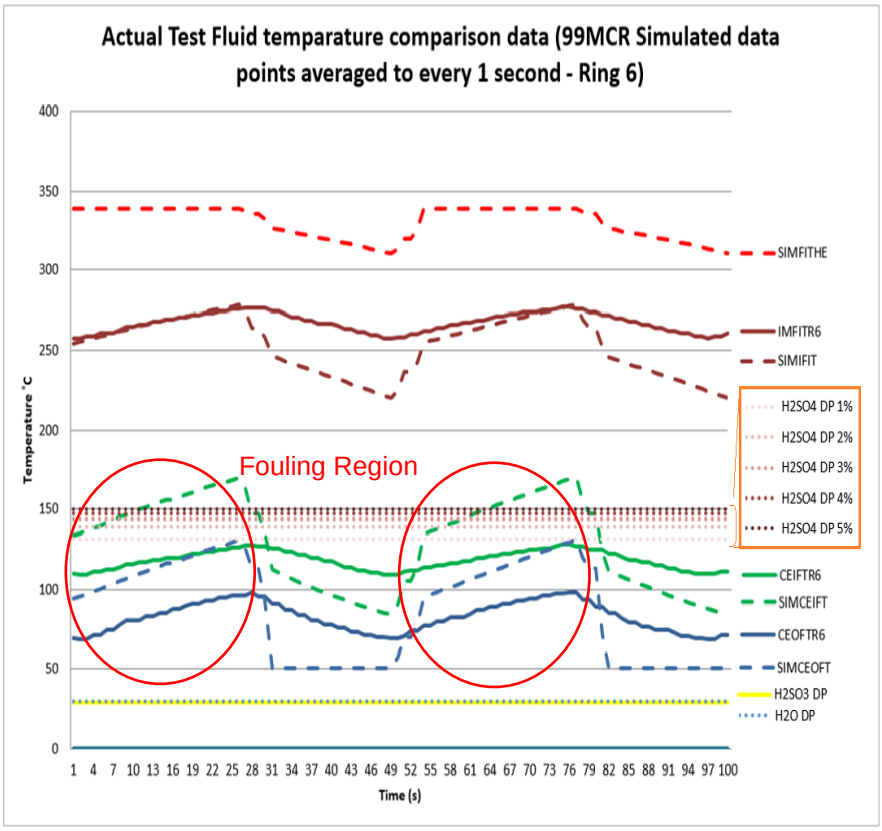

Tag name	Description
SIMFITHE	Simulation Fluid Inlet Temperature Hot End
SIMIFIT	Simulation Intermediate Fluid Inlet Temperature
SIMCEIFT	Simulation Cold End Inlet Fluid Temperature
SIMCEOFT	Simulation Cold End Outlet Fluid Temperature
SIMHEIMT	Simulation Hot End Inlet Metal Temperature
SIMIMIMT	Simulation Intermediate Inlet Metal Temperature
SIMCEIMT	Simulation Cold End Inlet Metal Temperature
SIMCEOMT	Simulation Cold End Outlet Metal Temperature
HEIMTR6	Measured Hot End Inlet Metal Temperature Ring 6
IMMITR6	Measured Intermediate Inlet Metal Temperature Ring 6
CEIMTR6	Measured Cold End Inlet Metal Temperature Ring 6
CEMTOR6	Measured Cold End Outlet Metal Temperature Ring 6
CEOFTR6	Measured Cold End Outlet Fluid Temperature Ring 6
CEIFTR6	Measured Cold End Inlet Fluid Temperature Ring 6
IMFITR6	Measured Intermediate Fluid Inlet Temperature Ring 6
HEFIR6	Measured Hot End Fluid Inlet Temperature Ring 6
HEFIR6	Measured Hot End Fluid Inlet Temperature Ring 6
H2SO4 DP 1%	Sulphuric Acid Dew Point with 1% of SO_2 converted to SO_3
H2SO4 DP 2%	Sulphuric Acid Dew Point with 2% of SO_2 converted to SO_3
H2SO4 DP 3%	Sulphuric Acid Dew Point with 3% of SO_2 converted to SO_3
H2SO4 DP 4%	Sulphuric Acid Dew Point with 4% of SO_2 converted to SO_3
H2SO4 DP 5%	Sulphuric Acid Dew Point with 5% of SO_2 converted to SO_3
H2SO3 DP	Sulphurous Acid Dew Point
H20 DP	Moisture Dew Point

Figure 5.14: Data comparison for Ring 6 fluid temperatures for the 99% MCR Data Set 2.

For a single rotation the simulated cold end inlet metal temperatures showed that for a 1% conversion of SO_2 to SO_3, 61.2% of these cold end inlet temperatures of the flue gas stream operate below the dew point temperature. For 5% conversion of SO_2 to SO_3 all the simulated cold end inlet metal temperatures operate below the sulphuric acid dew point temperatures. The simulated cold end fluid temperature showed that for a 1% conversion of SO_2 to SO_3, 4.7% of the temperatures operate below sulphuric acid dew point temperatures, and for 5% conversion of SO_2 to SO_3 54.1% operates below the sulphuric acid dew point temperature. Figure 5.13 illustrates that the measured metal temperatures were fully exposed to sulphuric acid dew point temperatures for all cases of SO_2 to SO_3 conversion. As expected, the temperatures never reach the sulphurous acid dew point temperatures or moisture dew point temperatures during normal operation. This result shows that at maximum load conditions sulphuric acid dew point temperatures are experienced in the cold end of the steel matrix (As seen in Table 5.6).

Table 5.6: Sulphuric acid formation time for the simulated and measured metal- and fluid temperatures (99%MCR).

Conversion SO_2 to SO_3	Inlet Cold end metal temperature exposure to sulphuric acid dew point temperatures	Inlet Cold end flue gas temperature operating below the sulphuric acid dew point temperatures	Measured cold end inlet metal temperatures operating below the sulphuric acid dew point temperatures	Measured cold end fluid inlet temperatures operating below the sulphuric acid dew point temperatures
1%	61,20%	4,70%	100%	100%
5%	100,00%	54,10%	100%	100%

The question remains what the actual conversion of sulphur dioxide to sulphur trioxide could be. To estimate this amount the following was considered: The sulphur dioxide measurement was normalised with two oxygen correction factors namely 10% and 6%. A value of 0.17% by volume of SO_2 in the flue gas was measured, which relates to a 10% O_2 normalised measurement, and for the 6% O_2 normalised a 0.23% SO_2 was measured. Using the 10% normalised value of 0.17% of measured SO_2, means that 1% to 5% conversion will give a range of 0.00171% to 0.00855% of SO_3 contained in flue gas, with an estimated excess air of 19.26%. The simulation results from the mass and energy balance indicated a 0.16% volume of SO_2. Table 5.7 shows the results for SO_3 content in flue gas for varying sulphur content of coal concluded by Ganapathy (1989). If this table is followed to determine the amount of SO_3 in the flue gas the expected amount would be based on a 1.43% (as received) sulphur in coal. According to the table the amount would be 16.03 ppm SO_3 (0.0016%) when using linear interpolation. The amount measured from the 99% MCR Data set 2 test was 17.1 ppm, which shows the estimated and measured values correlate well. If the 6% O_2 normalised value of 0.23% SO_2 was considered it would have given a range of 0.0023% to 0.0115% of SO_3 formed in the flue gas, which did not correlate well with the simulated value or the value estimated from Table 5.7. Based on the table (0.0016%) and the measured (0.017% $SO_{2\,@10\%}$ & 0,0023% $SO_{2\,@\,6\%}$) result, the assumption that +/-1% SO_2 converted to SO_3 holds, which further confirms that the cold end was indeed experiencing dew point related fouling for the 99% MCR conditions as explained in Table 5.8.

Table 5.7: SO3 content in flue gas for varying sulphur in coal (Ganapathy, 1986).

		Sulfur, %					
	Excess	0.5	1.0	2.0	3.0	4.0	5.0
Fuel	air, %	SO_3, ppm					
Oil	5	2	3	3	4	5	6
	11	6	7	8	10	12	14
Coal	25	3-7	7-14	14-28	20-40	27-54	33-66

Table 5.8: Summary of the Sulphur trioxide formation from the simulated and measured results (99%MCR).

	Measured SO_2 @ 10% normalised	Measured SO_2 @ 6% normalised	Simulated SO_2
SO_2	0,17%	0,23%	0,16%
1% SO_2 converted to SO_3	0,00171%	0,00230%	
5% SO_2 converted to SO_3	0,00855%	0,01150%	
Ganapathy Table 5.6			
Based on 1,43% Sulphur in coal (As received)	0,0016%		
Conclusion	Based on the Table 5.6 and the measured SO_2 it seems that +/-1% of SO_3 formed.		

The area and time of sulphuric acid formation must now be estimated. During the calculation process a metal temperature matrix was stored from the inlet to the outlet over the full height of a layer. For the third layer this was a 32 x 307 size matrix which contains the final set of cold end layer temperatures for the full height of the third layer. Figure 5.15 is a representation of a typical matrix formed for the cold end layer during a simulation process.

MATRIX : COLD END 32 x 307

Time of one rotation

time step

(Layer Heigth) Length of pack	t-step=0					t-step=307
l-step= 0	122,9489	123,7193	124,4946	125,2651		126,0315
	122,9489	123,7193	124,4946	125,2651		126,0315
.	122,9273	123,5845	124,2569	124,9355		125,6192
.	122,1582	122,8139	123,4787	124,1452		124,8136
.						
.						
.						
l-step= 32	76,64305	78,87007	79,69024	80,54348		76,56463

Figure 5.15: Temperature matrix formed during the iterative calculation process

This matrix shown in Figure 5.15 was used to estimate the area exposure to dew point related fouling that was experienced for one gas stream consisting of a subset of 32 x 84 temperatures of the total matrix. The 32 x 84 selection from the matrix takes into consideration time steps where the flue gas stream passed through the air heater and in this case specifically the third layer at the cold end of the air heater. For this subset the metal temperature was exposed 90.29% of the length and time step. Due to the fact that this will occur for every annular division it can be seen that the all of the cold end element pack will experience sulphuric acid deposition for 24.70 seconds of the total of 27.36 seconds of flue gas stream exposure. This time includes the time when the ash is captured in the seal area directly after the flue gas stream. This becomes a critical period which allows ash particles to condense and adhere to each other and the metal surfaces. The measured surface metal temperatures operated below the sulphuric acid dew

point temperatures for the full range of 1% - 5% conversion of SO_2 to SO_3. It shows that as expected dew point related fouling does occur in the third layer for the 99% MCR condition.

Figure 5.16 shows the results for the estimated sulphuric acid dew point temperatures experienced for the 99% MCR condition. This was for a 1.43% sulphur content in coal and 4.49% moisture in flue gas (as measured). Based on the 1% formation assumption the critical fouling temperature is estimated to be +/-133˚C.

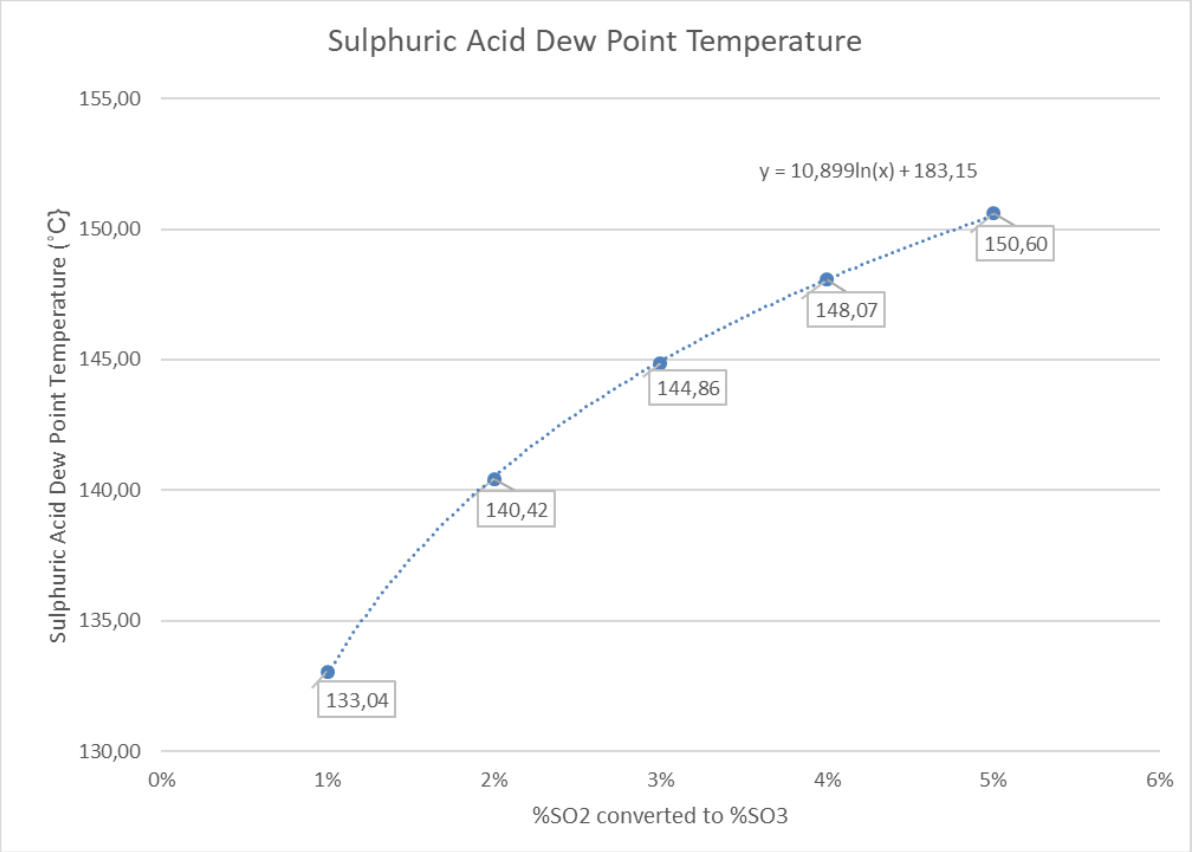

Figure 5.16: Sulphuric acid dew point temperatures for 1% to 5% SO_2 to SO_3 conversion for 99% MCR.

When fouling occurs the pressure drop across the third layer is expected to increase, as well as the overall differential pressure across the steel matrix. This effect will have an impact on the dew point temperatures. This impact was evaluated for the dew point temperatures for sulphuric acid, sulphurous acid and moisture for increments of 0.5kPa differential pressure increases across the steel matrix. These increments were calculated for a differential pressure range of 0kPa to 2.5kPa. The normal assumption is always made that when the differential pressure across the steel matrix is above 1kPa, the packs are assumed to be partially blocked. The results are illustrated in Figure 5.17. These results show that the increase in differential pressure from 0kPa to 2.5kPa does not change the temperature for sulphuric acid dew point temperatures by large margins, and therefore it can be assumed to have a negligible effect. The change in temperature with an increase in pressure will also not change the sulphurous acid dew point temperature to a large extent during normal operation. For sulphurous acid dew point temperatures the change was found to be less than 0.4 ˚C. The moisture does change to a large extent, the dew point temperature increases with +/-6.5 ˚C. But these temperatures will not

create a condition of fouling, because during normal operation the metal temperatures operate well above these moisture and sulphurous acid dew point temperatures.

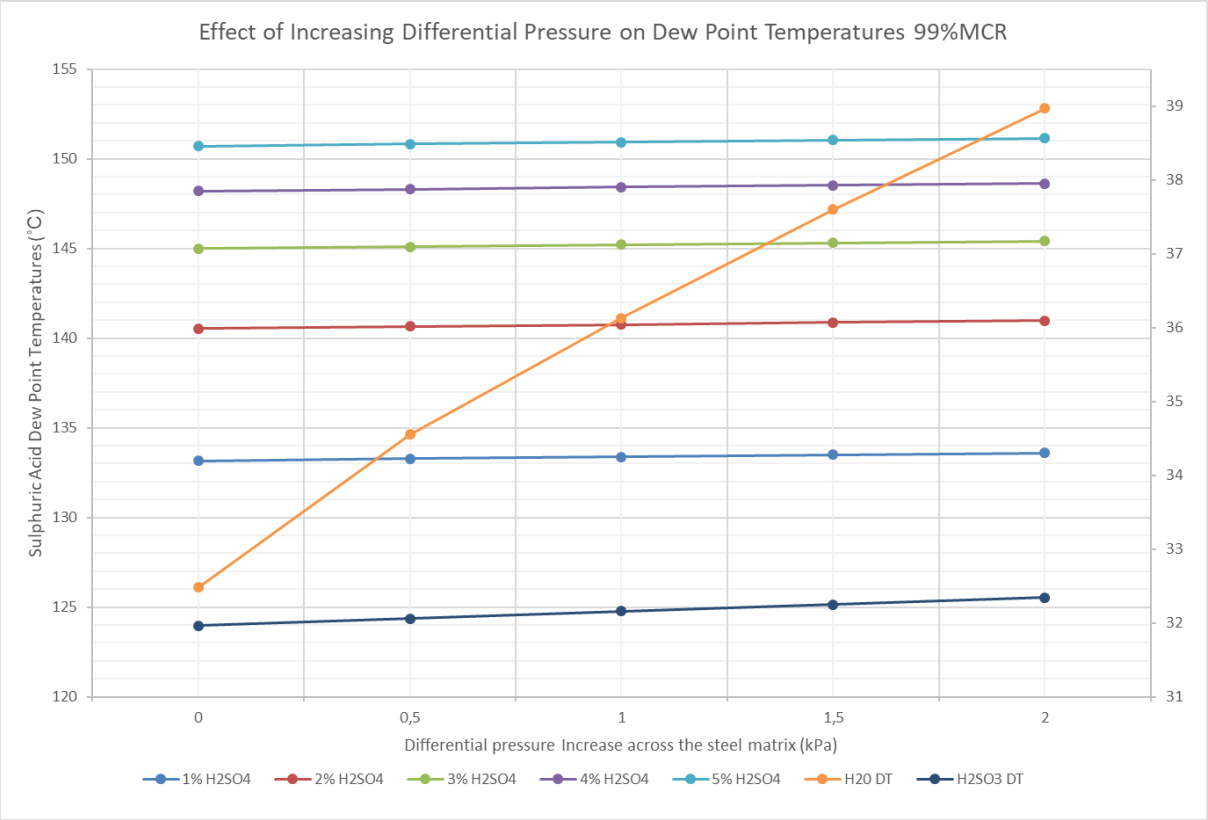

Figure 5.17: Effect of increasing differential pressures on dew point temperatures for 99% MCR.

Table C7 in Appendix C (C2: Data Set 2 - Results) is a representation of the results from the 99% MCR load actual test conducted from 00:00 – 04:00 on 24/02/2020. During this time the secondary air heater air inlet and outlet temperatures and pressures were measured using the DCS system. The flue gas inlet and outlet temperatures, leakage, flue gas composition pressure, density, and velocities were measured by the performance and testing team from the Eskom Research, Testing and Development department (RT&D). RT&D is a specialisation centre for plant performance measurements for the Eskom. Coal samples were collected by the onsite P&T (Performance and Testing) team and then prepared and sent for coal ultimate analysis. The onsite P&T team assist with power station based plant measurements specific to one power station. The coal samples were collected at the mill feeders and the process is explained in Appendix B2 – Experimental preparation & execution section.

Air heater gas outlet temperatures

The mixed flue gas temperature that takes leakage into consideration was measured to be 120˚C. This temperature showed a 13.2 % deviation from the VBA RAH result of 104.2˚C. This result was influenced by various factors such as leakage and errors in flue gas flow measurement. The undiluted temperature (temperature of the flue gas leaving the air heater before it is mixed with the leakage streams as illustrated in equation 3.14) leaving the pack was simulated to be 113˚C. The average cold end outlet fluid (flue gas and air) temperature measured was 85˚C. The difference in temperature is related to the explanation given in section 5.2 – Figure 5.10, which refers to the secondary air heater flue gas duct mostly experiencing

fluid temperatures well above the measured temperature at the element pack outlet. Through considering the maximum simulated outlet temperature at the outlet, a simulated temperature of 132˚C was reached within 24 seconds of one revolution, therefore it is possible that the flue gas temperature leaving the air heater after the outlet dampers, will experience higher temperatures due to its continuous exposure to this flue gas temperature. On the other hand the temperature measured at the element pack will experience both a hot flue gas and a cold air stream, therefore measuring a lower temperature. The method of using type K thermocouples unfortunately did not make it possible to reach the maximum temperature within the time that it was exposed to the flue gas stream. The same input parameters were simulated for the RAH model and an error of 0.09% between the VBA RAH model and the RAH model was evident. Based on this result, the simulation models again showed that the outlet temperatures were overestimated at higher loads. As explained in Section 5.7, a 17.7% deviation in flow was found due to incorrect measurements from the plant. Flue gas flow is also a variable that is calculated based on combustion air and coal flow, this value had to be used instead (due to incorrect measured flow) to simulated reasonable results.

Air heater air outlet temperatures
A 2.79% error occurred between the VBA RAH model and the measured value. This was a difference of 8.6˚C at the outlet for the air side. The error between the VBA RAH and the RAH models was 1.69%. This shows that the possible flue gas flow error compromised the simulated results, in this case the outlet air temperatures were also affected due to higher heat transfer rates.

Cold end metal temperatures
The comparison between the VBA RAH maximum plate temperatures and the measured maximum plate temperature indicated a 14.3% error. The minimum VBA RAH metal temperature was found to be 2.3% less than the measured value. Once again the temperatures operated in the same region but the error showed that the simulated value was higher in general in comparison to the simulated value. This error was once again incurred due to the factors mentioned in Figure 5.11. A 24.5% difference in the inlet metal temperature occurred between the results from the VBA RAH and RAH models, with a 2.9% deviation on the outlet metal temperatures. When comparing the measured value and the RAH value it is seen that the results from the RAH simulation are problematic. The rate of change in temperature for the solid area is higher in comparison to what is seen from the measurements. The minimum metal temperatures show values that correlate better with the simulated outlet temperature for the diluted flue gas stream (takes leakage into account). The simulated and measured minimum metal temperatures correlate, which is ideal for identifying the dew point fouling areas.

Flue gas properties
The flue gas properties were verified through measurements. A HORIBA analyser was used at the oxygen matrix system located at the flue gas inlet duct of the air heater to determine the composition. The oxygen matrix system is illustrated in Figure 5.18. This system consists of a nozzle that creates a differential pressure from atmosphere into the flue gas duct. The natural suction draws flue gas from three different heights in the duct and at four different cross sectional vertical sections. This system collects a mixed sample from a 3x4 matrix point sampling system. The mixed stream is then analysed for oxygen content. It was also used to connect the HORIBA analyser for flue gas composition analysis as shown in Figure 5.19. These results were compared to the mass balance results calculated from the coal composition. The amount of oxygen, moisture, carbon dioxide and sulphur dioxide in the flue gas were compared. The moisture test was performed at the same flue gas inlet duct of the air heater. In general the

moisture seems to be higher, because a moisture trap is used to determine the amount of H_20 in the flue gas in a Silica gel container. In this area where the test was performed the ash content in fly ash is high, due to the fact that it has not passed through the air heaters and electric precipitators yet. When the sample of flue gas is collected a great amount of ash also enters the trap, causing more moisture to stay behind in the trap with the silica gel. This causes an increase in the measured mass of the silica gel, which introduces an error for the moisture estimation. The calculation will show that the sampled mass is higher, therefore the measured moisture in the flue gas will be higher than the actual value. The fly ash that is trapped inside cannot be separated when the silica gel is weighed. With Data Set 2 the moisture did compare well with the mass balance result.

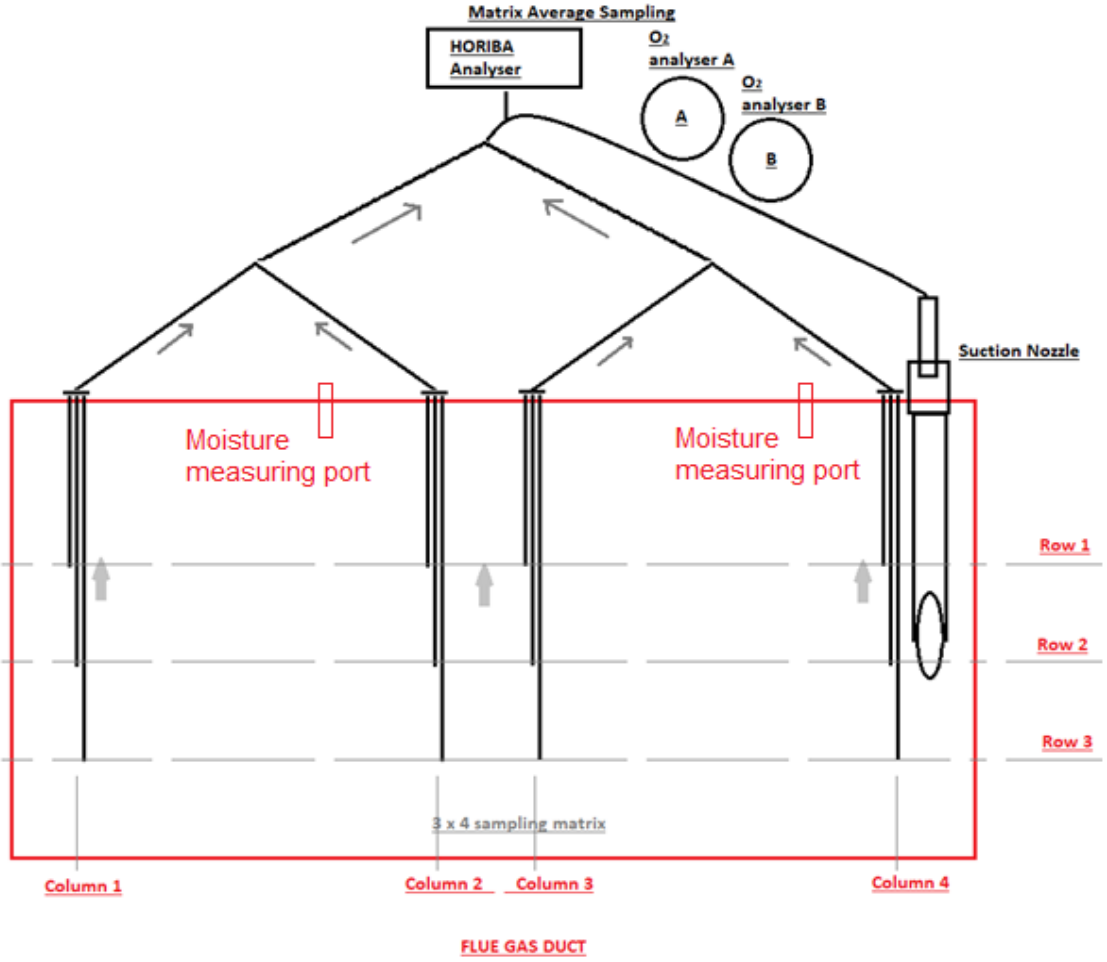

Figure 5.18: Oxygen Matrix configuration for sampling of flue gas.

The Horiba analyser that was used was a PG350 series. This model ideally measures samples with dust content less than $0.1g/m^3$. Therefore when samples for analysis are collected, the ideal location would be at the smoke stack where the ash content and operating temperatures are at a minimum. The Data set 2 measurements were taken before the air heaters as indicated in Figure 5.19. This location operates with temperatures above 300˚C and a flue gas density of $+/-0.53kg/m^3$ of which the ash content is $0.15kg/m^3$. Therefore the results can be compromised due to the high fly ash content. The high temperature requires cooling and therefore a cooler was used as per the required application.

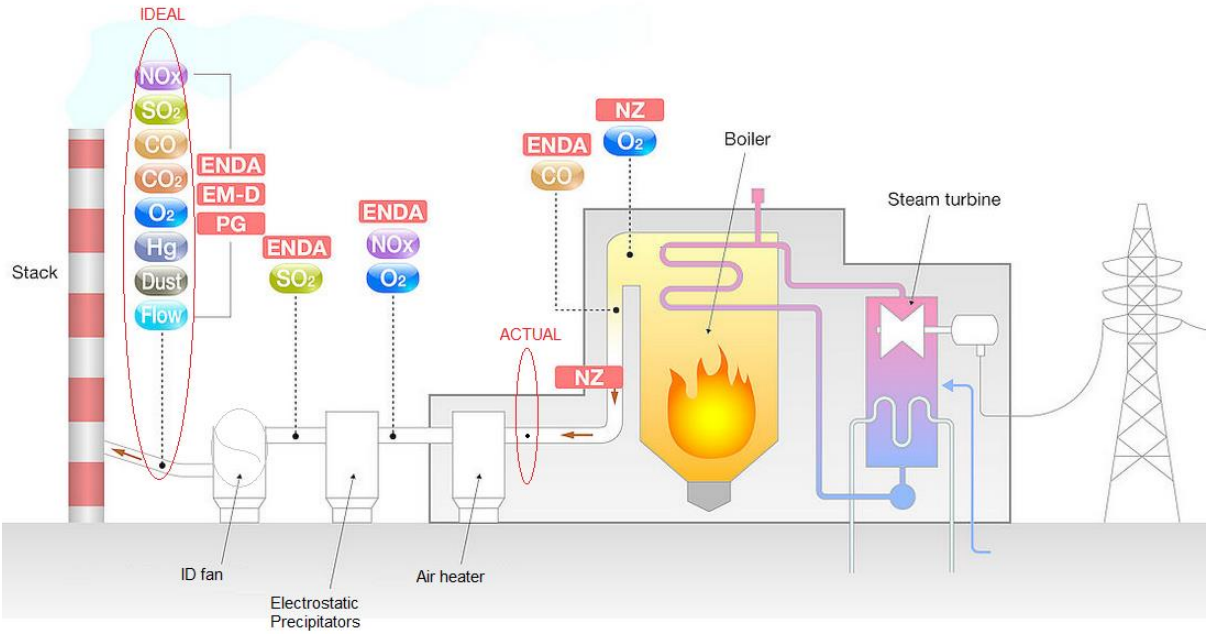

Figure 5.19: Flue gas composition measurement location

The estimated oxygen showed a 0.52% (v/v) difference in comparison to the measured oxygen. The measured carbon dioxide was 0.21% (v/v) lower than the estimated value. The sulphur dioxide showed a 0.1% (v/v) difference, but when comparing a normalised measurement at 10% oxygen the error was 0.04% (v/v). This difference could have been caused by the coal composition method that was followed. Coal samples were collected every 30 minutes at the feeders, but the samples were combined as Test sample for analysis. This poses the risk of not identifying the fluctuation in sulphur content over the period of four hours, which then also introduces a form of error by method. The same can be argued for the difference between the measured and estimated carbon dioxide. The estimated moisture was 4.62%, and the measured value was 4.49%, which showed good correlation. The difference in the moisture could also be affected by the location and the method used for measurement. The HORIBA analyser was already connected to the matrix, therefore duct measurements were taken for the moisture. Two ports were available and therefore the traverse measurement was compromised and the stratification could have influenced the readings. The measured values were used as input parameters instead of the simulated values. Although samples of coal were taken every 30 minutes during the test the samples were mixed for ultimate analysis for the specific load test (99% MCR, 80% MCR, and 68% MCR) which also introduced a form of error when the coal composition was estimated. The sulphur fluctuates and therefore ideally each 30 minute sample should have been evaluated for sulphur content to get a correct average for the four hours.

Air heater air flow

The same approach was followed as in the first tests, where the secondary air flow to the burners was used as inlet air flow for the simulation model. This method considers the sum of the total measured flow from twenty venturi ducts, where flow to each of the four burner corners for five levels of the boiler are measured. This total is divided by two to find the secondary air flow per air heater.

Air heater gas flow

The gas flow was measured using the measured velocity, density and flow area, which was then converted to mass flow. The method of estimating the flue gas flow through the mass

balance was also used. A 24% error existed between the measured and calculated values. For the 80% MCR and 68% MCR conditions the errors were 2.4% and 2.6%, which shows that the measured value for the 99% MCR condition was unreliable. Based on this, the simulation was done using the calculated value of 283 kg/s. This value still proved to not be accurate based on the explanation from Section 5.7 where a 17.7% error was identified.

Differential pressures
The FD fan discharge pressure was used as the inlet pressure and the cross over duct outlet pressure was used as the pressure after the air heater. This gave a differential pressure across the air heater for the air side of 1.21kPa. The differential pressure calculated by the VBA RAH model had an error of 36.1% below this. The gas side had an error of 14.6% less than the measured value. The fact that high differential pressures were measured confirms the condition of fouled element packs.

Habbitts (1998) and De Klerk (2001) also experienced similar findings where the estimated differential pressures showed a 30% error. Although the recently developed VBA RAH model calculates dew point related fouling conditions, it still does not take the fouling into consideration when the model estimates pressure drop across the element packs. This is an area that should be focused on for further research. An important fact to take into consideration is that the HC11 element profiles were designed to match the thermal properties of the 2.78DU type, but the hydraulic component was not taken into account. As mentioned in the previous section, Table C6 in Appendix C, is a summary of the results for the inlet and outlet temperatures along with the FD fan current and differential pressure for the condition before the installation and after the installation for each unit. When the air heater experiences fouling the load loss usually starts with increased differential pressures and FD and ID fan capacity. The HC11 packs do not benefit this condition. To compare the effect of both the HC11 and 2.78DU element packs, the OEM (Original Equipment Manufacturer) was requested to simulate the same conditions for verification purposes. These results are discussed in section 5.4.

Fluid Properties
For these tests the inlet density for flue gas was measured, and in comparison to the simulated value a 3.32% error existed. The density at the inlet between the VBA RAH and RAH models had a 0.37% difference. The fluid properties for the inlet and outlet heat capacity and velocity of each stream were calculated from both simulation models. The air inlet density, flue gas inlet heat capacity and air inlet heat capacity were identical. The density for the flue gas at the inlet had an error of 0.37% and the flue gas velocities at the inlet for flue gas had an error of 5.64%. The air inlet velocity varied by 2%. The outlet velocities had a greater error due to the outlet pressure being different for the simulations from the two models. The velocity is calculated in the simulation process uses the mass flow per unit area, divided by density of the fluid (flue gas or air) to estimate the velocity of the fluid. The calculated density is based on the average outlet temperature and pressure. With a difference in both the outlet temperature and pressure between the two models, a difference can be expected for the velocities estimated at the outlet of the air heater.

Energy Exchange
The VBA RAH model showed a result of 37.87 MW energy lost and 38.38 MW energy gained. This means the result is accurate with regard to the energy balance. The RAH model had an energy exchange of 36.72 MW lost and a 36.64 MW gained, which is also accurate. The error between the two models is due to the difference in outlet temperatures. When comparing the

two tests (preliminary and final), the second test seems to show less heat transfer occurring for the full load condition.

The detailed discussion for the 80%MCR results of Data Set 2 can be found in Appendix C4. Those results are in line with the results for maximum and minimum load conditions as discussed here.

5.3.2 Air heater performance results vs. VBA RAH simulated results at 465 MW (68% MCR)

For the 68% MCR load conditions, the plant readings and the simulated readings were combined for the metal and fluid temperatures to show where they operated. With previous tests the signals operated in the same regions, but for this load condition a large difference for the cold end layer temperature correlations were evident. Figure C9 (Appendix C) is a representation of this comparison. Figure 5.20 shows the measured and simulated metal temperatures for each layer, where the solid lines indicates the simulated profiles and the dashed lines illustrates the profile for the measured temperatures.

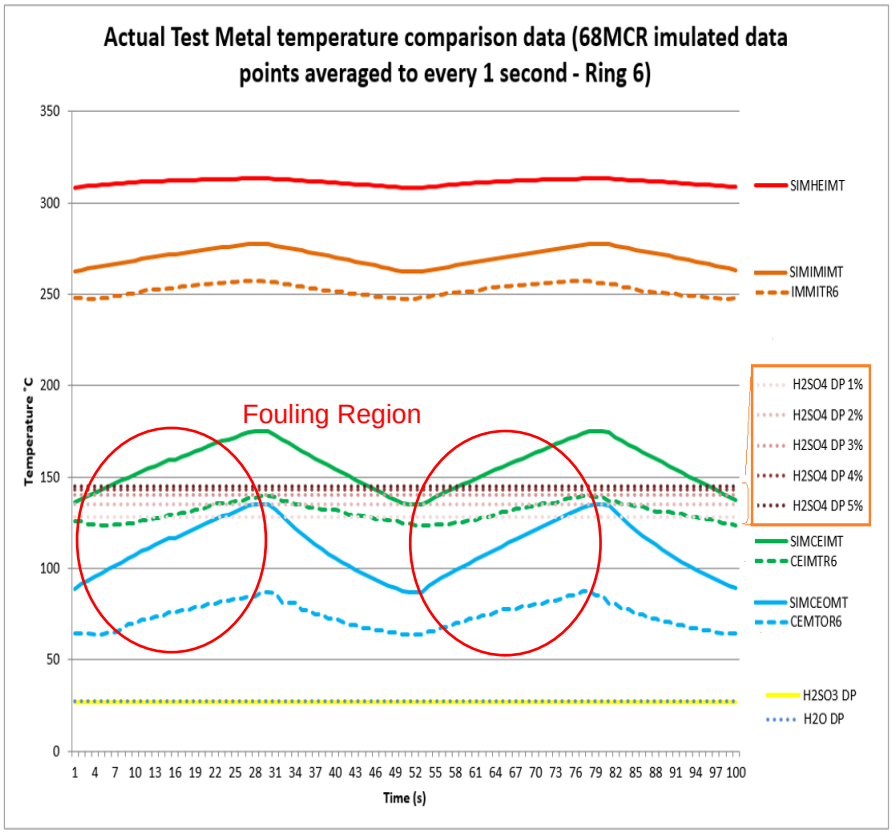

Tag name	Description
SIMFITHE	Simulation Fluid Inlet Temperature Hot End
SIMIFIT	Simulation Intermediate Fluid Inlet Temperature
SIMCEIFT	Simulation Cold End Inlet Fluid Temperature
SIMCEOFT	Simulation Cold End Outlet Fluid Temperature
SIMHEIMT	Simulation Hot End Inlet Metal Temperature
SIMIMIMT	Simulation Intermediate Inlet Metal Temperature
SIMCEIMT	Simulation Cold End Inlet Metal Temperature
SIMCEOMT	Simulation Cold End Outlet Metal Temperature
HEIMTR6	Measured Hot End Inlet Metal Temperature Ring 6
IMMITR6	Measured Intermediate Inlet Metal Temperature Ring 6
CEIMTR6	Measured Cold End Inlet Metal Temperature Ring 6
CEMTOR6	Measured Cold End Outlet Metal Temperature Ring 6
CEOFTR6	Measured Cold End Outlet Fluid Temperature Ring 6
CEIFTR6	Measured Cold End Inlet Fluid Temperature Ring 6
IMFITR6	Measured Intermediate Fluid Inlet Temperature Ring 6
HEFIR6	Measured Hot End Fluid Inlet Temperature Ring 6
HEFIR6	Measured Hot End Fluid Inlet Temperature Ring 6
H2SO4 DP 1%	Sulphuric Acid Dew Point with 1% of SO_2 converted to SO_3
H2SO4 DP 2%	Sulphuric Acid Dew Point with 2% of SO_2 converted to SO_3
H2SO4 DP 3%	Sulphuric Acid Dew Point with 3% of SO_2 converted to SO_3
H2SO4 DP 4%	Sulphuric Acid Dew Point with 4% of SO_2 converted to SO_3
H2SO4 DP 5%	Sulphuric Acid Dew Point with 5% of SO_2 converted to SO_3
H2SO3 DP	Sulphurous Acid Dew Point
H20 DP	Moisture Dew Point

Figure 5.20: Data comparison for ring 6 Metal temperatures for the 68% MCR pre-test condition.

The fluid temperatures again showed poor correlation, but the measured fluid temperatures showed better correlation with the measured metal temperas. This is a definite sign of thermal inertial affects that influenced the measurements. Figure 5.21 is an illustration of the measured and simulated fluid temperatures, where the solid lines indicates the measured profiles and the dashed lines illustrates the profile for the simulated temperatures.

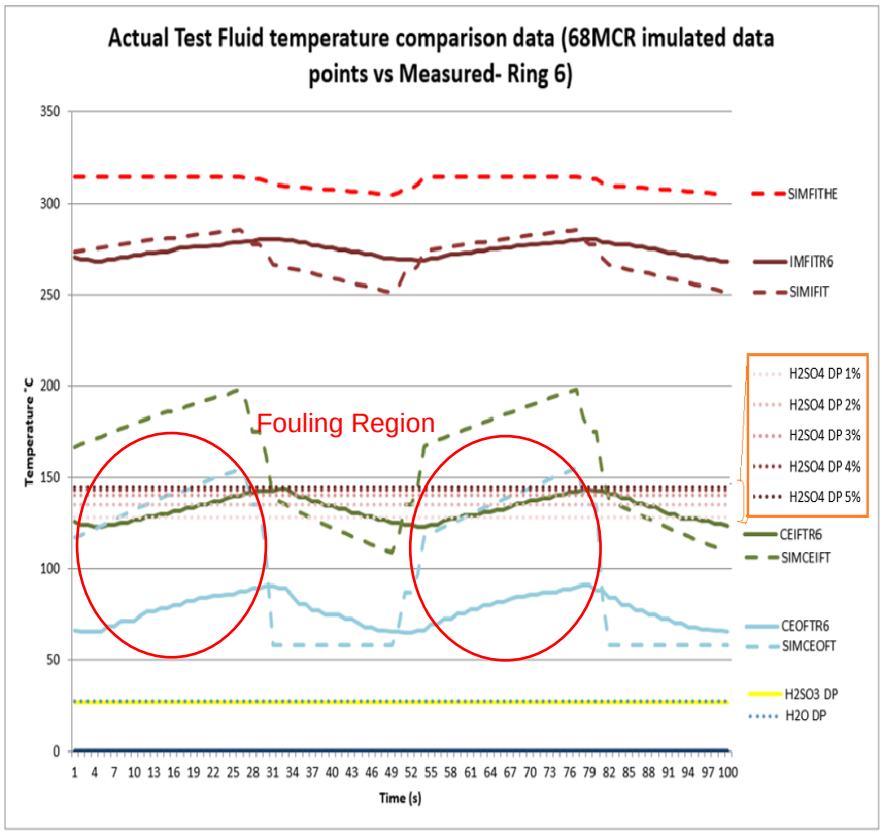

Tag name	Description
SIMFITHE	Simulation Fluid Inlet Temperature Hot End
SIMIFIT	Simulation Intermediate Fluid Inlet Temperature
SIMCEIFT	Simulation Cold End Inlet Fluid Temperature
SIMCEOFT	Simulation Cold End Outlet Fluid Temperature
SIMHEIMT	Simulation Hot End Inlet Metal Temperature
SIMIMIMT	Simulation Intermediate Inlet Metal Temperature
SIMCEIMT	Simulation Cold End Inlet Metal Temperature
SIMCEOMT	Simulation Cold End Outlet Metal Temperature
HEIMTR6	Measured Hot End Inlet Metal Temperature Ring 6
IMMITR6	Measured Intermediate Inlet Metal Temperature Ring 6
CEIMTR6	Measured Cold End Inlet Metal Temperature Ring 6
CEMTOR6	Measured Cold End Outlet Metal Temperature Ring 6
CEOFTR6	Measured Cold End Outlet Fluid Temperature Ring 6
CEIFTR6	Measured Cold End Inlet Fluid Temperature Ring 6
IMFITR6	Measured Intermediate Fluid Inlet Temperature Ring 6
HEFIR6	Measured Hot End Fluid Inlet Temperature Ring 6
HEFIR6	Measured Hot End Fluid Inlet Temperature Ring 6
H2SO4 DP 1%	Sulphuric Acid Dew Point with 1% of SO_2 converted to SO_3
H2SO4 DP 2%	Sulphuric Acid Dew Point with 2% of SO_2 converted to SO_3
H2SO4 DP 3%	Sulphuric Acid Dew Point with 3% of SO_2 converted to SO_3
H2SO4 DP 4%	Sulphuric Acid Dew Point with 4% of SO_2 converted to SO_3
H2SO4 DP 5%	Sulphuric Acid Dew Point with 5% of SO_2 converted to SO_3
H2SO3 DP	Sulphurous Acid Dew Point
H20 DP	Moisture Dew Point

Figure 5.21: Data comparison for ring 6 fluid temperatures for the 68% MCR pre-test condition.

As indicated in Figures 5.20 and 5.21 for the lower load condition, the rate of change for the simulation indicated a higher rate of temperature change in comparison to the measured values. This could be due to the fouled element packs that affects the heat transfer mechanisms more at lower loads. For lower loads the flow rate is less, and with ash blocking flow in the open spaces of the elements, less heat is transferred in fouled areas. With lower flows more settling of ash also occurs due to reduced amounts of energy to remove the deposits in the fouled areas, which can affect the actual measurements negatively. As mentioned from previously results (Figure 5.11) it is expected that the thermal inertia changes the rate of heat transfer, due to:

- Wear protection at the area where the thermocouples are installed.
- Accumulation of ash.
- Contact resistance.
- Reduced flow due to obstructions in the flow path.

With lower loads this condition deteriorates. The thermal inertia of a material is defined as the square root of the product of the material's bulk thermal conductivity and volumetric heat capacity, where the latter is the product of density and specific heat capacity. Equation 5.4 is an illustration of the theoretical approach to determine thermal inertia.

$$I = \sqrt{kpc} \qquad (5.4)$$

Where:

k - is thermal conductivity, with unit $W \cdot m^{-1} \cdot K^{-1}$

p - is density, with unit $kg \cdot m^{-3}$

c - is specific heat capacity, with unit $J \cdot kg^{-1} \cdot K^{-1}$

I - SI units of thermal inertia of $J \cdot m^{-2} \cdot K^{-1} \cdot s^{-1/2}$

In the case where ash accumulates in open spaces of the element packs, the bulk density of a conductive medium starts to increase and gets added to the existing conducting material. With lower flows bulk densities of ash in these open spaces will increase, due to the fact that less energy is available to force the deposit out of the spaces between the pack. The lower velocities also incur lower erosion rates, which in essence also reduce the removal of deposits on the elements. With ineffective soot blowing not removing the ash deposits, moisture is added to the ash. This moisture from the soot blowing reacts with the ash causing precipitation to elements in areas where low flows are experienced. These areas can experience temperatures below the sulphurous acid and moisture dew point temperatures due to the fact that less heat transfer occurs. In the case where cold air passes through a pack that has ash accumulated in some of the spaces, a cooling effect can be experienced causing the moisture and ash mixture to adhere to the plate. After the cold stream a hot flue gas stream passes through, which then heats up the plate with the fouled deposit adhered to it. This cycle continues and eventually hardens the deposits to the extent where high pressure washing is then required to remove these deposits. With lower loads the flows also decrease, which means that less energy is available to blow and erode these deposits out. The higher flows at higher loads also create increased velocities for the erosive fly ash, therefore ideally removing some of these fouled deposits from the cold end. Therefore this condition can cause a greater deviation in measured temperatures, when compared to theoretical calculated values. These effects are not taken into account for the modelling of the VBA RAH model. For Ring 6 both the measured fluid (flue gas) temperatures for the cold end and the simulated temperatures operated below the dew point temperatures for sulphuric acid.

The results showed that the inlet cold end metal temperatures did not operate below the sulphuric acid dew point temperature for 1% conversion of SO_2 to SO_3. The 2% conversion of SO_2 to SO_3, experienced a 5.88% exposure to the sulphuric acid dew point temperatures at the inlet of the cold end metal temperatures. For a 5% conversion, 25.82% of the inlet cold end metal temperatures operated below the sulphuric acid dew point temperature. The measured inlet cold end metal temperatures were exposed for 57.14% and complete exposure to sulphuric acid dew point temperatures for the cases of 3% to 5% SO_2 to SO_3 conversion. As expected the temperatures never reach the sulphurous acid dew point temperatures and moisture dew point temperatures during normal operation. The results are summarised in Table 5.9. It is clear that for lower loads dew point related fouling conditions are less likely to occur based on the fact that higher operating temperatures for the air heater flue gas outlet condition occurs. It is suspected that this is due to lower rates of heat transfer that occurs at lower load conditions. But if the leakage increase at lower load excessive fouling can still be evident at outlet of the third layer, where the cold air stream pass through underneath the seals to form part of the flue gas stream, exiting the steal matrix. When the streams cold air stream mix with the flue gas leaving the steel matrix, the outlet of the steel matrix experience a cooling effect, which can still allow temperatures to reduce below the sulphuric acid dew point temperatures.

Table 5.9: Sulphuric acid formation time for the simulated and measured metal- and fluid temperatures (68%MCR).

Conversion SO_2 to SO_3	Inlet Cold end metal temperature exposure to sulphuric acid dew point temperatures	Conversion SO_2 to SO_3	Measured cold end inlet metal temperatures operating below the sulphuric acid dew point temperatures
1%	0%	1%	57,14%%
2%	5,88%	3%	100%
5%	25,28%	5%	100%

The actual conversion of sulphur dioxide to sulphur trioxide was again estimated. Considering the measurements for SO_2 at 68% MCR, a value of 0.178% by volume of SO_2 in the flue gas was measured, this value relate to a 10% O_2 normalised measurement. For a 6% O_2 normalised measurement the value was measured to be 0.24% SO_2. Using the 0.178% of measured SO_2, means that 1% to 5% conversion will give a range of 0.00178% to 0.0089% of SO_3 contained in flue gas. The results from the mass and energy balance indicated a 0.12% volume of SO_2. Following Table 5.7 indicating the results for SO_3 content in flue gas for varying sulphur content of coal concluded by Ganapathy (1989), the amount of SO_3 in the flue gas would be based on a 1.15% (as received) sulphur in coal. According to the table the amount would be 10.14 ppm SO_3 (0.0010%) when using linear interpolation. The amount measured from the 68% MCR Data set 2 test the value was 0.178% (at 10% normalization) for SO_2, which shows the estimated and measured values are still close to each other. If the 6% O_2 normalised value of 0.24% SO_2 was considered it would have given a range of 0.0024 to 0.012% of SO_3 formed in the flue gas. Based on the table estimation (0.0010% SO_3) and the measured values (0.0178% $SO_{2\ @10\%}$ & 0.0024% $SO_{2\ @\ 6\%}$) result, the assumption that almost 1% of SO_2 converted to SO_3 holds, which further confirms that the cold end was also experiencing dew point related fouling for the 68% MCR conditions. Table 5.10 is a summary of the above mentioned results.

Table 5.10: Sulphuric acid formation time for the simulated and measured metal- and fluid temperatures (68%MCR).

	Measured SO_2 @ 10% normalised	Measured SO_2 @ 6% normalised	Simulated SO_2
SO_2	0,178%	0,24%	0,12%
1% SO_2 converted to SO_3	0,00178%	0,00240%	
5% SO_2 converted to SO_3	0,00890%	0,01200%	
Ganapathy Table 5.6			
Based on 1,43% Sulphur in coal (As received)	0,0010%		
Conclusion	Based on the Table 5.7 and the measured SO_2 it seems that +/-1% of SO_3 formed.		

Figure 5.22 is a representation of the sulphuric acid dew point temperatures from 1% to 5% conversion of SO_2 to SO_3 for the conditions measured during the 68% MCR conditions. Based on the conclusion that +/- 1% SO_3 formed in the flue gas, a critical temperature of 129.8 ˚C were identified for sulphuric acid dew point related fouling.

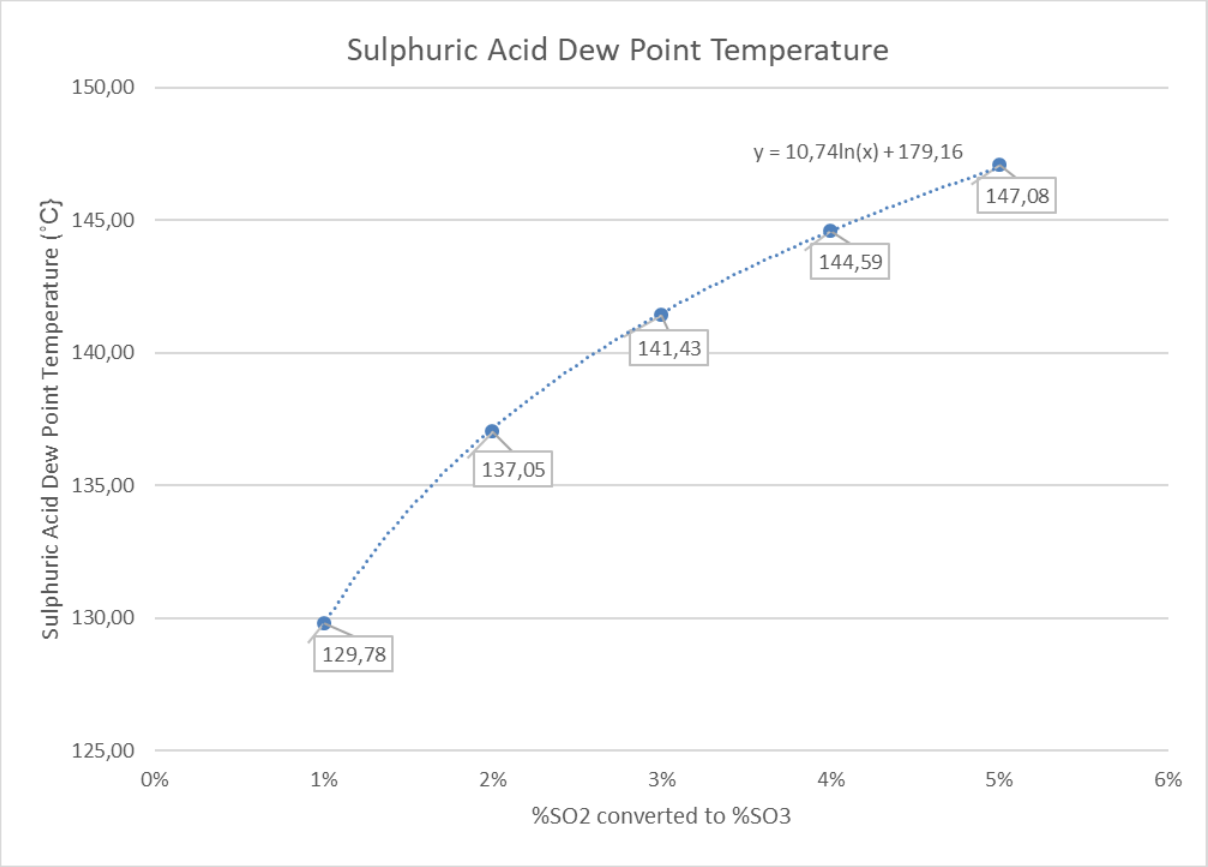

Figure 5.22: Sulphuric acid dew point temperatures for 1% to 5% SO_2 to SO_3 conversion for 68% MCR.

Assuming 1% of SO_2 converted to SO_3 a large portion of the cold end layer will be experiencing dew point related fouling. Using the 32 x 307 (Figure5.15) size matrix generated in the simulation, which contain the final set of cold end layer metal temperatures for the full height of the third layer, this amount can be estimated. For one gas stream a 32 x 84 subset of temperatures of the total matrix exist. For this subset the metal temperature will be exposed for 37.35% of the length and time step. The cold end element packs will experience sulphuric acid dew point conditions for 10.22 seconds of the total 27.36 seconds of the flue gas stream. These results indicate that dew point related fouling is more likely to occur at high loads.

The impact of a rise in differential pressure was also evaluated for the 68% MCR load condition, which can be seen in Figure 5.23.The same approach was used as the 99%MCR condition. This results showed that the increase in differential pressure from 0kPa to 2.5kPa varies the temperature for sulphuric acid dew point temperatures with less 1˚C. The result was also consistent with the 99% MCR and 80% MCR rate of temperature change. The same assumption holds as for the other load conditions, that a pressure rise from fouling will not deteriorate the sulphurous- and sulphuric acid dew point temperature by a large extent during normal operation, but the moisture dew point can rise with +/-6 ˚C. The air heater still does not operate within these ranges, only during light up and shut down conditions when transient states are experienced.

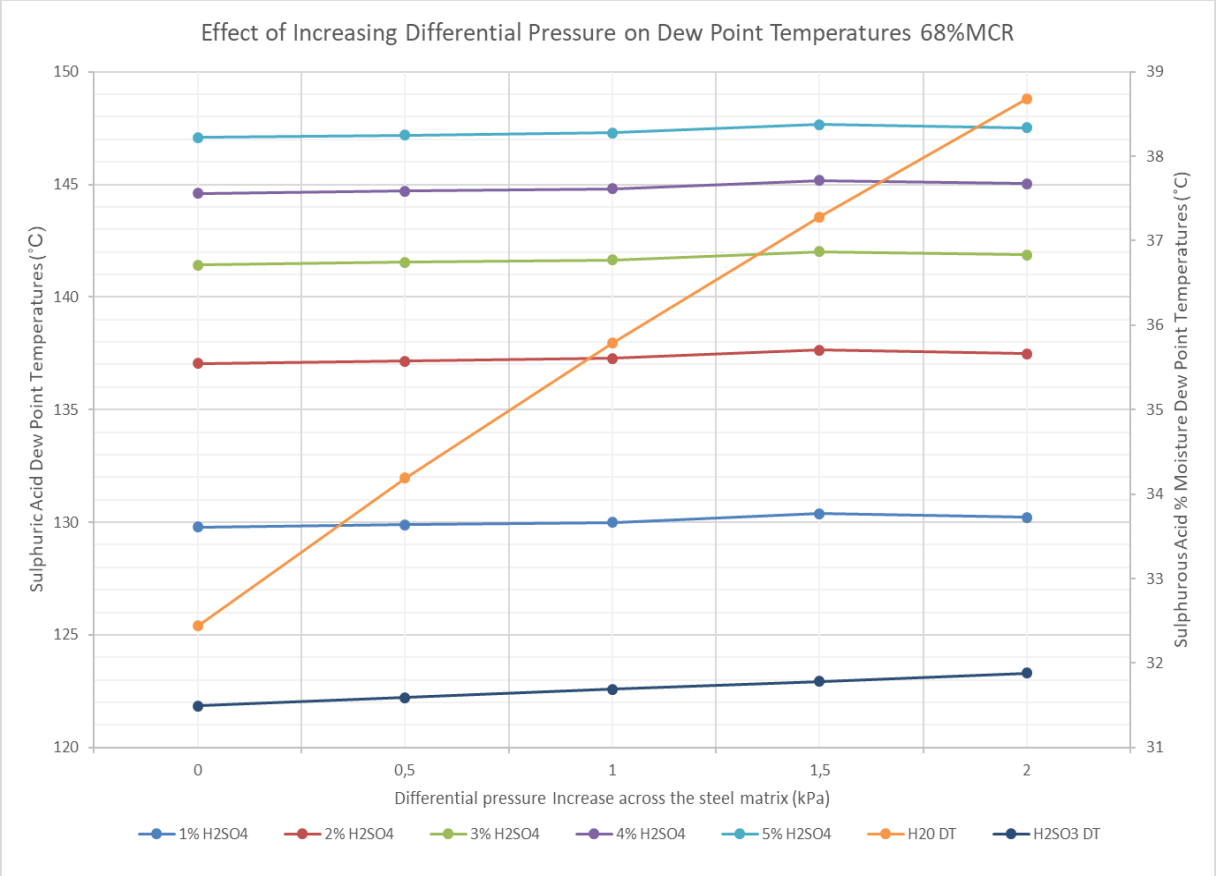

Figure 5.23: Effect of increasing differential pressures on dew point temperatures for 68% MCR.

Table C9 in Appendix C shows the results from the 68% MCR load actual test conducted from 00:00 – 04:00 on 26/02/2020.

Air heater gas outlet temperatures

The average of the measured temperature of 123˚C shows a 0.56% deviation from the VBA RAH result of 123.69˚C. The results were more accurate than the 80% MCR and 99% MCR, due to the fact that the flue gas flow was more accurate than the measured values for the other two tests. The same input parameters were simulated for the RAH (GB de Klerk) model and an error of 2.05% was evident. As with the previous tests, the results again showed that the simulation models tend to overestimate the outlet temperature at higher loads.

Air heater air outlet temperatures

A 4.9% error occurred between the VBA RAH model and the measured value. The error between the VBA RAH and the RAH (GB de Klerk) model was 1.04%. The air temperature showed that the simulation models overestimate the outlet temperature by a margin of 10 ˚C to 15 ˚C. The VBA RAH model is mostly one dimensional and does not consider the impact of factors mentioned in Figure 5.11. Therefore overestimation of outlet temperatures can be expected. In addition, the same principle holds as with the other load conditions, that the round off error in the iterative process either over estimate or under estimate the average temperatures used to calculate the fluid properties. This process influences the final temperature estimation.

Cold end metal temperatures

The comparison between the VBA RAH maximum plate temperatures and the measured maximum plate temperature indicated a 25.77% error. The minimum VBA RAH metal temperature was found to be 36.89% more than the measured value. As mentioned in the 80% and 99% MCR results discussion, the factors mentioned in Figure 5.11 affected the measurements. When comparing the measured value and the RAH (GB de Klerk) value, the simulated result again showed unrealistic values. The minimum metal temperatures for the simulated values and for the measured values correlate, which is ideal when the dew point related fouling areas are identified.

Flue gas properties
The estimated oxygen showed 0.1% (v/v) difference in comparison to the measured oxygen. The measured carbon dioxide was 0.11% (v/v) by volume lower than the estimated value. The sulphur dioxide measurement was 0.12 % (v/v) higher when using the 6% O_2 normalization correction factor, and a difference of 0.6% (v/v) when using an O_2 normalization correction factor of 10%. The estimated moisture was 5.4% (v/v), and the measured value was 7.41% (v/v). When the moisture is compared to the stack reading of 5.15 % (v/v) a better correlation was found. The same reasoning for errors as with the previous tests apply to the 68% MCR conditions.

Air heater gas flow
A 2.61% error existed between the measured and calculated value for the 68% MCR test. The simulation was done using the measured value of value of 237.65 kg/s.

Differential pressures
The differential pressure across the air for the air side was 0.68kPa. The differential pressure calculated by the VBA RAH model had an error of 22.06%. The gas side had an error of 25.55% between the measured and the VBA RAH result. As mentioned previously, the fact that high differential pressures were measured confirms the condition of fouled element packs.

Fluid Properties
For the 68% MCR actual test results the inlet density for flue gas was measured, and in comparison to the simulated value a 4.28% difference existed. The flue gas density at the inlet between the VBA RAH and RAH (De Klerk) model had a 0.04% difference. The air inlet density, flue gas inlet heat capacity and air inlet heat capacity were identical with no error. The flue gas velocities at the inlet for flue gas had a difference of 0.19 m/s. The air inlet velocity varied with 0.01 m/s difference. The outlet fluid properties had a greater error due to the outlet temperature and pressure affecting the estimated density, which was used to calculate the velocity from the mass flow velocity as explained in Appendix A3.

Energy Exchange
For the VBA RAH model the result (at 68% MCR) showed a result of 24.91MW energy lost and 25.70MW energy gain with a difference of less than 1MW on energy exchange. The RAH (GB de Klerk) model had an energy exchange of 25.15MW lost and a 24.95MW gained, which is also an estimation with a difference of less than 1MW. The error between the two models is due to the difference in outlet temperatures by the two simulation models.

5.3.3 Summary of Data Set 2 Results

For the 99% MCR predicted metal temperatures, 90% - 100% of the third layer metal surfaces were exposed to sulphuric acid dew point conditions for the flue gas stream duration. The measured values indicated a 100% exposure to sulphuric acid dew point conditions in the third layer, for 1% - 5% conversion of SO_2 to SO_3. Due to the fact that this will occur for every annular division (ring), the cold end element packs will experience condensation for +/-25 seconds of the total 27 seconds duration of exposure to the flue gas stream.

For the 80% MCR predicted metal temperatures, the full discussion of these results can be found in Appendix C4. An 81%-100% of the third layer element metal surfaces were exposed to sulphuric acid dew point conditions for the flue gas stream duration. The measured values indicated a 100% exposure to sulphuric acid dew point conditions in the third layer, for 1% - 5% conversion of SO_2 to SO_3. It can be deduced that the cold end packs will experience sulphuric acid dew point conditions for +/-22 seconds of the total 27 seconds of exposure to the flue gas stream.

For the 68% MCR predicted metal temperatures, 37%-100% of the third layer element metal surfaces were exposed to sulphuric acid dew point conditions. The measured values indicated a 46-100% exposure to sulphuric acid dew point conditions in the third layer, for 1% - 5% conversion of SO2 to SO3. It can be deduced that the cold end packs will experience sulphuric acid dew point conditions for 10 seconds of the total 27 seconds of exposure to the flue gas stream. Therefore it is clear that the air heater operates largely in these undesirable temperature ranges, and more specifically in the third layer.

For all three conditions the estimation of conversion from SO_2 to SO_3 was +/-1%. This showed that the following critical temperatures were identified to cause possible dew point related fouling during normal operation: 99%MCR - 133˚C, 80%MCR - 132 ˚C and 68%MCR - 129˚C.

Comparing the measured values to the simulated values, it was clear that the correlation was not ideal, and some forms of error existed. These errors were introduced through unaccounted-for thermal inertia, contact resistance, ash accumulation and incorrect flue gas flow measurements, as well as the use of incorrect measuring equipment for the application (Figure 5.11). Another form of error was also introduced in the measurement of flue gas properties, due to the location of the Horiba analyser, which was exposed to excessive ash conditions that can influence the readings.

The mass balance method used to find the flue gas composition was also verified and was not found to be accurate. The model was then compared to the products of combustion model used in Eskom which was tested by the North West University as a sound method for the application of mass balance. The VBA RAH model mass balance results correlated well with the Eskom products of combustion model. Therefore the location of measurement and high ash content in the flue gas affected the measured results for the flue gas composition. The method of coal sampling was not as successful. Ideally all samples had to be analysed individually for improved accuracy, instead of combining the samples for each load condition to get an average coal composition.

Considering the previous research outcomes mentioned in Chapter 2, the following was observed. The pressure drop error on average was found to be 30.8% between the three load test

results. This correlated with the 30% error found in pressure drop calculations estimated by Habbitts (1998). The error is a result of external factors, the effect of leakage on pressure drop and fouling conditions that cause increases in pressure drops. This is still an area of improvement for the simulation models. Considering the list of guide points to reduce the occurrence of air heater fouling from Mabena (2003), the research also contributed to these guidelines. Firstly, the ideal operating range for the excess oxygen in the flue gas to reduce the deposition rate for sulphuric acid formation becomes an unrealistic figure due to various challenges. Increased sulphur content, air heater leakage, plant deterioration, and deteriorated Rankine cycle efficiency affected by unavailability of high pressure and low pressure steam heaters and inadequate air cooled condensing, force the boiler heat input to increase. This effect enforces higher coal flow air flow rates to the extent that the flue gas excess oxygen decreases below the allowable limit of 2.5% volumetric percentage. As difficulties are experienced for Eskom to provide the required electricity supply, the power stations are forced to maintain maximum capacity. As indicated from the results, fouling is expected to occur more with higher loads, and based on Mabena's (2003) guide lines the deposition rates also increase at lower excess oxygen levels in the flue gas. Therefore, fouling is expected to increase. Secondly, the guide suggests that the air inlet temperature should be above 45 ˚C to avoid operating the air heater cold end below the set point of 90 ˚C. This research showed that it is ideal to operate above 45°C, but the 90 ˚C value does not protect the air heater from experiencing sulphuric acid dew point fouling, based on the ranges estimated from the three test load conditions.

Thirdly the guidelines refer to low pressure washing to be done after a tube leak, but based on the research it becomes evident that dew point related fouling will increase with increased levels of moisture in flue gas, which will cause severe blockage during tube leak conditions and low pressure washing will not be adequate. A combination of high pressure washing (600 bar for 96 hours) from the bottom and low pressure flushing (8 bar for 6 hours) from the top is recommended to be more effective to remove the deposits. This method was tested and proven to be successful without damaging the pack profile plates. This becomes a critical activity to be included in cyclic maintenance programs. The study of the effectiveness of this cleaning method is recommended for future research. Fourthly the research from Bailey (1999) showed that higher fouling rates will occur on fouled surfaces. If tube leaks occur the fouling rates are already increased and if only low pressure washing is used, the fouled surfaces are not cleaned effectively. Therefore, the air heater will tend to block at higher rates when placed back in operation after low pressure washing. The research results also correlated with the results from D'Agostini et al (1989) and Raask (1963), where the condensation rate was found to be higher at higher loads. This was based on the reduced surface temperatures at higher loads which ultimately correlated with higher condensation rates (Figure 2.12 and 2.13).

Further validation of the VBA RAH model was done by comparing results from research conducted by Habbitts (1998) and De Klerk (2001) as discussed in Section 5.7. The VBA RAH model was successfully developed to predict the onset of dew point related fouling and provides a platform to equip system engineers with the knowledge to enhance air heater performance. The impact of air heater operating and design amendments can be simulated to evaluate the impact on overall boiler performance. Section 5.7 elaborates on the capability that the VBA RAH model has with regard to evaluating the impact that amendments to air heater parameters and design configurations have on boiler performance.

5.4 Comparison of OEM model results with RAH and VBA RAH Models

The selection of element pack profiles is one of the most important considerations when designing an air heater for specific boiler designs. The tests conducted by Caby (1996), Kumar (1998), Gruen (1998), Habbitts (1998) and De Klerk (2001) considered the element packs available at that time. There have been numerous developments over the years regarding pack profiles and coating of element packs. Figure 5.24 shows the difference between the coating, profile and plate configuration for the 2.78DU, HC11 and NF6 (enamel coated) types of element packs. Part of these developments were the HC11 pack profiles designed by the OEM for Eskom power generating plants, along with enamel coating of element packs. These design configuration changes were not tested and documented within Eskom and therefore a grey area exists regarding the performance of these packs. The OEM however has the required design information to determine the thermal performance of the HC11 element packs. This information is regarded as intellectual property of the OEM and therefore cannot be shared with Eskom. The recommendation from the OEM was to make use of the 2.78DU profiles for the simulations, due to the fact that the design information is available to Eskom and the thermal performance is expected to be similar to the HC11 profiles. In light of this recommendation, the OEM was requested to simulate the 2.78DU and HC11 profiles using the same input parameters as the actual test data for the three different load conditions.

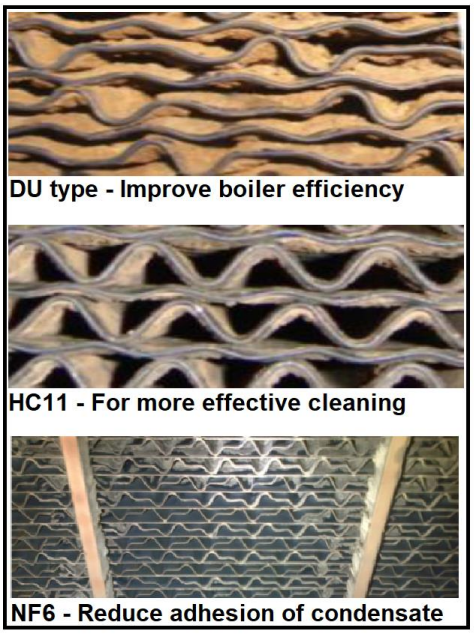

Figure 5.24: Various profile types of profiles available to industry (DU type, HC and NF6 enamel coated type).

The first temperature estimations in the simulation are usually for the flue gas stream. This is also the stream that has the chemical composition to incur dew point related fouling. The VBA-RAH and RAH model results and the OEM simulation model results for this stream were compared through considering the diluted and undiluted flue gas outlet temperatures and metal surface temperatures for the cold end. As mentioned previously one of the reasons for the deviation between the measured and the simulated (from the results in section 5.3), values could be that the performance of the installed HC11 packs is different in comparison to the 2.78DU simulation results. This effect is compared in Figure 5.25 (99% MCR input

parameters), Figure 5.26 (80% MCR input parameters) and Figure 5.27 (68% MCR input parameters). For all three cases (99% MCR, 80% MCR and 68% MCR) the results showed that the HC11 temperatures correlate with the 2.78DU temperatures.

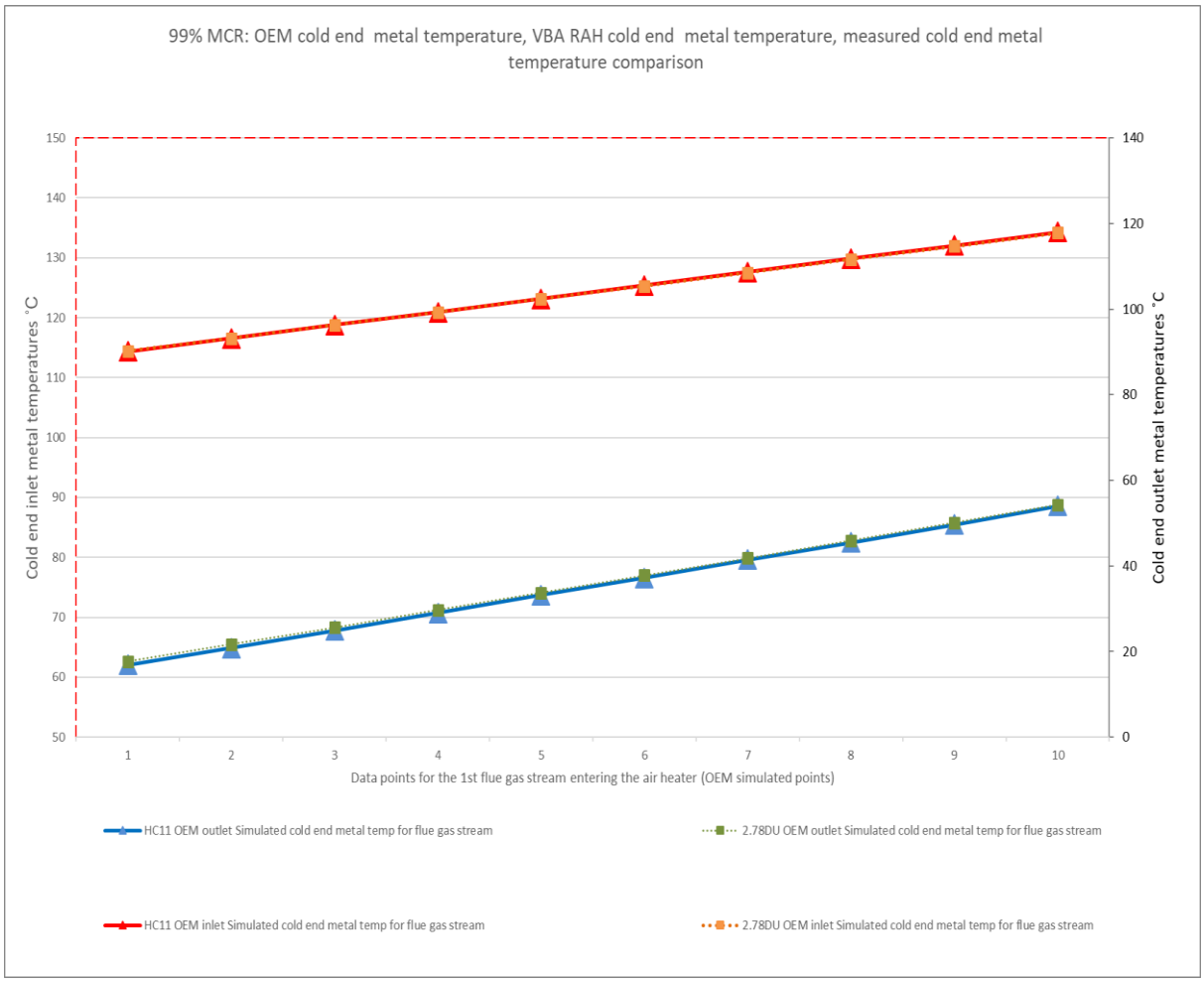

Figure 5.25: 99% MCR - OEM cold end metal temperature, inlet and outlet comparison for the HC11 and 2.78DU element profiles.

The logarithmic mean temperature difference is used to determine the temperature driving force for heat transfer in flow systems (LMTD). The LMTD was calculated for each model, along with the measured values to compare the driving forces for the three models and the measured values. For the 99% MCR results the three models had a LMTD of 40 ˚C (OEM), 39 ˚C (VBA RAH) and 41 ˚C (RAH). The measured values are estimated to be a LMTD of 54 ˚C, which means that in reality the driving force was higher than in the simulations. The product of the heat transfer coefficient, the heat transfer area and the LMTD gives the amount of heat energy exchanged in the system. Considering this, it shows that in reality the higher LMTD for the measured values implies that the heat transfer area is less (assuming the same heat transfer coefficient). This supports the likelihood of ash accumulating in the open spaces of the element packs. Although fouling is taken into consideration it seems that in reality the effect of ash accumulation in relation to the LMTD is still an area of improvement that should be investigated. Equations 5.5 and 5.6 are an illustration of the latter.

$$q = h \times A \times LMTD \tag{5.5}$$

Rearranging 5.5:

$$LMTD = q/(hA) \quad (5.6)$$

$LMTD$ - Log Mean Temperature difference
q – Exchanger heat transfer (Watts)
h - Overall heat transfer coefficient (Wm^2/K)
A - Suitable area for heat transfer (m^2)

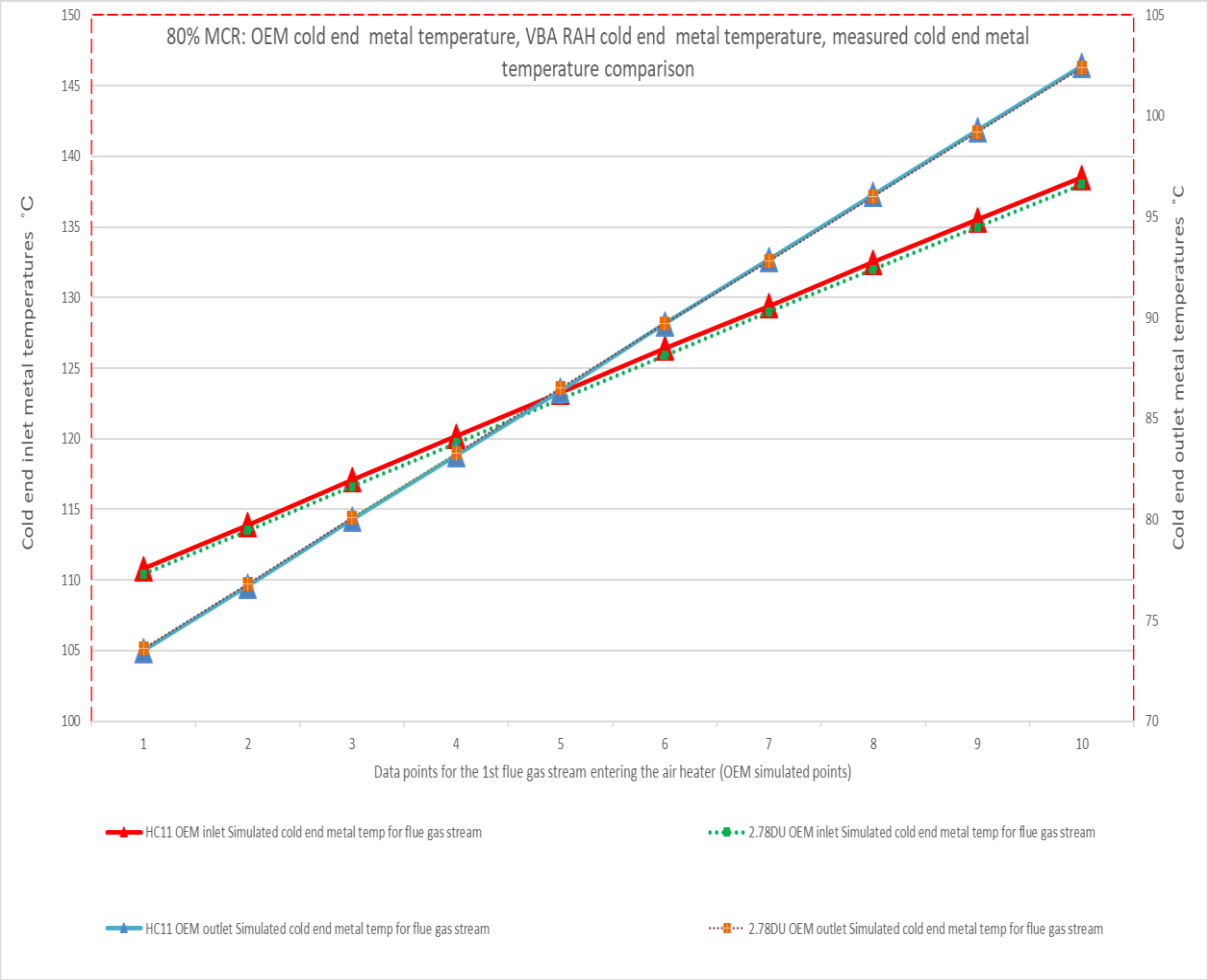

Figure 5.26: 80% MCR - OEM cold end metal temperature, inlet and outlet comparison for the HC11 and 2.78DU element profiles.

For the 80% MCR, Figure 5.26 shows how the two simulation models compare to the actual measurements. The three models had a LMTD of 34˚C (OEM), 34 ˚C (VBA RAH) and 35 ˚C (RAH). The measured values give a LMTD of 46 ˚C, which again indicates that in reality the driving force was higher than in the simulations. The same assumption can therefore be made that there is portion of unaccounted ash that restricts flow and therefore the heat transfer area is reduced.

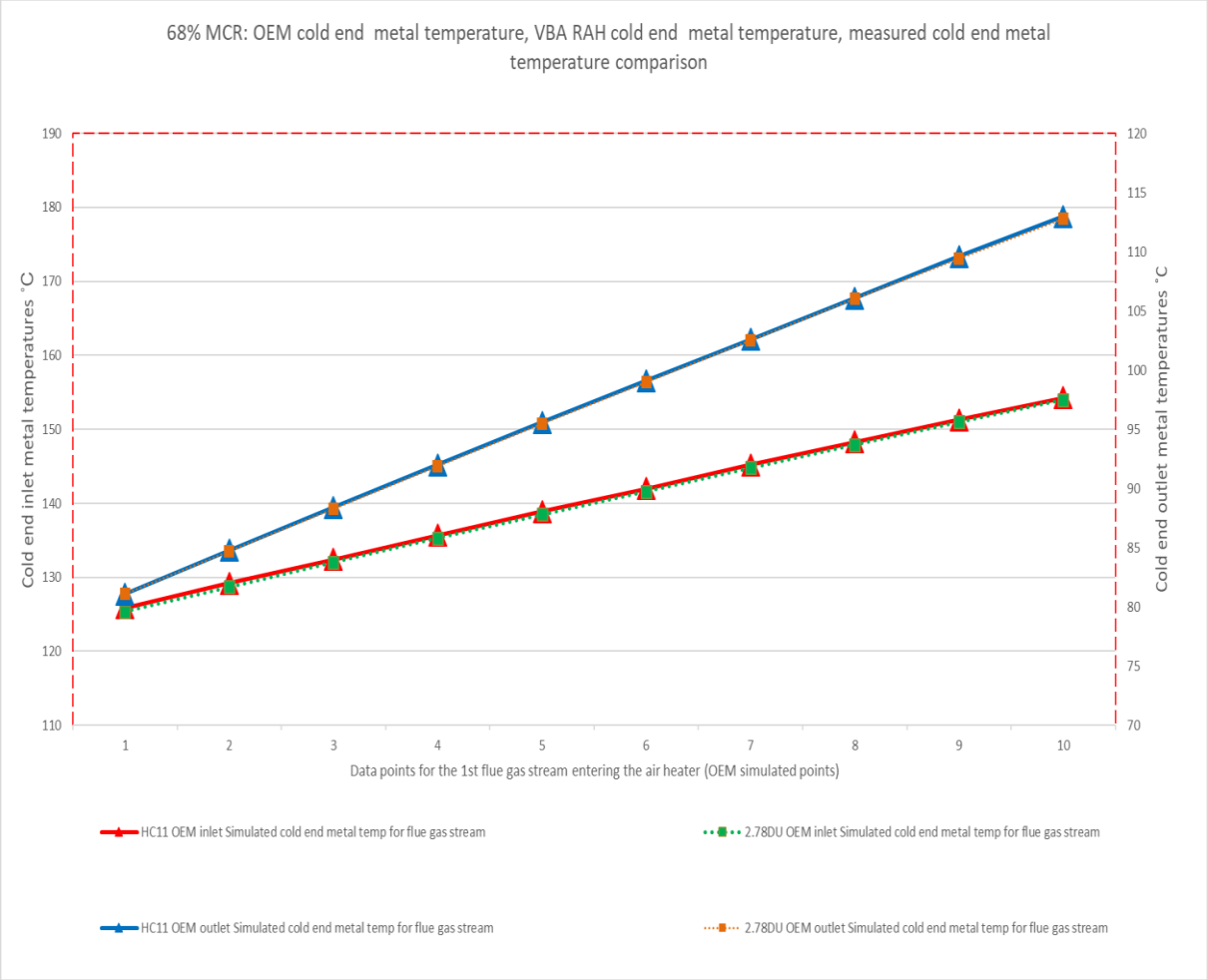

Figure 5.27: 68% MCR - OEM cold end metal temperature, inlet and outlet comparison for the HC11 and 2.78DU element profiles.

For the 68% MCR, Figure 5.27 shows how the OEM and VBA RAH models compare to the actual measurements. The three models had a LMTD of 32˚C (OEM), 32 ˚C (VBA RAH) and 35 ˚C (RAH). The measured values give a LMTD of 50 ˚C. This again shows that in reality the driving force was higher than in the simulations.

The OEM model, VBA RAH and RAH models were also compared and the fact that the OEM show a large deviation from the other two models could be due to the mathematical approach used for each model. Figures 5.28 and 5.29 illustrates the comparison of these model with regards to the undiluted (no leakage) and diluted (includes leakage) flue gas temperatures leaving the air heater. The OEM simulation model uses a method of manipulation of operating parameters to find the ideal model configuration. This model has a base design for a rotating matrix type of air heater; a rotating hood simulation requires input parameter manipulation to ensure the model provides accurate results. The VBA RAH and RAH models take the design parameters specific to a rotating hood type of air heater into account. For instance the flow area is specifically configured for the Eskom-specific design of steel matrix configuration. This takes the grease tunnel, radial and divisional plates and seal strips obstructing flow into account. The actual flow area is therefore reduced accordingly. The rotational speed is not a manipulated value, but rather the correct direct input.

The 80% MCR and 68% MCR results correlated better for both the diluted and undiluted flue gas outlet temperatures. The error in the flue gas flow estimation proved to have an effect on the results, which is also explained in section 5.7.

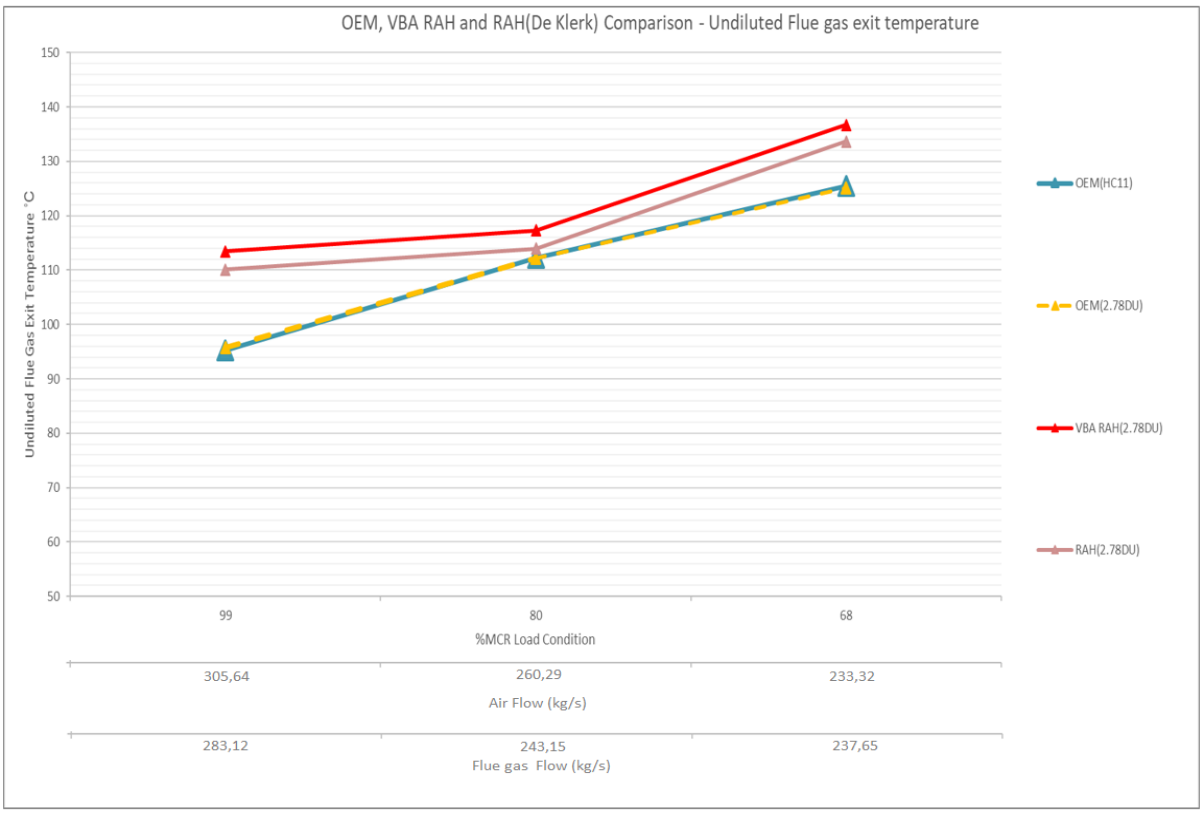

Figure 5.28: OEM, VBA RAH and RAH Comparison - Undiluted Flue gas exit temperature.

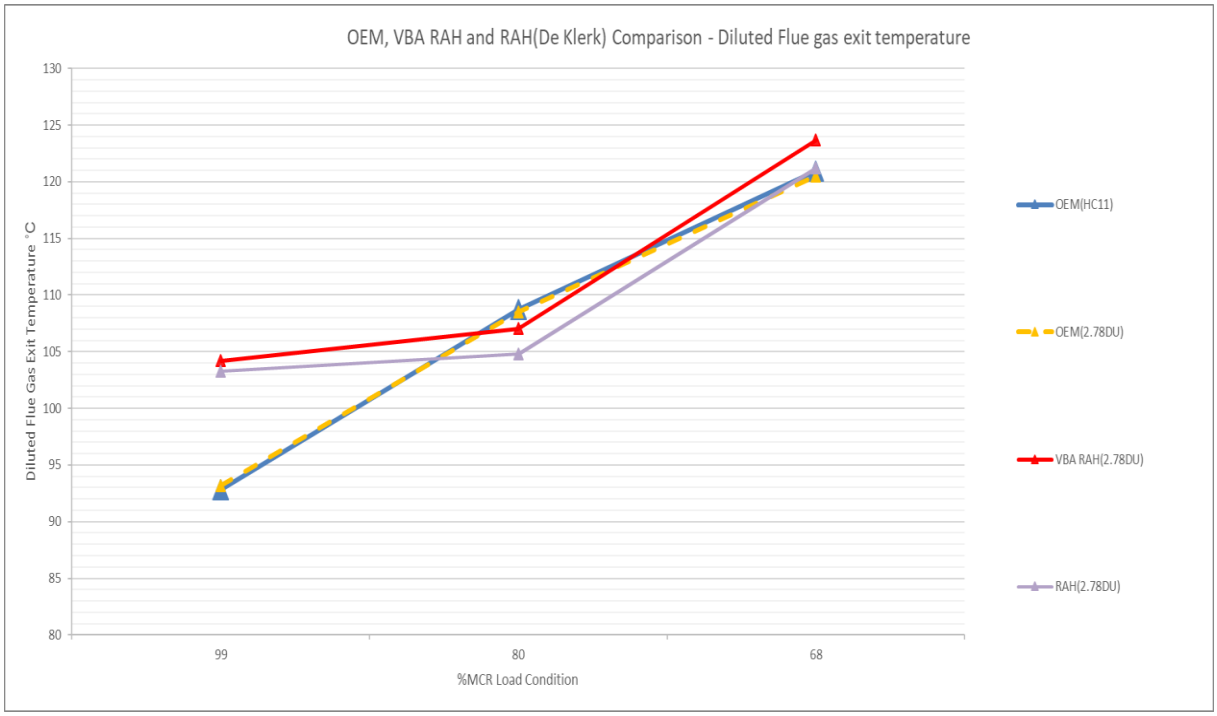

Figure 5.29: OEM, VBA RAH and RAH Comparison - Diluted Flue gas exit temperature.

5.5 VBA RAH Model Verification Using Previous Research Results

The next method elaborates on the possibility that the current pack configuration is the problem that caused large deviation between the measured and the simulated temperatures for Data set 1 and 2. The initial design pack selection for these air heaters consisted of different element pack heights. The selection was a H8 profile, with a plate thickness of 0.5mm, and a height of 1025 mm for layer one. Layer two was the same selection as layer one, but a KH11 profile with a thickness of 0.5 mm and a height of 300 mm was used for layer three. The current selection is a HC11 profile with a thickness of 0.5 mm and a height of 1100 mm for layer one and two, and the same HC11 profile and thickness for layer three with a height of 300 mm. The effect of increasing the heights and changing the element packs can be evaluated by comparing historical test data. De Klerk (2001) verified the RAH model by comparing plant measurements to the simulation results. From these results five conditions are selected to compare the performance simulated by the VBA RAH and RAH models, and measured values. The data set was collected in March 1995 for the research project done by Habbitts (1998). This data set is for the same power station and unit as in for this research project. The flue gas outlet temperature was 1.79% lower than the measured value for the VBA RAH simulation. Comparing to the RAH model the VBA RAH model was 0.13% higher. The air outlet temperature was 2.21% higher than the measured value for the VBA RAH simulation. Comparing to the RAH model air outlet temperature, the VBA RAH model was 0.83% less. For the temperature simulation this set of data showed that the VBA RAH and RAH models correlate well with each other. Figure 5.30 is a graphical illustration of these results. It does seem that the simulation tends to slightly over-estimate temperatures when compared to the measured data. But this still shows that the validity of both simulation tools is good and can be used for air heater performance analysis.

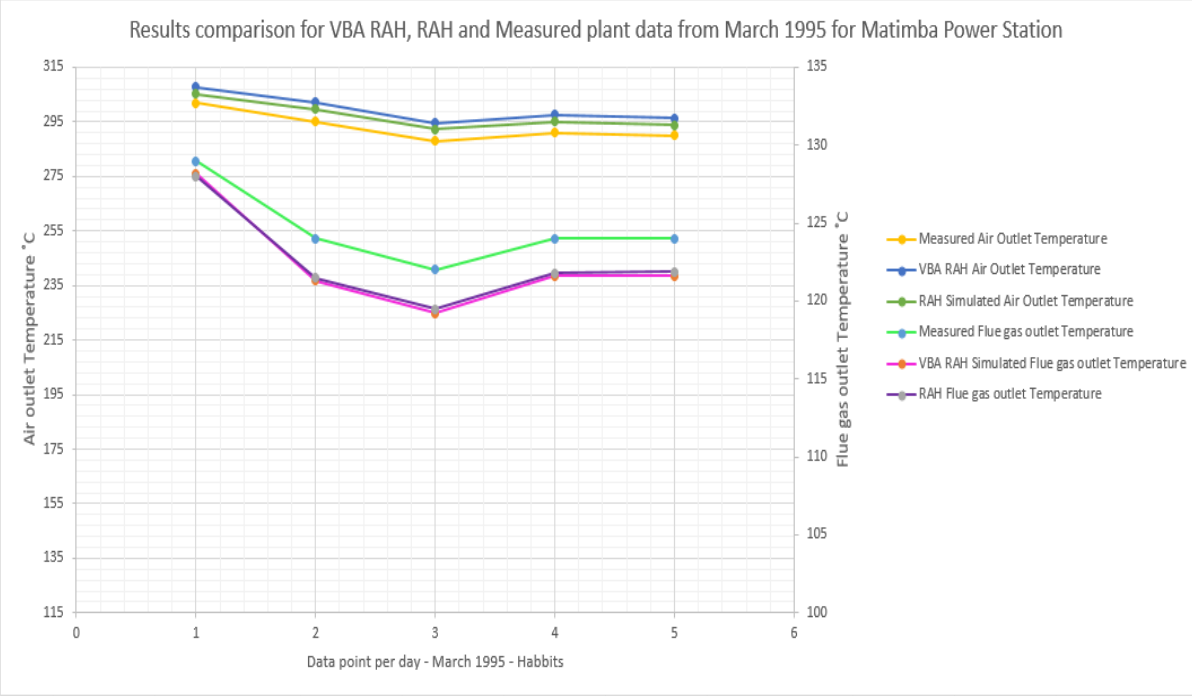

Figure 5.30: Results comparison for VBA RAH, RAH and Measured plant data from March 1995 for the same Eskom Power Station.

5.6 VBA RAH capability of reducing dew point related fouling

Through focusing on the dew point related fouling conditions of the flue gas along with the steel matrix temperatures, the research objective was to see whether the matrix metal temperatures could be controlled to prevent dew point related air heater fouling. This control would require amendments in operating parameters or design configurations. The operating changeable parameter is the inlet air temperature, which can be varied through the use of the pre-steam air heater installed before the air heater at the suction line before the FD fans. The air heater performance will however be influenced along with the boiler performance. The VBA RAH model has the capability of simulating these conditions in order to compare the boiler performance before and after the changes. The design configuration change will be based on changing of element pack profiles and pack configuration. The idea of the comparison is not to find the most accurate result in relation to plant operating parameters, but rather to measure the impact of the changes to the boiler performance. Both of the above-mentioned changes will be evaluated to find an ideal arrangement to reduce dew point related fouling. Based on the fact the maximum load conditions show a higher risk of dew point related fouling, the 99% MCR input parameters were used for this evaluation.

5.6.1 Increase of the air inlet temperature

The first option of increasing the air inlet temperature was evaluated to see how much it can assist with dew point conditions. Auxiliary steam is supplied to a pre-steam air heater, located in the air supply duct to the FD fan. This pre-steam air heater raise the air temperature supplied to the FD fans, to ensure that the cold end dew point related fouling condition is reduced to a minimum. From Figure 5.31 below, the metal temperatures show a definite improvement in reducing dew point related fouling conditions. Assuming 1% of SO_2 converted to SO_3 the portion of the cold end layer experiencing dew point related fouling was previously estimated to be 90.3%. This value reduced to a 68.1% chance of fouling when using an inlet air temperature of 70 ˚C. This temperature is based on the fact that the pre-steam air heater has the capacity to increase the air temperature above 70 ˚C, and that the increase in air temperature will increase the plate minimum temperature with +/-20 ˚C (from a 50 ˚C to 70 ˚C air inlet temperature). This will allow the metal temperature to operate with a higher initial metal temperature when the flue gas stream starts to blow through the cold end layer. In essence a higher maximum metal temperature will be reached forcing the cold end metal temperature to be exposed to dew point related fouling for shorter periods, reducing the deposition time to cause fouling. Assuming 5% of SO_2 converted to SO_3 the portion of the cold end layer experiencing dew point related fouling was previously estimated to be 100% for one gas stream. This value reduced to a 93.8% chance of dew point related fouling when using an inlet air temperature of 70 ˚C.

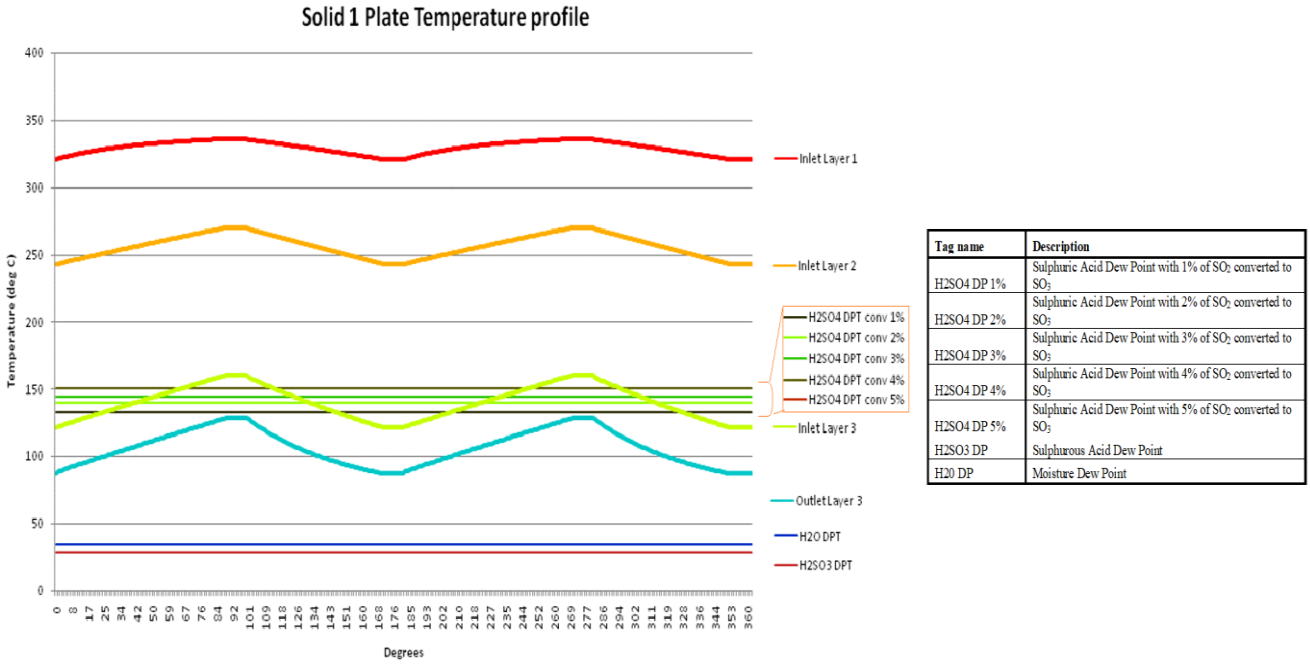

Tag name	Description
H2SO4 DP 1%	Sulphuric Acid Dew Point with 1% of SO_2 converted to SO_3
H2SO4 DP 2%	Sulphuric Acid Dew Point with 2% of SO_2 converted to SO_3
H2SO4 DP 3%	Sulphuric Acid Dew Point with 3% of SO_2 converted to SO_3
H2SO4 DP 4%	Sulphuric Acid Dew Point with 4% of SO_2 converted to SO_3
H2SO4 DP 5%	Sulphuric Acid Dew Point with 5% of SO_2 converted to SO_3
H2SO3 DP	Sulphurous Acid Dew Point
H20 DP	Moisture Dew Point

Figure 5.31: VBA RAH metal temperature profile for an increased air inlet temperature of 70 ˚C.

The impact on boiler performance can be seen from the results from the VBA RAH model. Figure 5.32 is a representation of the change in boiler performance due to the increased air inlet temperatures. The energy input to the boiler reduced by 1.6 MW, the coal flow reduced by 0.1 kg/s and the boiler efficiency improved by 0.2%. The cost saving with regards to a reduction in coal flow is R1 127 033.57 per year at a rate of R 357.38 per ton of coal. These figures show that the increase in air inlet temperature can both improve boiler performance and reduce the risk of experiencing dew point related fouling.

RESULTS OF THE ENERGY BALANCE CALCULATIONS		Changed State	Original State
Total energy input	MW	1657.4	1659
Energy recovered by steam	MW	1584	1584
Unburnt carbon in ash	% e/e	0.8	0.8
Losses in which:	MW	74.8	79
Carbon in ash	MW	12.8	12.8
Sensible heat in bottom ash and fly ash	MW	13.6	13.1
Dry flue gas losses	MW	44.7	48.8
Boiler efficiency (Useful Energy/Input Energy)	%	95.6	95.5
Boiler efficiency (input-losses)	%	95.5	95.2
HHV Boiler efficiency	%	91.8	91.6
Air Heater Leakage (w.r.t air entering A/H)	%	24.6	24.1
Air Heater Leakage (w.r.t gas entering A/H)	%	26.1	26.1

RESULTS OF THE MASS BALANCE CALCULATIONS		Changed State	Original State
Mass flowrate of coal calculated	kg/s	80.2	80.3
Total air flowrate into Cont. Vol (incl. ingress+seal air+leakage)	kg/s	873.3	873.3
Mass flow fg at A/H inlet calculated (w/o ash)	kg/s	762.9	766.7
Mass flow fg at A/H outlet calculated (w/o ash)	kg/s	927.2	928.1
Excess air	%	18.2	18.2

COMPARISON WITH OPERATING CONDITIONS			
Mass flowrate of coal measured	kg/s	80.2	80.2
Total air flowrate measured	kg/s	875.4	875.4
Calculated-measured coal flowrate difference	%	0	-0.1
Calculated-measured air flowrate difference	%	0.2	0.1

Figure 5.32: VBA RAH Boiler impact comparison for an increased air inlet temperature of 70 ˚C.

Changing the operating conditions in this way can be used as a method to reduce dew point related fouling, but this option is limited by the capacity of the pre-steam air heater and the fan design temperature. For the FD fans, the design maximum temperature is 50˚C. If the air temperature is increased beyond this point the fan will operate with air densities outside of its design range. Due to the fact that the fan is a constant volume machine, the volumetric flow

rate will be maintained. With this in mind the density will decrease with an increase in temperature. This process reduces the pressure difference across the fan. This reduction also causes a reduction in the air pressure entering the air heater. After the air heater, the air pressure is measured in the cross over duct, this is known as the cross over duct pressure. This pressure play an integral role in the secondary air supply to the furnace. If the cross over duct pressure is not maintained, the control system signals a demand to increase the secondary air supply by increasing the radial vane control dampers on the FD fans. When the fan operates at higher temperatures, and the air heater operates with blocked element packs, this cross over duct pressure is not maintained. In essence this effect forces the fan radial vanes to reach a maximum operating point, which then limits the fan supply capacity. Other changes will also be required to ensure the fan capacity is still maintained. A different approach is therefore required to reduce the differential pressure across the air heater. The third layer of element packs can be removed or the pack height can be reduced to reduce the differential pressure across the steel matrix. Figure 5.33 is an illustration on the schematic layout between the FD fans, air heaters and the cross over duct pressure.

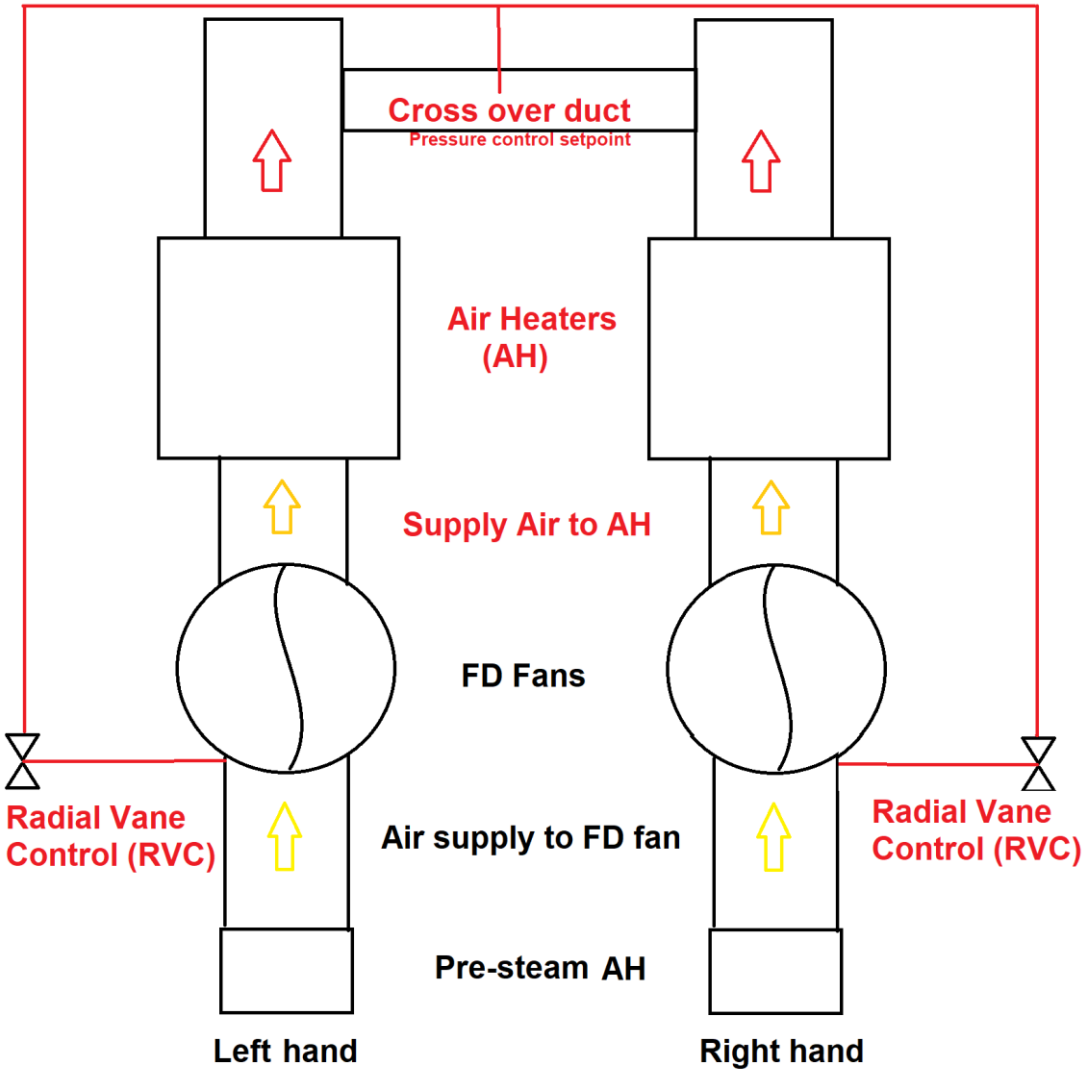

Figure 5.33: VBA RAH metal temperature profile for an increased air inlet temperature of 70 ˚C, and removal of the third layer element packs.

5.6.2 Increase of the air inlet temperature and removal of the third layer

If the pre-steam air heater has the maximum capacity of increasing the inlet air to 70 ˚C, the next option will be to amend the pack configuration. The 2.78DU element packs are the packs with the smallest conduction and surface heat transfer area (As per Element pack properties table in Appendix A). Therefore changes to the height or layer configuration are the other two options available to achieve a reduction in dew point related fouling. By reducing the height the resistance will be reduced therefore also reducing the dynamic pressure component of the fan performance. This can assist to reduce the fan total pressure leaving room for increased air supply capacity. Figure 5.34 is a representation of the metal temperatures in the case where the third layer is completely removed, which illustrates that dew point related fouling can be minimized to a large extent.

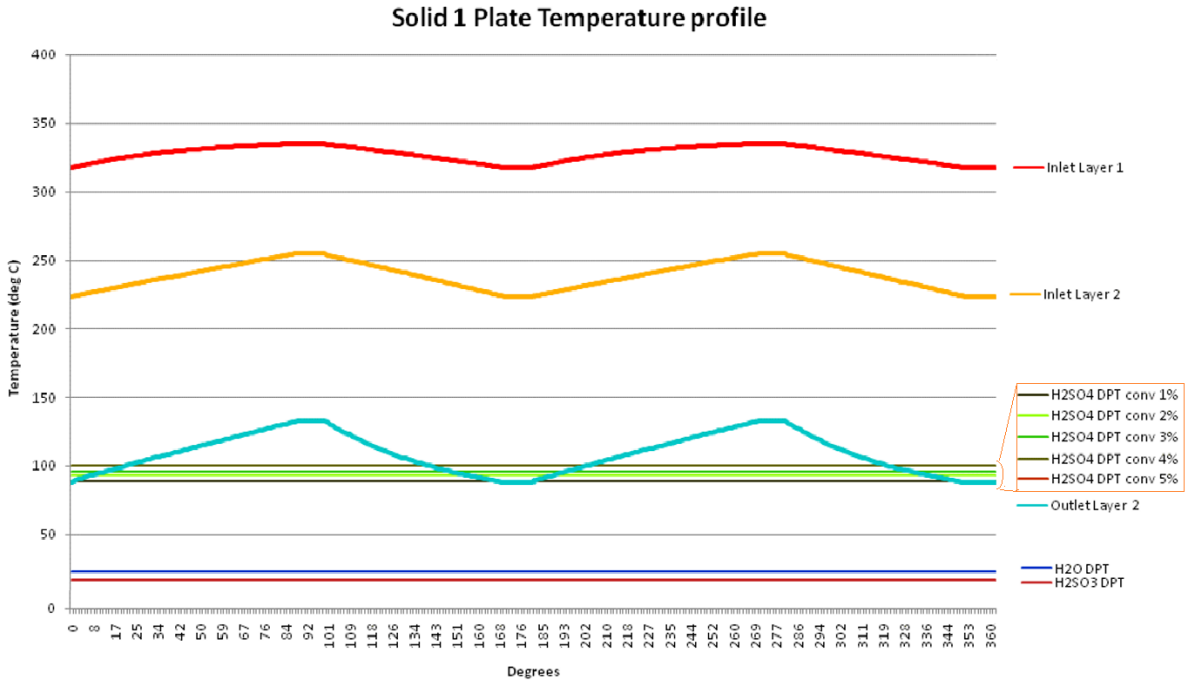

Figure 5.34: VBA RAH metal temperature profile for an increased air inlet temperature of 70 ˚C, and removal of the third layer element packs.

Assuming 1% of SO_2 converted to SO_3 the portion of the cold end layer experiencing dew point related fouling was previously estimated to be 90.3% for one gas stream. This reduced to a 16.5% chance of dew point fouling. Assuming 5% of SO_2 converted to SO_3 the portion of the cold end layer experiencing dew point fouling was previously estimated to be 100% for one gas stream. This reduced to a 28.3% chance of dew point fouling. Soot blowing will also be more effective, because less penetration by dry steam will be required for effective cleaning. This is a recommended field for further research, to identify the amount of energy required to remove fouled deposits from element packs.

The impact on boiler performance can be seen from the results generated by the VBA RAH model. Figure 5.35 is a representation of the impact on the boiler performance using the original results simulated for the 99% MCR conditions and the increased air inlet temperature. The

energy input from the boiler increased by 0.5 MW, the coal flow remained unchanged and the boiler efficiency improved by 0.1%. These figures show that the increase in air inlet temperature and removing of the third layer can both improve boiler performance and reduce the risk of experiencing dew point related fouling.

RESULTS OF THE ENERGY BALANCE CALCULATIONS		Changed State	Original State
Total energy input	MW	1659.5	1659
Energy recovered by steam	MW	1584	1584
Unburnt carbon in ash	% e/e	0.8	0.8
Losses in which:	MW	76.6	79
Carbon in ash	MW	12.8	12.8
Sensible heat in bottom ash and fly ash	MW	13.7	13.1
Dry flue gas losses	MW	46.5	48.8
Boiler efficiency (Useful Energy/Input Energy)	%	95.5	95.5
Boiler efficiency (input-losses)	%	95.4	95.2
HHV Boiler efficiency	%	91.7	91.6
Air Heater Leakage (w.r.t air entering A/H)	%	24.6	24.1
Air Heater Leakage (w.r.t gas entering A/H)	%	26.1	26.1

RESULTS OF THE MASS BALANCE CALCULATIONS		Changed State	Original State
Mass flowrate of coal calculated	kg/s	80.3	80.3
Total air flowrate into Cont. Vol (incl. ingress+seal air+leakage)	kg/s	874.4	874.4
Mass flow fg at A/H inlet calculated (w/o ash)	kg/s	763.8	766.7
Mass flow fg at A/H outlet calculated (w/o ash)	kg/s	928.4	928.1
Excess air	%	18.2	18.2

COMPARISON WITH OPERATING CONDITIONS			
Mass flowrate of coal measured	kg/s	80.2	80.2
Total air flowrate measured	kg/s	875.4	875.4
Calculated-measured coal flowrate difference	%	-0.1	-0.1
Calculated-measured air flowrate difference	%	0.1	0.1

Figure 5.35: VBA RAH Boiler impact comparison for an increased air inlet temperature of 70 ˚C, and removal of the third layer of element packs.

This option still poses a risk of causing high emissions for the downstream conditions after the air heater. From the test results in section 5.3 the measured flue gas temperature was 120 ˚C. The simulated value was 104 ˚C for the mixed gas outlet temperature, which includes all forms of leakage into the flue gas stream. The risk exists that if the actual gas temperature was 16 ˚C higher than the simulated value and the simulated value here is 122°C, the actual mixed flue gas temperature could be 138 ˚C. The lower temperature is believed to be caused by an error in flue gas flow as per the conclusion from section 5.7. Therefore the correct flue gas flow was simulated and the result showed that the flue gas outlet temperature was 138.7°C, which provides proof of the possible increase in the ash resistivity due to the elevated flue gas outlet temperatures. The ash resistivity is directly influenced by the flue gas temperature, which will cause a reduction of the efficiency of the electrostatic precipitators. This will also have a negative impact on the particulate matter emissions. When the flue gas temperature is high the ash resistivity will increase causing less ash particles to precipitate to the electrostatic screens. More particles therefore pass through the ESP's directly to the smoke stack. This effect increases the particulate matter count leaving the stack, which could lead to the legislated emissions limit being exceeded. The relationship for ash resistivity and temperature can be seen in Figure 5.36 (Mohanty, et al., 2011).

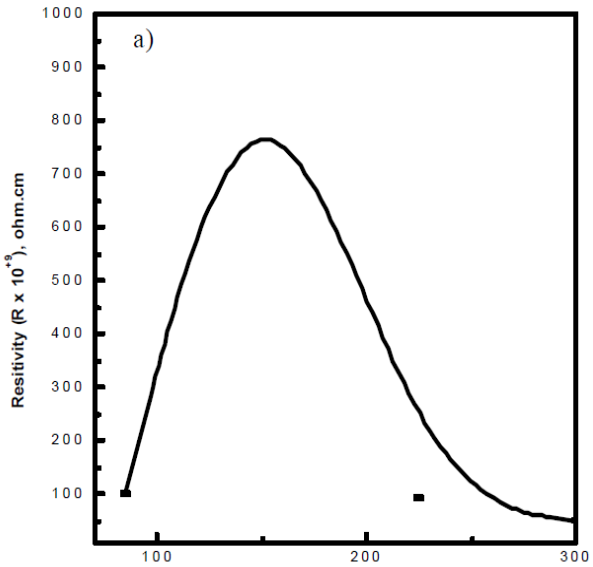

Figure 5.36: Relationship of Temperature and resistivity of ash (Mohanty, et al., 2011).

5.6.3 Reduction of the air inlet temperature to 50°C, removal of the third layer and increase of cold end (second layer) element pack thickness

The risk of high ash resistivity due to increased flue gas temperatures can still be changed through changing of inlet air temperatures and element plate thickness. The first option would be to ensure that the inlet air temperature is set at an adequate lower inlet temperature to allow the mixed flue gas temperature to operate between 125 ˚C to 130 ˚C, along with increasing the plate thicknesses from 0.5mm to 0.8mm. This increase in plate thickness will provide more conduction area, which in turn will reduce the outlet temperature.

This effect will also improve the efficiency of the SO_3 lances installed at the electrostatic precipitator (ESP) inlet casing, to reduce the ash resistivity as indicated in Figure 5.37. These lances inject SO_3 to improve the collection rates of the ESP's. The ESP inlet temperature also includes the flue gas exit tubular air heater temperature (primary air heater). To avoid sulphuric acid formation on the SO_3 lance nozzles, causing blockage of the injection ports, the flue gas temperature is set to operate above 123 ˚C. Figure 5.38 is an illustration of the cold end of the air heater where the flue gas stream and air stream give a combined temperature known as the cold combined temperature. This temperature is used to operate the air heater above the dew point related fouling set point of +/- 90 ˚C, and to maintain the ESP inlet temperature above 123˚C through heating of the air entering the FD fan.

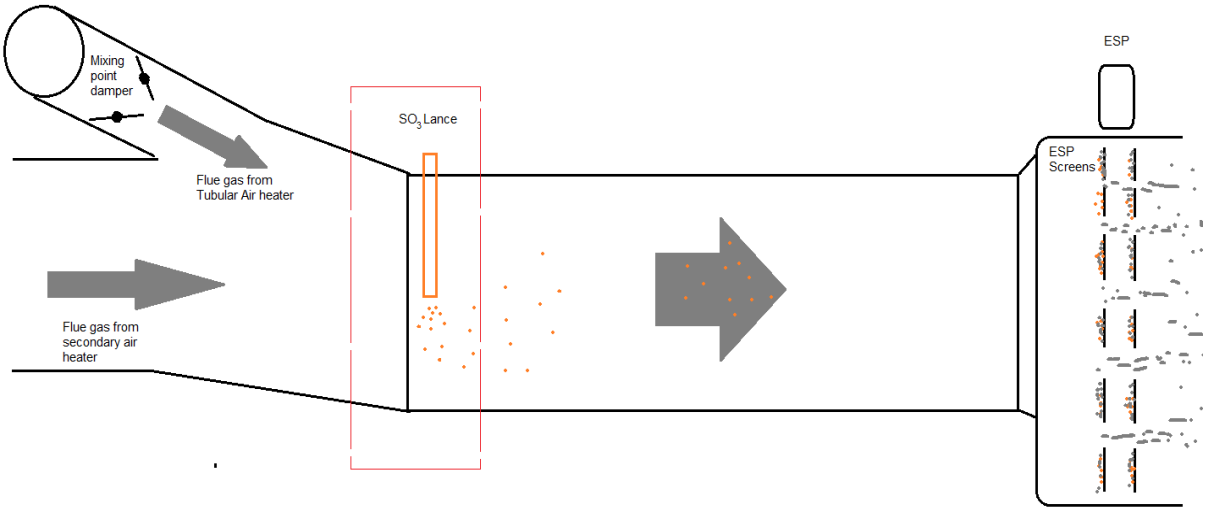

Figure 5.37: SO_3 injection to the flue gas entering the ESP

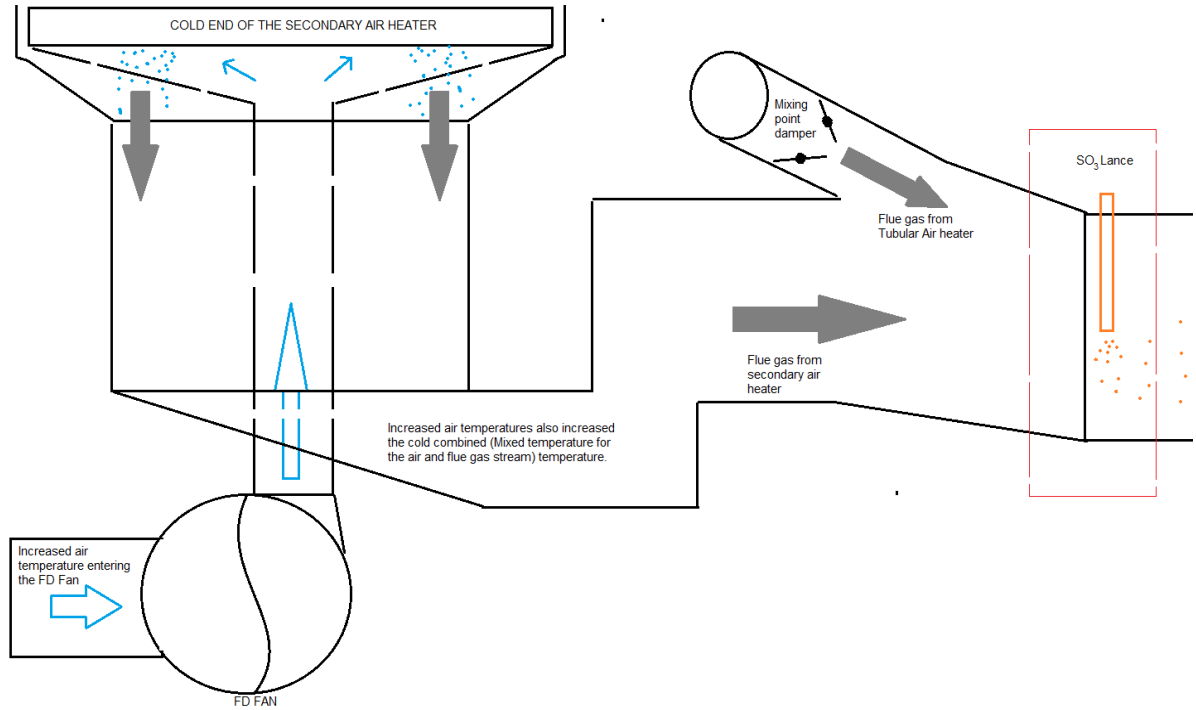

Figure 5.38: Cold combined temperature formation at the cold end of the air heater.

With this control system in mind, the possibility of reducing the inlet temperature to 50°C was simulated. It shows that the second layer will only be exposed 26.2% to 37.2% for a 1% to 5% SO_2 to SO_3 conversion respectively. When comparing this condition to the original configuration, where the fouling was expected between 90.3% and 100%, the reduced fouling will require less cleaning capacity. The mixed flue gas mixture temperature of 102.6 ˚C for this configuration of packs and operating parameters is 1.6 ˚C less than the original temperature measured. Considering the possibility that there was an error in flow, the correct flue gas flow was simulated and the flue gas outlet temperature was found to be +/-124˚C. This value is still

more than the 123 ˚C, which is the flue gas temperature required to prevent the fouling of the SO_3 lances. The risk still exist that when changes in load or flows occur the flue gas temperature may operate below this temperature. The boiler performance indicated that an increase of coal mass flow of 0.03 kg/s will be incurred and 0.05 MW of heat energy input into the boiler. The temperature profiles for the two layers can be seen in Figure 5.39.

The air inlet temperature was further reduced to 35 ˚C, but this showed an increase in exposure to fouling. The range of exposure increased to 32.8-43.3% for a 1% to 5% SO_2 to SO_3 conversion respectively. It would therefore be advised that the inlet temperature remain at +/- 50˚C.

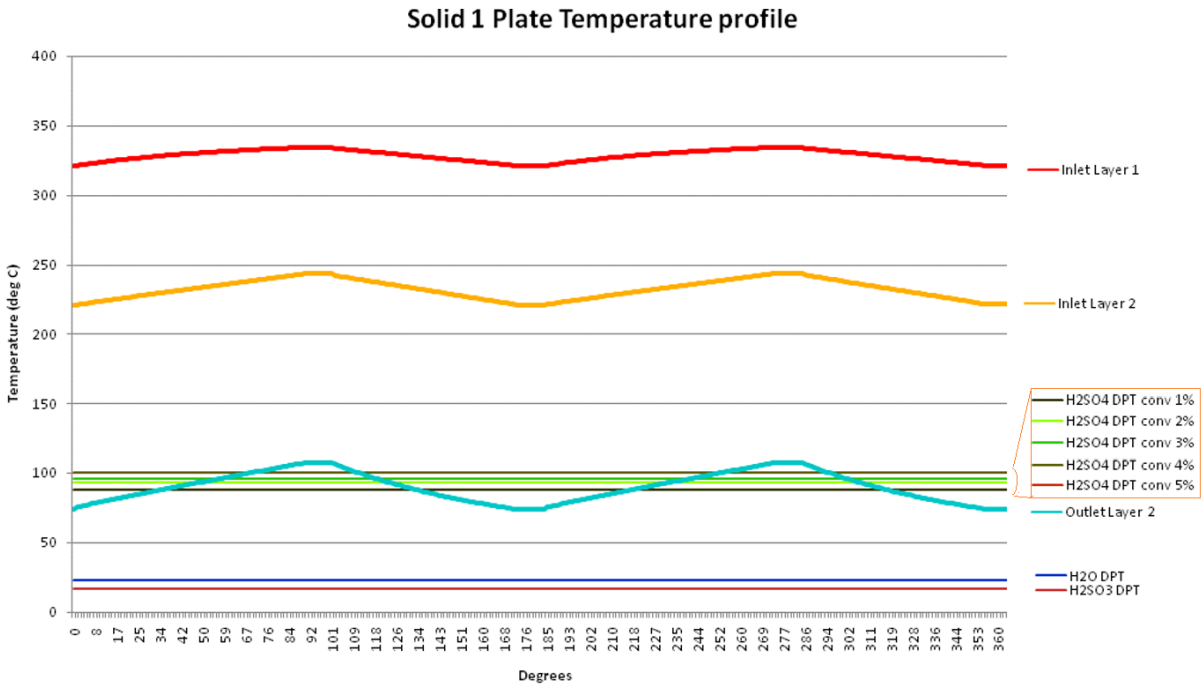

Figure 5.39: The metal surface temperature profile for operating condition where the third layer is removed and the inlet air temperature is 50 ˚C.

5.6.4 Impact of leakage on Air heater performance

The leakage was measured to be 8.7% during the tests conducted by Habbitts, in March 1995. This is a clear indication that the air heater leakage was low compared to the leakage experienced in the tests conducted in February 2020. The impact of an increase in leakage was therefore also assessed to see how it affects air heater performance and boiler performance. From these results it shows that air heater leakage causes increased differential pressures for the flue gas and air streams, placing additional strain on the FD and ID fan capacities. As expected the radial vane will open more causing the fan to handle greater volumes of air (FD fans) and diluted flue gas (ID fans) respectively. The second effect is the increase in the dry flue gas loss. This loss is directly proportional to boiler efficiency deterioration, as explained in section 3.1. Figure 5.40 is an illustration of the air heater operating temperatures leaving the air heater. This shows how the air heater performance deteriorates with an increase in leakage. To maintain the excess air in the flue gas and the set point air pressure (measured after the air

heater at the cross over duct as shown in Figure 5.33) the FD fan also operates at higher capacity when leakage increases. In essence both the ID fan and FD fan start to operate at higher operating currents, therefore incurring additional auxiliary power consumption. In addition to this the coal flow rates increase which then also requires more combustion air. The augmented volumes of combustion air and coal introduce increased flue gas volumes, which places additional strain on the ID fan capacity.

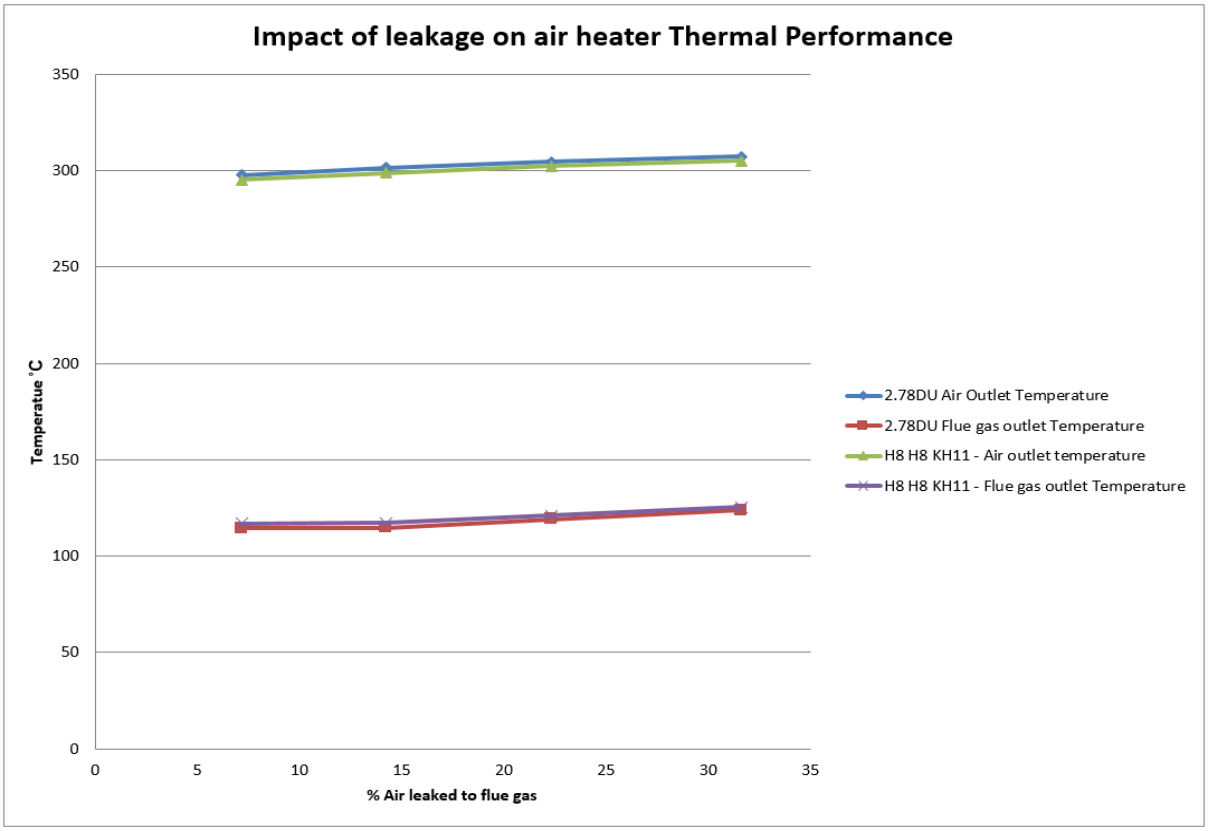

Figure 5.40: Impact of leakage on air heater thermal performance for the configuration of 2.78DU element packs and the original design combination of H8(0.5mm, 1025mm high) for hot end, H8(0.5mm,1025mm high) intermediate, KH11(0.8mm, 300mm high) for cold end.

Over the years the Rankine cycle efficiency for the boiler starts to deteriorate due to increased losses to the condensate system along with unavailability of high pressure steam heaters and low pressure steam heaters. These losses require additional heat energy to be recovered by the boiler. This lost energy must be recovered by increasing the coal flow into the boiler. The boiler in general operates at higher heat input rates which requires increased volumes of combustion air and extracted flue gas from the boiler. The additional work required from the boiler adds more strain to the capacity of the boiler auxiliaries such as FD and ID fans. If air heaters operate with high blockage and leakage these results clearly show that the fan will start to operate at its maximum capacity. With a simulation tool such as the VBA RAH model variations of plant operation and configuration can add value to make decisions to improve the air heater performance and in turn also add to the boiler efficiency and life expectancy of the boiler plant. The impact of leakage on differential pressure from the air heaters, boiler performance, coal flow rate and dry flue gas losses can be seen in the following figures.

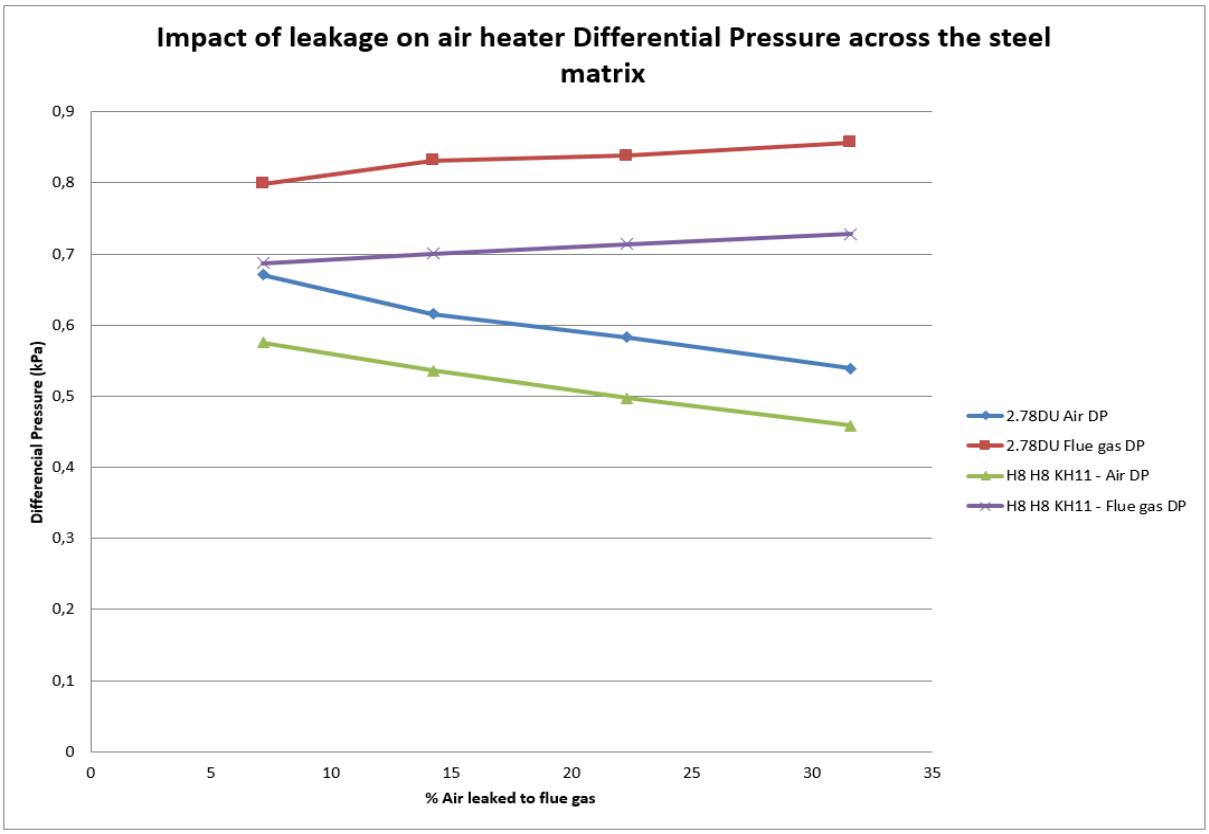

Figure 5.41: Impact of leakage on air heater Differential Pressure for the configuration of 2.78DU element packs and the original design combination of H8(0.5mm, 1025mm high) for hot end, H8(0.5mm,1025mm high) intermediate, KH11(0.8mm, 300mm high) for cold end.

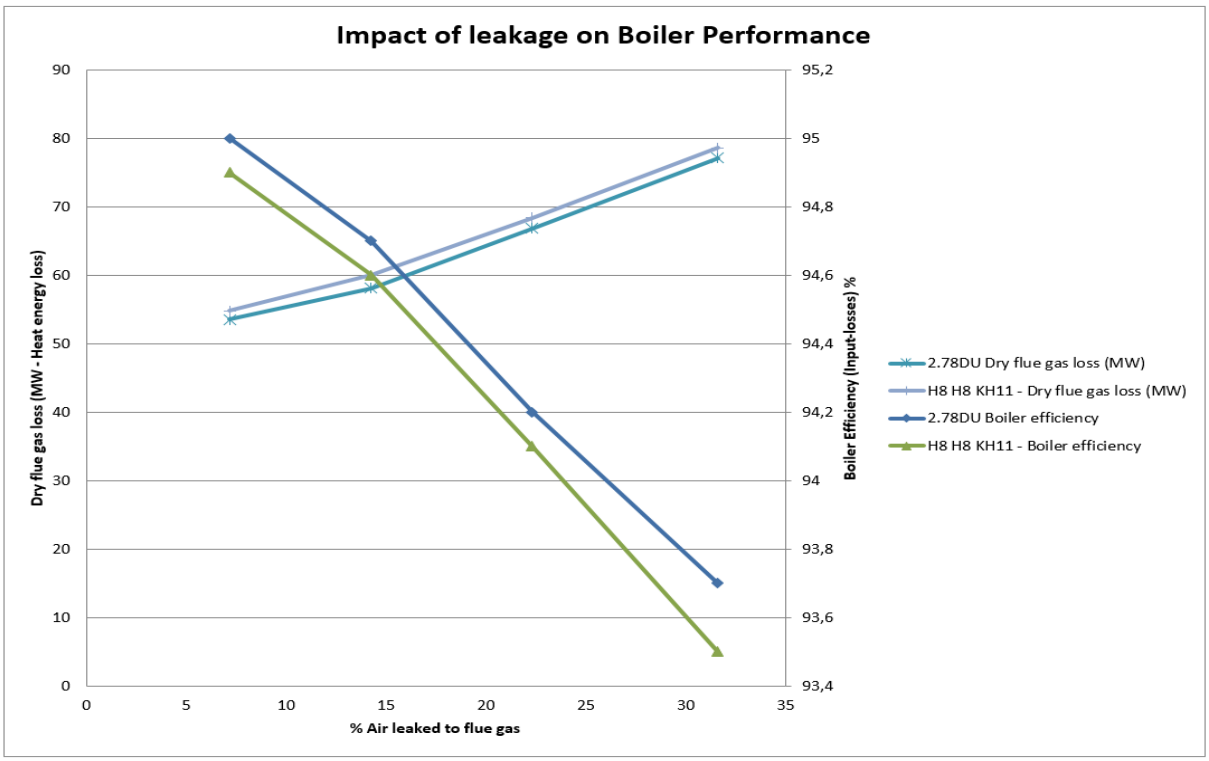

Figure 5.42: Impact of leakage on Boiler Performance for the configuration of 2.78DU element packs and the original design combination of H8(0.5mm, 1025mm high) for hot end, H8(0.5mm,1025mm high) intermediate, KH11(0.8mm, 300mm high) for cold end.

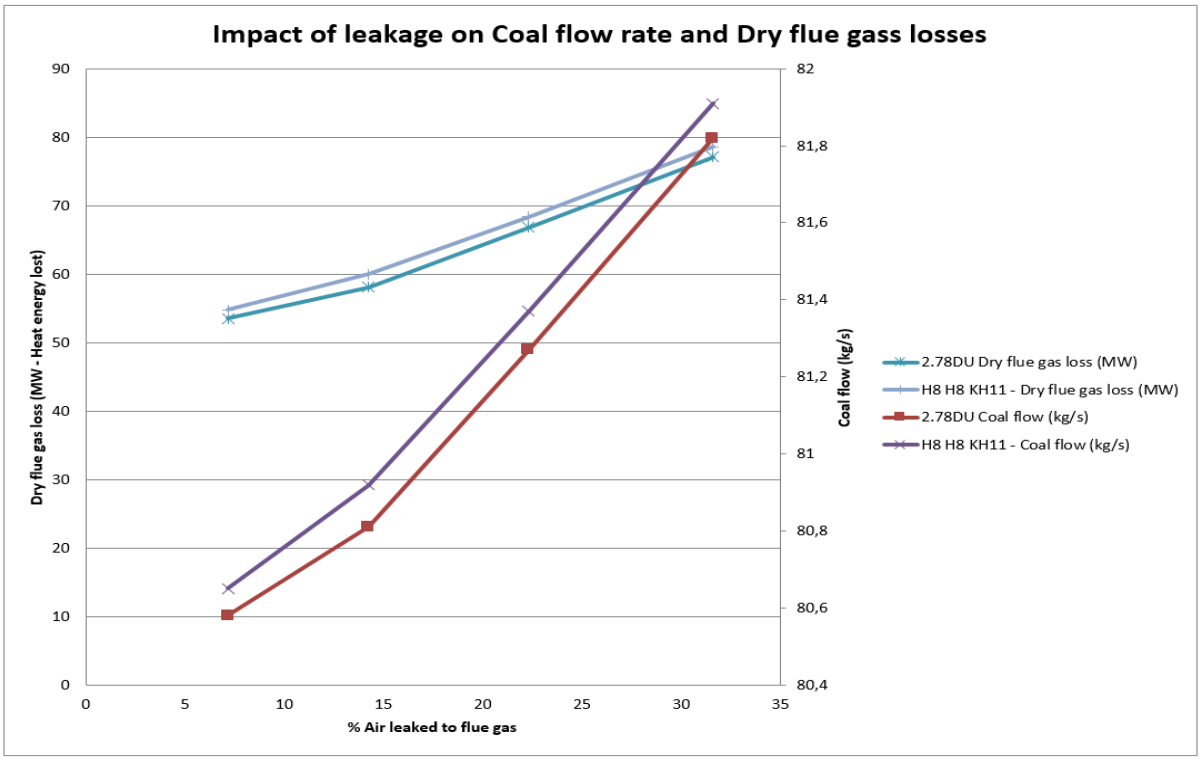

Figure 5.43: Impact of leakage on coal flow rate and Dry flue gas losses for the configuration of 2.78DU element packs and the original design combination of H8(0.5mm, 1025mm high) for hot end, H8(0.5mm,1025mm high) intermediate, KH11(0.8mm, 300mm high) for cold end.

5.6.5 Impact of blockage on air heater performance

The configuration to operate the inlet temperature at +/- 50 ˚C, removing the third layer and increasing the second layer thickness (as mentioned in section 5.6.3), seems to be a promising solution. But there is still a risk that the mixed flue gas temperature could be too low. The previous assumption was that the higher measured temperature exists due to the fact that the maximum flue gas temperature is reached in small continuous cycles. When measuring after the air heater discharge dampers, a higher outlet temperature is therefore expected. Another possibility exists that the element packs experience blockage at the cold end which in turn causes higher outlet temperatures. To test this theory, the input parameters were used from the 99% MCR test to see how a 30% air heater blockage will impact the air heater and boiler performance. The results indicated that the mixed flue gas outlet temperature was 0.18% higher than the measured temperature. Considering the error in flue gas flow as stated in section 5.7, the corrected flow condition was also simulated. This result indicated that a 30% blockage condition will result in an average flue gas outlet temperature of 118.7 ˚C, which is +/- 2 ˚C lower than the temperature from the original flue gas flow used in the 99%MCR test conditions. In this case the air outlet temperature seemed to show a larger error. The outlet air temperature was 4.31% less than the measured value. The maximum plate temperature for the cold end was 17.9% higher and the minimum was 16% higher. Therefore, when comparing the measured cold end metal temperatures the deviation shows less correlation to the measured values for the 99% MCR condition (Figure 5.44), which shows some uncertainty to the fact that the cold end experienced excessive blockage at the cold end. Table 5.11 is a summary of the results for the case where the cold end experience 30% blockage.

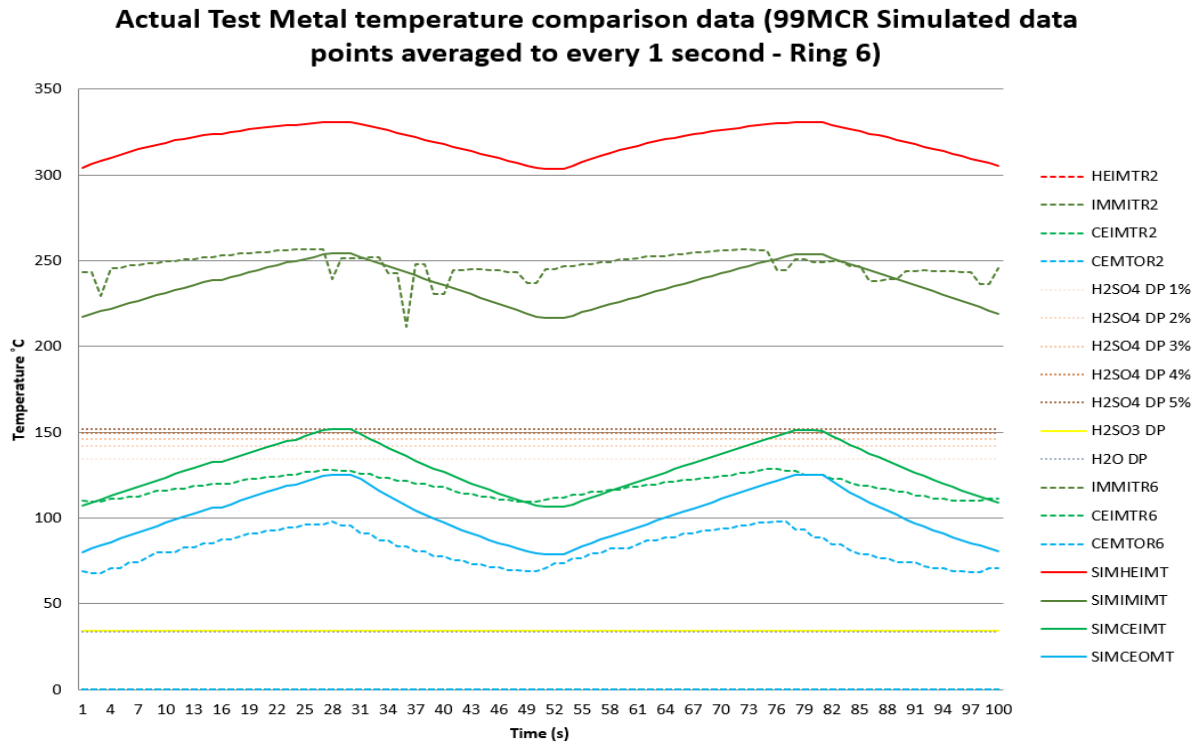

Figure 5.44: The metal surface temperature profile for operating condition where the air heater is 30% blocked, using the same input parameter as the 99% MCR actual test conditions.

Table 5.11: Comparison of results for operating condition where the air heater is 30% blocked, using the same input parameter as the 99% MCR actual test conditions and the original measured results.

ACTUAL-TEST RESULTS					
PARAMATERS	UNITS	99 MCR			MEASUREMENT SOURCE
				ERROR	
		MEASURED DATA	RAH VBA	%MEAS	
GEN LOAD 1	MW	672			
	DAY/MONTH/YEAR	24/02/2020			
	HR:MIN:SEC-HR:MIN:SEC	00:00:00 - 04:00:00			
		MEASURED DATA	RAH VBA	%MEAS	
LH SEC A/H GAS IN T	CEL	339	339	0,00	RT&D
LH SEC A/H GAS OUT T	CEL	120	120,22	0,18	DCS
			30% blockage		
LH SEC A/H INL T	CEL	50,54	50,54	0,00	DCS
LH SEC A T	CEL	307,98	294,7	-4,31	DCS
COMBINED TEMPERATURES			30% blockage		
LH AH COMBINED TEMPS CALCULATED		85,27	85,38	0,13	ESTIMATED
LH AH COMBINED TEMPS	CEL	85,27	85,38	0,13	DCS
COLD END OUTLET METAL TEMPERATURES TEMPERATURES			30% blockage		
MAXIMUM	CEL	128,6	151,6	17,88	INSTALLED THERMOCOUPLE
MINIMUM	CEL	68,1	78,99	15,99	INSTALLED THERMOCOUPLE
AVERAGE	CEL	98,35	115,295	17,23	ESTIMATED
PRESSURES			30% blockage		
LH FDF DIS P	KPA	3,688	3,688	N/A	DCS
SEC A C/OVER DUCT P	KPA	2,477	N/A	N/A	DCS
AIR HEATER AIR DP air	KPA	1,211	1,13	-6,69	DCS
LH SEC AH INLET GAS P	KPA	-1,0944	-1,0944	N/A	RT&D
LH SEC AH OUTLET GAS P	KPA	-0,235	N/A	N/A	RT&D
AIR HEATER DP gas	KPA	0,8594	1,13	31,49	RT&D
ENERGY			30% blockage		
FG HEAT ENEREGY LOST	MW	NOT MEASURED	-34,32	N/A	ESTIMATED
AIR HEAT ENERGY GAINED	MW	NOT MEASURED	34,95	N/A	ESTIMATED

Figure 5.45 is an illustration of the air heater temperature air and flue gas outlet temperatures for increases in blockage from 10% to 80%. From this illustration it is clear that after 70% blockage the air heater performance deteriorates excessively (air outlet temperature decreasing about 11 ˚C), but between 10% and 60% the impact on air outlet temperature reduction ranges between 1.2 ˚C to 6 ˚C. The figure also shows that after 70% blockage the flue gas outlet heater performance deteriorates excessively with the flue gas outlet temperature increasing by 8 ˚C, but between 10% and 60% the impact on flue gas outlet temperature increases between 0.82 ˚C and 2.85 ˚C.

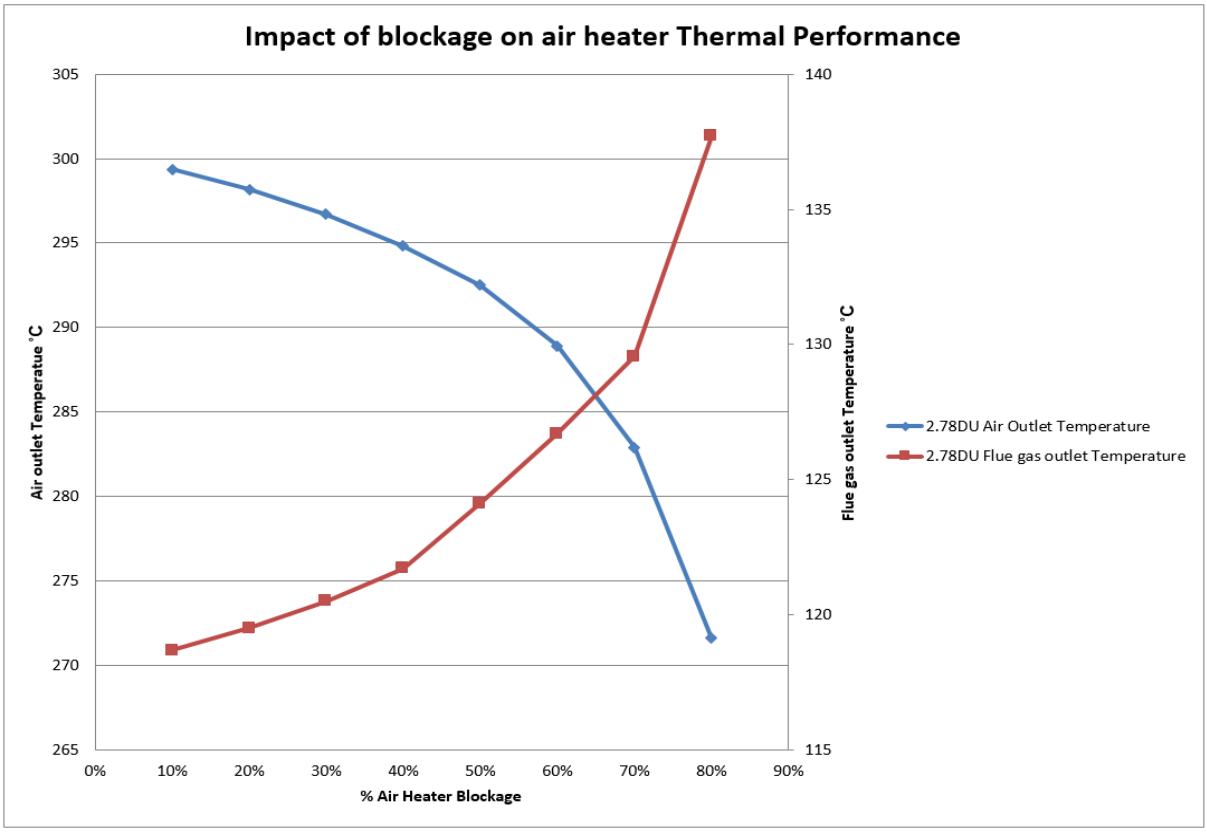

Figure 5.45: Impact of blockage on air heater thermal performance for the configuration of 2.78DU element packs.

Due to the deterioration of air heater performance, higher thermal flue gas losses are incurred and furthermore the boiler coal flow rates also increase to compensate for the thermal losses. The boiler efficiency deteriorates accordingly. As mentioned with the effects of leakage, to maintain the set point air pressure (after the air heater at the cross over duct) and excess air in the flue gas, the FD fan also operates at higher capacity when leakage increases. Figures 5.46 and 5.47 illustrate the effects of blockage on boiler performance, coal flow rates and dry flue gas losses.

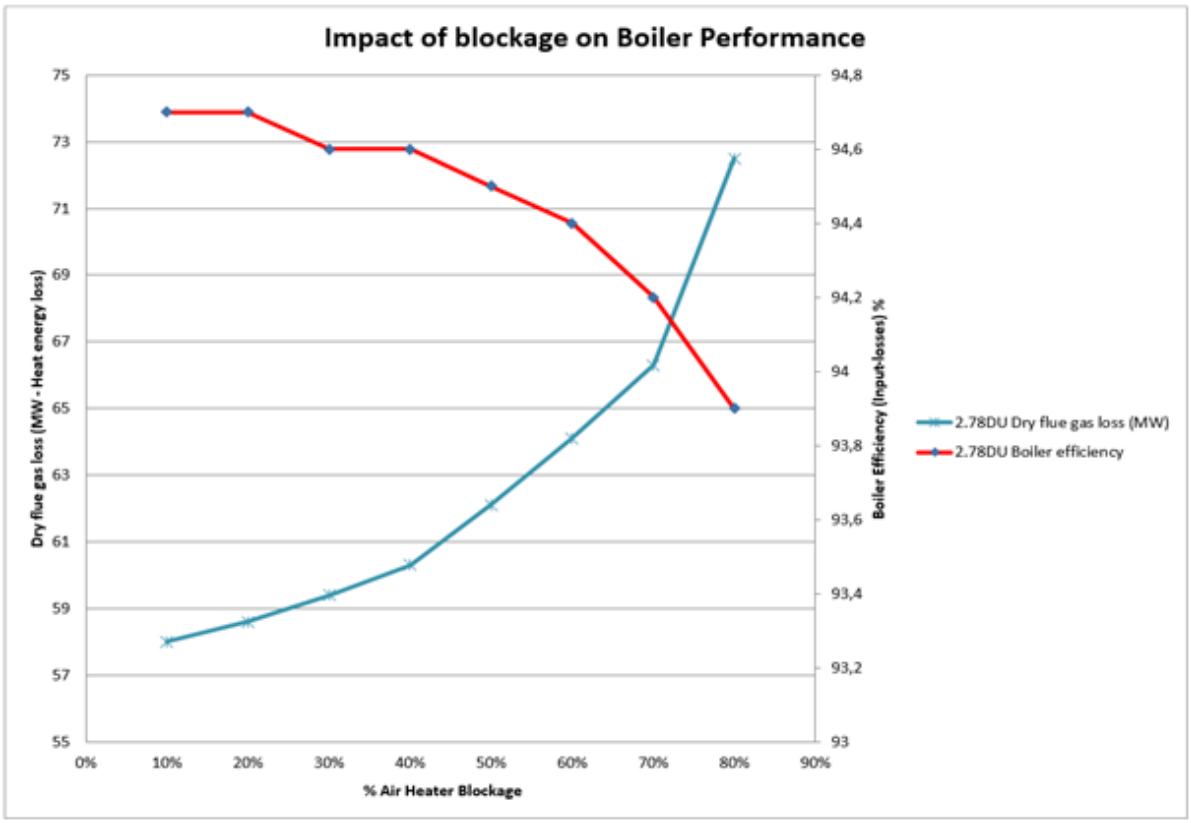

Figure 5.46: Impact of blockage on boiler performance for the configuration of 2.78DU element packs.

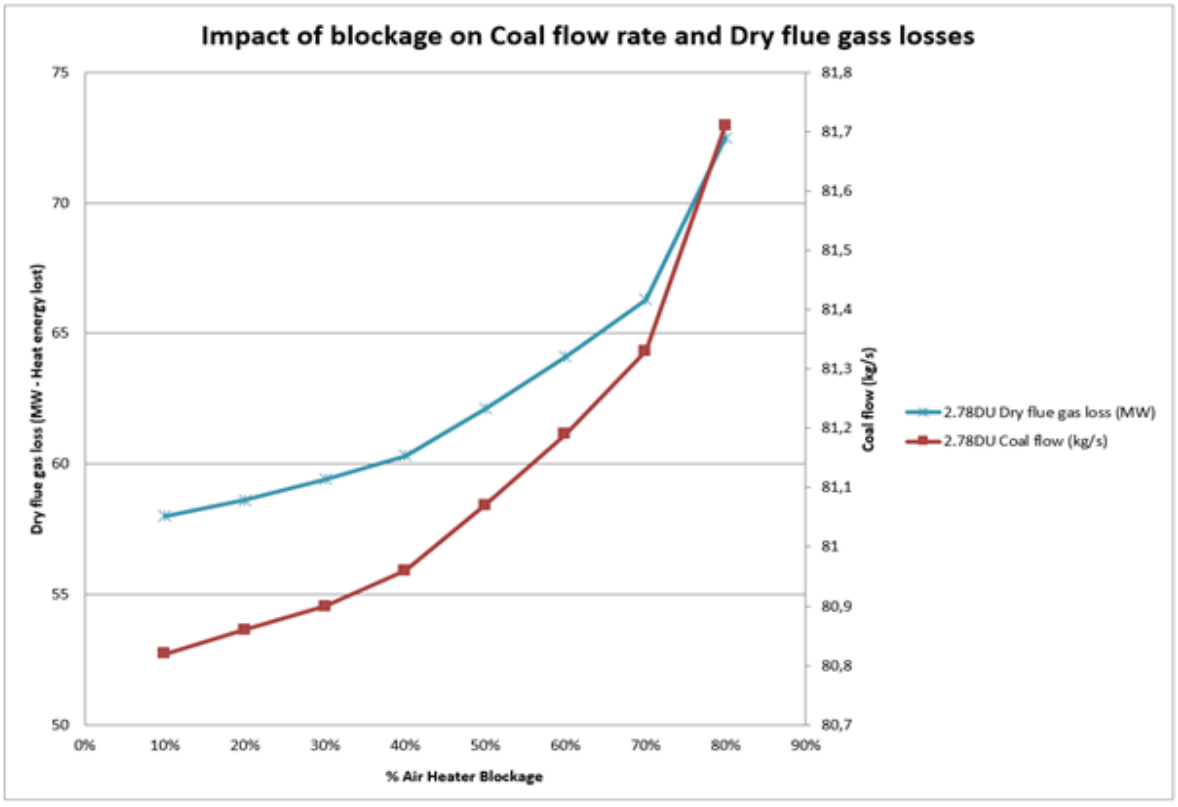

Figure 5.47: Impact of blockage on coal flow and dry flue gas loss (MW) for the configuration of 2.78DU element packs.

5.6.6 Impact of the combined effect of leakage and blockage on air heater performance

For blockage and leakage the impacts on boiler performance were assessed separately, but in reality both these conditions are experienced. To see how the combination of the effects impact boiler performance the condition of 30% blockage and 30% leakage was simulated. The results were then compared to the original state of 2% blockage and 8.7% leakage. This clearly shows the impact of the combined effect of fouling along with leakage on boiler efficiency. The coal flow rate increases by 2.13 kg/s, the dry flue gas loss increases with a 28.6 MW heat energy loss and the boiler efficiency reduced by 1.6%. Considering the increase in coal flow only, a total boiler heat input energy of 32 MW is required to compensate for these losses. The flue gas flow through the ID fans increases to 173.7 kg/s and the secondary air 172.6 kg/s. This excludes the additional impact on the auxiliary consumption that will increase due to increase in volume. Table 5.12 is a summary of the combined impact of leakage and fouling on the air heater and boiler performance.

Table 5.12: Comparison of results for 30% blockage, 30% leakage and the combination of both 30% blockage and 30% leakage, and the impact of each to boiler performance.

VBA RAH				
Blockage%	2%	30%	2%	30%
Leakage%	7,18	7,18	30	30
278DU- Air out T Mix	296,0	296,7	307,0	304,8
278DU- Air out T	297,6	298,4	309,02	306,5
278DU- Gas out T undiluted	117,9	125,7	146,53	147,7
278DU- Gas out T Diluted	115,4	121,1	131,2	132,2
278DU- Gas out T Mixed	114,3	120,5	130,2	131,2
278DU- Gas DP	0,7989	0,8112	0,8894	1,5357
278DU- Air DP	0,6711	0,6187	0,6902	1,1483
Boiler eff 278DU (input-losses)	94,9	94,7	93,4	93,3
Coal flow kg/s	80,58	80,86	82,07	82,13
Dry flue gas loss (MW)	53,5	58,4	81,2	82,1

For the same fluid density the fluid volume increases due to an increase in mass flow. The shaft power input is directly proportional to the volumetric flow of the fan. If the shaft power increases the electrical power increases as well. In essence the fans will not only run with saturated capacities, but it will also operate with higher operating currents. A partial load loss will be incurred due to the limitation on the fan capacity operating at a maximum.

$$Power\ Input\ to\ Fan\ Shaft = \frac{Volume\ of\ fluid \times total\ pressure}{(fan\ efficiency)} \tag{5.7}$$

$$Power\ Input\ to\ the\ motor = \frac{Power\ Input\ to\ Fan\ Shaft}{(efficiency\ of\ motor\ at\ corresponding\ loading \times transmission\ system\ efficiency)} \tag{5.8}$$

5.7 Flue gas flow estimation error

For the other measurements taken regarding the flue gas flow rates for 80% MCR and 68% MCR, the velocities measured at the flue gas duct were used to determine the flow. Considering the fact that the area was based on a design drawing, the flow area did not cause the error. The densities however did have an error of 3.32% (99% MCR), 3.06% (80% MCR) and 4.28% (68% MCR). The density will only affect the velocity by +/-0.35 m/s. The actual error comes from the velocity measured. If the mass flow measured is incorrect by 17,7 % (based on the mass flow difference of 333.1 kg/s – 283.1 kg/s from the above mentioned table) on average the measured velocity was 1,9m/s less than the velocity estimated from the previous research by De Klerk (2001). But this is still not an accurate error estimation due to the different operating parameters from the two different research experimental conditions.

The velocities are determined using the static and differential pressure measurements. Differential-pressure (DP) devices (such as Pitot tubes) and flow restrictors (such as airfoils and Venturis) are commonly used because the measurement principles have been in use since the beginning of coal fired power generation. However, the challenges facing coal-fired power plants (such large ducts; limited metering runs; poor velocity and temperature profiles; vibration; and high temperatures) make using DP primary elements and flow restrictors a less-than-ideal choice when trying to achieve low operating cost, low maintenance, high accuracy, and high repeatability. Pitot tubes are also better suited for particulate-free air flow. Coal plant combustion air contains fly ash particulates that require a purge system to ensure the primary element stays reasonably close to the original factory performance. Any particulates are prone to plug the Pitot tube and impulse lines, and will affect the accuracy of flowrate readings. The source of the K factor for this type of measurement is the manufacturer of any obstructions to the flow, such as filters or dampers.

Another important factor to be considered is the K factor of the flow measuring instrument. The manufacturers specify that a K factor should be used. It was suspected that the K factor was not used on the first set of tests for the 99%MCR condition. The following derivation was used to show what the K factor would have been if a flow of 333.1 kg/s were used.

$$Q_{ideal} = v_{ideal} \times A \times k \quad (5.9)$$

$$Q_{meas} = v_{meas} \times A \times k_{meas} \quad (5.10)$$

If the k factor for the 99%MCR condition were not considered the assumption can be made that k_{meas}=1. The measured velocity is the same as the ideal velocity, the only difference is k factor, therefore v_{ideal} is equal to $v_{measure}$. To find the correct k factor the following derivation could be used:

$$(Q_{ideal} - Q_{meas}) = v_{ideal}Ak - v_{ideal}Ak_{meas} \quad (5.11)$$

$$k = [v_{meas}(1) - ((Q_{ideal} - Q_{meas})/A)]/v_{meas} \quad (5.12)$$

Table 5.13: Estimation of the K factor for the 99%MCR condition

	Units	Values
Average Flue Gas Density	kg/m^3	0,528658
Average Flue Gas Velocity	m/s	14,99
Flue Gas Volumetric Flow Rate	m^3/s	732,71

Total Mass Flow (Measured)	kg/s	384,22
Simulated Mass flow (In initial results)	kg/s	283,12
Ideal Mass flow	kg/s	330
Flue gas duct Area	m^2	48,88
Ideal Volumetric flow rate	m^3/s	624,2
K factor	factor	0,85

The flow kinetics manometer used has a specified K factor of 0.85. Taking the result from the above mentioned K factor a 0.09 difference is found. This further proves that the K factor were not used during the flow measurement for the 99%MCR test condition. Table 5.13 is a comparison of three different methods used to find a suitable flue gas flow rate. Taking the above mentioned factors with regards to obstructions and duct configurations into account the flow factor can be influenced further. A suitable flow was also considered during the simulations to provide a flue gas exit temperature that closely resembles the measured flue gas temperature for the 99% MCR condition. This flow rate was found to be 312 kg/s and yielded a flue gas exit temperature of 120˚C. This reduction in flue gas flow would suggest a K factor of 0.80 must be used instead of 0.85. The other two operating conditions were reduced accordingly.

Table 5.14: Flue gas outlet temperatures versus flue gas flows for measured data, simulated data and simulated data considering the measured data including the correction factor for the 99%MCR condition.

%MCR	Measured flue gas mass flow	Measured flue gas outlet temperature	**Initial Simulated Condition**	**Initial simulation result**	**Deviation %**	**Correction factor included flue gas mass flow**	**Correction factor included flue gas outlet temperature**	**Deviation %**	**Correction factor reduced flue gas mass flow**	**Correction factor included flue gas outlet temperature**	**Deviation %**
68%	245,37	123	**237,67**	**123**	**0%**	**245,37**	**126**	2,44%	**233,88**	**120**	-2,44%
80%	251,62	117	**243,15**	**107**	**-9%**	**251,62**	**113**	-3,42%	**239,84**	**105**	-10,26%
99%	384,22	120	**283,12**	**104**	**-13%**	**333,1**	**129**	7,50%	**312**	**120**	0,00%
			Average Deviation		-7,29%	Average Deviation		2,17%	**Average Deviation**		**-4,23%**

The correct flow was simulated to also show how the air heater would be affected with dew point related fouling. Figure 5.48 shows the metal temperature profile for this condition.

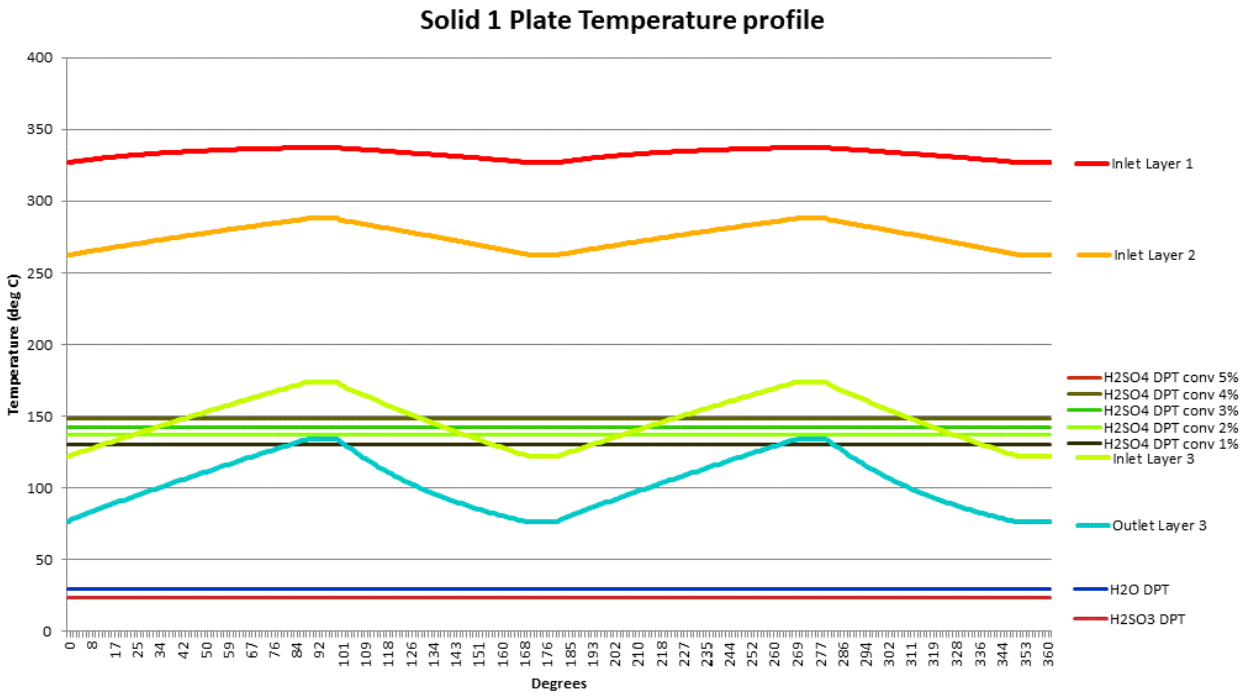

Figure 5.48: The metal surface temperature profile for operating condition where the flue gas flow is corrected to 312 kg/s, using the same input parameter as the 99% MCR actual test conditions.

Following the same matrix of a 32 x 84 selection from Figure 5.15 in section 5.3.2,the matrix takes into consideration time steps where the flue gas stream passed through the air heater and in this case specifically the third layer at the cold end of the air heater. For this subset the metal temperature operated below the 1% SO_2 to SO_3 conversion sulphuric acid dew point temperature of 133.04˚C, for 52.75% of the length and time step. It shows that as expected dew point related fouling does occur in the third layer for the 99% MCR condition even with the correct flue gas flow. As mentioned in section 5.6.3, the fouling condition will be reduced with the removal of the third layer, and keeping the air inlet temperature above 50 ˚C. The flue gas temperature will be operated above 124 ˚C, which will still be in the temperature range that would be ideal for the ESP plant to operate effectively. This combination must first be verified through plant experiments, but through the use of the VBA RAH model, in theory a possible solution exist.

In summary the RAH model and VBA RAH model show good correlation. The VBA RAH model will be an ideal tool to analyse different operating and design change configurations to optimize plant performance and minimize dew point related fouling. From the results taken from the research conducted by Habbitts (1998) and De Klerk (2001), the main contributor to errors in the testing related to incorrect velocity measurements. At low loads the velocities seem have been measured more accurately and therefore the results yielded better correlations.

6. RESEARCH CONCLUSION

The objective for this research project was firstly to identify dew point related fouling parameters with regard to coal composition, flue gas composition and process parameters. Secondly, to carry out modelling of dew point related fouling conditions of a rotary regenerative air heater using the new VBA RAH model. Thirdly, to verify the fouling conditions and simulated results by means of plant experiments to prove the accuracy of the model.

For the first objective, the aim of identifying critical parameters related to dew point fouling was met. Critical parameters such as sulphur, moisture and ash content in coal, were identified and used to determine the operating conditions causing dew point related fouling. The VBA RAH model used these parameters to evaluate the onset of dew point related fouling, where the sulphuric acid, sulphurous acid dew point and moisture dew point temperatures of the flue gas were estimated.

For the second objective, the aim of developing a simulation tool to indicate the onset of dew point related fouling was met. The model was developed, and simulations were done using measured plant parameters. The VBA RAH model was based on the same theoretical principles of the RAH model developed by de Klerk (2001). In addition the model was also developed with the capability of identifying the onset of dew point related fouling, changing of design and operating parameters and evaluating the impact of these changes to air heater and boiler performance.

For the third objective, the newly developed modelling tool was verified to indicate the accuracy and reliability of the prediction of dew point related fouling. The simulation results were validated by means of three load condition experiments, namely 99% MCR, 80% MCR and 68% MCR. These results showed that the experimental method was not ideal, but it was adequate to indicate the onset of dew point related fouling. For all three tests the radial temperature was found to be lower closer to the periphery, due to increased leakage at the periphery of the steel matrix. It was proven that the flow used for the simulation was not accurate, and was also one of the main contributors to poor correlation between the simulated and measured results for the full load condition. For further validation historical data was used which showed that the VBA RAH model correlates well with the RAH model. This result also proved that the VBA RAH model can be used as an acceptable method to analyse changes in air heater operating and design parameters. The model also has the capability to analyse the impact of these changes to the boiler performance.

A possible solution to reduce dew point fouling was suggested by increasing the air inlet temperature, remove then the third layer of the air heater element packs, and increasing the element thickness of the second layer for the air heater design configuration. This proved to have a promising result, but the possibility exists that the flue gas temperatures leaving the air heater could pose a risk of increasing the ash resistivity therefore impacting the particulate emissions negatively, for the case of ESP's. This is another recommendation for further study. A research project is required to evaluate the performance characteristics of an air heater in the case of removing the third layer of element packs. This test must also be validated by experimental research. If this option is proven to be valid, it will improve the maintenance costs for the air heater, pack installation costs, reduced FD and ID fan capacity requirements, and possibly will increase the life expectancy of element packs. A feasibility study must be done

to compare the increased cost due to increased coal flow required in comparison to the possibility of running without a partial load loss condition.

As further evaluation of the capability of the VBA RAH model the effects of blocked air heaters and increased leakage rates were simulated. The results yielded that the air heater performance deteriorates with an increase in leakage, causing increased thermal dry flue gas losses and deteriorating the boiler performance. In essence both the ID fan and FD fan start to operate at higher operating capacities and electrical currents, therefore incurring additional auxiliary power consumption. In addition to this the coal flow rates increase which then also requires more combustion air. The augmented volumes of combustion air and coal introduce increased flue gas volumes, which places additional strain on the ID fan capacity.

Over the years, the Rankine cycle efficiency started to deteriorate due to increased losses to the condensate system along with unavailability of High Pressure steam heaters and Low Pressure steam heaters. These losses require additional heat energy to be recovered by the boiler. This lost energy must be recovered by increasing the heat energy input to the boiler. The boiler in general operates at higher heat input rates which requires increased volumes of combustion air and increased volume of flue gas extracted from the boiler. The additional work required from the boiler adds more strain to the capacity of the boiler. If the air heaters operate with excessive blockage and leakage, the research results clearly show that the fan will start to operate at its maximum capacity. For the case of experiencing both blockage and leakage, the impact on boiler performance was assessed. The results showed ultimately a load reduction (partial load loss) will be required, due to the limitation on the fan capacity operating at a maximum.

This research showed that the dew point related fouling tool has the ability to assess and evaluate methods of avoiding these load losses. The VBA RAH model can equip system engineers with the knowledge to enhance operating conditions and maintenance strategies. The research showed that the VBA RAH model can assist to improve life expectancy of air heater element packs, and draught group components such as ducting, dampers and supple joints. It can reduce the risk of the occurrence of dew point related fouling, and improve cleaning of the element packs. It further evaluates the impact of air heater operating and design amendments, to the overall boiler performance. Although the simulation results did not exactly correlate to the measured performance, the impact of changes in boiler performance can be evaluated, providing a platform for performance analysis. The research benefits Eskom coal fired power generating plants through providing a platform of evaluating methods to reduce maintenance costs and production losses, which will contribute to improved and sustainable operating of coal fired power generation plants.

7. RECOMMENDATIONS

For this research project the dew point related fouling prediction tool showed numerous areas for improvement and possibilities of further research requirements. Limitations were also evident in terms of the effects of each variable in the air heater processes. These limitations include:

- The effects of mal-distribution of flow.
- The effects of heat transfer to surroundings on the thermal performance.
- The effects of heat transfer from the steel matrix and the baskets used for improving fitment of packs.
- The effect of fouling to the heat transfer surface impacting the heat transfer coefficients.
- The effect of gaps between the layers.
- The required soot blowing pressures to remove fouled deposits.
- The effects of adding condensate during ineffective soot blowing and the affects it has on fouling conditions.
- Accuracy and effects of entrained ash to fouling and thermal performance.
- The effects of deposition rates for regenerative rotary air heaters.

Recommendation for areas of improvement and further research:

- There were numerous challenges regarding the thermocouple installation process. The installation technique of press fitting the metal temperature thermocouples was not effective and requires better contact between the thermocouple and the element sheet, with adequate insulation for the abrasive environment of the air heaters. More effective and alternative methods must be found to measure pack metal and fluid temperatures.
- The measuring techniques could have been improved based on the flue gas error identified from the flue gas measurements. The effects of mal-distribution and reverse flow, due to incorrect measuring point allocation must be investigated. This will assist to introduce correction factors to the measurements taken at these points.
- The ideal method of validation requires measurements taken from a new set of element packs. The factor of fouled element packs even after high pressure washing introduced some variability into the expectation for the results.
- Ideally the validity of the model must be tested on other regenerative air heaters. It is recommended to do plant experiments for other regenerative air heaters to further evaluate the VBA RAH model validity
- The measurement of the sulphuric acid dew point temperature was limited by the ash content in flue gas. Therefore, it could not be included in this research project, although other methods were identified, but due to the specialization and costly nature of equipment required to measure this parameter, the project budget did not cater for this activity. It is recommended to include this in future research projects for further validation of the estimation of sulphuric acid dew point temperatures.
- Some stations have two separate primary and secondary air heaters. For these cases a control system exists to control flow to each air heater from the economiser flue gas exit flow. This control system creates variability with regard to the flow distribution for the air heaters. This is not taken into account and is recommended to be added to the VBA RAH capability for future use.

- The availability of the latest technological developments such us element pack profile changes, seal arrangement changes and enamel coating of element packs must be investigated and identified. This information can then be used to test the effects on thermal properties of these developments.
- It is recommended to further research the air heater cleaning capacity requirements and capabilities for Eskom power plants to ensure that the installed soot blowing equipment can prolong the life expectancy of element packs.
- Another recommended field for further research is measure pressure drop more accurately, and to identify methods of improving the error from simulation models to better suit the actual differential pressures.
- It is recommended to investigate the performance characteristics of the air heater in the case of removing the third layer of element packs. This test must also be validated by experimental experiments. If this option is proven to be valid it will improve the maintenance costs for the air heater, pack installation costs, reduced FD and ID fan capacity requirements and possibly will increase the life expectancy of element packs. A feasibility study must be done to compare the increased cost due to increased coal flow required in comparison to the possibility of running without a partial load loss condition.

8. REFERENCES

Abel E, 1946. The vapor phase above the system sulfuric acid-water. *J. Phys. Chem,* Volume 50, pp. 260-282.

Abel E, 1947. On the experimental bases for the calculation of the sulfuric acid vapor pressure above the sulfuric acid-water system. *J. Phys. Chem.,* Volume 50, pp. 908-914.

Africa, U. o. S., 2018. *Computer integration in the classroom.* CIC2601/1/2019 ed. Muckleneuk, Pretoria: University of South Africa.

Bailey, K., 1999. Optimize heat exchanger operations by minimizing fouling.. *Hydrocarbon Processing,* 78(6), pp. 113-117.

Brandt, W., 2015. *Unit 2 BMFT due to inadequate secondary air flow (<20% BMCR),* Lephalale: ESKOM Matimba Power Station.

Brandt, W., 2018. *Engineering Change Root Cause Analysis for Air heater Ash fouling Report,* Lephalale: Eskom Matimba Power Station.

Caby, M. J., 1996. *Experimental Investigation of Heat Transfer in Regenerative Heat Exchangers,* Johannesburg: MSc(Eng) dissertation, University of the Witwatersrand.

Chojnowski, B. C. P., 1981. *Performance and operational aspects of power station Regenerative air Preheaters.* s.l., New Energy Conservation Technologies and their Commercialisation, Proceedings of an international conference.

Crookes, R. A., 2000. *Erosion by Fly Ash of Regenerative Air Pre-heater Elements in Power Stations,* Johannesburg: MSc(Eng) dissertation, University of the Witwatersrand.

D'Agostini, M. D., Levy, E. & Eskenazi, D., 1989. *Condensation and Evaporation of acid in regenerative air heaters.* Knoxville, Tennesse, Heat-rate Improvement Conference..

Davis, B. R., 2020. *Medium.com.* [Online]
Available at: https://medium.com/@brianrusseldavis/things-to-consider-before-implementing-byod-in-your-organization-fbba0919a2ea
[Accessed 10 10 2021].

De Klerk, G., 2001. *An Improved Simulation Model for Rotary Regenerative Air Heaters,* Johannesburg: MSc(Eng) dissertation, University of the Witwatersrand.

De Klerk, G. B., Sheer, T. J., Jawurek, H. H. & M., L., 2013. A Versatile Computor Simulation Model for Rotary Regenerative Heat Exchangers. *Heat Transfer Engineering,* 3 April, pp. 1-13.

Dekenah, M. & Heunis, S., 2010. A load profile prediction model for residential consumers. *Energize,* pp. 46-49.

Dudley, B., 2017. BP Statistical Review of World Energy 2017 - full report. *BP Statistical Review of World Energy 2017,* June, p. 52.

Eskom, 2017. *Eskom Heritage - Power Stations,* Johannesburg: Eskom.

ESKOM, S. G. M., 2018. *Fossil Fuel Firing Regulation.* Revision 2 ed. s.l.:ESKOM - Generation Division.

Feng J F, S. Y. T. Y. R. C., 2003. Principle and Calculation of the Boiler. *Science Pres,* pp. 371-373.

Ganapathy, V., 1989. *Cold end corrosion: Causes and cures.* Texas(Abeline): ABCO Industries.

Giauque W F, e. a., 1963. The thermodynamic properties of aqueous sulfuric acid solutions and hydrates from 15 to 300 K. *J. Am. Chem. Soc,* Volume 85, pp. 287-289.

Govendsamy, R., 2014. *Thermal Performance Evaluation of Heat Exchangers in Pulverised coal boilers,* Johannesburg: MSc(Eng) dissertation, University Of the Witwatersrand, Combustion Engineering.

Gruen, K., 1998. *Heat transfer and pressure drop of regenerative air preheaters elements,* Johannesburg: MSc(Eng) dissertation, University of the Witwatersrand.

Haase R, B. H. W., 1963. Präzisionsmessungen zur ermittlung von sauertaupunkten. *Korrosion,* Volume 15, pp. 47-49.

Habbitts, S., 1998. *Computer Simulation of Power Station Regenerative heat exchangers,* Johannesburg: MSc(Eng) dissertation, University of the Witwatersrand.
Halstead W D, T. J., n.d. Sulphuric acid dew point in power station flue gases. *J. Energy Inst,* Volume 53, pp. 142-145.

Han H, H. Y. L. T. W. Q., 2013. A numerical study of the deposition characteristics of sulfuric acid vapor on heat exchanger surfaces. *Chem. Eng. Sci,* Volume 101, pp. 620-630.
He Y, e. a., 2015. Sulfuric acid deposition characteristics of H-type finned tube bank with 10 rows. *Int. J. Heat Mass Transfer,* Volume 81, pp. 137-141.

H, K. Y., 1981. Predicting dew points of acid gases. *Chem. Eng,* 2(9), p. 127.
Hodge F G, S. W. L., 1994. Predicting the corrosivity of an operating FGD system. *Power Eng,* Volume 12, pp. 30-33.

International, E. A., 2013. *Key World Energy Statistics,* s.l.: s.n.,

Jones, L. J., 1993. *A review for the mechanisms of sulphuric acid formation and deposition, and dew point corrosion in coal fired boilers,* s.l.: ESKOM TSI Materials Technology.

Kalisz, S. et al., 2015. *DEVELOPMENT OF A ROTARY AIR HEATER CONTROL SYSTEM (RAH+) FOR BETTER AVAILABILITY AND A SAFE LOWERING OF EXIT FLUE GAS TEMPERATURE,* Gliwice: Silesian University of Technology, Institute of Power Engineering and Turbomachinery, Gliwice, Poland.

Kiang Y H, 1981. Predicting dew points of acid gases. *Chem. Eng,* 2(9), p. 127.

Kleynhans, H., 2015. *Draught group training for System Engineers.* Pretoria, Eskom.

Kleynhans, H. & Eganza, J., 2016. *ID Fans At Maximum Capacity. Guideline-Possible Causes and Contributors Guideline,* s.l.: ESKOM, Technology Engineering.

Kumar, K. P., 1998. *Heat transfer charachteristics of air heater heating elements,* Johannesburg: MSc(Eng) dissertation, University of the Witwatersrand.

Kunze E, 2000. *Korrosion Und Korrosionsschutz.* s.l.:Wiley.

Kunz, R. G., 2011. Environmental Calculations: A multimedia approach. In: s.l.:John Wiley & Sons.

Larsen & Toubro, L., 2018. *L&T Power.* [Online]
Available at: http://www.lntpower.com/products-services/coal-based-power-plants/power-block-auxiliaries/[Accessed 20 February 2018].

Laubscher, E., 2015. *Eskom Fact Sheet,* Johannesburg: Eskom.

Levy E K, W. R. W., 1989. A method for calculating acid deposition rates in regenerative air preheaters, in. *National Heat Transfer Equipment Fundamentals, Design, Applications and Operating Problems,* pp. 289-296.

Mabena, B. S., 2003. *Fouling in boiler regenerative air preheaters,* Johannesburg: MSc(Eng) dissertation, University of the Witwatersrand.

Mallikarjuna, V., Jashuva, N. & Reddy, B. R. B., 2014. IMPROVING BOILER EFFICIENCY BY USING AIR PREHEATER. *International Journal of Advanced Research in Engineering and Applied Sciences,* February, 3(2), pp. 1-14.

Maskew, J. T. et al., 1998. *EVALUATION OF AIR HEATER PERFORMANCE AND THE ACCURACY OF THE RESULT,* New York: CONSOL R&D LIBRQRY.

Mathebula, N. V., 2014. *Observation and the classification of the fouling mechanisms in rotary air heaters,* Johannesburg: MSc(Eng) dissertation, University of the Witwatersrand.

Mbabazi, J. G., Sheer, T. & Shandu, R., 2003. A model to predict erosion on mild steel surfaces impacted. *Elsevier,* 16 June, p. 13.

Mbabazi, J. & Sheer, T., 2005. Computational prediction of erosion of air heater. *Elsevier,* 28 July, p. 15.

Mohanty, C. R., Swar, A. K., Meikap, B. C. & Sahu, J. N., 2011. Studies on factors influencing fly ash resistivity from electrostatic precipitator with reference to India. *Journal of Scientific & Industrial Research,* Volume 70, pp. 795-803.

Müller, P., 1959. Contribution to the problem of the action of sulfuric acid on the dew point temperature of flue gases. *Chem. Eng. Technol.,* Volume 31, pp. 345-450.

Mullisen R S, L. R. I., 1986. A transient heat exchanger evaluation test for arbitrary fluid inlet temperature variation and longitudinal core conduction.. *Journal of Heat transfer,* May.Volume 108.

Okkes A G, B. B. V., 1987. Get acid dew point of flue gas. *Hydrocarbon Process,* pp. 53-55.

Qin K F, F. J. R. C. Z. H., 1994. Boiler and Heat Exchanger Fouling, Slagging, Abrasion and Corrosion Prevention Principles and Calculation. *Science Press,* pp. 377-389.

Raask, E., 1963. *Reactions of coal impurities during combustion and deposition of ash constituants on cooled surfaces.* s.l., The Mechanism of Corrosion by Fuel Impurities, pp. 145-155.

Raask, E., 1985. *Mineral Impurities in Coal Combustion,* s.l.: Hemispher Publications.

Reid, R. C., Prausnitz, J. M. & Poling, B. E., 1986. The properties of gasses and liquids. In: Fourth ed. s.l.:McGraw-Hill Book Company, p. 407 & 530.

Scheidegger, R., 2013. *Matimba Air preheater site visit,* Johannesburg: Clyde Bergemann Africa (Pty) Ltd.

Sonntag, R. E. B. C. a. V. W. G. J., 2003. *Fundamentals of Thermodynamics.* 6 ed. s.l.:Wiley & Sons, Inc..

Spot, P. B. C. B., 2016. *Power By Coal,* s.l.: Thermal Power Plant.

Van Alphen, D. C., 2018. *Matimba: Air Heater Ash,* Johannesburg: Eskom: Fuel combustion - Plant performance and optimization.

Van der Hooven, A., 1998. Thermal Power Station Air Heater Blockage. *South African Mechanical Engineer,* 48(5), pp. 13-16.

Van der Hoven, A., 1998. Thermal Power Station Air heater blockage. *South African Mechanical Engineer,* 48(5), pp. 13-16.

Van Wyk, C., 2010. *Boiler Mass and Energy Guideline, Rev 4,* Middelburg: ESKOM PU3 Engineering Head Office.

Verhoff F H, B. J. T., 1974. Predicting dew points of flue gases. *Chem.Eng. Prog,* 70(8), pp. 171-172.

W M Kays, A. L. L., 1984. Compact Heat Exchangers. In: Third, ed. New York: McGraw-Hill.

WAIN, B. &. & ENERGY, A., 2016. *Regenerative Heat exchangers,* s.l.: BURMEISTER & WAIN ENERGY A/S.

Wang Y C, T. G. H., 2014. Acid condensation and heat transfer characteristics on H-type fin surface with bleeding dimples and longitudinal vortex generators. *Chin. Phys. Lett,* 59(33), pp. 4405-4417.

Wang Y C, T. G. H., 2016. Prediction of sulfuric acid dew point temperature on heat transfer fin surface. *Appl. Therm. Eng,* Volume 98, pp. 492-501.

Wei W, F. S. Y. S. M., 2017. Theoretical prediction of acid dew point and safe operating temperature of heat exchangers for coal-fired power plants. *Applied Thermal Engineering,* Volume 123, pp. 782-790.

Williams, A., Pourkashanian, M., J, M. J. & Skorupska, N., 2018. Properties of coal. In: *Combustion and Gasification of coal.* s.l.:s.n.

Wilson R W, 1989. *Condensation of Sulfuric Acid and Water Mixtures in Laminar Flow,* s.l.: Lehigh University.

Wilson, R. W., Sheer, T. J. & Jawurek, H. H., 1998. Erosion Prediction in Rotary Regenerative Air Preheaters. *South African Conference on applied mechanics,* 2(2nd), pp. 1127-1137.

Xiang B X, X. W. C. L. J. F. e. a., 2014. The measurement and correction of correlation formulas of flue gas acid dew point. *Boiler Technol,* 45(1), pp. 1-4.

Xiang B X, Z. C. H. D. Y. J. e. a., 2015. Measuring and analyzing the prediction model on the acid dew point in flue gas. *J. Tsinghua Univ (Sci. Technol.),* 55(10), pp. 1117-1124.

Xiang B, e. a., 2016. Predicting acid dew point with a semi-empirical model. *Appl. Therm. Eng.,* Volume 106, pp. 992-1001.

ZareNezhad B, A. A., 2010. A multi-layer feed forward neural network model for accurate prediction of flue gas sulfuric acid dew points in process industries. *Appl. Therm. Eng,* 30(6), pp. 692-696.

9. APPENDICES
A. APPENDIX - Theoretical Technical Data

A1: Element pack properties table

Table A1: Heat transfer and pressure drop correlations for all the element packs tested (De Klerk, et al., 2013).

PROFILE	Mass	Area of Conv	Area of Cond	A	B	C	D	THICK CORR	THICK UND
278DU	31.05000	16.34000	0.00817	0.13550	-0.35430	0.72940	-0.40360	0.50000	0.50000
278DU	49.46000	16.07000	0.01286	0.17040	-0.37080	1.18350	-0.44460	0.80000	0.80000
278DU	39.33000	16.09000	0.01010	0.16740	-0.37040	1.10660	-0.44680	0.50000	0.80000
H8(ROT)	35.89000	18.34000	0.00917	0.06420	-0.28350	0.56980	-0.40190	0.50000	0.50000
H8(H)	35.32000	18.03000	0.00900	0.06940	-0.28170	0.55190	-0.39710	0.50000	0.50000
K4	57.08000	28.89000	0.01440	0.07870	-0.29160	0.68930	-0.45140	0.50000	0.50000
K5	51.24000	26.20000	0.01310	0.08130	-0.29450	0.98220	-0.48940	0.50000	0.50000
K5	62.91000	25.40000	0.01610	0.07680	-0.30000	0.89650	-0.47930	0.50000	0.80000
K6	47.58000	23.57000	0.01180	0.11140	-0.28160	0.86940	-0.46020	0.50000	0.50000
K6	59.67000	24.03000	0.01510	0.06290	-0.27230	0.65650	-0.44070	0.50000	0.80000
K6G	60.47000	31.73000	0.01590	0.00390	-0.00510	0.03630	-0.17410	0.50000	0.50000
K8	37.88000	19.30000	0.00970	0.06130	-0.27880	0.69360	-0.43700	0.50000	0.50000
K8	60.22000	18.73000	0.01500	0.05780	-0.27910	0.49330	-0.41260	0.80000	0.80000
K8	47.44000	18.73000	0.01170	0.04720	-0.24860	0.57740	-0.42720	0.50000	0.80000
K8G	45.60000	23.36000	0.01150	0.01010	-0.10660	0.15310	-0.30090	0.50000	0.50000
K8G	71.43000	23.64000	0.01890	0.00330	-0.00430	0.09130	-0.28630	0.80000	0.80000
K8G	54.85000	23.21000	0.01450	0.00830	-0.08130	0.14950	-0.31100	0.50000	0.80000
KH10	38.96000	19.71000	0.00990	0.00660	-0.06860	0.17740	-0.34290	0.50000	0.50000
KH11	33.83000	17.78000	0.00900	0.05670	-0.28140	0.46840	-0.39220	0.50000	0.50000
KH11	49.75000	16.00000	0.01280	0.04070	-0.24220	0.27700	-0.33560	0.80000	0.80000
KH11	39.67000	16.47000	0.01050	0.03680	-0.22360	0.59770	-0.43090	0.50000	0.80000
V75	40.63000	21.60000	0.01080	0.06400	-0.28620	0.62160	-0.43710	0.50000	0.50000
V75	61.61000	20.40000	0.01630	0.06480	-0.28540	0.37680	-0.38120	0.80000	0.80000
V75	50.76000	21.03000	0.01320	0.05180	-0.26130	0.59050	-0.43840	0.50000	0.80000
N/A	0.00000	0.00000	0.00000	0.00000	0.00000	0.00000	0.00000	0.00000	0.00000

A2: Calculation of the heat transfer coefficient

As described in chapter 2, a thermal test facility was built by Caby (1996) to measure the heat transfer coefficient and pressure drop of a sample pack. The facility was built to test all the available element packs, but packs with equal thickness plates were only considered. Gruen's research indicated how severe the changes in thermal properties are when different thicknesses are used. The heat transfer model from Habbitts (1998) did not take this aspect into account. De Klerk (2001) reviewed the simulation code to add the capability of simulating alternating thickness of the element plates. Table A1 is a representation of the results from this test, showing the constants for calculating both the Colburn j factor and the Fanning friction factor

in relation to the Reynolds number. Area of conduction, area of convection, mass and plate thickness are included. This information is used to calculate the thermal properties to estimate the gas and metal temperatures of the air heaters. The change of the heat transfer coefficient is calculated at every time step for each layer. Using Table A1 of, the heat transfer and pressure drop correlations for all the tested plate configurations a heat transfer coefficient can be generated. During these tests, a range of the Reynolds numbers was used with face velocities between 0, 4 m/s to 12 m/s. For each pack type a set of values for Colburn-j factors versus Reynolds number were obtained. The Colburn-j factor can be calculated using Stanton number multiplied with Prandtl number to the power of 2/3. This is illustrated in equation 1 (Habbitts, 1998):

$$j = St \times (Pr)^{2/3} \quad (1)$$

Colburn-j factor relationship with the Reynolds number can be expressed using factor A and B from the heat transfer and pressure drop correlations for all the tested plate configurations.

$$j = A \times Re^{B} \quad (2)$$

Substituting equation 1 into 2:

$$A \times Re^{B} = St \times (Pr)^{2/3} \quad (3)$$

The Stanton number is a relationship of the heat transfer coefficient divided by the product of heat capacity of the fluid and the mass velocity of the fluid (Habbitts, 1998):

$$A \times Re^{B} = (h/(G \cdot C_f)) \times (Pr)^{2/3} \quad (4)$$

Prandtl number is the product of the dynamic viscosity and the heat capacity of the fluid, divided by the conductivity of the fluid (Habbitts, 1998):

$$Pr = \mu \cdot C_f / k_f \quad (5)$$

The fluid mass velocity relationship is the mass flow rate divided by the free flow area:

$$G = \dot{m}/[(1 - A_{cond}/A_{total\ flow}) \times A_{total\ flow}] \quad (6)$$

Using equations 5 and 6, the heat transfer coefficient (h) equation can be written by rearranging equation 4:

$$h = \frac{(A \times Re^{B})(\dot{m} \cdot C_f / [(1 - A_{cond}/A_{total\ flow}) \times A_{total\ flow}])}{(Pr)^{2/3}} \quad (7)$$

A3: Calculation of the pressure drop

The results of the pressure drop tests were formulated in terms of the Fanning friction factor versus the Reynolds number. For an air heater element pack the Reynolds number can be calculated using the hydraulic diameter (equation 8) multiplied with the fraction of the average velocity (m/s) of flow in the pack divided by the kinematic viscosity (m^2/s). Habbitts used the mass velocity (kg/ m^2s) and the dynamic viscosity (kg/ms) as indicated in equation 74.

$$D_h = \frac{4 \cdot (1 - A_{cond}/A_{total\ flow}) \cdot L}{A_{conv}/A_{total\ flow}} \quad (8)$$

$$Re = D_h \cdot \frac{G}{\mu} \quad (9)$$

The pressure drop is calculated using the fanning friction factor equation 10. This equation takes into consideration the entrance and exit factors to isolate the losses associated with the fluid flowing through the pack. The loss coefficients K_c (Equation 11) and K_e (Equation 12) are calculated by the formulae presented by Kays and London (1984) for triangular duct geometry (De Klerk, 2001). The fanning friction factor can also be represented as a relationship with the Reynolds number. This relationship was illustrated with factor C and D from the table of heat transfer and pressure drop correlations for all the tested plate configurations in table 1. Equation 13 is an illustration of this relationship.

$$f = \frac{D_h}{4L}\left[2\rho\left(\frac{\Delta P}{G^2}\right) - (K_c + K_e)\right] \quad (10)$$

Entrance of contraction loss coefficient:

$$K_c = -0.3834\left(1 - A_{cond}/A_{total\ flow}\right)^2 - 0.0029\left(1 - A_{cond}/A_{total\ flow}\right) + 0.5566 \quad (11)$$

Exit of expansion loss coefficient:

$$K_e = 0.9930\left(1 - A_{cond}/A_{total\ flow}\right)^2 - 2.1385\left(1 - A_{cond}/A_{total\ flow}\right) + 0.9935 \quad (12)$$

The fitted curve of the form $y=Ax^B$ is fitted for each set of results. For the pressure drop the coefficient C and D is used to calculate the fanning friction factor$f$.

$$f = C \cdot Re^D \quad (13)$$

The final pressure drop equation can now be formulated by substituting equation 13 in equation 10 making pressure drop the independent variable:

$$\Delta P = \left(\frac{4L \cdot (C \cdot Re^D)}{D_h} + (K_c + K_e)\right) \cdot \left(\frac{G^2}{2\rho}\right) \quad (14)$$

This pressure drop can now be used to calculate the partial pressures for the constituents of the fluids in the air heater to determine what the dew point temperatures will be.

A4: Air heater leakage derivation

- ***Air in - leakage***

$$\dot{m}_{leak} = \dot{m}_{a,out} - \dot{m}_{a,in} \quad (1)$$

$$\%Air\ leakage = (\dot{m}_{\ leak} / \dot{m}_{a,in}) \times 100 \quad (2)$$

$\dot{m}_{leak}$– Mass flow of the air leaking to the flue gas stream internal to the air heater
$\dot{m}_{a,in}$– Mass flow of the air entering the air heaters
$\dot{m}_{a,out}$– Mass flow of the air exiting the air heaters
$\dot{m}_{fg,sah,in}$ – Mass flow of the flue gas entering the secondary air heater
$\dot{m}_{fg,sah,out}$– Mass flow of the flue gas exiting the secondary air heater

The mass fraction of O_2 is used to predict leakage, assuming that no flue gas leaks into the air stream and that the mass fraction of O_2 at both the inlet- and outlet-airstreams is 23%:

$$\dot{m}_{fg,sah,in} + \dot{m}_{a,in} = \dot{m}_{fg,sah,out} + \dot{m}_{a,out} \quad (3)$$

$$(O_{2\ fg,sah,in} \times \dot{m}_{fg,sah,in}) + (O_{2\ a,in} \times \dot{m}_{a,in}) = (O_{2\ fg,sah,out} \times \dot{m}_{fg,sah,out}) + (O_{2\ a,out} \times \dot{m}_{a,out}) \quad (4)$$

$O_{2\ a,in}$– Mass fraction of the oxygen entering the air heaters
$O_{2\ a,out}$– Mass fraction low of the oxygen exiting the air heaters
$O_{2\ fg,sah,in}$ – Mass fraction of the oxygen in the flue gas entering the secondary air heater
$O_{2\ fg,sah,out}$– Mass fraction of the oxygen in the flue gas exiting the secondary air heater

$$(O_{2\ a,in} \times \dot{m}_{a,in}) = (O_{2\ fg,sah,out} \times \dot{m}_{fg,sah,out}) + (O_{2\ a,out} \times \dot{m}_{a,out}) - (O_{2\ fg,sah,in} \times \dot{m}_{fg,sah,in}) \quad (5)$$

Rearranging equation 3:

$$\dot{m}_{a,out} = \dot{m}_{fg,sah,in} + \dot{m}_{a,in} - \dot{m}_{fg,sah,out} \quad (6)$$

Substitute equation 6, into equation 4 (include the assumption of 23 %,O_{2air}):

$$(O_{2\ fg,sah,in} \times \dot{m}_{fg,sah,in}) + (0.23 \times \dot{m}_{a,in}) = (O_{2\ fg,sah,out} \times \dot{m}_{fg,sah,out}) + (0.23 \times (\dot{m}_{fg,sah,in} + \dot{m}_{a,in} - \dot{m}_{fg,sah,out})) \quad (7)$$

Simplify equation 7 to find the mass flow of the flue gas exiting the air heater

$$\dot{m}_{fg,sah,out} = \frac{\dot{m}_{fg,sah,in} \times (0.23 - O_{2\ fg,sah,in})}{(0.23 - O_{2\ fg,sah,out})} \quad (8)$$

Substitute equation 8 into equation 3:

$$\dot{m}_{fg,sah,in} + \dot{m}_{a,in} = \frac{\dot{m}_{fg,sah,in} \times (0.23 - O_{2\ fg,sah,in})}{(0.23 - O_{2\ fg,sah,out})} + \dot{m}_{a,out} \quad (9)$$

$$\dot{m}_{leak} = \dot{m}_{a,in} - \dot{m}_{a,out} = \frac{\dot{m}_{fg,sah,in} \times (0.23 - O_{2\,fg,sah,in})}{(0.23 - O_{2\,fg,sah,out})} - \dot{m}_{fg,sah,in} \quad (10)$$

Rewrite equation 2:

$$\%Air\ leakage = \left[\frac{\dot{m}_{fg,sah,in} \times (0.23 - O_{2\,fg,sah,in})}{(0.23 - O_{2\,fg,sah,out})} - \dot{m}_{fg,sah,in}\right] \times \frac{1}{\dot{m}_{a,in}} \times 100 \quad (11)$$

$$\%Air\ leakage = \left[\frac{(0.23 - O_{2\,fg,sah,in})}{(0.23 - O_{2\,fg,sah,out})} - 1\right] \times \frac{\dot{m}_{fg,sah,in}}{\dot{m}_{a,in}} \times 100 \quad (12)$$

$$\%Air\ leakage = \left[\frac{(0.23 - O_{2\,fg,sah,in})}{(0.23 - O_{2\,fg,sah,out})} - \frac{(0.23 - O_{2\,fg,sah,out})}{(0.23 - O_{2\,fg,sah,out})}\right] \times \frac{\dot{m}_{fg,sah,in}}{\dot{m}_{a,in}} \times 100 \quad (13)$$

$$\%Air\ leakage = \left[\frac{(O_{2\,fg,sah,out} - O_{2\,fg,sah,in})}{(0.23 - O_{2\,fg,sah,out})}\right] \times \frac{\dot{m}_{fg,sah,in}}{\dot{m}_{a,in}} \times 100 \quad (14)$$

A5: Lee-Kesler simple fluid compressibility factor graph

Table A5: The compressibility factor (Z) for 1 mole of gas at 1atmospheric pressure (Mathebula 2014).

T(°K)	T(°F)	Air	N_2	O_2	Ar	CO_2	CO	H_2O
300	80.3	0.9999	0.9998	0.9994	0.9995	0.9950	0.9997	-
450	350.33	1.0003	1.0003	1.0002	1.00015	0.9988	1.0003	0.993
600	620.33	1.0004	1.0004	1.0003	1.0003	0.9997	1.0005	0.998
1000	1340.33	1.0004	1.0003	1.0003	1.0002	1.0003	1.0004	1.000

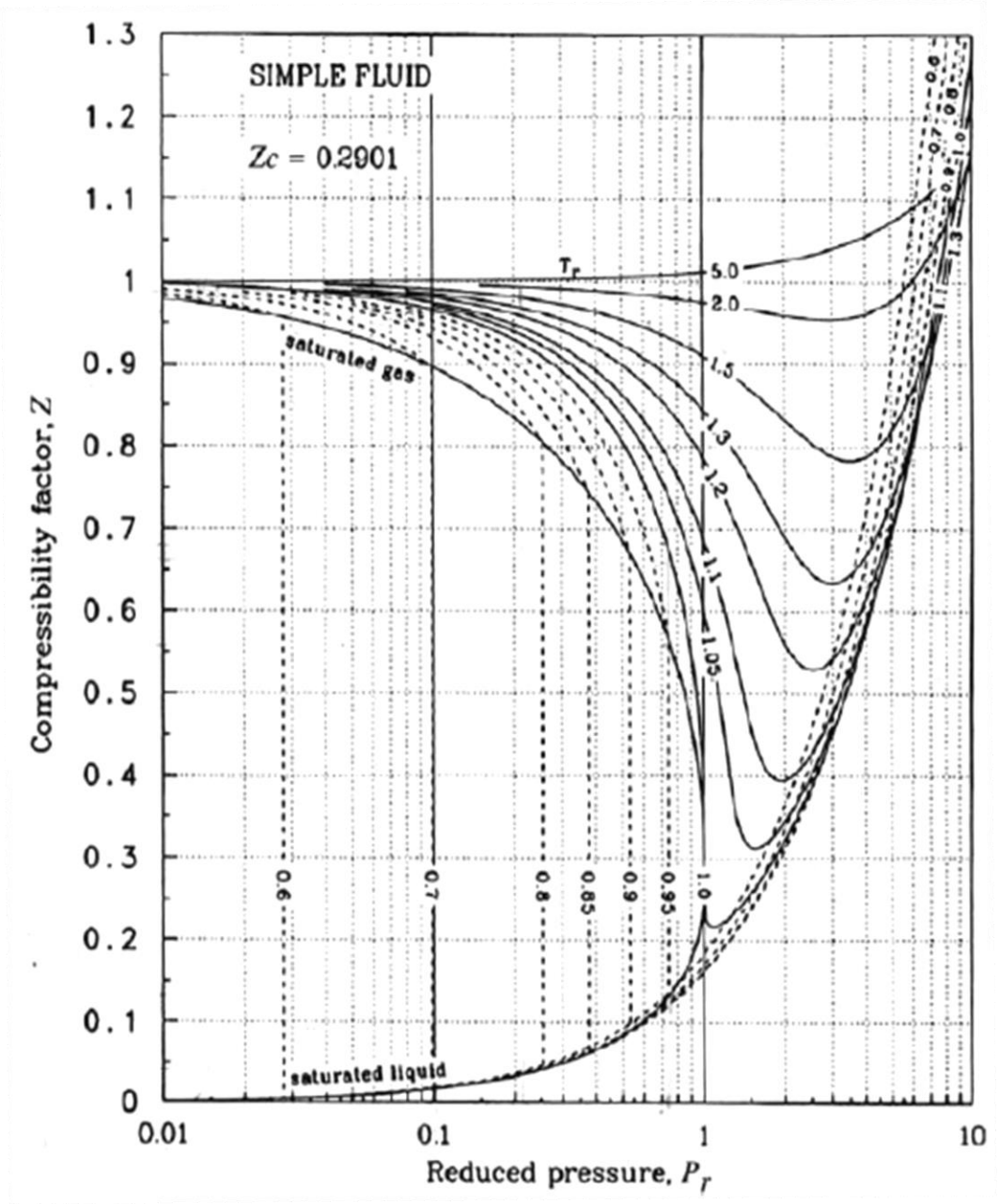

Figure A5: The Lee-Kesler simple fluid compressibility factor graph (Sonntag et al, 2003).

The compressibility factors for the flue gases can be seen in the table in Appendix A5, along with the Lee-Kesler simple fluid compressibility graph. For sulphur dioxide the compressibility

factor can be obtained from the Lee-Kesler simple fluid compressibility factor graph (Sonntag, 2003). This graph shows that sulphur dioxide has approximately a compressibility factor of 1. The pressure and temperature reduction can be calculated using the formulas from Sontag et al (2003). The pressure and temperature can then be used to establish the compressibility factors from the Lee-Kesler graph.

$$P_r = \frac{P}{P_c} \tag{3.73}$$

$$T_r = \frac{T}{T_c} \tag{3.74}$$

P – Absolute pressure of the flue gas, in kPa
T – Temperature for which the compressibility is determined, in °K
P_r – Reduced pressure
T_r – Reduced temperature
P_c – Critical pressure of flue gas component
T_c – Critical temperature of the flue gas component

B. APPENDIX - Drawing Register – Experimental Setup

B1: Experimental Setup Drawing Register

ASSEMBLY DRAWINGS

Drawing number	Title
AL100	Layer 1 TP assembly 1 of 2
	Layer 1 TP assembly 2 of 2
AL200	Layer 2 TP assembly
AL300	Layer 3 TP assembly
DP01	Dew point probe guide
DP00	Cable clamp
AT00	Experimental setup Total Assembly 1 of 2
	Experimental setup Total Assembly 2 of 2

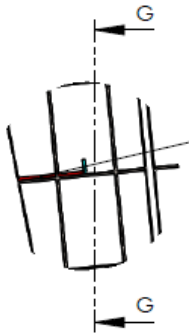

DETAIL B - Ring 6 Top and bottom installation
SCALE 1 : 20

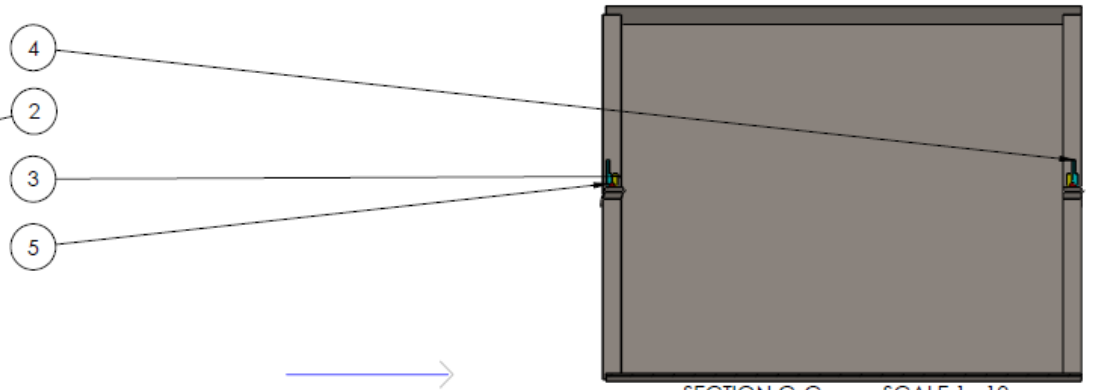

Flue gas entering

SECTION G-G; SCALE 1 : 10

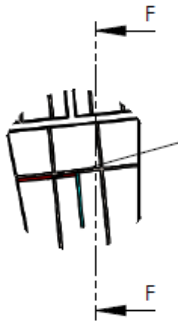

DETAIL D - Ring 2 Top and bottom installation
SCALE 1 : 20

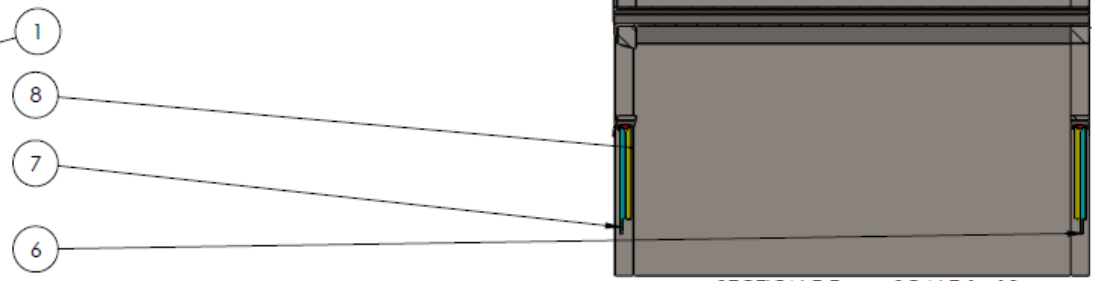

SECTION F-F : SCALE 1 : 10

ITEM NO.	REFERENCE DRAWING	DESCRIPTION	QTY.
1	AL100-TD01	Compensating wire protection - Angle Iron (R2)	2
2	AL100-TD03	Compensating wire protection - Angle Iron (R6)	2
3	AL100-TD04	Thermocouple protection Metal Temp Probe - 12x12 square tube (R6)	2
4	AL100-TD09	Thermocouple protection Gas Temp Probe - 12x12 square tube (R6)	1
5	AL100-TD11	Thermocouple protection Gas Temp Probe Top - 12x12 square tube (R6)	1
6	AL100-TD10	Thermocouple protection Gas Temp Probe - 12x12 square tube (R2)	1
7	AL100-TD12	Thermocouple protection Gas Temp Probe Top - 12x12 square tube (R2)	1
8	AL100-TD05	Thermocouple protection Metal Temp Probe - 12x12 square tube (R2)	2

Notes:
1) Ensure Item 1,2 are installed as indicated in ring 2 & 6 respectively, at the top and bottom support structure
2) Ensure Item 3 & 8(same component for bottom and top), 4,5,6 & 7 are installed as indicated in ring 6 and 2 (section G-G), at the top and bottom support structure
3) All components to be seal welded
4) Fill all hollow areas with high temperature silicone
5) Ensure that the compensating wire are inserted before the components are welded
6) Component to be machined using a tolerance of +-0.05mm
7) Drill 2, 10 mm holes as indicated in the drawing sheet 2 of 2, each 5mm to the left of ring 6 support arm where the angle iron is attached
8) Drill 1, 10 mm holes as indicated in the drawing sheet 2 of 2, 5mm to the right of ring 2 support arm where the angle iron is attached
9) Ensure that the direction of the Gas temperature probes protection shields are installed as indicated in the drawing section G-G and F-F

SCALE:1:50

MATERIAL:
Mildsteel

	NAME	SIGNATURE	DATE
DRAWN	W Brandt		
CHK'D	Pr. J Sheer		
APPV'D	Pr. W Schmitz		
MFG			
Q.A			

TITLE:

LAYER 1 TEST POINT ASSEMBLY

DWG NO. AL100

UNIVERSITY OF THE WITWATERSRAND

SHEET 1 OF 2

Eskom

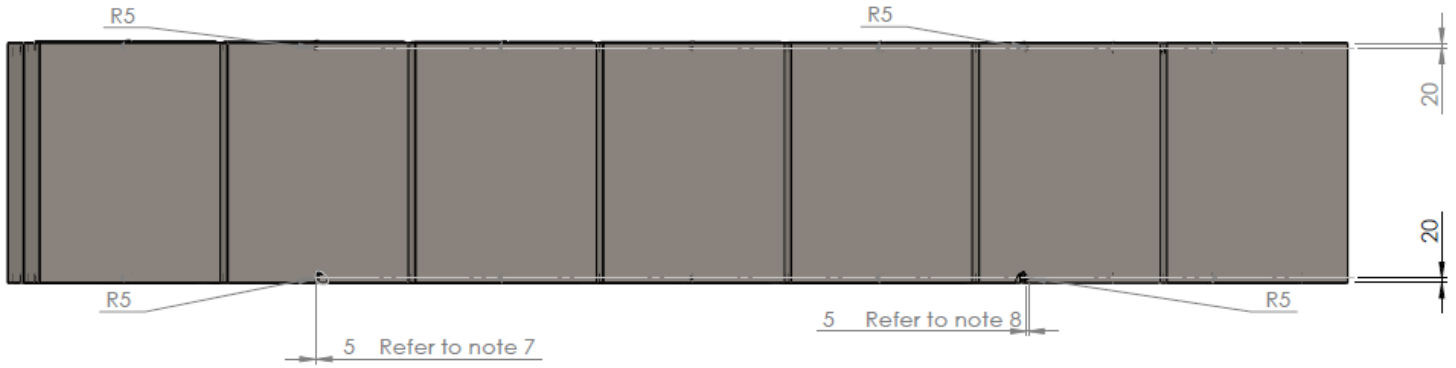

Notes:
1) Ensure Item 1,2 are installed as indicated in ring 2 & 6 respectively, at the top and bottom support structure
2) Ensure Item 3 & 8(same component for bottom and top), 4,5,6 & 7 are installed as indicated in ring 6 and 2 (section G-G), at the top and bottom support structure
3) All components to be seal welded
4) Fill all hollow areas with high temperature silicone
5) Ensure that the compensating wire are inserted before the components are welded
6) Component to be machined using a tolerance of +-0.05mm
7) Drill 2, 10 mm holes as indicated in the drawing sheet 2 of 2, each 5mm to the left of ring 6 support arm where the angle iron is attached
8) Drill 1, 10 mm holes as indicated in the drawing sheet 2 of 2, 5mm to the right of ring 2 support arm where the angle iron is attached
9) Ensure that the direction of the Gas temperature probes protection shields are installed as indicated in the drawing section G-G and F-F

SCALE:1:50

MATERIAL:
Mildsteel

	NAME	SIGNATURE	DATE
DRAWN	W Brandt		
CHK'D	Pr. J Sheer		
APP'D	Pr. W Schmitz		
MFG			
Q.A			

TITLE:
LAYER 1 TEST POINT ASSEMBLY

DWG NO. AL100

SHEET 2 OF 2

UNIVERSITY OF THE WITWATERSRAND

Eskom

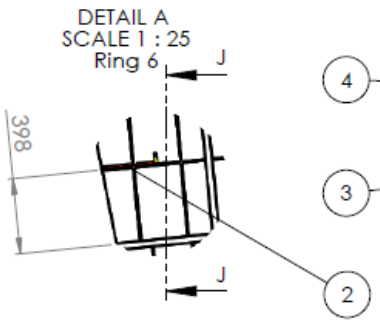

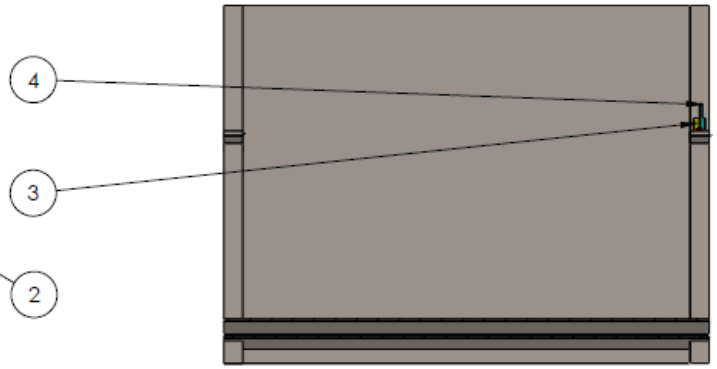

SECTION J-J: Ring 6 & 4 Temp Probes

SCALE 1 : 10

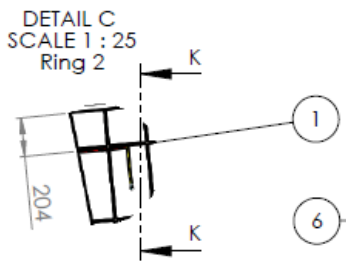

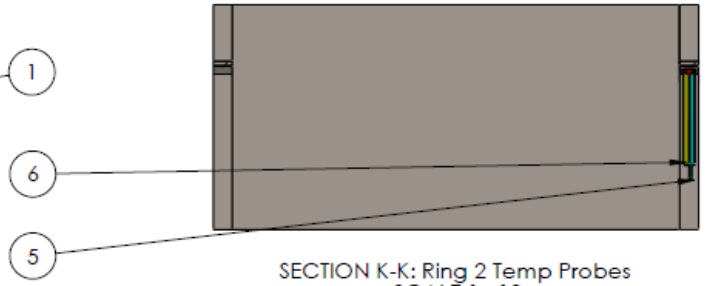

SECTION K-K: Ring 2 Temp Probes
SCALE 1 : 10

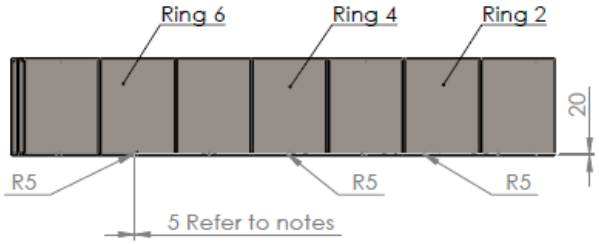

ITEM NO.	REFERENCE DRAWING	DESCRIPTION	QTY.
1	AL100-TD01	Compensating wire protection - Angle Iron (R2)	1
2	AL100-TD03	Compensating wire protection - Angle Iron (R6)	1
3	AL100-TD04	Thermocouple protection Metal Temp Probe - 12x12 square tube (R6)	1
4	AL100-TD09	Thermocouple protection Gas Temp Probe - 12x12 square tube (R6)	1
5	AL100-TD10	Thermocouple protection Gas Temp Probe - 12x12 square tube (R2)	1
6	AL100-TD05	Thermocouple protection Metal Temp Probe - 12x12 square tube (R2)	1

Notes:
1) Ensure item 2, 3 & 4 are installed as indicated in ring 6 , at the bottom support structure
2) Ensure item 1, 5 & 6 are installed as indicated at ring 2, at the bottom support structure
3) All components to be seal welded
4) Ensure that the compensating wire are inserted before the components are welded
5) Component to be machined using a tolerance of +-0.05mm
6) Drill 2, 10 mm holes as indicated in the drawing, each 5mm to the left of ring 6 support arm where the angle iron is attached
7) Drill 1, 10 mm holes as indicated in the drawing, 5mm to the right of ring 2 support arm where the angle iron is attached
8) Fill the hollow areas with high temperature silicone

SCALE:1:50

MATERIAL:
Mildsteel

	NAME	SIGNATURE	DATE
DRAWN	W Brandt		
CHK'D	Pr. J Sheer		
APPV'D	Pr. W Schmiltz		
MFG			
Q.A			

TITLE:
LAYER 2 TEST POINT ASSEMBLY

DWG NO. AL200

SHEET 1 OF 1

UNIVERSITY OF THE WITWATERSRAND

Eskom

Layer 3 Bottom view

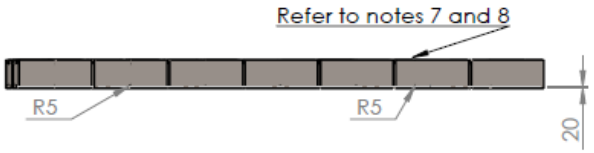

DETAIL F - Ring 2
SCALE 1 : 20

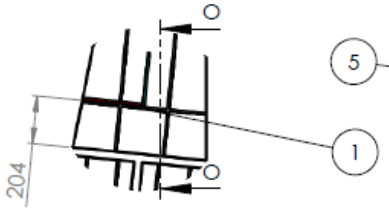

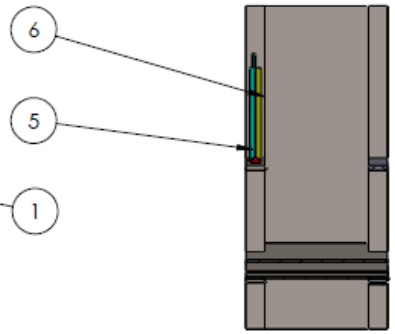

SECTION O-O

SCALE 1 : 10

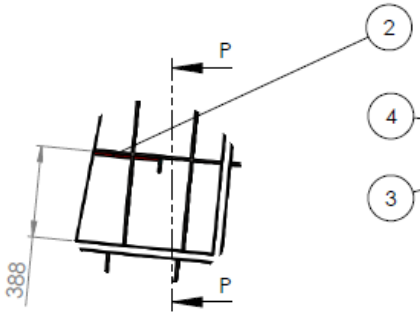

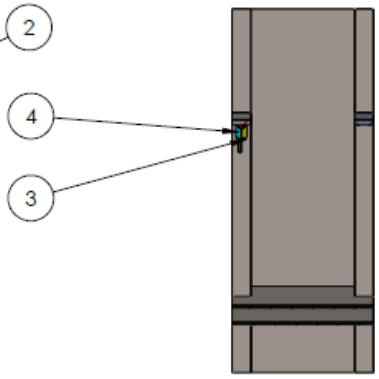

Flue Gas Entering

DETAIL J - Ring 6
SCALE 1 : 20

SECTION P-P

SCALE 1 : 10

ITEM NO.	REFERENCE DRAWING	DESCRIPTION	QTY.
1	AL100-TD01	Compensating wire protection - Angle Iron (R2)	1
2	AL100-TD03	Compensating wire protection - Angle Iron (R6)	1
3	AL100-TD04	Thermocouple protection Metal Temp Probe - 12x12 square tube (R6)	1
4	AL100-TD09	Thermocouple protection Gas Temp Probe - 12x12 square tube (R6)	1
5	AL100-TD10	Thermocouple protection Gas Temp probe - 12x12 square tube (R2)	1
6	AL100-TD05	Thermocouple protection Metal Temp Probe - 12x12 square tube (R2)	1

Notes:
1) Ensure item 1,2,3,4,5 & 6 are installed as indicated in ring 6 & 2 respectively, at the bottom support structure
2) Fill all the hollow areas with high temperature silicone
3) All components to be seal welded
4) Ensure that the compensating wire are inserted before the components are welded
5) Drill 5, 10 mm holes as indicated in the drawing, each 5mm to the left of ring 6 support arms where the angle iron is attached
6) Drill 1, 10 mm holes as indicated in the drawing, 5mm to the right of ring 2 support arm where the angle iron is attached

SCALE:1:50

MATERIAL:
Mildsteel

	NAME	SIGNATURE	DATE
DRAWN	W Brandt		
CHK'D	Pr. J Sheer		
APPV'D	Pr. W Schmitz		
MFG			
Q.A			

TITLE:

LAYER 3 TEST POINT ASSEMBLY

DWG NO. AL300

SHEET 1 OF 1

UNIVERSITY OF THE WITWATERSRAND

Eskom

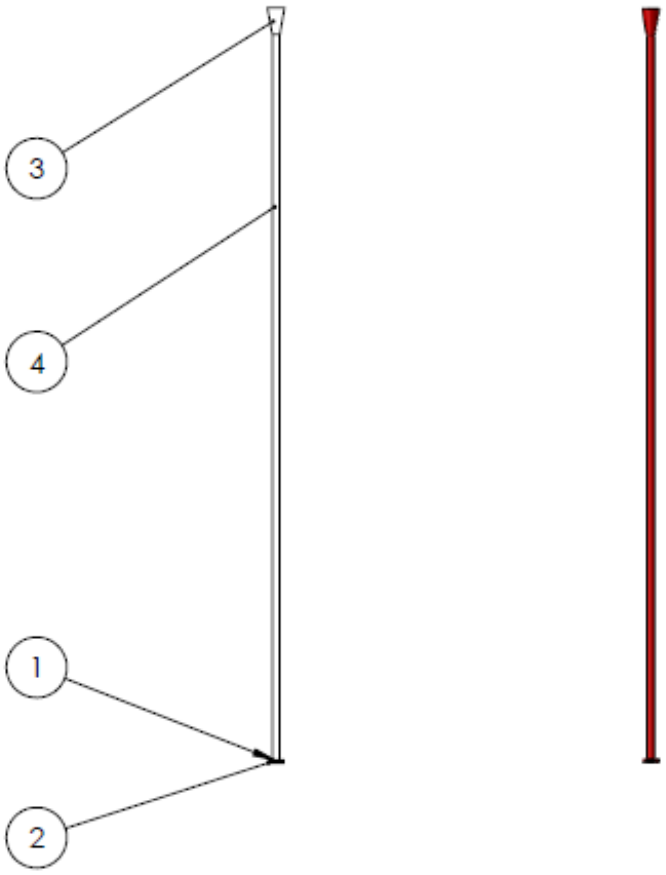

ITEM NO.	PART NUMBER	DESCRIPTION	QTY.
1	DP01-00	Insertion base plate	2
2	DP01-01	Insertion base plate lid	2
3	DP01-02	Dew point probe guide tube	2
4	DP01-03	Dew point probe guide tip	2

Notes:
1) Tolerance +/-0.5mm unless otherwise stated
2) Remove all sharp edges and burrs
3) N16 Finish all over unless otherwise stated

SCALE:1:50

MATERIAL: Mildsteel

QTY:

	NAME	SIGNATURE	DATE
DRAWN	W Brandt		
CHK'D	Pr. J Sheer		
APPV'D	Pr. W Schmitz		
MFG			
Q.A			

TITLE: DEW POINT PROBE GUIDE

UNIVERSITY OF THE WITWATERSRAND

DWG NO. DP01

Eskom

SHEET 1 OF 1

Layer 1 compensating cables
1) L1R2CEGT-IN -Ring 2, hot end gas temperature entering
2) L1R2CEMT-IN -Ring 2, hot end metal temperature entering
3) L1R2CEGT-OUT -Ring 2, hot end gas temperature exiting
4) L1R2CEMT-OUT -Ring 2, hot end metal temperature exiting
5) L1R4CEGT-IN -Ring 4, hot end gas temperature entering
6) L1R4CEMT-IN -Ring 4, hot end metal temperature entering
7) L1R4CEGT-OUT -Ring 4, hot end gas temperature exiting
8) L1R4CEMT-OUT -Ring 4, hot end metal temperature exiting
9) L1R6CEGT-IN -Ring 6, hot end gas temperature entering
10) L1R6CEMT-IN -Ring 6, hot end metal temperature entering
11) L1R6CEGT-OUT -Ring 6, hot end gas temperature exiting
12) L1R6CEMT-OUT -Ring 6, hot end metal temperature exiting

Layer 2 compensating cables
13) L2R2CEGT-OUT -Ring 2, hot end gas temperature exiting
14) L2R2CEMT-OUT -Ring 2, hot end metal temperature exiting
15) L2R4CEGT-OUT -Ring 4, hot end gas temperature exiting
16) L2R4CEMT-OUT -Ring 4, hot end metal temperature exiting
17) L2R6CEGT-OUT -Ring 6, hot end gas temperature exiting
18) L2R6CEMT-OUT -Ring 6, hot end metal temperature exiting

Layer 3 compensating cables
19) L3R1CEGT -Ring 1, cold end gas temperature
20) L3R1CEMT -Ring 1, cold end metal temperature
21) L3R2CEGT -Ring 2, cold end gas temperature
22) L3R2CEMT -Ring 2, cold end metal temperature
23) L3R3CEGT -Ring 3, cold end gas temperature
24) L3R3CEMT -Ring 3, cold end metal temperature
25) L3R4CEGT -Ring 4, cold end gas temperature
26) L3R4CEMT -Ring 4, cold end metal temperature
27) L3R5CEGT -Ring 5, cold end gas temperature
28) L3R5CEMT -Ring 5, cold end metal temperature
29) L3R6CEGT -Ring 6, cold end gas temperature
30) L3R6CEMT -Ring 6, cold end metal temperature
31) L3R7CEGT -Ring 7, cold end gas temperature
32) L3R7CEMT -Ring 7, cold end metal temperature

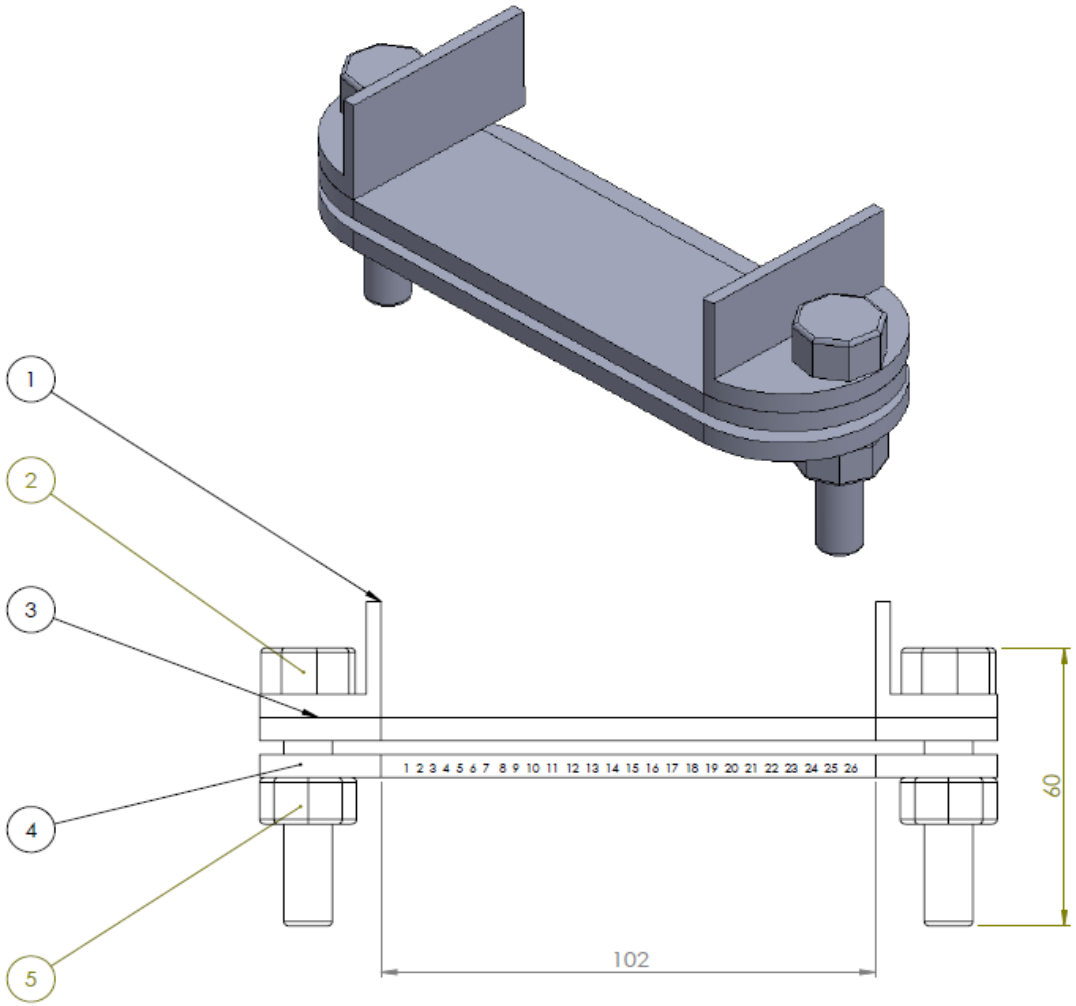

ITEM NO.	PART NUMBER	DESCRIPTION	QTY.
1	DP00-01	CABLE CLAMP SIDE	1
2	BOLT	2 x HEX M10 50mm	2
3	DP00-02	CABLE CLAMP TOP	1
4	DP00-03	CABLE CLAMP BOTTOM	1
5	NUT	HEX M10 NUT	2

Notes:
1) Remove all sharp edges and burrs
2) Component to be machined using a tolerance of +-0.05mm
3) Seal weld Item 1. Attach the Item to the bottom of the external vertical cable channel
4) locate each cable to its allocated number during installation

SCALE:1:1

MATERIAL:
Mildsteel

	NAME	SIGNATURE	DATE
DRAWN			
CHK'D			
APPV'D			
MFG			
Q.A			

TITLE:
CABLE CLAMP

DWG NO. DP00

SHEET 1 OF 1

UNIVERSITY OF THE WITWATERSRAND
Eskom

General Notes
- The cables must be installed before the components are seal welded
- Each cable must be installed from the point where the thermocouple will be inserted
- Ensure all that no cables are exposed
- All the exposed areas must be sealed by means of seal welding
- Each compensating cable must be marked according to its allocated channel marking as described on sheet 2

Item 9 :
- Each vertical channel must be alighned with the holes drilled through the Radial plate.
- 2 Long vertical channels must be installed as indicated in the top right hand corner drawing
- 2 compesating wires must be inserted through each stator hole

Item 5,6,7 & 8:
1) Item 8 to be installed in between the bottom and intermediate element packs, for ring 7 and 6
2) Item 7 to be installed at the coldend directly underneath the coldend element packs.
3) Ensure that item 7 is installed without obstructing the rotation of the hood
4) Ensure that item 6 are seal welded at the outer ring exiting the stator
5) Ensure that item 6 is completely sealed off on the inner ring of ring 1
6) Ensure that each cable is placed in the specified clamp allocation as per item 5 drawing AT01-01(specified drawing for compensating cable clamp allocation

Item 1,2 & 3:
1) Install the compensating cable channel as indedicated in the assembly drawings AL100,AL200 & AL300

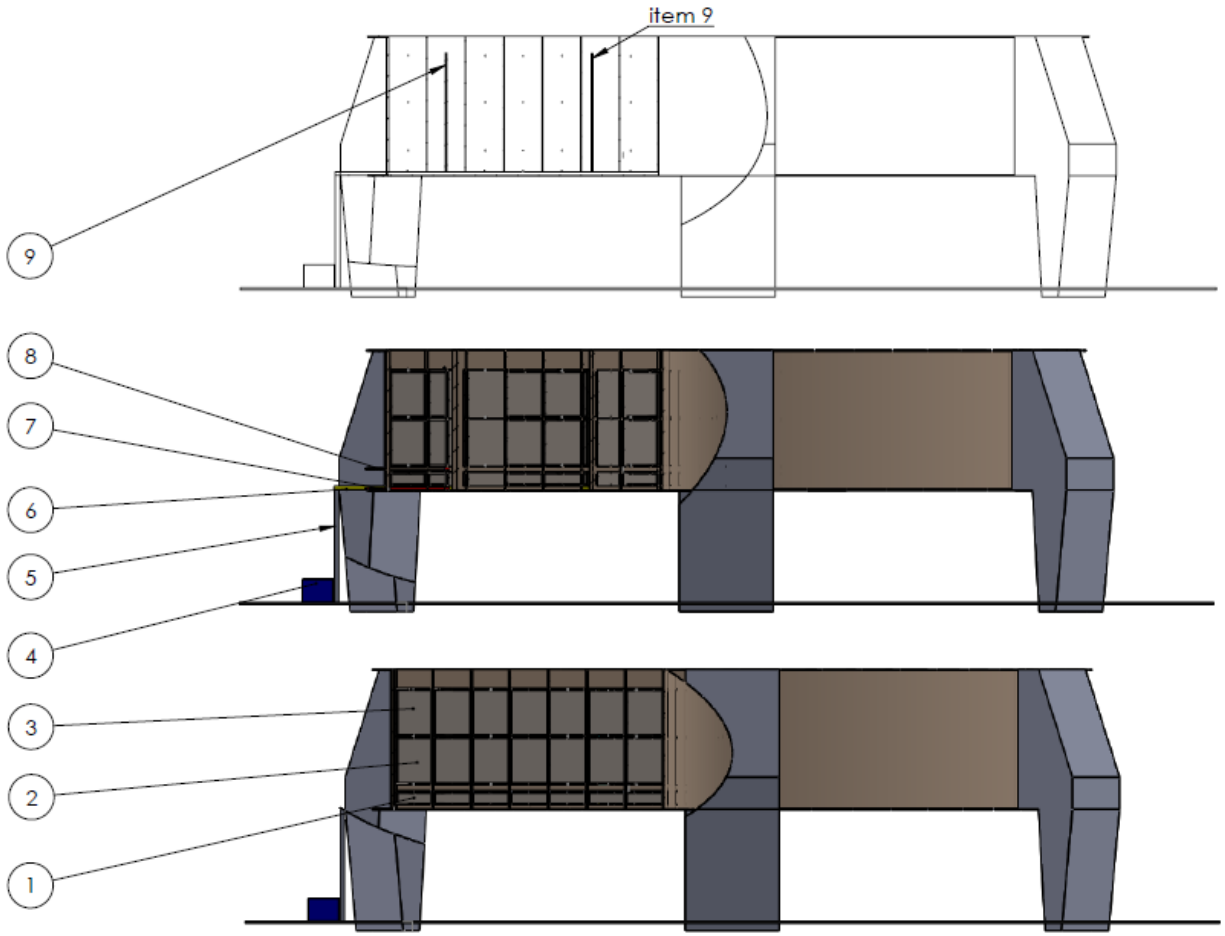

ITEM NO.	DRAWING NO.	DESCRIPTION	QTY.
1	AL100	LAYER 1 TP ASSEMBLY	1
2	AL200	LAYER 2 TP ASSEMBLY	1
3	AL300	LAYER 3 TP ASSEMBLY	1
4	RECAB	RECORDING CABINET	1
5	AT01	EXTERNAL VERTICAL CABLE CHANNEL	1
6	AT02	CABLE CHANNEL HALF CYLINDER	1
7	DP01	DEW POINT PROBE GUIDE 1	1
8	DP01	DEW POINT PROBE GUIDE 2	1
9	AT04	VERTICAL CABLE GUIDE	2

Notes:
1) To install item 1,2,3,7,8 & 9 remove the element packs on each side of the radial plate that must be installed
2) Item 7 & 8 must be inserted in the holes, dedicated for the probes guides, without the cone tip. The cone tip must be welded on after the guides are mounted into the stator
3) Dimensions for installation can be found on AT00 sheet 2 Of 2
4) All components to be seal welded
5) Ensure that the compensating wire are inserted before the components are welded
6) Item 1,2 & 3 to be modified as per drawing references in the item list table.
7) Ensure that item 1,2 & 3 are installed behind of the radial plate where item 9 & 10 are installed
8) Remove all sharp edges and burrs
9) Ensure the compensating cable channels are filled with high temperature silicone(> 300 degC)

SCALE:1:200

MATERIAL:
Mildsteel

	NAME	SIGNATURE	DATE
DRAWN	W Brandt		
CHK'D	Pr W Schmits		
APPV'D	M Lander		
MFG			
Q.A			

TITLE:
Experimental Setup Assembly

DWG NO. AT00

UNIVERSITY OF THE WITWATERSRAND

SHEET 1 OF 2

Eskom

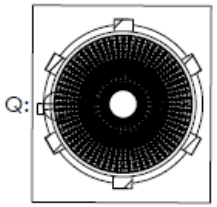

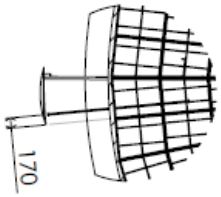

DETAIL Q: Dew Point probe
SCALE 1 : 80

SECTION N-N : SCALE 1 : 500

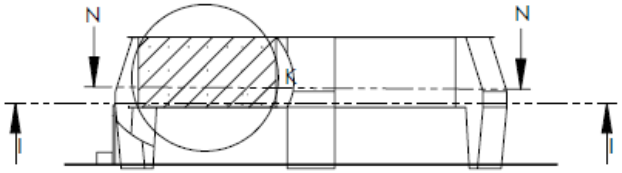

DETAIL K - Radial Plate drilling dimensions
SCALE 1 : 40

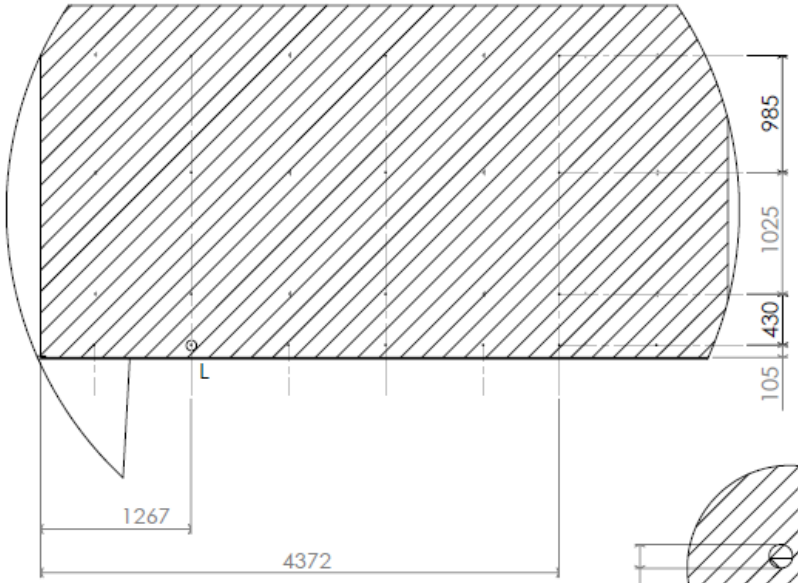

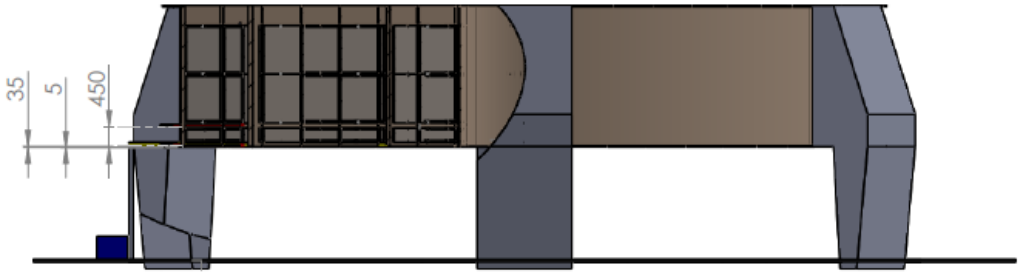

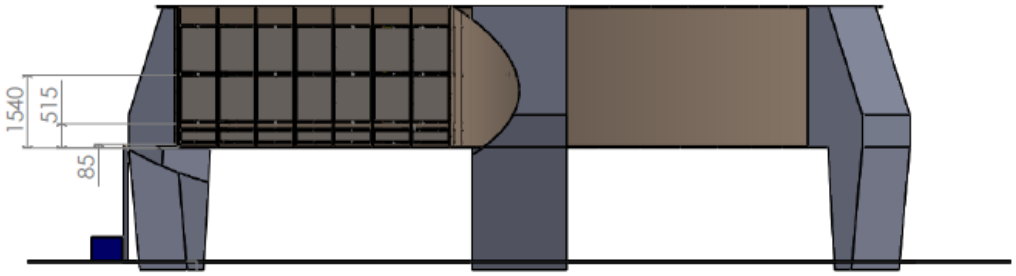

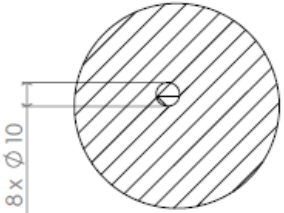

Hole dimension
DETAIL L
SCALE 1 : 2

Notes:
1) Remove all sharp edges and burrs
2) Ensure the holes on the outer casing of each layer aligns with the holes allocated on the stator radial plate

SCALE:1:200

MATERIAL:
Mildsteel

	NAME	SIGNATURE	DATE
DRAWN	W Brandt		
CHK'D	Pr W Schmitz		
APPV'D	M Lander		
MFG			
Q.A			

TITLE:
Experimental Setup Assembly

DWG NO.
AT00

UNIVERSITY OF THE WITWATERSRAND

SHEET 2 OF 2

TECHNICAL DRAWINGS

Drawing number	Title
AL100-TD01	Compensating wire protection – Angel Iron (R2)
AL100-TD03	Compensating wire protection – Angel Iron (R6)
AL100-TD04	Thermocouple Protection Metal Temp Probe (R6)
AL100-TD05	Thermocouple Protection Metal Temp Probe (R2)
AL100-TD09	Thermocouple Protection Gas Temp Probe (R6)
AL100-TD10	Thermocouple Protection Gas Probe (R2)
AL100-TD11	Thermocouple Protection Gas Temp Probe Top (R6)
AL100-TD12	Thermocouple Protection Gas Temp Probe Top (R2)
AT01	External vertical cable channel
AT02	Cable channel half cylinder
AT03	Layer 3 Exit temp vertical cable guide
AT04	General vertical cable guide
DP01-00	Insertion base plate
DP01-01	Insertion base plate lid
DP01-02	Dew point probe guide tube
DP01-03	Dew point probe guide tip
DP00-01	Cable clamp side
DP00-02	Cable clamp top
DP00-03	Cable clamp bottom

FACE GRINDING

6.3 U.O.S

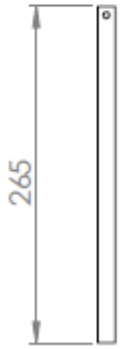

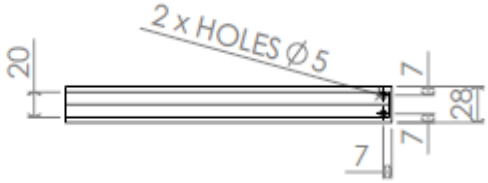

Notes:
1) Tolerance +/-0.5mm unless otherwise stated
2) Remove all sharp edges and burrs
3) N16 Finish all over unless otherwise stated

SCALE1:5

MATERIAL: Mildsteel

QTY: 4

	NAME	SIGNATURE	DATE
DRAWN	W Brandt		
CHK'D	Pr. J Sheer		
APPV'D	Pr. W Schmitz		
MFG			
Q.A			

TITLE: Compensating wire Protection - Angle Iron (R2)

UNIVERSITY OF THE WITWATERSRAND

DWG NO. AL100-TD01

Eskom

SHEET 1 OF 1

FACE GRINDING

6.3 U.O.S

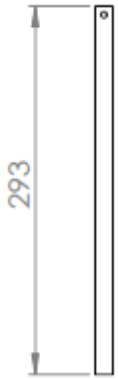

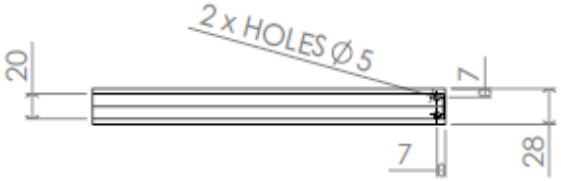

Notes:
1) Tolerance +/-0.5mm unless otherwise stated
2) Remove all sharp edges and burrs
3) N16 Finish all over unless otherwise stated

SCALE1:5

MATERIAL: Mildsteel

QTY: 4

	NAME	SIGNATURE	DATE
DRAWN	W Brandt		
CHK'D	Pr. J Sheer		
APPV'D	Pr. W Schmitz		
MFG			
Q.A			

TITLE: Compensating wire Protection - Angle Iron (R6)

UNIVERSITY OF THE WITWATERSRAND

DWG NO. AL100-TD03

Eskom

SHEET 1 OF 1

FACE GRINDING

6.3 U.O.S

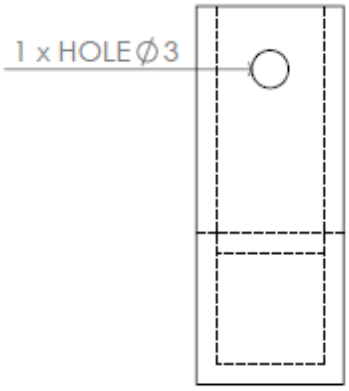

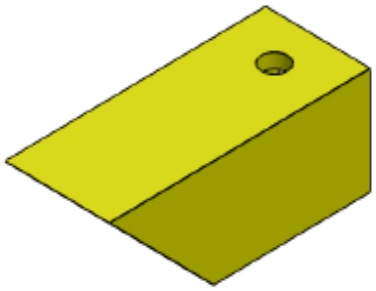

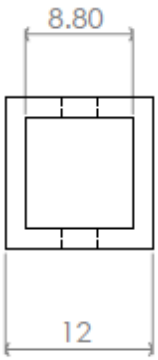

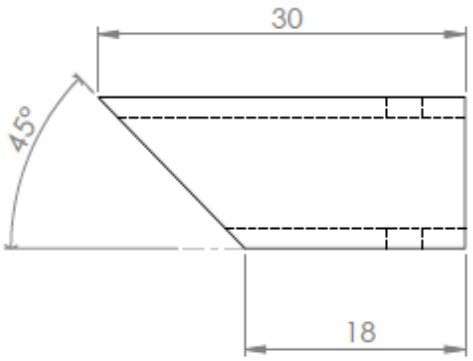

Notes:
1) Tolerance +/-0.5mm unless otherwise stated
2) Remove all sharp edges and burrs
3) N16 Finish all over unless otherwise stated

SCALE:2:1

MATERIAL: Mildsteel

QTY: 4

	NAME	SIGNATURE	DATE
DRAWN	W Brandt		
CHK'D	Pr. J Sheer		
APPV'D	Pr. W Schmiltz		
MFG			
Q.A			

TITLE: Thermocouple Protection Metal Temp Probe R6

UNIVERSITY OF THE WITWATERSRAND

DWG NO. AL100-TD04

Eskom

SHEET 1 OF 1

FACE GRINDING

6.3 U.O.S

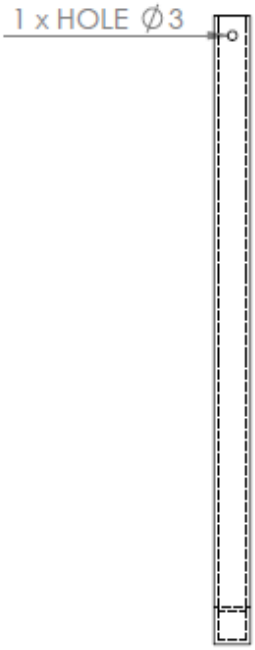

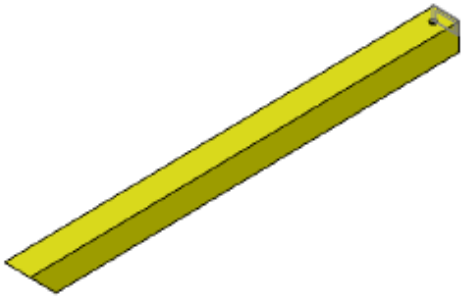

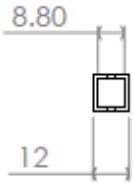

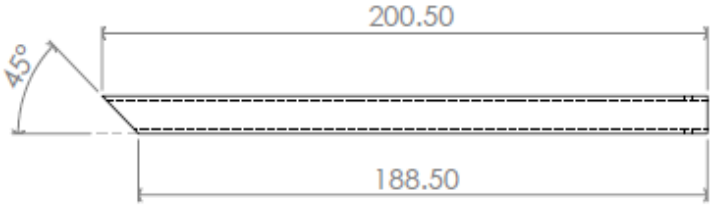

Notes:
1) Tolerance +/-0.5mm unless otherwise stated
2) Remove all sharp edges and burrs
3) N16 Finish all over unless otherwise stated

SCALE:1:2

MATERIAL: Mildsteel

QTY: 5

	NAME	SIGNATURE	DATE
DRAWN	W Brandt		
CHK'D	Pr. J Sheer		
APPV'D	Pr. W Schmitz		
MFG			
Q.A			

TITLE: Thermocouple Protection Metal Temp Probe R2

DWG NO. AL100-TD05

SHEET 1 OF 1

UNIVERSITY OF THE WITWATERSRAND

Eskom

FACE GRINDING

6.3 U.O.S

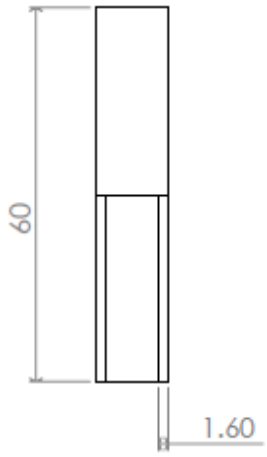

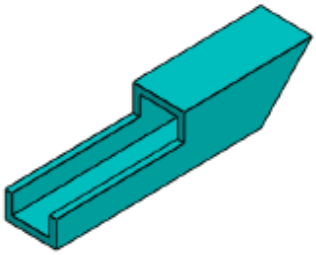

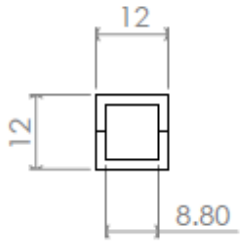

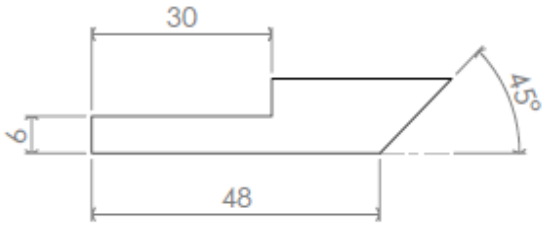

Notes:
1) Tolerance +/-0.5mm unless otherwise stated
2) Remove all sharp edges and burrs
3) N16 Finish all over unless otherwise stated

SCALE:1:1

MATERIAL: Mildsteel

QTY: 3

	NAME	SIGNATURE	DATE
DRAWN	W Brandt		
CHK'D	Pr. J Sheer		
APPV'D	Pr. W Schmitz		
MFG			
Q.A			

TITLE: Thermocouple Protection Gas Temp- (R6)

DWG NO. AL100-TD09

SHEET 1 OF 1

UNIVERSITY OF THE WITWATERSRAND

Eskom

FACE GRINDING

6.3 U.O.S

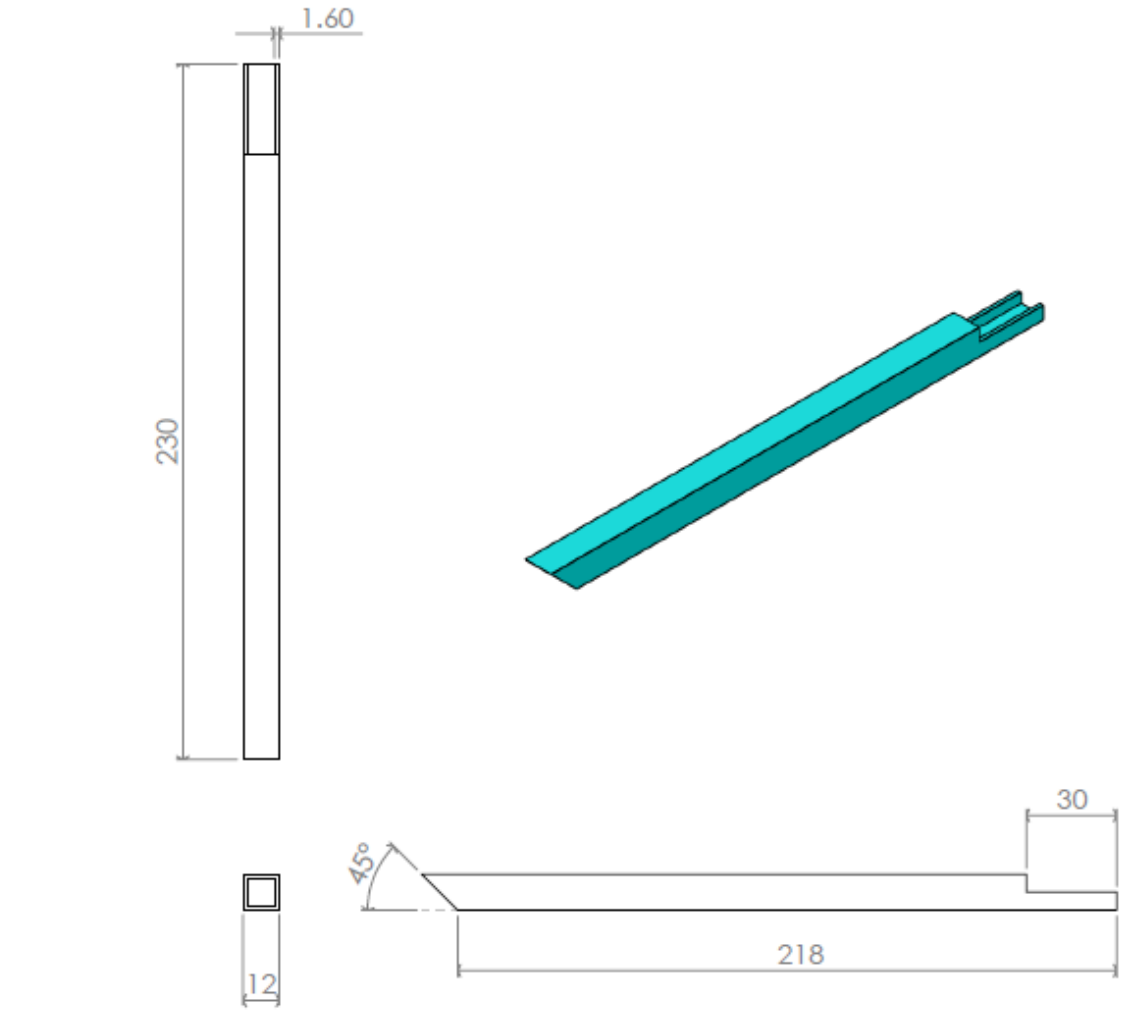

Notes:
1) Tolerance +/-0.5mm unless otherwise stated
2) Remove all sharp edges and burrs
3) N16 Finish all over unless otherwise stated

SCALE:1:5

MATERIAL: Mildsteel

QTY: 3

	NAME	SIGNATURE	DATE
DRAWN	W Brandt		
CHK'D	Pr. J Sheer		
APPV'D	Pr. W Schmitz		
MFG			
Q.A			

TITLE:
Thermocouple Protection Gas Temp- (R2)

UNIVERSITY OF THE WITWATERSRAND

DWG NO.
AL100-TD10

Eskom

SHEET 1 OF 1

FACE GRINDING

6.3 U.O.S

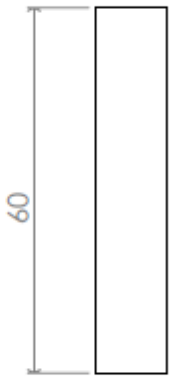

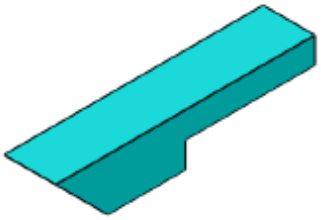

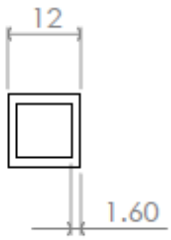

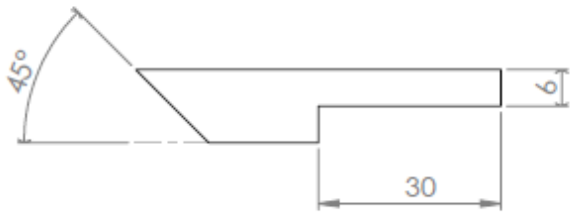

Notes:
1) Tolerance +/-0.5mm unless otherwise stated
2) Remove all sharp edges and burrs
3) N16 Finish all over unless otherwise stated

SCALE:1:1

MATERIAL: Mildsteel

QTY: 1

	NAME	SIGNATURE	DATE
DRAWN	W Brandt		
CHK'D	Pr. J Sheer		
APPV'D	Pr. W Schmitz		
MFG			
Q.A			

TITLE: Thermocouple Protection Gas Top Temp- (R6)

DWG NO. AL100-TD11

SHEET 1 OF 1

UNIVERSITY OF THE WITWATERSRAND

Eskom

FACE GRINDING

6.3 U.O.S

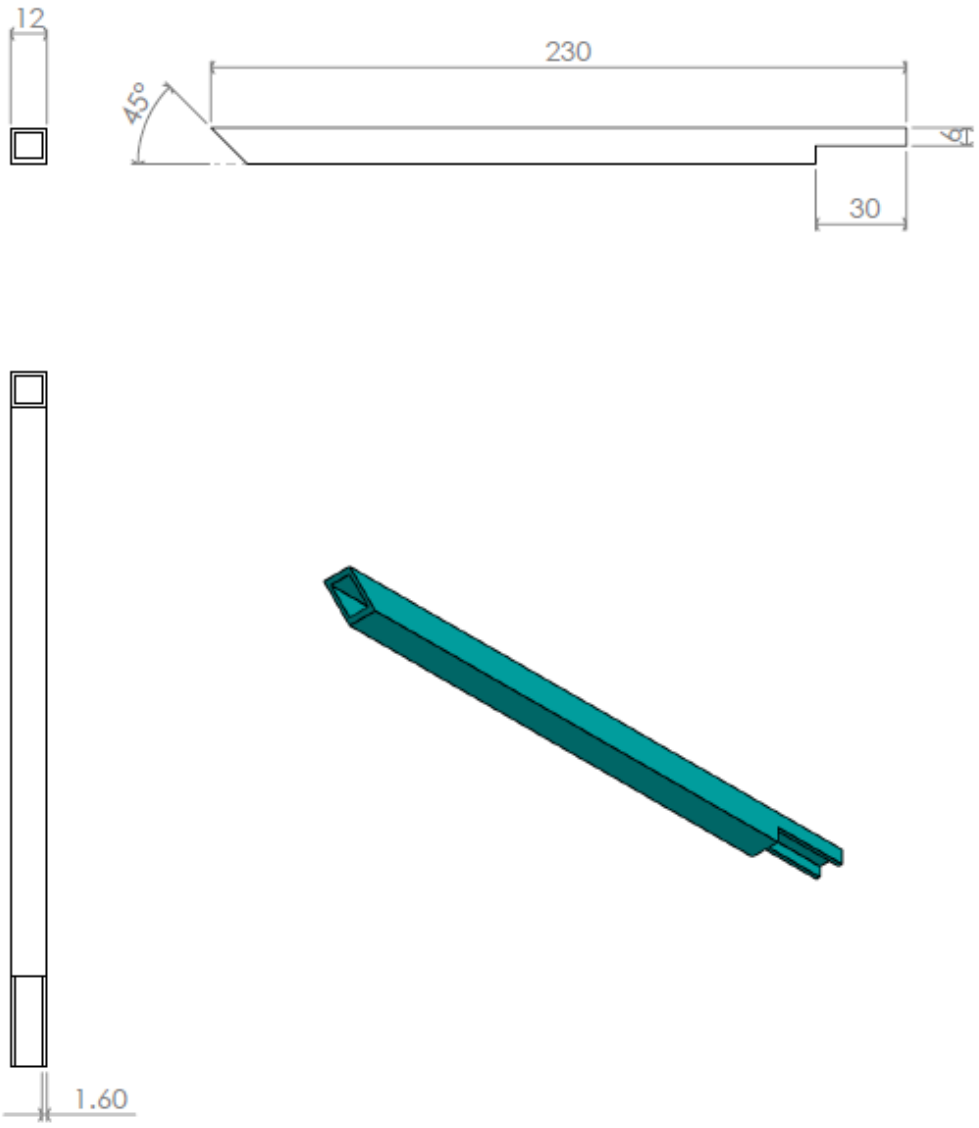

Notes:
1) Tolerance +/-0.5mm unless otherwise stated
2) Remove all sharp edges and burrs
3) N16 Finish all over unless otherwise stated

SCALE:1:5

MATERIAL: Mildsteel

QTY: 1

	NAME	SIGNATURE	DATE
DRAWN	W Brandt		
CHK'D	Pr. J Sheer		
APPV'D	Pr. W Schmiltz		
MFG			
Q.A			

TITLE: Thermocouple Protection Gas Top Temp- (R2)

UNIVERSITY OF THE WITWATERSRAND

DWG NO. AL100-TD12

Eskom

SHEET 1 OF 1

FACE GRINDING

6.3 U.O.S

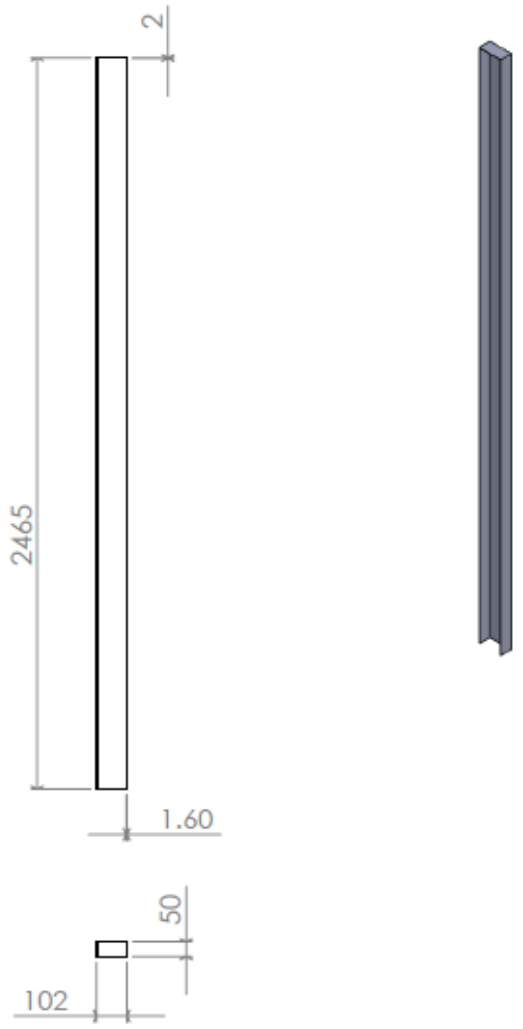

Notes:
1) Tolerance +/-0.5mm unless otherwise stated
2) Remove all sharp edges and burrs
3) N16 Finish all over unless otherwise stated

SCALE:1:20

MATERIAL: Mildsteel

QTY: 1

	NAME	SIGNATURE	DATE
DRAWN	W Brandt		
CHK'D	Pr. J Sheer		
APPV'D	Pr. W Schmitz		
MFG			
Q.A			

TITLE:

EXTERNAL VERTICAL CABLE CHANNEL

DWG NO.

AT01

SHEET 1 OF 1

UNIVERSITY OF THE WITWATERSRAND

Eskom

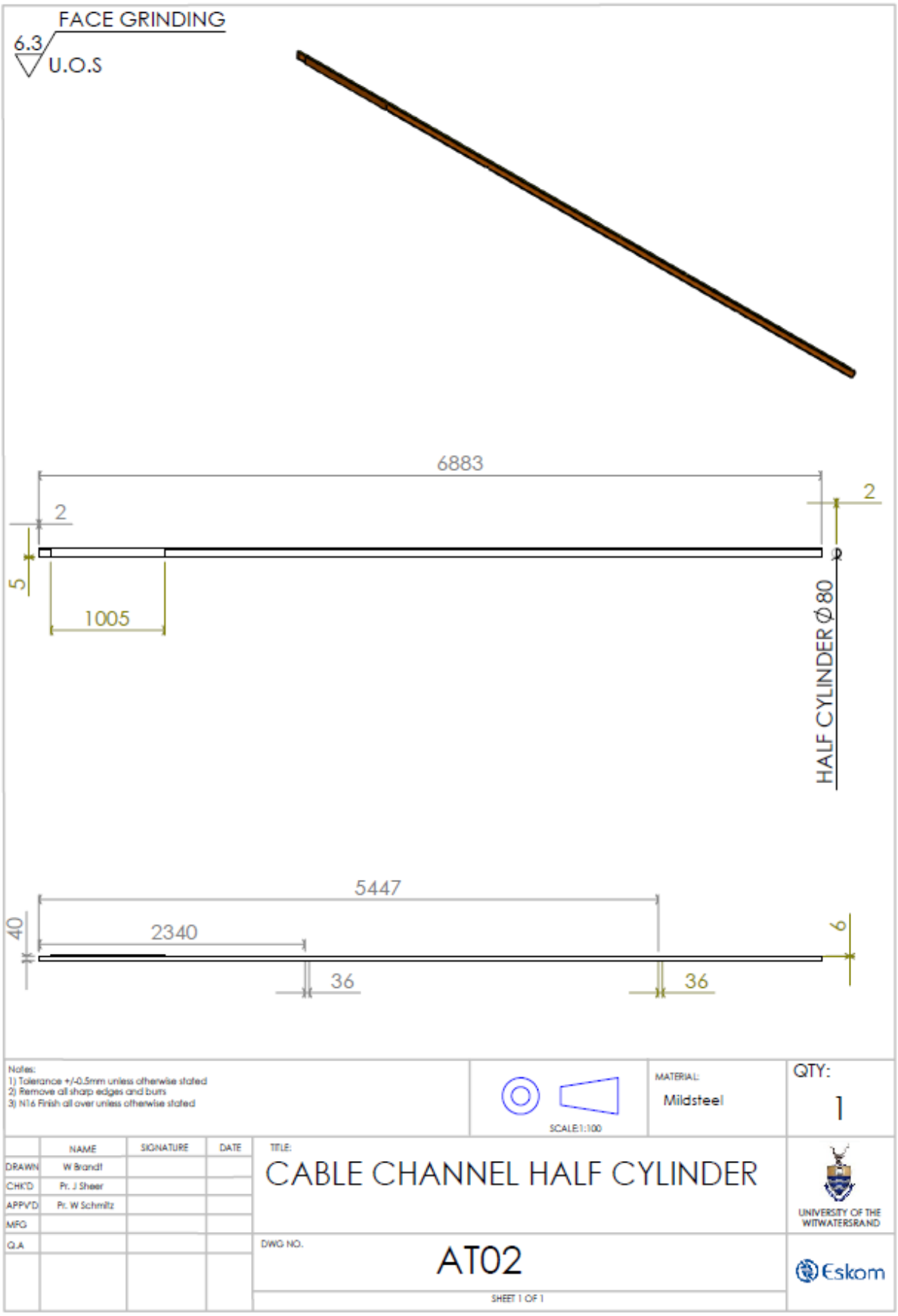

Notes:
1) Tolerance +/-0.5mm unless otherwise stated
2) Remove all sharp edges and burrs
3) N16 Finish all over unless otherwise stated

SCALE:1:100

MATERIAL: Mildsteel

QTY: 1

	NAME	SIGNATURE	DATE
DRAWN	W Brandt		
CHK'D	Pr. J Sheer		
APPV'D	Pr. W Schmitz		
MFG			
Q.A			

TITLE: CABLE CHANNEL HALF CYLINDER

UNIVERSITY OF THE WITWATERSRAND

DWG NO. AT02

SHEET 1 OF 1

Eskom

FACE GRINDING

6.3 U.O.S

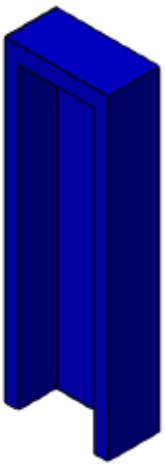

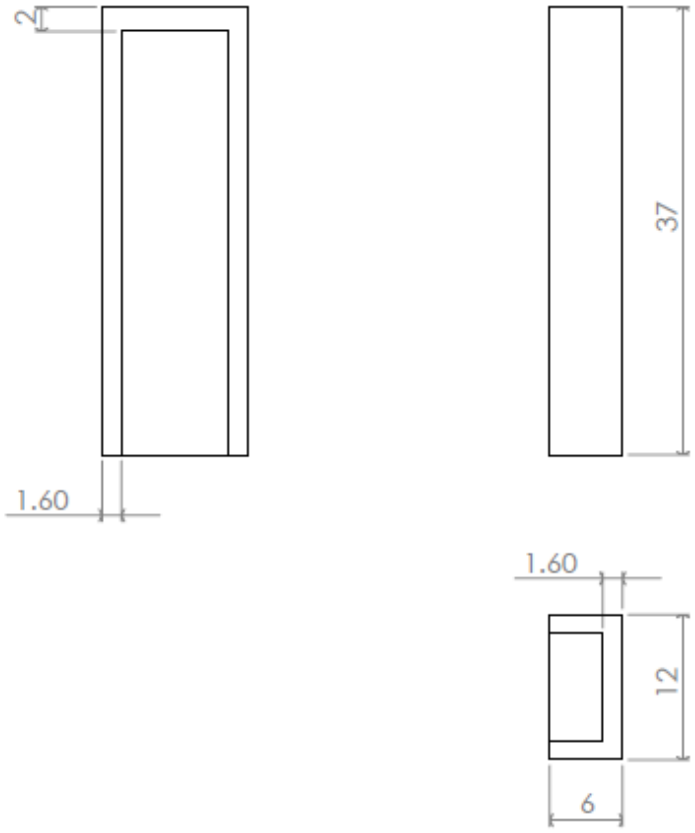

Notes:
1) Tolerance +/-0.5mm unless otherwise stated
2) Remove all sharp edges and burrs
3) N16 Finish all over unless otherwise stated

SCALE:2:1

MATERIAL: Mildsteel

QTY: 4

	NAME	SIGNATURE	DATE
DRAWN	W Brandt		
CHK'D	Pr. J Sheer		
APPV'D	Pr. W Schmitz		
MFG			
Q.A			

TITLE: LAYER 3 EXIT TEMP VERTICAL GUIDE

DWG NO. AT03

SHEET 1 OF 1

UNIVERSITY OF THE WITWATERSRAND

Eskom

FACE GRINDING

6.3 U.O.S

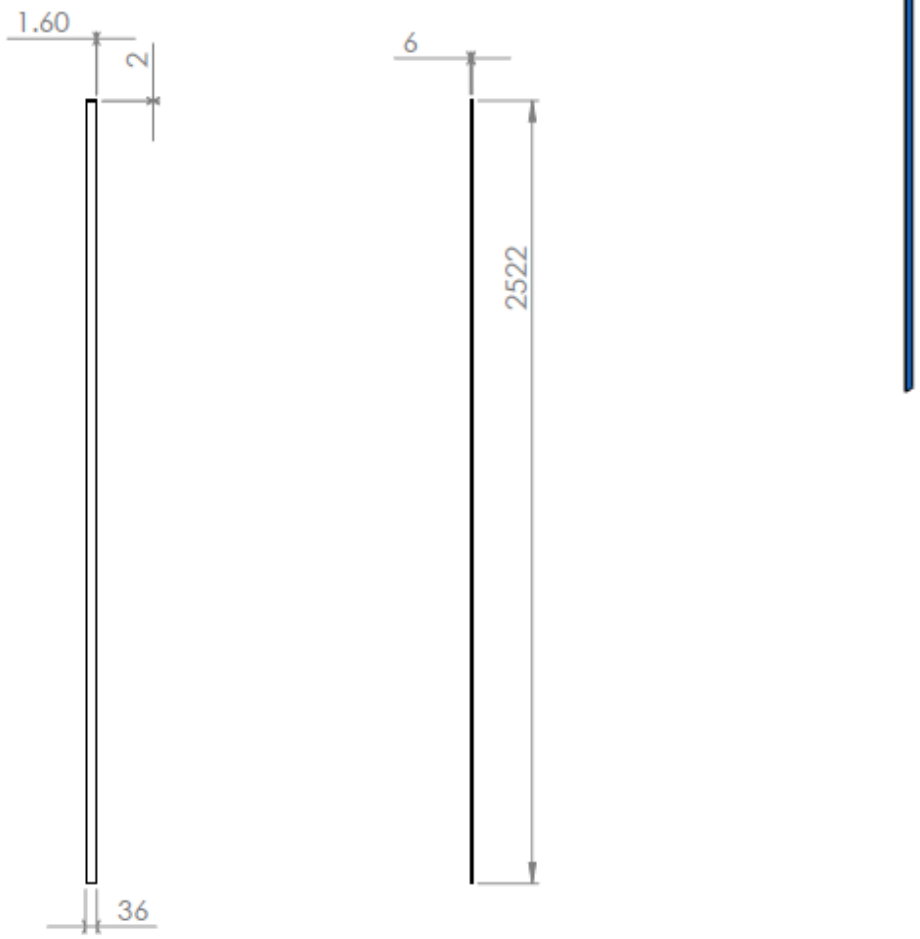

Notes:
1) Tolerance +/-0.5mm unless otherwise stated
2) Remove all sharp edges and burrs
3) N16 Finish all over unless otherwise stated

SCALE:1:20

MATERIAL: Mildsteel

QTY: 3

	NAME	SIGNATURE	DATE
DRAWN	W Brandt		
CHK'D	Pr. J Sheer		
APPV'D	Pr. W Schmitz		
MFG			
Q.A			

TITLE: GENERAL VERTICAL GUIDE

DWG NO. AT04

SHEET 1 OF 1

UNIVERSITY OF THE WITWATERSRAND

Eskom

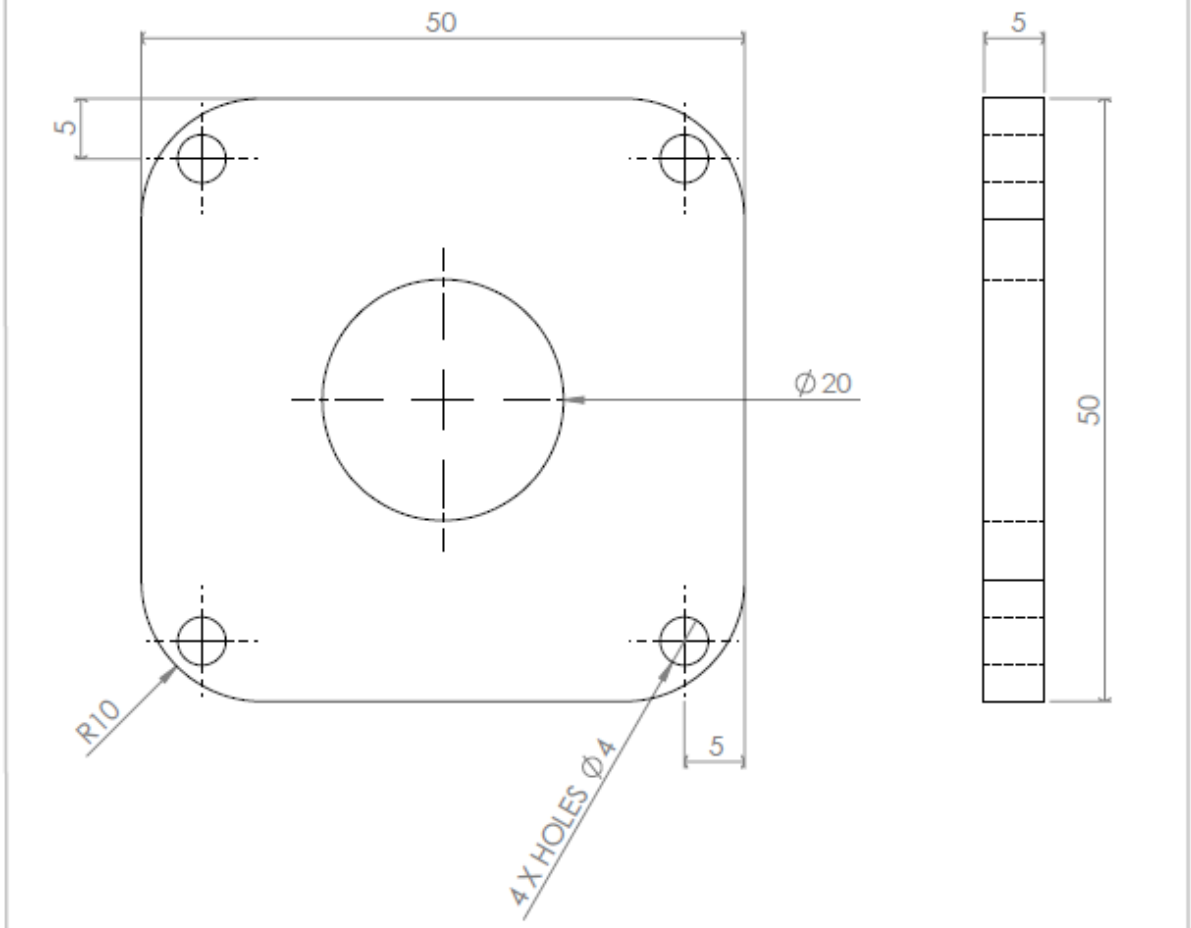

Notes:
1) Tolerance +/-0.5mm unless otherwise stated
2) Remove all sharp edges and burrs
3) N16 Finish all over unless otherwise stated

SCALE:2:1

MATERIAL: Mildsteel

QTY: 2

	NAME	SIGNATURE	DATE
DRAWN	W Brandt		
CHK'D	Pr. J Sheer		
APPV'D	Pr. W Schmitz		
MFG			
Q.A			

TITLE:

INSERTION BASE PLATE

UNIVERSITY OF THE WITWATERSRAND

DWG NO.

DP01-00

Eskom

SHEET 1 OF 1

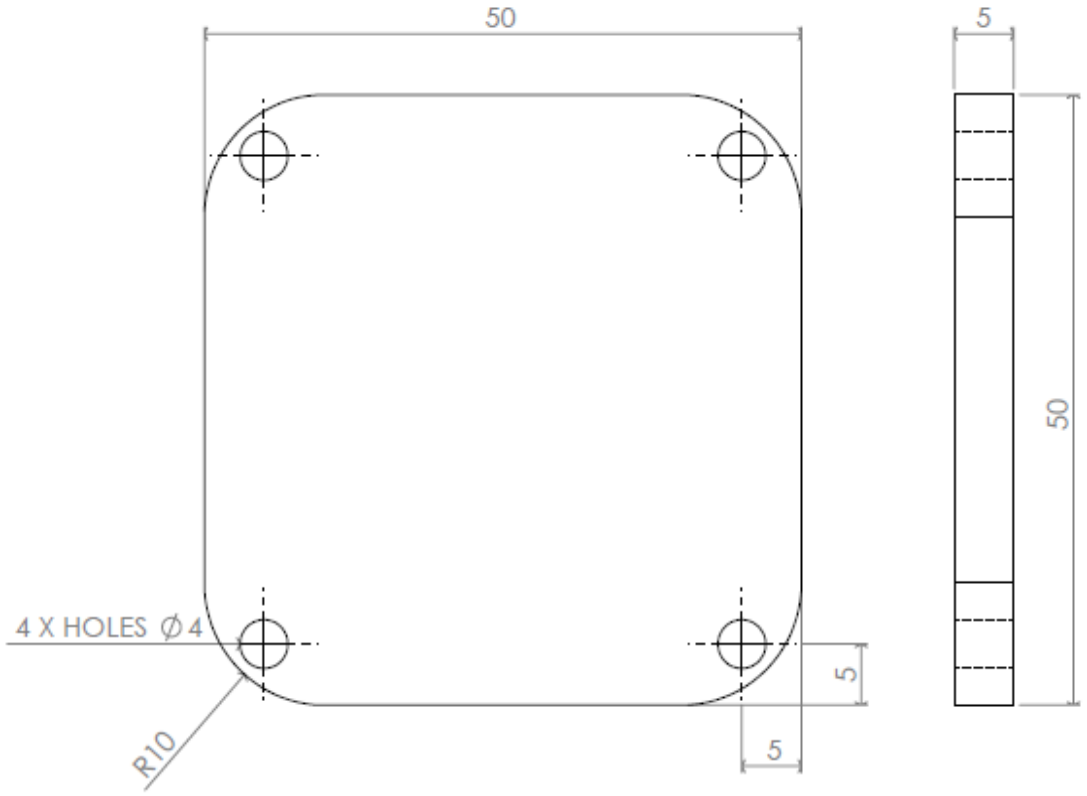

Notes:
1) Tolerance +/-0.5mm unless otherwise stated
2) Remove all sharp edges and burrs
3) N16 Finish all over unless otherwise stated

SCALE:2:1

MATERIAL: Mildsteel

QTY: 2

	NAME	SIGNATURE	DATE
DRAWN	W Brandt		
CHK'D	Pr. J Sheer		
APPV'D	Pr. W Schmitz		
MFG			
Q.A			

TITLE:

INSERTION BASE PLATE LID

UNIVERSITY OF THE WITWATERSRAND

DWG NO.

DP01-01

Eskom

SHEET 1 OF 1

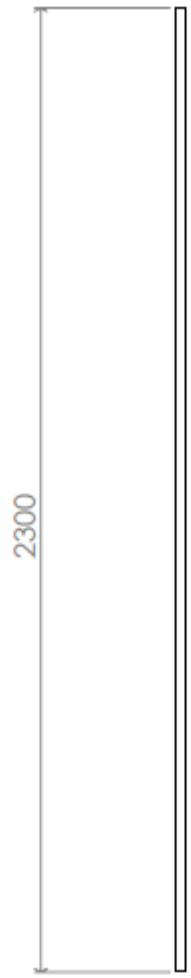

Notes:
1) Tolerance +/-0.5mm unless otherwise stated
2) Remove all sharp edges and burrs
3) N16 Finish all over unless otherwise stated

SCALE 1:50

MATERIAL: Mildsteel

QTY: 2

	NAME	SIGNATURE	DATE
DRAWN	W Brandt		
CHK'D	Pr. J Sheer		
APPV'D	Pr. W Schmitz		
MFG			
Q.A			

TITLE:

DEW POINT PROBE GUIDE TUBE

UNIVERSITY OF THE WITWATERSRAND

DWG NO.

DP01-02

Eskom

SHEET 1 OF 1

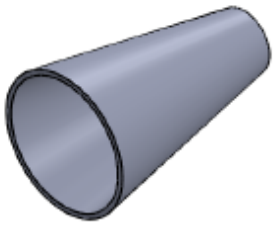

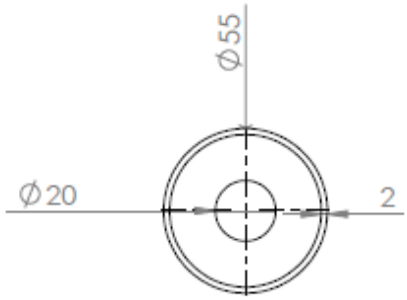

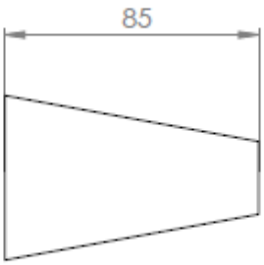

Notes:
1) Tolerance +/-0.5mm unless otherwise stated
2) Remove all sharp edges and burrs
3) N16 Finish all over unless otherwise stated

SCALE:1:2

MATERIAL: Mildsteel

QTY: 2

	NAME	SIGNATURE	DATE
DRAWN	W Brandt		
CHK'D	Pr. J Sheer		
APPV'D	Pr. W Schmitz		
MFG			
Q.A			

TITLE: DEW POINT PROBE GUIDE TIP

UNIVERSITY OF THE WITWATERSRAND

DWG NO. DP01-03

Eskom

SHEET 1 OF 1

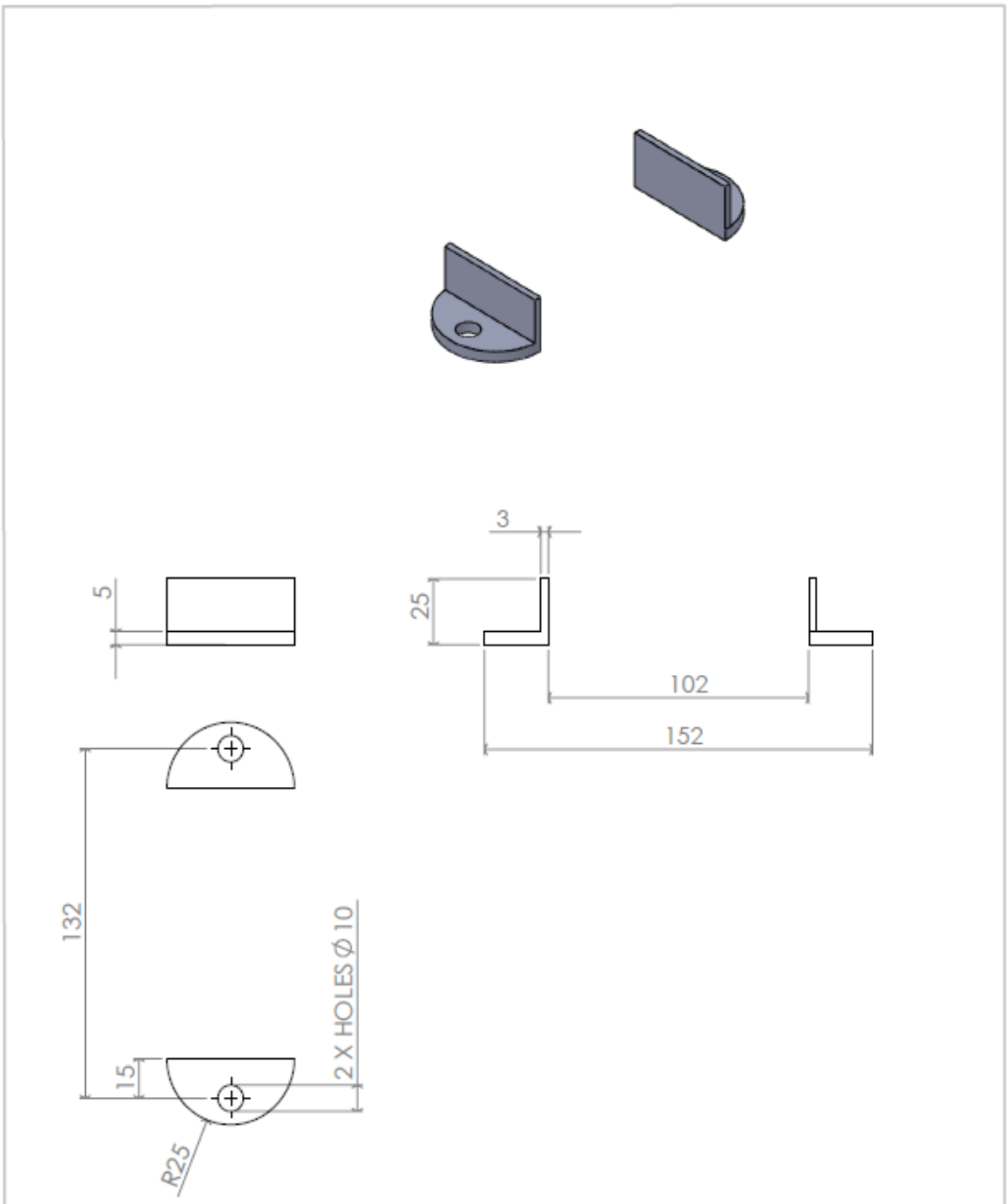

Notes:
1) Tolerance +/-0.5mm unless otherwise stated
2) Remove all sharp edges and burrs
3) N16 Finish all over unless otherwise stated

SCALE:1:2

MATERIAL: Mildsteel

QTY: 2

	NAME	SIGNATURE	DATE
DRAWN	W Brandt		
CHK'D	Pr. J Sheer		
APPV'D	Pr. W Schmitz		
MFG			
Q.A			

TITLE: CABLE CLAMP SIDE SECTIONS

DWG NO. DP00-01

SHEET 1 OF 1

UNIVERSITY OF THE WITWATERSRAND

Eskom

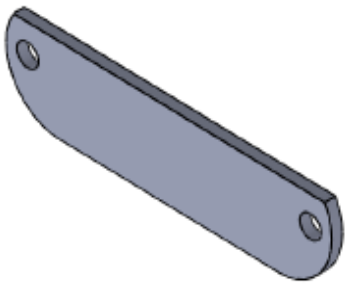

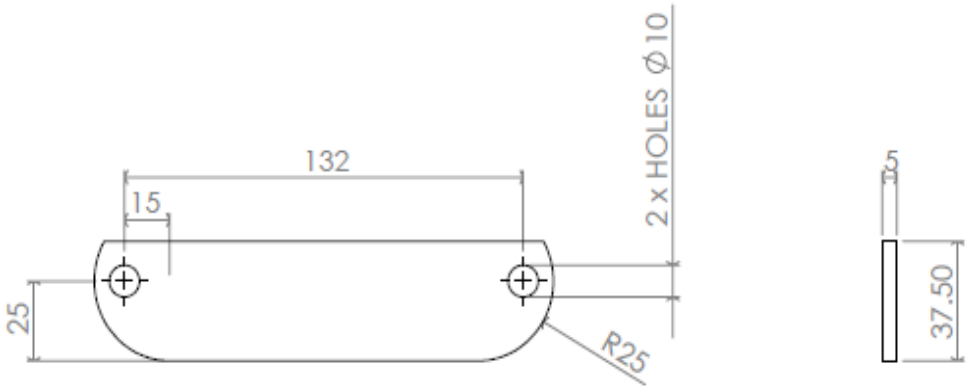

Notes:
1) Tolerance +/-0.5mm unless otherwise stated
2) Remove all sharp edges and burrs
3) N16 Finish all over unless otherwise stated

SCALE:1:2

MATERIAL: Mildsteel

QTY: 2

	NAME	SIGNATURE	DATE
DRAWN	W Brandt		
CHK'D	Pr. J Sheer		
APPV'D	Pr. W Schmitz		
MFG			
Q.A			

TITLE:

CABLE CLAMP TOP SECTION

UNIVERSITY OF THE WITWATERSRAND

DWG NO.

DP00-02

Eskom

SHEET 1 OF 1

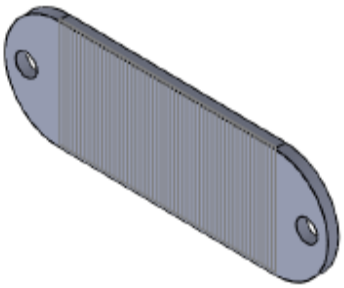

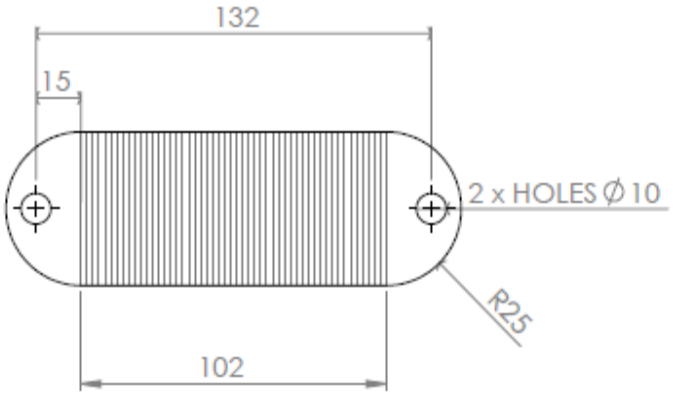

Notes:
1) Tolerance +/-0.5mm unless otherwise stated
2) Remove all sharp edges and burrs
3) N16 Finish all over unless otherwise stated

SCALE:1:2

MATERIAL: Mildsteel

QTY: 2

	NAME	SIGNATURE	DATE
DRAWN	W Brandt		
CHK'D	Pr. J Sheer		
APPV'D	Pr. W Schmitz		
MFG			
Q.A			

TITLE:

CABLE CLAMP BOTTOM SECTION

UNIVERSITY OF THE WITWATERSRAND

DWG NO.

DP00-03

Eskom

SHEET 1 OF 1

B2: Experimental Preparation & Execution

Prior to the air heater performance tests the following had to be completed:

- All measuring equipment had to be calibrated.
- O_2 matrix temperatures had to be verified along with the O_2 matrix readings along with purging of the O_2 matrix system.
- Boiler cleaning had to be done by the operator two hours prior to the testing period.
- The frequency control and AGC (Automatic Grid Control) system had to be switched off.

Pre-Testing Preparation:
The following preparation was required prior to the commencement of testing;

- All mechanical plant required for the selected tests had to be completely installed and operational according to mechanical set-up specification.
- All valves, dampers and vanes had to be set up mechanically and stroked. Mechanical stops had to be set and stroke length and traveling time recorded and confirmed to be within process and design requirements.
- The control system had to be fully commissioned to fit the design requirements of the mechanical plant and optimised.
- All simulations implemented on the DCS (Digital Control System) had to be removed. Any simulations deemed required had to be recorded and agreed to by all parties involved.
- All feed heater banks (Low Pressure (LP) and High Pressure (HP)) had to be available and in service.
- All the mills had to be kept in service with no oil support in service during each test.
- All the measurement equipment relevant to the control system had to be operational and calibrated. As a minimum all the control and protection measuring equipment had to be wet calibrated and calibration certificates had to be available.
- All protection circuits had to be functional tested from the field and records available, for investigative purposes after testing.
- All set point parameters had to be pre-set according to the plants operational requirements.
- Operated plant from pre-stock piled coal, with CV (Calorific Value) and moisture content within specification
- Prior to commencement of the actual tests, critical areas of the mechanical plant had to be available and reliable, to prevent a possible trip condition occurring during the duration of the test, which included the following (as a minimum);
  - All oil burners
  - All standby drives and motors effected by the tests
  - All milling plant to be effected by the test
  - Feed and extraction standby systems
  - Availability of HP and LP Bypass systems
  - Availability of main-steam and reheat spray water systems
  - All Air Cooled Condition (ACC) fans to be available
  - All HP and LP heaters to be in service

In the case of no availability of any mechanical plant for what-ever reason, optimisation still had to be attempted within the specific limitations, and the safe and reliable operation of the plant had to be demonstrated. All the known defects had to be logged in the shift logs. Once faulted mechanical plant was returned to service, the optimisation process had to be completed and the specified test re- conducted.

Test Co-ordination:
The following schedule was followed:

- Coal sampling according to the schedule shown in Table B1.
- Continuous flue gas composition measurement
- Continuous flue gas pressure measurement
- Continuous air heater fluid temperature measurement at the inlet of the hot end layer ring 6 and ring 2
- Continuous air heater metal temperature measurement at the inlet of the hot end layer ring 6 and ring 2
- Continuous air heater fluid temperature measurement at the inlet of the intermediate layer ring 6 and ring 2
- Continuous air heater metal temperature measurement at the inlet of the intermediate layer ring 6 and ring 2
- Continuous air heater fluid temperature measurement at the inlet of the cold end layer ring 6 and ring 2
- Continuous air heater metal temperature measurement at the inlet of the cold end layer ring 6 and ring 2
- Continuous air heater fluid temperature measurement at the outlet of the cold end layer ring 6 and ring 2
- Continuous air heater metal temperature measurement at the outlet of the cold end layer ring 6 and ring 2

Table B1: Testing Schedule for Air Heater Performance Test

•

	Test 1: 99% MCR load							
	00:00:00 AM-04:00 AM							
Location	30 min	30 min	30 min	30 min	30 min	30 min	30 min	30 min
Feeder 1	6 kg	6 kg	6 kg	6 kg	6 kg	6 kg	6 kg	6 kg
Feeder 2	6 kg	6 kg	6 kg	6 kg	6 kg	6 kg	6 kg	6 kg
Feeder 3	6 kg	6 kg	6 kg	6 kg	6 kg	6 kg	6 kg	6 kg
Feeder 4	6 kg	6 kg	6 kg	6 kg	6 kg	6 kg	6 kg	6 kg
Total per Sample kg	24 kg	24 kg	24 kg	24 kg	24 kg	24 kg	24 kg	24 kg
sample	1	2	3	4	5	6	7	8
Notes	• Mills in operation without oil support • Load maintained at 670 MW (99% Maximum Continues Rating (MCR)) • Do coal sampling as per schedule • Do flue gas sampling • Measure AH performance (fluid temperatures, metal temperatures and pressure) • Do air leakage tests							
	Test 2: 80% MCR load							
	00:00:00 AM-04:00 AM							
.Location	30 min	30 min	30 min	30 min	30 min	30 min	30 min	30 min
Feeder 1	6 kg	6 kg	6 kg	6 kg	6 kg	6 kg	6 kg	6 kg
Feeder 2	6 kg	6 kg	6 kg	6 kg	6 kg	6 kg	6 kg	6 kg
Feeder 3	6 kg	6 kg	6 kg	6 kg	6 kg	6 kg	6 kg	6 kg

Feeder 4	6 kg	6 kg	6 kg	6 kg	6 kg	6 kg	6 kg	6 kg
Total per Sample kg	24 kg	24 kg	24 kg	24 kg	24 kg	24 kg	24 kg	24 kg
sample	1	2	3	4	5	6	7	8
Notes	• Mills in operation without oil support • Load maintained at 544 MW (80% MCR) • Do coal sampling as per schedule • Do flue gas sampling • Measure AH performance (fluid temperatures, metal temperatures and pressure) • Do air leakage tests							
	Test 1: 68% MCR load							
	00:00:00 AM-04:00 AM							
Location	30 min	30 min	30 min	30 min	30 min	30 min	30 min	30 min
Feeder 1	6 kg	6 kg	6 kg	6 kg	6 kg	6 kg	6 kg	6 kg
Feeder 2	6 kg	6 kg	6 kg	6 kg	6 kg	6 kg	6 kg	6 kg
Feeder 3	6 kg	6 kg	6 kg	6 kg	6 kg	6 kg	6 kg	6 kg
Feeder 4	6 kg	6 kg	6 kg	6 kg	6 kg	6 kg	6 kg	6 kg
Total per Sample kg	24 kg	24 kg	24 kg	24 kg	24 kg	24 kg	24 kg	24 kg
sample	1	2	3	4	5	6	7	8
Notes	• Mills in operation without oil support • Load maintained at 465 MW (68% MCR) • Do coal sampling as per schedule • Do flue gas sampling • Measure AH performance (fluid temperatures, metal temperatures and pressure) • Do air leakage tests							

C. APPENDIX - Experimental Results

C1: Data Set 1 - Results

Table C1: Metal and fluid temperature comparison table between ring 2 and 6.

Name	Channel	99 MCR – 670 MW	80 MCR – 544 MW	68 MCR – 465 MW
		Ring 2 Average Temperature °C		
HE inlet MT	CH-01	336.3	323.1	312,2
IM inlet MT	CH-02	252.3	259.2	250,7
CE inlet MT	CH-03	102.1	132.6	124,2
CE outlet MT	CH-04	72.6	83.6	78,6
HE inlet FT	CH-05	341.4	328.7	317,9
IM inlet FT	CH-06	282.6	283.7	277,4
CE inlet FT	CH-07	133.3	146.1	141,1
CE outlet FT	CH-08	76.4	86.7	83,2
Name	**Channel**	**Ring 6 Average Temperature °C**		
HE inlet MT	CH-09	331.7	319.3	308,6
IM inlet MT	CH-10	255.9	261.4	252,4
CE inlet MT	CH-11	125.1	138.7	130,6
CE outlet MT	CH-12	67.8	77.8	73,9
HE inlet FT	CH-13	341.4	326.7	315,9
IM inlet FT	CH-14	280.1	281.1	274,5
CE inlet FT	CH-15	125.4	137.9	132,6
CE outlet FT	CH-16	72.7	79.3	77,2

Table C2: List of input parameters to the VBA RAH model for the pre-test results

PRE-TEST RESULTS					
PARAMATERS	UNITS	99 MCR	80 MCR	68 MCR	MEASUREMENT SOURCE
		MEASURED DATA	MEASURED DATA	MEASURED DATA	
GEN LOAD 1	MW	672	545,00	465	
DATE	DAY/MONTH/YEAR	23/12/2019	22/12/2019	22/12/2019	
TIME	HR:MIN:SEC-HR:MIN:SEC	06:00:00 - 06:01:40	14:27:55 - 14:29:35	20:17:06 - 20:18:46	
		MEASURED DATA	MEASURED DATA		
LH SEC A/H GAS IN T	CEL	343,2	333,10	320,8	DCS
LH SEC A/H GAS OUT T	CEL	129,3	130,60	113,4	DCS
LH SEC A/H INL T	CEL	36,5	48,10	45,8	DCS
LH SEC A T	CEL	317,9	309,50	301,1	DCS
FLUE GAS PROPERTIES					
FLUE GAS BEFORE AH OXYGEN	%	3,5	3,50	3,5	COAL ANALYSIS
FLUE GAS AFTER AH OXYGEN	%	5,9	5,90	5,9	LEAKAGE TEST
FLUE GAS BEFORE AH CARBON DIOXIDE	%	12,73	10,98	10,65	DCS
FLUE GAS BEFORE AH SULPHUR DIOXIDE	%	0,126	0,12	0,11	DCS
FLUE GAS BEFORE AH MOISTURE	%	4,86	4,24	4,16	DCS
FLOWS					
FLUE GAS FLOW	kg/s	323,67	286,22	250,25	ESTIMATED
SEC A FLOW	kg/s	347,00	290,20	248,20	DCS
ASH FLOW	kg/s	7,13	7,13	7,13	ESTIMATED
LH FDF DIS P	KPA	3,91	3,43	3,02	DCS
SEC A C/OVER DUCT P	KPA	2,49	2,43	2,29	DCS
AIR HEATER AIR DP	KPA	1,42	1,00	0,73	DCS
LH SEC AH INLET GAS P	KPA	-0,772	-0,77	-0,772	C-SCHEDULE

Table C3:Pre-Test Result Comparison Sheet for a 99% MCR load condition.

PRE-TEST RESULTS							
PARAMATERS	UNITS	99 MCR					MEASUREMENT SOURCE
					ERROR		
		MEASURED DATA	RAH VBA	RAH DELPHI	%MEAS	%DELPHI	
GEN LOAD 1	MW	672					
DATE	DAY/MONTH/YEAR	23/12/2019					
TIME	HR:MIN:SEC-HR:MIN:SEC	06:00:00 - 06:01:40					
		MEASURED DATA	RAH VBA	RAH DELPHI	%MEAS	%DELPHI	
LH SEC A/H GAS IN T	CEL	343,2	343,2	343,2	N/A	N/A	DCS / RT&D
LH SEC A/H GAS OUT T	CEL	129,3	90,73	89,02	-29,83	-1,92	DCS
LH SEC A/H INL T	CEL	36,5	36,5	36,5	N/A	N/A	DCS
LH SEC A T	CEL	317,9	312,05	313,54	-1,84	0,48	DCS
COMBINED TEMPERATURES							
LH AH COMBINED TEMPS	CEL	94,7	63,615	62,76	-32,82	-1,36	DCS
CE OUTLET METAL TEMPERATURES TEMPERATURES							
MAXIMUM	CEL	137,2	128,22	192,285	-6,55	33,32	MEASURED
MINIMUM	CEL	53,1	52,53	54,772	-1,07	4,09	MEASURED
AVERAGE	CEL	95,15	90,375	123,5285	-5,02	26,84	MEASURED
FLUE GAS PROPERTIES							
FLUE GAS BEFORE AH OXYGEN	%	3,5	3,5	3,5	N/A	N/A	COAL ANALYSIS
FLUE GAS AFTER AH OXYGEN	%	5,9	5,9	5,9	N/A	N/A	ASSUMPTION
FLUE GAS BEFORE AH CARBON DIOXIDE	%	12,73	12,73	12,73	N/A	N/A	ESTIMATED
FLUE GAS BEFORE AH SULPHUR DIOXIDE	%	0,126	0,126	N/A	N/A	N/A	ESTIMATED
FLUE GAS BEFORE AH MOISTURE	%	4,86	4,86	4,86	N/A	N/A	COAL ANALYSIS
FLOWS							
FLUE GAS FLOW	kg/s	323,67	323,67	323,67	N/A	N/A	ESTIMATED
SEC A FLOW	kg/s	347,00	347,00	347,00	N/A	N/A	DCS
SEC A FLOW AFTER LEAKAGE	kg/s	NM	312,80	313,43	N/A	0,20	ESTIMATED
ASH FLOW	kg/s	7,13	7,13	7,13	N/A	N/A	ESTIMATED
AH LEAKAGE	kg/S	NM	34,20	33,57	N/A	-1,88	ESTIMATED
PRESSURES							
LH FDF DIS P	KPA	3,91	3,91	3,91	N/A	N/A	DCS
SEC A C/OVER DUCT P	KPA	2,49	N/A	N/A	N/A	N/A	DCS
AIR HEATER AIR DP	KPA	1,42	0,885	0,7285	-37,68	-21,48	DCS
LH SEC AH INLET GAS P	KPA	-0,772	N/A	N/A	N/A	N/A	C-SCHEDULE
AIR HEATER FLUE GAS DP	KPA	NOT MEASURED	0,898	0,7882	N/A	-13,93	ESTIMATED
FLUID PROPERTIES							
FG DENSITY AT INLET SIMULATED	kg/m³	NOT MEASURED	0,536	0,536	N/A	0,00	ESTIMATED
FG DENSITY AT OUTLET SIMULATED	kg/m³	NOT MEASURED	0,886	0,904	N/A	1,99	ESTIMATED
AIR DENSITY AT INLET SIMULATED	kg/m³	NOT MEASURED	1,1417	1,1417	N/A	0,00	ESTIMATED
AIR DENSITY AT OUTLET SIMULATED	kg/m³	NOT MEASURED	0,602	0,6119	N/A	1,62	ESTIMATED
FG HEAT CAPCITY AT INLET SIMULATED	kJ/kgK	NOT MEASURED	1,08	1,0845	N/A	0,41	ESTIMATED
FG HEAT CAPCITY AT OUTLET SIMULATED	kJ/kgK	NOT MEASURED	1,017	1,0195	N/A	0,25	ESTIMATED
AIR HEAT CAPCITY AT INLET SIMULATED	kJ/kgK	NOT MEASURED	1,0108	1,0108	N/A	0,00	ESTIMATED
AIR HEAT CAPCITY AT OUTLET SIMULATED	kJ/kgK	NOT MEASURED	1,054	1,053	N/A	-0,09	ESTIMATED
FG VELOCITY AT INLET SIMULATED	m/s	NOT MEASURED	8,97	8,6577	N/A	-3,61	ESTIMATED
FG VELOCITY AT OUTLET SIMULATED	m/s	NOT MEASURED	5,43	5,6605	N/A	4,07	ESTIMATED
AIR VELOCITY AT INLET SIMULATED	m/s	NOT MEASURED	5,3572	5,3585	N/A	0,02	ESTIMATED
AIR VELOCITY AT OUTLET SIMULATED	m/s	NOT MEASURED	10,149	9,0327	N/A	-12,36	ESTIMATED
ENERGY							
FG HEAT ENEREGY LOST	MW	NOT MEASURED	-47,67	-44,226	0,00	-7,79	ESTIMATED
AIR HEAT ENERGY GAINED	MW	NOT MEASURED	47,84	44,167	0,00	-8,32	ESTIMATED

Table C4:Pre-Test Result Comparison Sheet for an 80% MCR load condition.

PRE-TEST RESULTS							
PARAMATERS	UNITS	80 MCR					MEASUREMENT SOURCE
					ERROR		
		MEASURED DATA	RAH VBA	RAH DELPHI	%MEAS	%DELPHI	
GEN LOAD 1	MW	545,00					
DATE	DAY/MONTH/YEAR	22/12/2019					
TIME	HR:MIN:SEC-HR:MIN:SEC	14:27:55 - 14:29:35					
		MEASURED DATA	RAH VBA	RAH DELPHI	%MEAS	%DELPHI	
LH SEC A/H GAS IN T	CEL	333,10	333,10	333,10	N/A	N/A	DCS / RT&D
LH SEC A/H GAS OUT T	CEL	130,60	104,39	106,26	20,07	1,76	DCS
LH SEC A/H INL T	CEL	48,10	48,10	48,10	N/A	N/A	DCS
LH SEC A T	CEL	309,50	310,53	305,77	-0,33	-1,56	DCS
COMBINED TEMPERATURES							
LH AH COMBINED TEMPS	CEL	89,35	76,24	78,62	14,67	3,02	DCS
CE OUTLET METAL TEMPERATURES TEMPERATURES							
MAXIMUM	CEL	149,20	142,90	190,64	4,22	25,04	MEASURED
MINIMUM	CEL	66,00	66,85	65,03	-1,29	-2,80	MEASURED
AVERAGE	CEL	107,60	104,88	127,84	2,53	17,96	MEASURED
FLUE GAS PROPERTIES							
FLUE GAS BEFORE AH OXYGEN	%	3,50	3,50	3,50	N/A	N/A	COAL ANALYSIS
FLUE GAS AFTER AH OXYGEN	%	5,90	5,90	5,90	N/A	N/A	ASSUMPTION
FLUE GAS BEFORE AH CARBON DIOXIDE	%	10,98	10,98	10,98	N/A	N/A	ESTIMATED
FLUE GAS BEFORE AH SULPHUR DIOXIDE	%	0,12	0,12	N/A	N/A	N/A	ESTIMATED
FLUE GAS BEFORE AH MOISTURE	%	4,24	4,24	4,24	N/A	N/A	COAL ANALYSIS
FLOWS							
FLUE GAS FLOW	kg/s	286,22	286,22	286,22	N/A	N/A	ESTIMATED
SEC A FLOW	kg/s	290,20	290,20	290,20	N/A	N/A	DCS
SEC A FLOW AFTER LEAKAGE	kg/s	NM	261,02	260,52	N/A	N/A	ESTIMATED
ASH FLOW	kg/s	7,13	7,13	7,13	N/A	N/A	ESTIMATED
AH LEAKAGE	kg/S	NM	29,18	29,68	N/A	1,68	ESTIMATED
PRESSURES							
LH FDF DIS P	KPA	3,43	3,43	3,43	N/A	N/A	DCS
SEC A C/OVER DUCT P	KPA	2,43	N/A	N/A	N/A	N/A	DCS
AIR HEATER AIR DP	KPA	1,00	0,70	0,62	29,60	-12,98	DCS
LH SEC AH INLET GAS P	KPA	-0,77	-0,77	-0,77	N/A	N/A	C-SCHEDULE
AIR HEATER FLUE GAS DP	KPA	NOT MEASURED	0,73	0,61	N/A	-19,44	ESTIMATED
FLUID PROPERTIES							
FG DENSITY AT INLET SIMULATED	kg/m³	NOT MEASURED	0,54	0,54	N/A	-0,01	ESTIMATED
FG DENSITY AT OUTLET SIMULATED	kg/m³	NOT MEASURED	0,85	0,86	N/A	1,90	ESTIMATED
AIR DENSITY AT INLET SIMULATED	kg/m³	NOT MEASURED	1,10	1,10	N/A	0,00	ESTIMATED
AIR DENSITY AT OUTLET SIMULATED	kg/m³	NOT MEASURED	0,60	0,61	N/A	1,21	ESTIMATED
FG HEAT CAPCITY AT INLET SIMULATED	kJ/kgK	NOT MEASURED	1,07	1,07	N/A	0,00	ESTIMATED
FG HEAT CAPCITY AT OUTLET SIMULATED	kJ/kgK	NOT MEASURED	1,02	1,02	N/A	-0,06	ESTIMATED
AIR HEAT CAPCITY AT INLET SIMULATED	kJ/kgK	NOT MEASURED	1,01	1,01	N/A	0,00	ESTIMATED
AIR HEAT CAPCITY AT OUTLET SIMULATED	kJ/kgK	NOT MEASURED	1,05	1,05	N/A	-0,14	ESTIMATED
FG VELOCITY AT INLET SIMULATED	m/s	NOT MEASURED	7,83	7,58	N/A	-3,36	ESTIMATED
FG VELOCITY AT OUTLET SIMULATED	m/s	NOT MEASURED	5,00	5,24	N/A	4,53	ESTIMATED
AIR VELOCITY AT INLET SIMULATED	m/s	NOT MEASURED	4,65	4,65	N/A	0,05	ESTIMATED
AIR VELOCITY AT OUTLET SIMULATED	m/s	NOT MEASURED	8,47	7,52	N/A	-12,64	ESTIMATED
ENERGY							
FG HEAT ENEREGY LOST	MW	NOT MEASURED	-37,67	-35,49	0,00	-6,15	ESTIMATED
AIR HEAT ENERGY GAINED	MW	NOT MEASURED	38,02	35,38	0,00	-7,45	ESTIMATED

Table C5:Pre-Test Result Comparison Sheet for a 68% MCR load condition.

PRE-TEST RESULTS							
PARAMATERS	UNITS	68 MCR					MEASUREMENT SOURCE
					ERROR		
		MEASURED DATA	RAH VBA	RAH DELPHI	%MEAS	%DELPHI	
GEN LOAD 1	MW	465					
DATE	DAY/MONTH/YEAR	22/12/2019					
TIME	HR:MIN:SEC-HR:MIN:SEC	20:17:06 - 20:18:46					
LH SEC A/H GAS IN T	CEL	320,8	320,80	320,80	N/A	N/A	DCS / RT&D
LH SEC A/H GAS OUT T	CEL	113,4	102,07	107,38	-9,99	4,95	DCS
LH SEC A/H INL T	CEL	45,8	45,80	45,80	N/A	N/A	DCS
LH SEC A T	CEL	301,1	301,55	297,47	0,15	-1,37	DCS
COMBINED TEMPERATURES							
LH AH COMBINED TEMPS	CEL	79,6	73,94	76,59	-7,12	3,47	DCS
CE OUTLET METAL TEMPERATURES TEMPERATURES							
MAXIMUM	CEL	138,4	139,99	183,31	1,15	23,63	MEASURED
MINIMUM	CEL	66,2	66,52	63,85	0,48	-4,18	MEASURED
AVERAGE	CEL	102,3	103,26	123,58	0,93	16,45	MEASURED
FLUE GAS PROPERTIES							
FLUE GAS BEFORE AH OXYGEN	%	3,5	3,50	3,50	N/A	N/A	COAL ANALYSIS
FLUE GAS AFTER AH OXYGEN	%	5,9	5,90	5,90	N/A	N/A	ASSUMPTION
FLUE GAS BEFORE AH CARBON DIOXIDE	%	10,65	10,65	10,65	N/A	N/A	ESTIMATED
FLUE GAS BEFORE AH SULPHUR DIOXIDE	%	0,11	0,11	0,11	N/A	N/A	ESTIMATED
FLUE GAS BEFORE AH MOISTURE	%	4,16	4,16	4,16	N/A	N/A	COAL ANALYSIS
FLOWS							
FLUE GAS FLOW	kg/s	250,25	250,25	250,25	N/A	N/A	ESTIMATED
SEC A FLOW	kg/s	248,20	248,20	248,20	N/A	N/A	DCS
SEC A FLOW AFTER LEAKAGE	kg/s	N/A	221,87	222,24	N/A	0,17	ESTIMATED
ASH FLOW	kg/s	7,13	7,13	7,13	N/A	N/A	ESTIMATED
AH LEAKAGE	kg/S	N/A	26,33	25,96	N/A	-1,43	ESTIMATED
PRESSURES							
LH FDF DIS P	KPA	3,02	3,02	3,02	N/A	N/A	DCS
SEC A C/OVER DUCT P	KPA	2,29	N/A	N/A	N/A	N/A	DCS
AIR HEATER AIR DP	KPA	0,73	0,55	0,47	-25,07	-15,89	DCS
LH SEC AH INLET GAS P	KPA	-0,772	-0,772	-0,772	N/A	N/A	C-SCHEDULE
AIR HEATER FLUE GAS DP	KPA	NOT MEASURED	0,58	0,49	N/A	-17,13	ESTIMATED
FLUID PROPERTIES							
FG DENSITY AT INLET SIMULATED	kg/m³	NOT MEASURED	0,55	0,56	N/A	0,83	ESTIMATED
FG DENSITY AT OUTLET SIMULATED	kg/m³	NOT MEASURED	0,85	0,88	N/A	2,53	ESTIMATED
AIR DENSITY AT INLET SIMULATED	kg/m³	NOT MEASURED	1,11	1,11	N/A	0,00	ESTIMATED
AIR DENSITY AT OUTLET SIMULATED	kg/m³	NOT MEASURED	0,61	0,62	N/A	1,10	ESTIMATED
FG HEAT CAPCITY AT INLET SIMULATED	kJ/kgK	NOT MEASURED	1,07	1,08	N/A	0,47	ESTIMATED
FG HEAT CAPCITY AT OUTLET SIMULATED	kJ/kgK	NOT MEASURED	1,02	1,02	N/A	-0,19	ESTIMATED
AIR HEAT CAPCITY AT INLET SIMULATED	kJ/kgK	NOT MEASURED	1,01	1,01	N/A	0,00	ESTIMATED
AIR HEAT CAPCITY AT OUTLET SIMULATED	kJ/kgK	NOT MEASURED	1,05	1,05	N/A	-0,14	ESTIMATED
FG VELOCITY AT INLET SIMULATED	m/s	NOT MEASURED	6,71	6,45	N/A	-3,97	ESTIMATED
FG VELOCITY AT OUTLET SIMULATED	m/s	NOT MEASURED	4,33	4,52	N/A	4,20	ESTIMATED
AIR VELOCITY AT INLET SIMULATED	m/s	NOT MEASURED	3,95	3,95	N/A	0,05	ESTIMATED
AIR VELOCITY AT OUTLET SIMULATED	m/s	NOT MEASURED	7,14	6,32	N/A	-12,93	ESTIMATED
ENERGY							
FG HEAT ENEREGY LOST	MW	NOT MEASURED	-31,04	-29,59	0,00	-4,89	ESTIMATED
AIR HEAT ENERGY GAINED	MW	NOT MEASURED	31,66	29,48	0,00	-7,40	ESTIMATED

Table C6: Summary of the air heater operating conditions before and after the replacement of the 2.78DU profile element packs with the HC11 element packs.

FD FAN AMPS													
	U1		U2		U3		U4		U5		U6		AVERAGE
	LH	RH	LH	RH	LH	RH	LH	RH	LH	RH	LH	RH	INCREASE
Averages BEFORE PC	201.5	205.3	203.2	203.4	175.1	176.0	205.3	212.5	200.1	198.4	191.5	192.0	IN AMPS
Averages AFTER PC	210.7	211.1	215.9	212.1	210.6	207.6	218.7	224.3	226.6	224.7	218.7	212.5	19.10
FD FAN PRESSURE													AVERAGE INCREASE
Averages BEFORE PC	3.114	3.092	3.444	3.079	3.397	3.791	3.412	3.603	3.410	3.469	3.389	3.330	IN DP
Averages AFTER PC	3.502	3.360	3.760	3.527	3.660	3.927	3.812	3.624	3.520	3.745	3.649	3.607	0.26
AIR INLET T													AVERAGE INCREASE
Averages BEFORE PC	58.7	52.3	53.5	53.4	52.7	60.2	56.1	53.9	55.0	53.4	60.0	53.9	IN TEMP
Averages AFTER PC	58.6	55.8	57.2	60.4	55.5	58.7	56.4	59.2	57.6	55.0	57.3	54.5	1.92
AIR OUT T													AVERAGE INCREASE
Averages BEFORE PC	301.7	309.3	294.5	303.9	291.9	284.6	297.9	302.6	309.3	277.8	302.9	303.9	IN TEMP
Averages AFTER PC	306.9	313.5	314.5	318.6	284.7	302.0	309.8	315.8	306.8	298.2	308.	306.8	8.83
FLUE GAS IN T													AVERAGE INCREASE
Average	318.8	329.9	327.2	325.3	335.5	334.8	323.3	330.5	324.1	325.5	340.0	332.0	IN TEMP
FLUE GAS OUT T													AVERAGE DECREASE
Averages BEFORE PC	124.8	134.2	132.2	133.0	133.0	125.4	128.4	13	125.3	129.6	126.3	134.2	IN TEMP
Averages AFTER PC	122.8	135.0	129.8	130.6	134.9	131.2	125.7	129.3	127.2	131.8	128.	132.4	0.03

Figure C1 in- Data set 1 (Pre-Testing Phase) Result, is a representation of the temperature profiles simulated for each layer in comparison to the measured temperature profiles for each layer specific to Ring 6 measurements at a 99% MCR load condition. This graphical representation has a top horizontal axis, indicating the time for one rotation (0-100 seconds), and a bottom horizontal axis indicating the angle of rotation in degrees for one full rotation (0 -360˚). It also has one vertical axis which indicates temperature. The temperature range is applicable to the fluid and metal temperatures. The simulated metal temperatures (solid lines) and simulated fluid temperatures (broken dotted dashed lines) are compared to the measured metal temperatures (long dashed lines) and measured fluid temperatures (short dashed lines) for the inlet and outlet condition of each layer. The comparison referred to in Figure C4 only takes into consideration Ring 6, due to the fact that it correlates more with the simulation curve. It is clear that the load condition affects the amplitude of the thermal profile curve. A higher load shows an increased rate of heat transfer through the higher rate of temperature change which is directly connected to the flue gas and air flow rates. A higher flow rate is experienced at higher loads, along with reduced leakage rates, which therefore increase the rate of temperature change along with reduced outlet flue gas temperatures. This is also a reason why an increase in seal during higher loads are experienced. The increased thermal performance at higher load are directly related to the thermal expansion of the air heater. The thermal expansion is greater causing more affective sealing

The 80% MCR were simulated and the results were compared to the measured values. Figure C2 in Appendix C- C1: Pre- Testing Phase Results is a representation of the combined results, where the simulation data had a time step of 0.333 seconds and the measured values were logged every second. This figure shows that there was a large deviation in the intermediate layer outlet temperatures, but the intermediate hot end and cold end inlet temperatures shows a correlation. The comparison referred to in Figure C2 only takes into consideration Ring 6, due to the fact that it correlates more with the simulation curve. During the second pre-test results at 80% MCR Ring 2 and Ring 6 results were compared. Ring 2 once again represented a flattened curve in comparison to Ring 6. As mentioned previously, this could be due to the fact that thermocouples were exposed to both the fluid region and surrounding metal surfaces, therefore it measured a combined temperature which showed less fluctuation.

The 68% MCR parameters were simulated and the results were compared to the measured values which are represented in Figure C4 in Appendix C – C1 Pre-Testing Phase results. This is a representation of the combined results, where the simulation data had a time step of 0.333 seconds and the measured values were logged every second. This is the same process followed for the two previous load conditions. Once again a deviation in the intermediate layer inlet temperatures were found, but the hot end inlet and cold end inlet and outlet temperatures showed improved correlations. During this phase the fluid temperatures measured, also had a similar profile to the metal temperature as with the previous pre-test results.

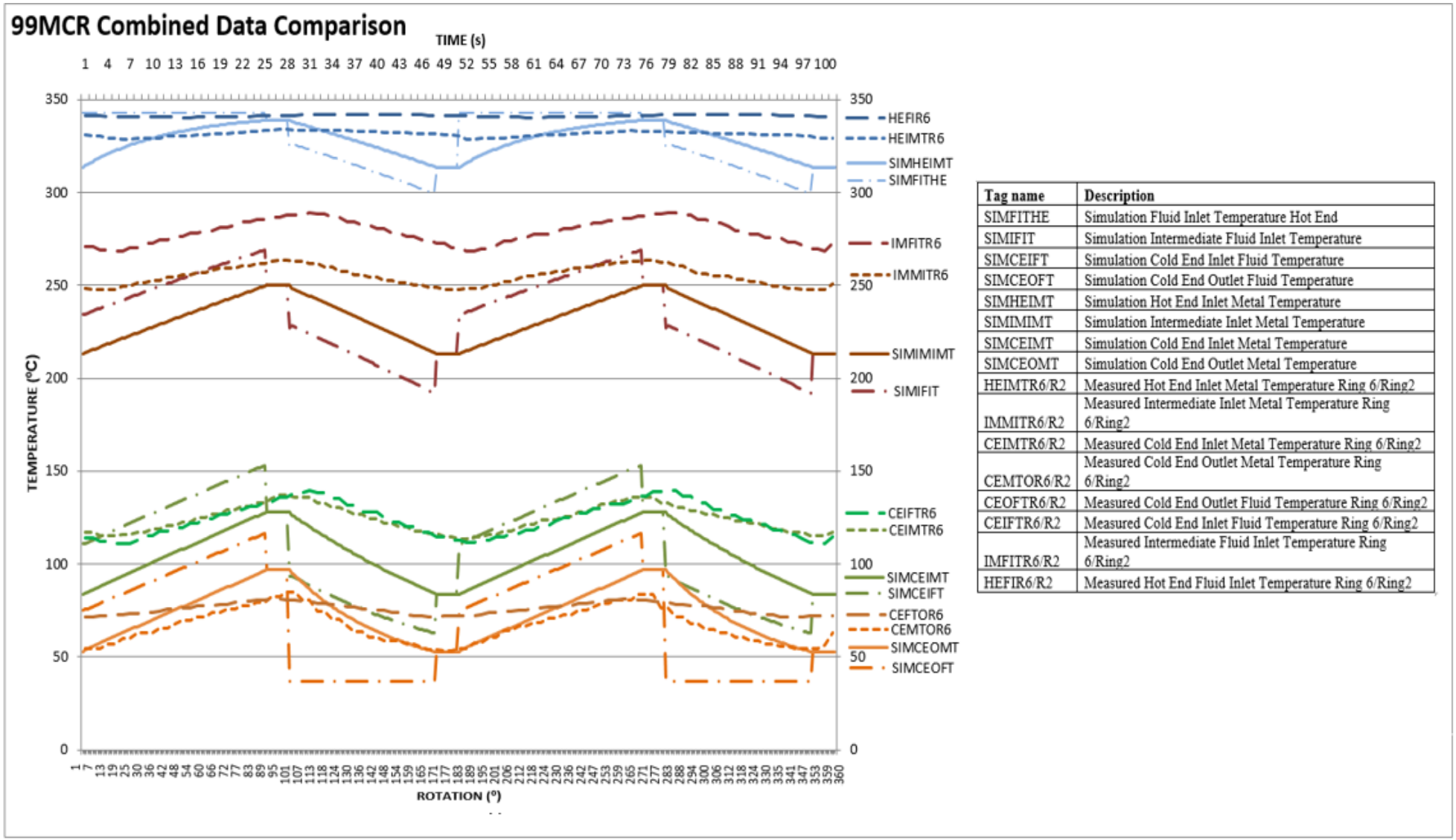

Tag name	Description
SIMFITHE	Simulation Fluid Inlet Temperature Hot End
SIMIFIT	Simulation Intermediate Fluid Inlet Temperature
SIMCEIFT	Simulation Cold End Inlet Fluid Temperature
SIMCEOFT	Simulation Cold End Outlet Fluid Temperature
SIMHEIMT	Simulation Hot End Inlet Metal Temperature
SIMIMIMT	Simulation Intermediate Inlet Metal Temperature
SIMCEIMT	Simulation Cold End Inlet Metal Temperature
SIMCEOMT	Simulation Cold End Outlet Metal Temperature
HEIMTR6/R2	Measured Hot End Inlet Metal Temperature Ring 6/Ring2
IMMITR6/R2	Measured Intermediate Inlet Metal Temperature Ring 6/Ring2
CEIMTR6/R2	Measured Cold End Inlet Metal Temperature Ring 6/Ring2
CEMTOR6/R2	Measured Cold End Outlet Metal Temperature Ring 6/Ring2
CEOFTR6/R2	Measured Cold End Outlet Fluid Temperature Ring 6/Ring2
CEIFTR6/R2	Measured Cold End Inlet Fluid Temperature Ring 6/Ring2
IMFITR6/R2	Measured Intermediate Fluid Inlet Temperature Ring 6/Ring2
HEFIR6/R2	Measured Hot End Fluid Inlet Temperature Ring 6/Ring2

Figure C1: Pre-test comparison for 99% MCR operating condition.

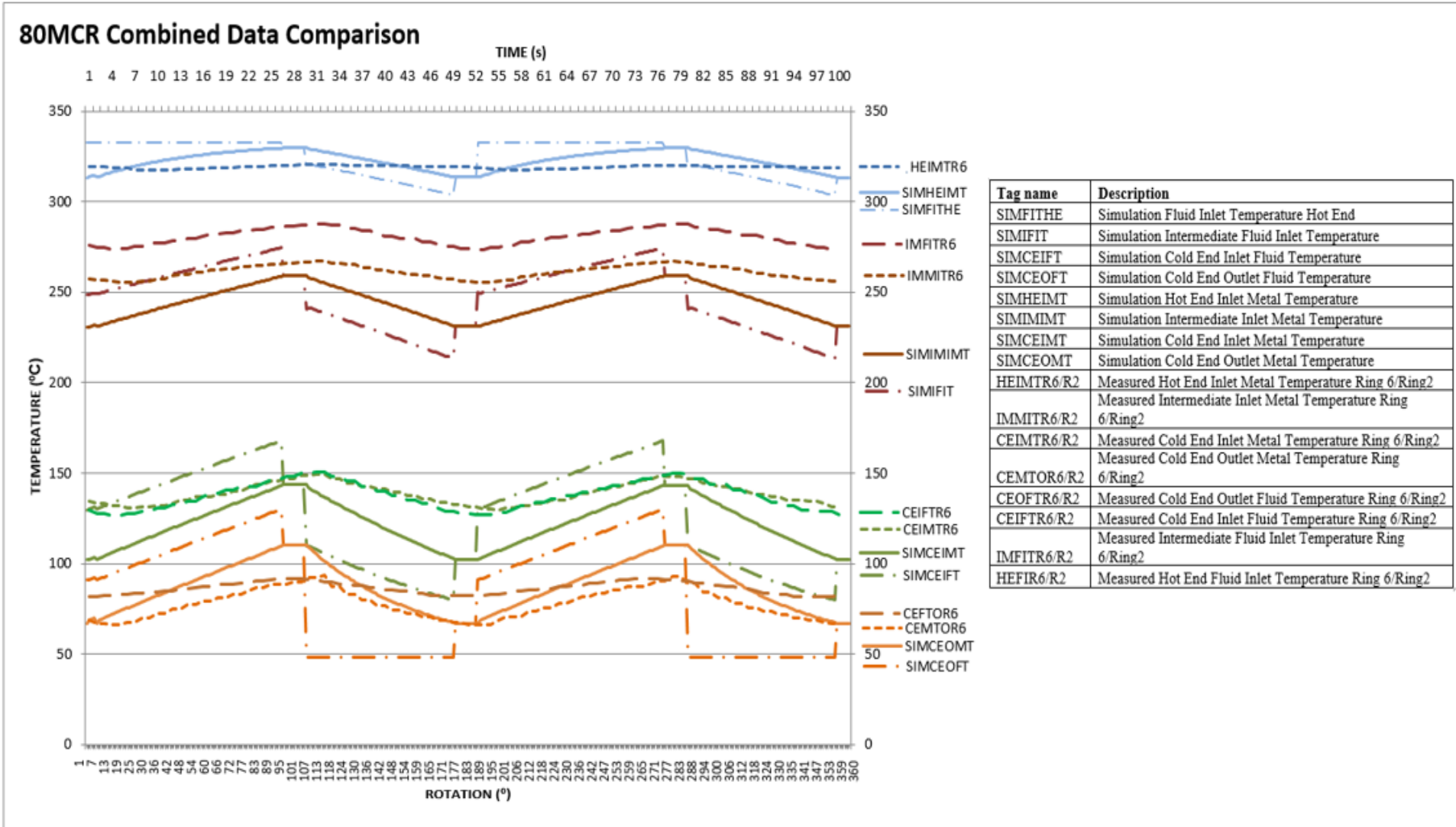

Tag name	Description
SIMFITHE	Simulation Fluid Inlet Temperature Hot End
SIMIFIT	Simulation Intermediate Fluid Inlet Temperature
SIMCEIFT	Simulation Cold End Inlet Fluid Temperature
SIMCEOFT	Simulation Cold End Outlet Fluid Temperature
SIMHEIMT	Simulation Hot End Inlet Metal Temperature
SIMIMIMT	Simulation Intermediate Inlet Metal Temperature
SIMCEIMT	Simulation Cold End Inlet Metal Temperature
SIMCEOMT	Simulation Cold End Outlet Metal Temperature
HEIMTR6/R2	Measured Hot End Inlet Metal Temperature Ring 6/Ring2
IMMITR6/R2	Measured Intermediate Inlet Metal Temperature Ring 6/Ring2
CEIMTR6/R2	Measured Cold End Inlet Metal Temperature Ring 6/Ring2
CEMTOR6/R2	Measured Cold End Outlet Metal Temperature Ring 6/Ring2
CEOFTR6/R2	Measured Cold End Outlet Fluid Temperature Ring 6/Ring2
CEIFTR6/R2	Measured Cold End Inlet Fluid Temperature Ring 6/Ring2
IMFITR6/R2	Measured Intermediate Fluid Inlet Temperature Ring 6/Ring2
HEFIR6/R2	Measured Hot End Fluid Inlet Temperature Ring 6/Ring2

Figure C2: Pre-test comparison for 80% MCR operating condition

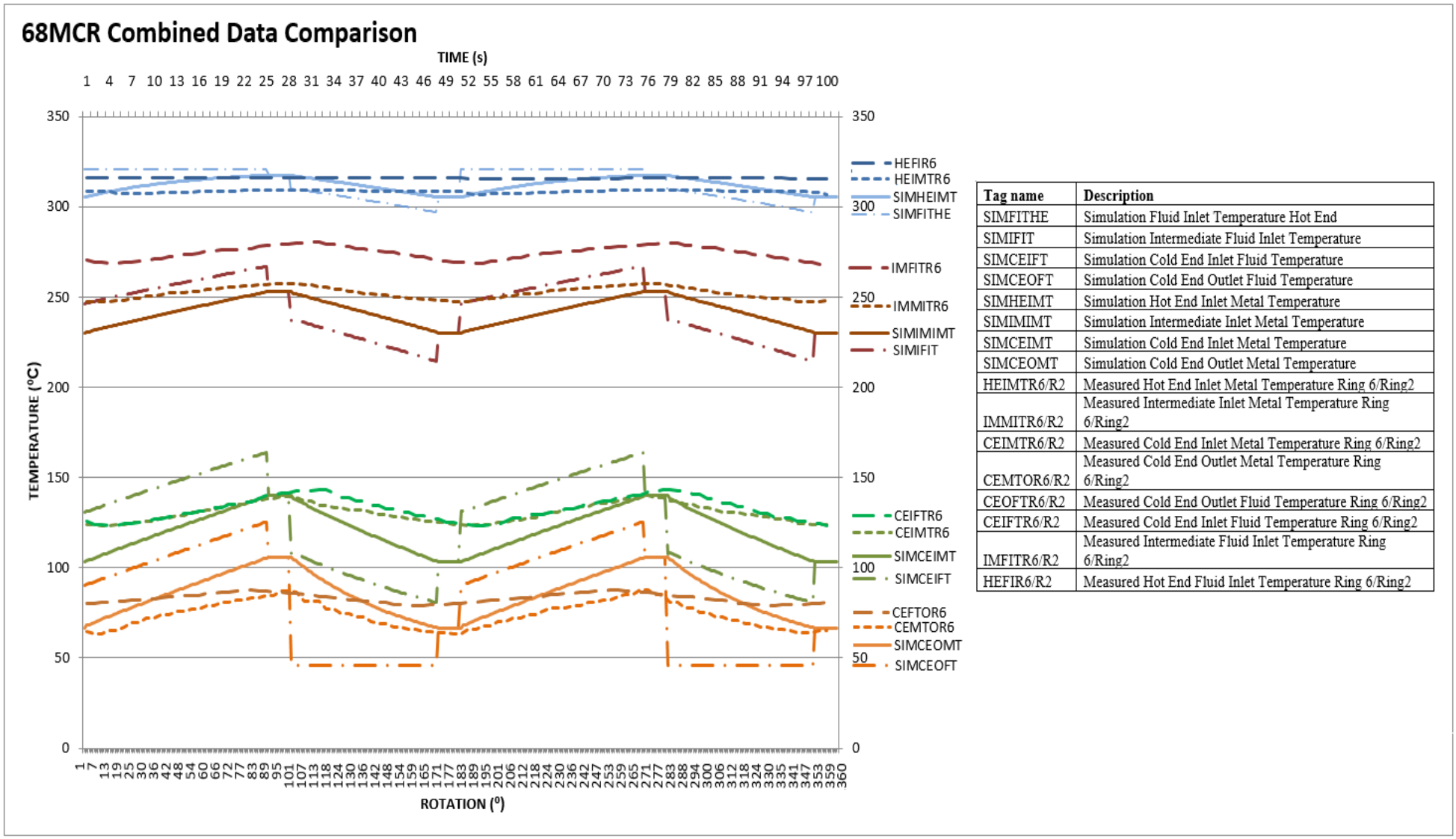

Tag name	Description
SIMFITHE	Simulation Fluid Inlet Temperature Hot End
SIMIFIT	Simulation Intermediate Fluid Inlet Temperature
SIMCEIFT	Simulation Cold End Inlet Fluid Temperature
SIMCEOFT	Simulation Cold End Outlet Fluid Temperature
SIMHEIMT	Simulation Hot End Inlet Metal Temperature
SIMIMIMT	Simulation Intermediate Inlet Metal Temperature
SIMCEIMT	Simulation Cold End Inlet Metal Temperature
SIMCEOMT	Simulation Cold End Outlet Metal Temperature
HEIMTR6/R2	Measured Hot End Inlet Metal Temperature Ring 6/Ring2
IMMITR6/R2	Measured Intermediate Inlet Metal Temperature Ring 6/Ring2
CEIMTR6/R2	Measured Cold End Inlet Metal Temperature Ring 6/Ring2
CEMTOR6/R2	Measured Cold End Outlet Metal Temperature Ring 6/Ring2
CEOFTR6/R2	Measured Cold End Outlet Fluid Temperature Ring 6/Ring2
CEIFTR6/R2	Measured Cold End Inlet Fluid Temperature Ring 6/Ring2
IMFITR6/R2	Measured Intermediate Fluid Inlet Temperature Ring 6/Ring2
HEFIR6/R2	Measured Hot End Fluid Inlet Temperature Ring 6/Ring2

Figure C4: Pre-test comparison for 68% MCR operating condition.

C2: Data Set 2 - Results

Table C7: 99% MCR Actual test results comparison table.

ACTUAL-TEST RESULTS							
PARAMATERS	UNITS	99 MCR			ERROR		MEASUREMENT SOURCE
		MEASURED DATA	RAH VBA	RAH DELPHI	%MEAS	%DELPHI	
GEN LOAD 1	MW	672					
	DAY/MONTH/YEAR	24/02/2020					
	HR:MIN:SEC-HR:MIN:SEC	00:00:00 - 04:00:00					
		MEASURED DATA	RAH VBA	RAH DELPHI	%MEAS	%DELPHI	
LH SEC A/H GAS IN T	CEL	339	339	339	0,00		RT&D
LH SEC A/H GAS OUT T	CEL	120	104,21	103,28	-13,16		DCS
LH SEC A/H INL T	CEL	50,54	50,54	50,54	0,00		DCS
LH SEC A T	CEL	307,98	316,58	311,33	2,79		DCS
COMBINED TEMPERATURES							
LH AH COMBINED TEMPS CALCULATED		85,27	77,375	76,91	-9,26		ESTIMATED
LH AH COMBINED TEMPS	CEL	85,27	77,375	76,91	-9,26		DCS
COLD END OUTLET METAL TEMPERATURES							
MAXIMUM	CEL	128,6	147,01	194,82	14,32		INSTALLED THERMOCOUPLE
MINIMUM	CEL	68,1	69,67	67,71	2,31		INSTALLED THERMOCOUPLE
AVERAGE	CEL	98,35	108,34	131,265	10,16		ESTIMATED
COAL PROPERTIES (Air dried)							
Carbon	%	54,94	54,94	N/A	N/A	N/A	P&T COAL SAMPLING
Hydrogen	%	2,52	2,52	N/A	N/A	N/A	P&T COAL SAMPLING
Nitrogen	%	1,19	1,19	N/A	N/A	N/A	P&T COAL SAMPLING
Total Sulphur	%	1,51	1,51	N/A	N/A	N/A	P&T COAL SAMPLING
Carbonate	%	2,76	2,76	N/A	N/A	N/A	P&T COAL SAMPLING
Oxygen (by difference)	%	3,98	3,98	N/A	N/A	N/A	P&T COAL SAMPLING
Analytical moisture	%	2,1	2,1	N/A	N/A	N/A	P&T COAL SAMPLING
Surface Moisture	%	4,9	4,9	N/A	N/A	N/A	P&T COAL SAMPLING
Inherent Moisture (as received)	%	2	2	N/A	N/A	N/A	P&T COAL SAMPLING
Total Moisture	%	6,9	6,9	N/A	N/A	N/A	P&T COAL SAMPLING
Ash	%	31	31	N/A	N/A	N/A	P&T COAL SAMPLING
TOTAL	**%**	**100**	**100**	N/A	N/A	N/A	RT&D
Fly Ash	**Ratio**	0,9	0,9	N/A	N/A	N/A	ASSUMED
Bottom Ash	**Ratio**	0,1	0,1	N/A	N/A	N/A	ASSEMED
Gross CV (As received)	MJ/KG	20,56	20,56	N/A	N/A	N/A	P&T COAL SAMPLING
Coal flow	MJ/s	1649,08	1649,08	N/A	N/A	N/A	DCS
FLUE GAS PROPERTIES							
FLUE GAS BEFORE AH OXYGEN @6% O2	%	3,24	3,24	3,24	-1,54	N/A	RT&D

FLUE GAS BEFORE AH OXYGEN (ESTIMATED)	%	3,29	3,29	N/A		N/A	SIMULATED
FLUE GAS AFTER AH OXYGEN @6% O2	%	6,88	6,88	6,88	N/A	N/A	RT&D
FLUE GAS BEFORE AH CARBON DIOXIDE @6% O2	%	13,49	13,49	13,49		N/A	RT&D
FLUE GAS BEFORE AH CARBON DIOXIDE (ESTIMATED)	%	16,1	16,10	N/A	-19,35	N/A	SIMULATED
FLUE GAS BEFORE AH SULPHUR DIOXIDE @6% O2	%	0,23	0,23	0,17		N/A	RT&D
FLUE GAS BEFORE AH SULPHUR DIOXIDE (ESTIMATED)	%	0,16	0,16	N/A	30,43	N/A	SIMULATED
FLUE GAS BEFORE AH MOISTURE @6% O2	%	4,49	4,49	4,49		N/A	RT&D
FLUE GAS BEFORE AH MOISTURE (ESTIMATED)	%	5,52	5,52	N/A	-22,94	N/A	SIMULATED
FLOWS							
TOT COAL FLOW	kg/s	80,21	80,21	80,21	0,00		ESTIMATED (DCS AND MEASURED CV)
FLUE GAS FLOW	kg/s	384,22	Not used	Not used	N/A	N/A	RT&D
ESTIMATED FLUE GAS FLOW	kg/s	283,12	283,12	283,12	0,00		ESTIMATED (DCS AND MEASURED CV)
Error in gas flow	%	24,10	24,10	24,10	0,00		ESTIMATED
SEC A FLOW	kg/s	305,64	305,64	305,64	0,00		DCS
TOTAL AIRFLOW TO BURNERS	kg/s	783,02	783,02	783,02	783,02		DCS
ASHFLOW	kg/s	11,19	11,19	11,19	11,19		ESTIMATED
AH LEAKAGE	%	26,78	26,78	26,78			DCS
PRESSURES							
LH FDF DIS P	KPA	3,688	3,688	3,688	N/A	N/A	DCS
SEC A C/OVER DUCT P	KPA	2,477	N/A	N/A	N/A	N/A	DCS
AIR HEATER AIR DP air	KPA	1,211	0,774	0,6133	-36,09		DCS
LH SEC AH INLET GAS P	KPA	-1,0944	-1,0944	-1,0944	N/A	N/A	RT&D
LH SEC AH OUTLET GAS P	KPA	-0,235	N/A	N/A	N/A	N/A	RT&D
AIR HEATER DP gas	KPA	0,8594	0,7339	0,6071	-14,60		RT&D
FLUID PROPERTIES							
FG DENSITY AT INLET SIMULATED	kg/m^3	0,53	0,55	0,54	3,32		RT&D
FG DENSITY AT OUTLET SIMULATED	kg/m^3	NOT MEASURED	0,858527	0,8827	N/A		ESTIMATED
AIR DENSITY AT INLET SIMULATED	kg/m^3	NOT MEASURED	1,0908	1,0908	N/A		ESTIMATED
AIR DENSITY AT OUTLET SIMULATED	kg/m^3	NOT MEASURED	0,59714	0,6028	N/A		ESTIMATED
FG HEAT CAPCITY AT INLET SIMULATED	kJ/kgK	NOT MEASURED	1,078199	1,0782	N/A		ESTIMATED
FG HEAT CAPCITY AT OUTLET SIMULATED	kJ/kgK	NOT MEASURED	1,01752	1,0161	N/A		ESTIMATED
AIR HEAT CAPCITY AT INLET SIMULATED	kJ/kgK	NOT MEASURED	1,0116	1,0116	N/A		ESTIMATED
AIR HEAT CAPCITY AT OUTLET SIMULATED	kJ/kgK	NOT MEASURED	1,0552	1,054	N/A		ESTIMATED
FG VELOCITY AT INLET SIMULATED	m/s	NOT MEASURED	7,688	7,2778	N/A		ESTIMATED
FG VELOCITY AT OUTLET SIMULATED	m/s	NOT MEASURED	4,892	5,219	N/A		ESTIMATED
AIR VELOCITY AT INLET SIMULATED	m/s	NOT MEASURED	4,9389	4,8421	N/A		ESTIMATED
AIR VELOCITY AT OUTLET SIMULATED	m/s	NOT MEASURED	9,02	7,4406	N/A		ESTIMATED
ENERGY							
FG HEAT ENEREGY LOST	MW	NOT MEASURED	-37,87	-36,7238	N/A		ESTIMATED
AIR HEAT ENERGY GAINED	MW	NOT MEASURED	38,38	36,6428	N/A		ESTIMATED

Table C8: 80% MCR Actual test results comparison table.

ACTUAL-TEST RESULTS								
PARAMATERS	UNITS	99 MCR	80 MCR					MEASUREMENT SOURCE
		ERROR				ERROR		
		%DELPHI	MEASURED DATA	RAH VBA	RAH DELPHI	%MEAS	%DELPHI	
GEN LOAD 1	MW		545,00					
	DAY/MONTH/YEAR	24/02/2020	25/02/2020					
	HR:MIN:SEC-HR:MIN:SEC	00:00:00 - 04:00:00	00:00:00 - 04:00:00					
		%DELPHI	MEASURED DATA	RAH VBA	RAH DELPHI	%MEAS	%DELPHI	
LH SEC A/H GAS IN T	CEL		320	320,00	320,00	N/A	N/A	RT&D
LH SEC A/H GAS OUT T	CEL		117	107,34	104,79	8,26		DCS
LH SEC A/H INL T	CEL		56	56,00	56,00	N/A	N/A	DCS
LH SEC A T	CEL		297	302,90	300,37	-1,99		DCS
COMBINED TEMPERATURES								
LH AH COMBINED TEMPS CALCULATED			86,50	81,67	80,40			ESTIMATED
LH AH COMBINED TEMPS	CEL		105,50	N/A	N/A	N/A	N/A	DCS
COLD END OUTLET METAL TEMPERATURES								
MAXIMUM	CEL		149,20	149,52	188,02	-0,21		INSTALLED THERMOCOUPLE
MINIMUM	CEL		66,00	76,86	73,60	-16,45		INSTALLED THERMOCOUPLE
AVERAGE	CEL		107,60	113,19	130,81	-5,20		ESTIMATED
COAL PROPERTIES (Air dried)								
Carbon	%	N/A	56,52	56,52	N/A	N/A	N/A	P&T COAL SAMPLING
Hydrogen	%	N/A	2,62	2,62	N/A	N/A	N/A	P&T COAL SAMPLING
Nitrogen	%	N/A	1,34	1,34	N/A	N/A	N/A	P&T COAL SAMPLING
Total Sulphur	%	N/A	1,28	1,28	N/A	N/A	N/A	P&T COAL SAMPLING
Carbonate	%	N/A	2,86	2,86	N/A	N/A	N/A	P&T COAL SAMPLING
Oxygen (by difference)	%	N/A	4,08	4,08	N/A	N/A	N/A	P&T COAL SAMPLING
Analytical moisture	%	N/A	2,3	2,3	N/A	N/A	N/A	P&T COAL SAMPLING
Surface Moisture	%	N/A	7,9	7,9	N/A	N/A	N/A	P&T COAL SAMPLING
Inherent Moisture (as received)	%	N/A	2,1	2,1	N/A	N/A	N/A	P&T COAL SAMPLING
Total Moisture	%	N/A	10,0	10,0	N/A	N/A	N/A	P&T COAL SAMPLING
Ash	%	N/A	29,0	29,0	N/A	N/A	N/A	P&T COAL SAMPLING
TOTAL	**%**	N/A	**100**	**100**	N/A	N/A	N/A	RT&D
Fly Ash	**Ratio**	N/A	0,9	0,9	N/A	N/A	N/A	ASSUMED
Bottom Ash	**Ratio**	N/A	0,1	0,1	N/A	N/A	N/A	ASSEMED
Gross CV (As received)	MJ/KG	N/A	20,51	20,51	N/A	N/A	N/A	P&T COAL SAMPLING
Coal flow	MJ/s	N/A	1331,59	1331,59	N/A	N/A	N/A	DCS
FLUE GAS PROPERTIES								
FLUE GAS BEFORE AH OXYGEN @6% O2	%	N/A	4,3	4,30	4,30		N/A	RT&D
FLUE GAS BEFORE AH OXYGEN (ESTIMATED)	%	N/A	4,35	4,35	N/A	-1,16	N/A	SIMULATED
FLUE GAS AFTER AH OXYGEN @6% O2	%	N/A	8,84	8,84	8,84	N/A	N/A	RT&D

FLUE GAS BEFORE AH CARBON DIOXIDE @6% O2	%	N/A	14,76	14,76	14,76		N/A	RT&D
FLUE GAS BEFORE AH CARBON DIOXIDE (ESTIMATED)	%	N/A	15,12	15,12	N/A	-2,44	N/A	SIMULATED
FLUE GAS BEFORE AH SULPHUR DIOXIDE @6% O2	%	N/A	0,24	0,24	0,24		N/A	RT&D
FLUE GAS BEFORE AH SULPHUR DIOXIDE (ESTIMATED)	%	N/A	0,13	0,13	N/A	45,83	N/A	SIMULATED
FLUE GAS BEFORE AH MOISTURE @6% O2	%	N/A	3,47	3,47	3,47		N/A	RT&D
FLUE GAS BEFORE AH MOISTURE (ESTIMATED)	%	N/A	5,77	5,77	N/A	-66,28	N/A	SIMULATED
FLOWS								
TOT COAL FLOW	kg/s		64,92	64,92	64,92	N/A	N/A	ESTIMATED (DCS AND MEASURED CV)
FLUE GAS FLOW	kg/s	N/A	243,15	243,15	243,15	N/A	N/A	RT&D
ESTIMATED FLUE GAS FLOW	kg/s		249,82	Not used	Not used	N/A	N/A	ESTIMATED (DCS AND MEASURED CV)
Error in gas flow	%		-2,74	-2,74	-2,74	N/A	N/A	ESTIMATED
SEC A FLOW	kg/s		260,29	260,29	260,29	N/A	N/A	DCS
TOTAL AIRFLOW TO BURNERS	kg/s		687,59	687,59	687,59	N/A	N/A	DCS
ASHFLOW	kg/s		8,47	8,47	8,47	N/A	N/A	ESTIMATED
AH LEAKAGE	%		36,23	36,23	36,23	N/A	N/A	DCS
PRESSURES								
LH FDF DIS P	KPA	N/A	3,3	3,30	3,30	N/A	N/A	DCS
SEC A C/OVER DUCT P	KPA	N/A	2,439	N/A	N/A	N/A	N/A	DCS
AIR HEATER AIR DP air	KPA		0,861	0,61	0,47	29,67		DCS
LH SEC AH INLET GAS P	KPA	N/A	-0,807	-0,807	-0,80	N/A	N/A	RT&D
LH SEC AH OUTLET GAS P	KPA	N/A	-0,258	N/A	N/A	N/A	N/A	RT&D
AIR HEATER DP gas	KPA		0,549	0,56	0,45	-1,82		RT&D
FLUID PROPERTIES								
FG DENSITY AT INLET SIMULATED	kg/m^3		0,55	0,56	0,56	-3,06		RT&D
FG DENSITY AT OUTLET SIMULATED	kg/m^3		NOT MEASURED	0,85	0,88	N/A		ESTIMATED
AIR DENSITY AT INLET SIMULATED	kg/m^3		NOT MEASURED	1,07	1,07	N/A		ESTIMATED
AIR DENSITY AT OUTLET SIMULATED	kg/m^3		NOT MEASURED	0,61	0,61	N/A		ESTIMATED
FG HEAT CAPCITY AT INLET SIMULATED	kJ/kgK		NOT MEASURED	1,07	1,07	N/A		ESTIMATED
FG HEAT CAPCITY AT OUTLET SIMULATED	kJ/kgK		NOT MEASURED	1,01	1,01	N/A		ESTIMATED
AIR HEAT CAPCITY AT INLET SIMULATED	kJ/kgK		NOT MEASURED	1,01	1,01	N/A		ESTIMATED
AIR HEAT CAPCITY AT OUTLET SIMULATED	kJ/kgK		NOT MEASURED	1,05	1,05	N/A		ESTIMATED
FG VELOCITY AT INLET SIMULATED	m/s		NOT MEASURED	6,38	6,16	N/A		ESTIMATED
FG VELOCITY AT OUTLET SIMULATED	m/s		NOT MEASURED	4,22	4,70	N/A		ESTIMATED
AIR VELOCITY AT INLET SIMULATED	m/s		NOT MEASURED	4,28	4,28	N/A		ESTIMATED
AIR VELOCITY AT OUTLET SIMULATED	m/s		NOT MEASURED	7,50	6,12	N/A		ESTIMATED
ENERGY								
FG HEAT ENEREGY LOST	MW		NOT MEASURED	-28,69	-28,55	N/A		ESTIMATED
AIR HEAT ENERGY GAINED	MW		NOT MEASURED	28,37	28,43	N/A		ESTIMATED

Table C9: 68% MCR Actual test results comparison table.

ACTUAL-TEST RESULTS									
PARAMATERS	UNITS	99 MCR ERROR	80 MCR ERROR	68 MCR			ERROR		MEASUREMENT SOURCE
		%DELPHI	%DELPHI	MEASURED DATA	RAH VBA	RAH DELPHI	%MEAS	%DELPHI	
GEN LOAD 1	MW			462					
	DAY/MONTH/YEAR	24/02/2020	25/02/2020	26/02/2020					
	HR:MIN:SEC-HR:MIN:SEC	00:00:00 - 04:00:00	00:00:00 - 04:00:00	00:00:00 - 04:00:00					
		%DELPHI	%DELPHI	MEASURED DATA	RAH VBA	RAH DELPHI	%MEAS	%DELPHI	
LH SEC A/H GAS IN T	CEL		N/A	314,53	314,53	314,53	N/A	N/A	RT&D
LH SEC A/H GAS OUT T	CEL			123	123,69	121,21	0,56	-2,05	DCS
LH SEC A/H INL T	CEL		N/A	57,97	57,97	57,97	N/A	N/A	DCS
LH SEC A T	CEL			290,53	305,00	301,85	4,98	-1,04	DCS
COMBINED TEMPERATURES									
LH AH COMBINED TEMPS CALCULATED				90,49	90,83	89,59	0,38	-1,37	ESTIMATED
LH AH COMBINED TEMPS	CEL		N/A	101,2	N/A	N/A	N/A	N/A	DCS
COLD END OUTLET METAL TEMPERATURES									
MAXIMUM	CEL			139,3	175,20	186,27	25,77	5,94	INSTALLED THERMOCOUPLE
MINIMUM	CEL			63,7	87,20	79,80	36,89	-9,27	INSTALLED THERMOCOUPLE
AVERAGE	CEL			101,5	131,2	133,0355	29,26	1,38	ESTIMATED
COAL PROPERTIES (Air dried)									
Carbon	%	N/A	N/A	54,35	54,35	N/A	N/A	N/A	P&T COAL SAMPLING
Hydrogen	%	N/A	N/A	2,58	2,58	N/A	N/A	N/A	P&T COAL SAMPLING
Nitrogen	%	N/A	N/A	1,06	1,06	N/A	N/A	N/A	P&T COAL SAMPLING
Total Sulphur	%	N/A	N/A	1,23	1,23	N/A	N/A	N/A	P&T COAL SAMPLING
Carbonate	%	N/A	N/A	2,83	2,83	N/A	N/A	N/A	P&T COAL SAMPLING
Oxygen (by difference)	%	N/A	N/A	4,55	4,55	N/A	N/A	N/A	P&T COAL SAMPLING
Analytical moisture	%	N/A	N/A	2,2	2,2	N/A	N/A	N/A	P&T COAL SAMPLING
Surface Moisture	%	N/A	N/A	6,4	6,4	N/A	N/A	N/A	P&T COAL SAMPLING
Inherent Moisture (as received)	%	N/A	N/A	2,1	2,1	N/A	N/A	N/A	P&T COAL SAMPLING
Total Moisture	%	N/A	N/A	8,5	8,5	N/A	N/A	N/A	P&T COAL SAMPLING
Ash	%	N/A	N/A	31,2	31,2	N/A	N/A	N/A	P&T COAL SAMPLING
TOTAL	**%**	N/A	N/A	**100**	**100**	N/A	N/A	N/A	RT&D
Fly Ash	**Ratio**	N/A	N/A	0,9	0,9	N/A	N/A	N/A	ASSUMED
Bottom Ash	**Ratio**	N/A	N/A	0,1	0,1	N/A	N/A	N/A	ASSEMED
Gross CV (As received)	MJ/KG	N/A	N/A	20,1	20,1	N/A	N/A	N/A	P&T COAL SAMPLING
Coal flow	MJ/s	N/A	N/A	1105,58	1105,58	N/A	N/A	N/A	DCS
FLUE GAS PROPERTIES									
FLUE GAS BEFORE AH OXYGEN @6% O2	%	N/A	N/A	5,1	5,10	5,10		N/A	RT&D
FLUE GAS BEFORE AH OXYGEN (ESTIMATED)	%	N/A	N/A	5,2	5,20	N/A	-1,96	N/A	SIMULATED
FLUE GAS AFTER AH OXYGEN @6% O2	%	N/A	N/A	9,77	9,77	9,77	N/A	N/A	RT&D
FLUE GAS BEFORE AH CARBON DIOXIDE @6% O2	%	N/A	N/A	14,32	14,32	14,32	-0,77	N/A	RT&D

FLUE GAS BEFORE AH CARBON DIOXIDE (ESTIMATED)	%	N/A	N/A	14,43	14,43	N/A		N/A	SIMULATED
FLUE GAS BEFORE AH SULPHUR DIOXIDE @6% O2	%	N/A	N/A	0,24	0,24	0,24		N/A	RT&D
FLUE GAS BEFORE AH SULPHUR DIOXIDE (ESTIMATED)	%	N/A	N/A	0,11	0,11	N/A	54,17	N/A	SIMULATED
FLUE GAS BEFORE AH MOISTURE @6% O2	%	N/A	N/A	7,41	7,41	7,41		N/A	RT&D
FLUE GAS BEFORE AH MOISTURE (ESTIMATED)	%	N/A	N/A	5,4	5,40	N/A	27,13	N/A	SIMULATED
FLOWS									
TOT COAL FLOW	kg/s		N/A	55,00	55,00	55,00	N/A	N/A	ESTIMATED (DCS AND MEASURED CV)
FLUE GAS FLOW	kg/s	N/A	N/A	237,65	237,65	237,65	N/A	N/A	RT&D
ESTIMATED FLUE GAS FLOW	kg/s		N/A	231,44	Not used	Not used	N/A	N/A	ESTIMATED (DCS AND MEASURED CV)
Error in gas flow	%		N/A	2,61	2,61	2,61	N/A	N/A	ESTIMATED
SEC A FLOW	kg/s		N/A	233,32	233,32	233,32	N/A	N/A	DCS
TOTAL AIRFLOW TO BURNERS	kg/s		N/A	631,91	631,91	631,91	N/A	N/A	DCS
ASHFLOW	kg/s		N/A	7,72	7,72	7,72	N/A	N/A	ESTIMATED
AH LEAKAGE	%		N/A	40,09	40,09	40,09	N/A	N/A	DCS
PRESSURES									
LH FDF DIS P	KPA	N/A	N/A	3,11	3,11	3,11	N/A	N/A	DCS
SEC A C/OVER DUCT P	KPA	N/A	N/A	2,43	N/A	N/A	N/A	N/A	DCS
AIR HEATER AIR DP air	KPA			0,68	0,53	0,38	-22,06	-38,60	DCS
LH SEC AH INLET GAS P	KPA	N/A	N/A	-0,755	-0,755	-0,755	N/A	N/A	RT&D
LH SEC AH OUTLET GAS P	KPA	N/A	N/A	-0,301	N/A	N/A	N/A	N/A	RT&D
AIR HEATER DP gas	KPA			0,454	0,570	0,480	25,55	-18,43	RT&D
FLUID PROPERTIES									
FG DENSITY AT INLET SIMULATED	kg/m^3			0,54	0,56	0,56	4,28	-0,04	RT&D
FG DENSITY AT OUTLET SIMULATED	kg/m^3			NOT MEASURED	0,80	0,83	N/A	3,83	ESTIMATED
AIR DENSITY AT INLET SIMULATED	kg/m^3			NOT MEASURED	1,07	1,07	N/A	0,00	ESTIMATED
AIR DENSITY AT OUTLET SIMULATED	kg/m^3			NOT MEASURED	0,61	0,62	N/A	0,99	ESTIMATED
FG HEAT CAPCITY AT INLET SIMULATED	kJ/kgK			NOT MEASURED	1,09	1,09	N/A	0,00	ESTIMATED
FG HEAT CAPCITY AT OUTLET SIMULATED	kJ/kgK			NOT MEASURED	1,04	1,04	N/A	-0,23	ESTIMATED
AIR HEAT CAPCITY AT INLET SIMULATED	kJ/kgK			NOT MEASURED	1,01	1,01	N/A	0,00	ESTIMATED
AIR HEAT CAPCITY AT OUTLET SIMULATED	kJ/kgK			NOT MEASURED	1,05	1,05	N/A	-0,11	ESTIMATED
FG VELOCITY AT INLET SIMULATED	m/s			NOT MEASURED	6,26	6,07	N/A	-3,16	ESTIMATED
FG VELOCITY AT OUTLET SIMULATED	m/s			NOT MEASURED	4,40	4,89	N/A	10,18	ESTIMATED
AIR VELOCITY AT INLET SIMULATED	m/s			NOT MEASURED	3,85	3,86	N/A	0,04	ESTIMATED
AIR VELOCITY AT OUTLET SIMULATED	m/s			NOT MEASURED	6,75	5,36	N/A	-25,85	ESTIMATED
ENERGY									
FG HEAT ENEREGY LOST	MW			NOT MEASURED	-24,91	-25,15	N/A	0,94	ESTIMATED
AIR HEAT ENERGY GAINED	MW			NOT MEASURED	25,70	24,95	N/A	-3,00	ESTIMATED

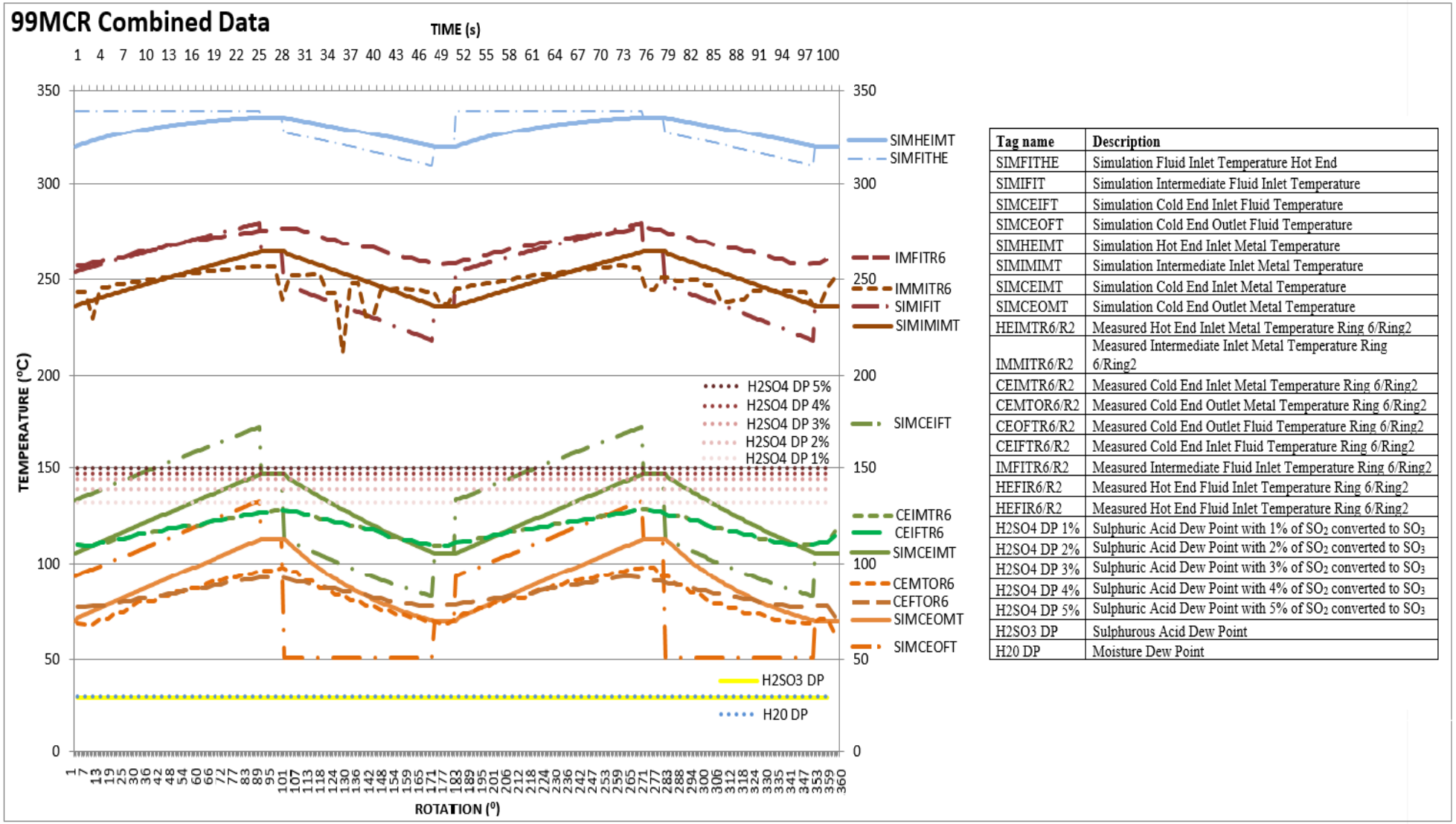

Tag name	Description
SIMFITHE	Simulation Fluid Inlet Temperature Hot End
SIMIFIT	Simulation Intermediate Fluid Inlet Temperature
SIMCEIFT	Simulation Cold End Inlet Fluid Temperature
SIMCEOFT	Simulation Cold End Outlet Fluid Temperature
SIMHEIMT	Simulation Hot End Inlet Metal Temperature
SIMIMIMT	Simulation Intermediate Inlet Metal Temperature
SIMCEIMT	Simulation Cold End Inlet Metal Temperature
SIMCEOMT	Simulation Cold End Outlet Metal Temperature
HEIMTR6/R2	Measured Hot End Inlet Metal Temperature Ring 6/Ring2
IMMITR6/R2	Measured Intermediate Inlet Metal Temperature Ring 6/Ring2
CEIMTR6/R2	Measured Cold End Inlet Metal Temperature Ring 6/Ring2
CEMTOR6/R2	Measured Cold End Outlet Metal Temperature Ring 6/Ring2
CEOFTR6/R2	Measured Cold End Outlet Fluid Temperature Ring 6/Ring2
CEIFTR6/R2	Measured Cold End Inlet Fluid Temperature Ring 6/Ring2
IMFITR6/R2	Measured Intermediate Fluid Inlet Temperature Ring 6/Ring2
HEFIR6/R2	Measured Hot End Fluid Inlet Temperature Ring 6/Ring2
HEFIR6/R2	Measured Hot End Fluid Inlet Temperature Ring 6/Ring2
H2SO4 DP 1%	Sulphuric Acid Dew Point with 1% of SO_2 converted to SO_3
H2SO4 DP 2%	Sulphuric Acid Dew Point with 2% of SO_2 converted to SO_3
H2SO4 DP 3%	Sulphuric Acid Dew Point with 3% of SO_2 converted to SO_3
H2SO4 DP 4%	Sulphuric Acid Dew Point with 4% of SO_2 converted to SO_3
H2SO4 DP 5%	Sulphuric Acid Dew Point with 5% of SO_2 converted to SO_3
H2SO3 DP	Sulphurous Acid Dew Point
H20 DP	Moisture Dew Point

Figure C5: Actual-test comparison for 99% MCR operating condition.

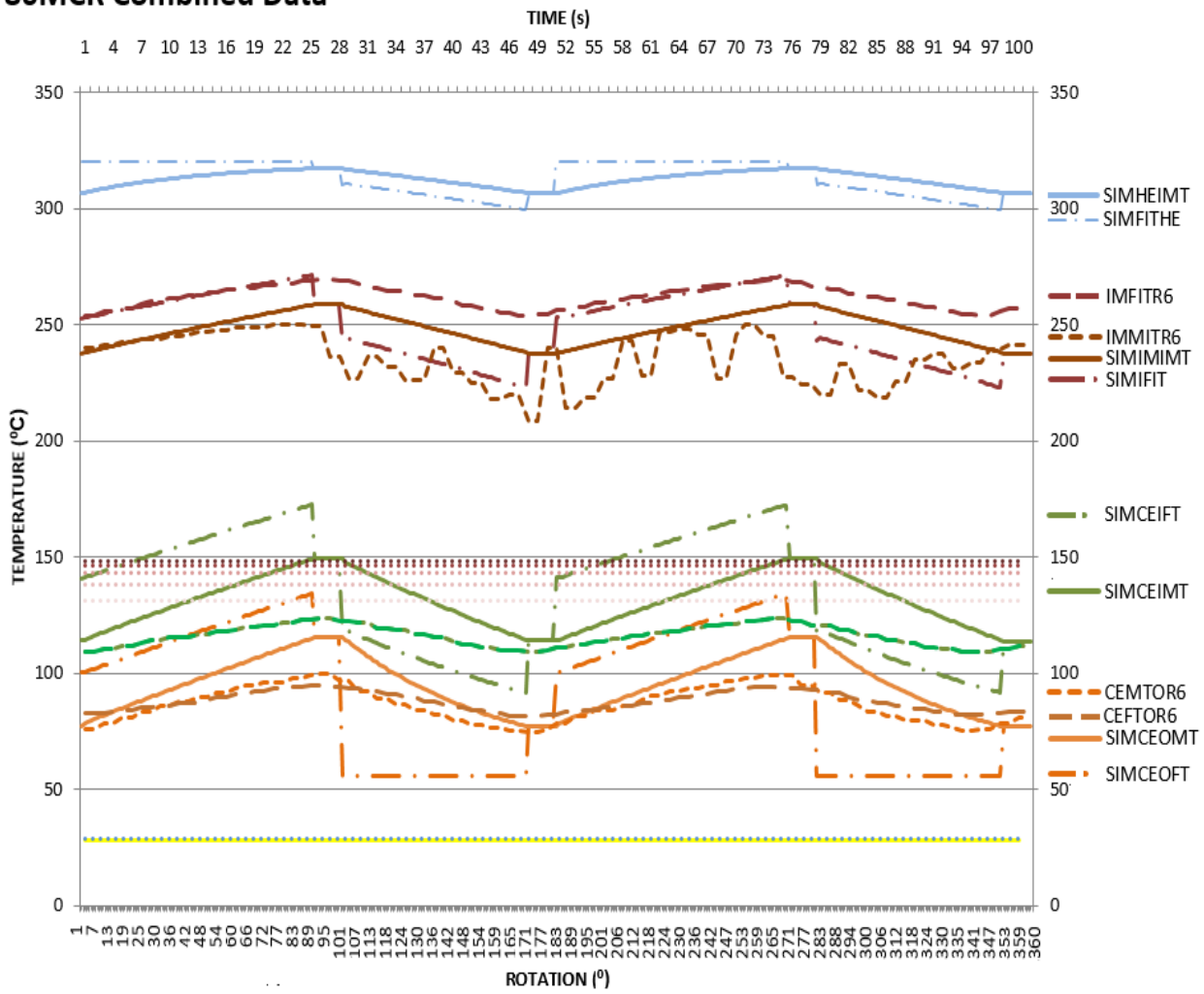

Tag name	Description
SIMFITHE	Simulation Fluid Inlet Temperature Hot End
SIMIFIT	Simulation Intermediate Fluid Inlet Temperature
SIMCEIFT	Simulation Cold End Inlet Fluid Temperature
SIMCEOFT	Simulation Cold End Outlet Fluid Temperature
SIMHEIMT	Simulation Hot End Inlet Metal Temperature
SIMIMIMT	Simulation Intermediate Inlet Metal Temperature
SIMCEIMT	Simulation Cold End Inlet Metal Temperature
SIMCEOMT	Simulation Cold End Outlet Metal Temperature
HEIMTR6/R2	Measured Hot End Inlet Metal Temperature Ring 6/Ring2
IMMITR6/R2	Measured Intermediate Inlet Metal Temperature Ring 6/Ring2
CEIMTR6/R2	Measured Cold End Inlet Metal Temperature Ring 6/Ring2
CEMTOR6/R2	Measured Cold End Outlet Metal Temperature Ring 6/Ring2
CEOFTR6/R2	Measured Cold End Outlet Fluid Temperature Ring 6/Ring2
CEIFTR6/R2	Measured Cold End Inlet Fluid Temperature Ring 6/Ring2
IMFITR6/R2	Measured Intermediate Fluid Inlet Temperature Ring 6/Ring2
HEFIR6/R2	Measured Hot End Fluid Inlet Temperature Ring 6/Ring2
HEFIR6/R2	Measured Hot End Fluid Inlet Temperature Ring 6/Ring2
H2SO4 DP 1%	Sulphuric Acid Dew Point with 1% of SO_2 converted to SO_3
H2SO4 DP 2%	Sulphuric Acid Dew Point with 2% of SO_2 converted to SO_3
H2SO4 DP 3%	Sulphuric Acid Dew Point with 3% of SO_2 converted to SO_3
H2SO4 DP 4%	Sulphuric Acid Dew Point with 4% of SO_2 converted to SO_3
H2SO4 DP 5%	Sulphuric Acid Dew Point with 5% of SO_2 converted to SO_3
H2SO3 DP	Sulphurous Acid Dew Point
H20 DP	Moisture Dew Point

Figure C6: Actual-test comparison for 80% MCR operating condition

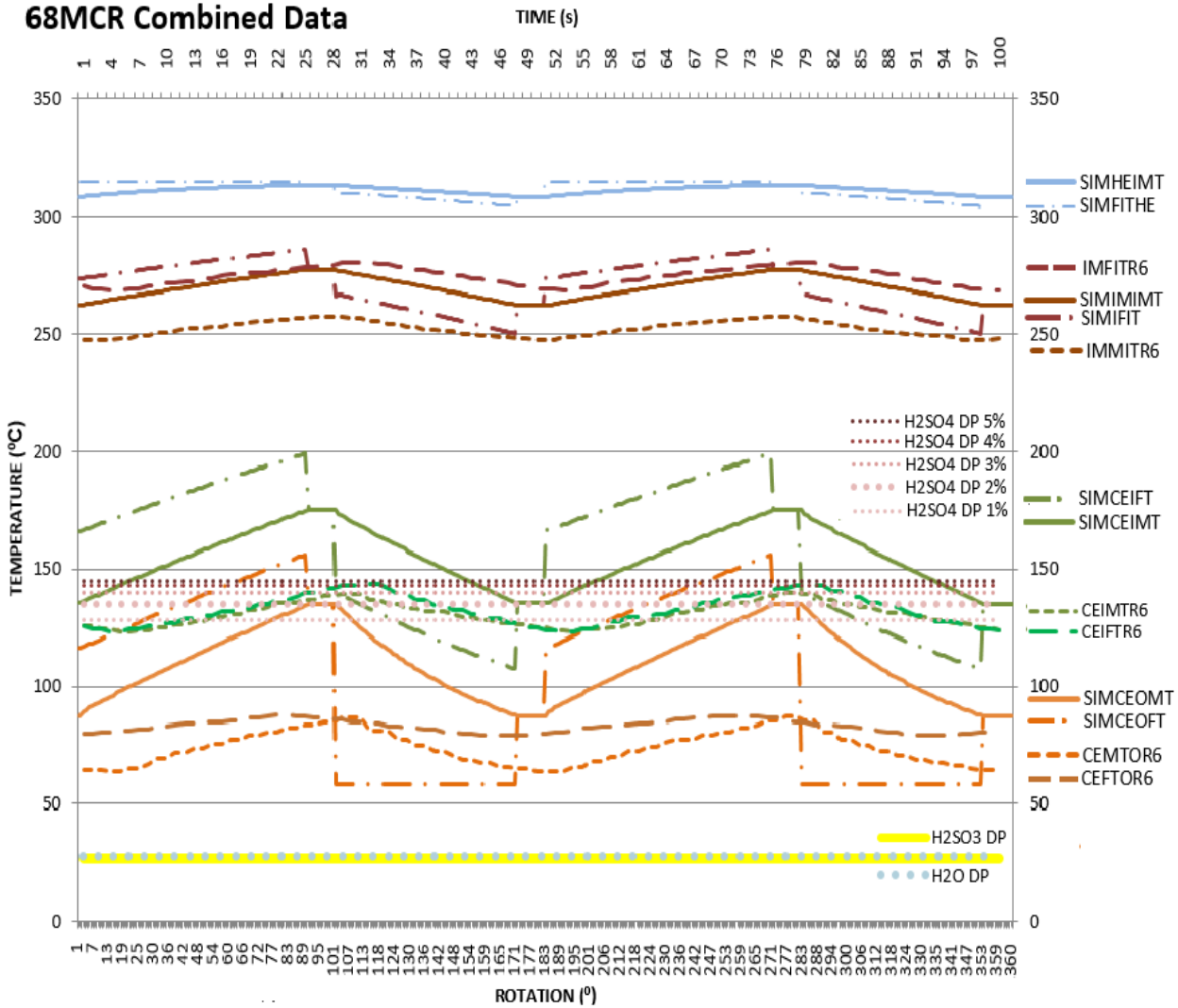

Tag name	Description
SIMFITHE	Simulation Fluid Inlet Temperature Hot End
SIMIFIT	Simulation Intermediate Fluid Inlet Temperature
SIMCEIFT	Simulation Cold End Inlet Fluid Temperature
SIMCEOFT	Simulation Cold End Outlet Fluid Temperature
SIMHEIMT	Simulation Hot End Inlet Metal Temperature
SIMIMIMT	Simulation Intermediate Inlet Metal Temperature
SIMCEIMT	Simulation Cold End Inlet Metal Temperature
SIMCEOMT	Simulation Cold End Outlet Metal Temperature
HEIMTR6/R2	Measured Hot End Inlet Metal Temperature Ring 6/Ring2
IMMITR6/R2	Measured Intermediate Inlet Metal Temperature Ring 6/Ring2
CEIMTR6/R2	Measured Cold End Inlet Metal Temperature Ring 6/Ring2
CEMTOR6/R2	Measured Cold End Outlet Metal Temperature Ring 6/Ring2
CEOFTR6/R2	Measured Cold End Outlet Fluid Temperature Ring 6/Ring2
CEIFTR6/R2	Measured Cold End Inlet Fluid Temperature Ring 6/Ring2
IMFITR6/R2	Measured Intermediate Fluid Inlet Temperature Ring 6/Ring2
HEFIR6/R2	Measured Hot End Fluid Inlet Temperature Ring 6/Ring2
HEFIR6/R2	Measured Hot End Fluid Inlet Temperature Ring 6/Ring2
H2SO4 DP 1%	Sulphuric Acid Dew Point with 1% of SO_2 converted to SO_3
H2SO4 DP 2%	Sulphuric Acid Dew Point with 2% of SO_2 converted to SO_3
H2SO4 DP 3%	Sulphuric Acid Dew Point with 3% of SO_2 converted to SO_3
H2SO4 DP 4%	Sulphuric Acid Dew Point with 4% of SO_2 converted to SO_3
H2SO4 DP 5%	Sulphuric Acid Dew Point with 5% of SO_2 converted to SO_3
H2SO3 DP	Sulphurous Acid Dew Point
H20 DP	Moisture Dew Point

Figure C7: Actual-test comparison for 68% MCR operating condition.

During the 99% MCR pre-test phase, for Ring 2, this average yielded a difference of 7.12˚C for the hot end metal temperature, 19.75˚C for the intermediate layer inlet metal temperature, 16.02 ˚C for the cold end inlet metal temperature and -9.18˚C for the cold end outlet metal temperature. As mentioned previously Ring 2 had a greater deviation in comparison to Ring 6. Ring 6 showed to have an improved correlation in comparison to Ring 2 for the outlet metal temperature of the third layer. For Ring 6, this average yielded a difference of 11.00˚C for the hot end metal temperature, 44.45˚C for the intermediate layer inlet metal temperature, 15.41 ˚C for the cold end inlet metal temperature and -7.18˚C for the cold end outlet metal temperature. The fluid temperatures (flue gas and air) the same process was followed to find the deviation in temperature. The deviation for the fluid temperatures showed a greater deviation due to the thermal inertia affecting the measured values. For Ring 2 the pre-test results showed a deviation -4.06˚C for the hot end fluid temperature, 22.97˚C for the intermediate layer inlet fluid temperature, 24.57 ˚C for the cold end inlet fluid temperature and -9.18˚C for the cold end outlet fluid temperature. Ring 6 average deviation yielded a difference of 10.96˚C for the hot end fluid temperature, 22.72˚C for the intermediate layer inlet fluid temperature, 18.02 ˚C for the cold end inlet fluid temperature and -7.18˚C for the cold end outlet fluid temperature.

During the pre-test 80% MCR phase, for Ring 2, this average yielded a difference of -0.39˚C for the hot end metal temperature, 13.24˚C for the intermediate layer inlet metal temperature, 9.41˚C for the cold end inlet metal temperature and -4.87˚C for the cold end outlet metal temperature. Ring 6 had a greater deviation in comparison to Ring 2. For Ring 6, this average yielded a difference of -5.03˚C for the hot end metal temperature, 33.16˚C for the intermediate layer inlet metal temperature, -11.82 ˚C for the cold end inlet metal temperature and -10.51˚C for the cold end outlet metal temperature. The fluid temperatures (flue gas and air) the same process was followed to find the deviation in temperature. For Ring 2 the pre-test results showed a deviation 2.49˚C for the hot end fluid temperature, a deviation of 36.04˚C for the intermediate layer inlet fluid temperature, 19.91˚C for the cold end inlet fluid temperature and -4.87˚C for the cold end outlet fluid temperature. Ring 6 average deviation yielded a difference of 2.35˚C for the hot end fluid temperature, 15.47˚C for the intermediate layer inlet fluid temperature, and 7.48 ˚C for the cold end inlet fluid temperature and -10.51˚C for the cold end outlet metal temperature. There are numerous reasons for the large deviation as mentioned from the previous pre-test at 99% MCR.

During the pre-test 68% MCR phase for Ring 2, the average deviation yielded a difference of -0.59˚C for the hot end metal temperature, 8.28˚C for the intermediate layer inlet metal temperature, 7.49˚C for the cold end inlet metal temperature and -7.13˚C for the cold end outlet metal temperature. For Ring 6, this average yielded a difference of 2.45˚C for the hot end metal temperature, 30.46˚C for the intermediate layer inlet metal temperature, 7.14˚C for the cold end inlet metal temperature and -12.13˚C for the cold end outlet metal temperature. The fluid temperatures (flue gas and air) the same process was followed to find the deviation in temperature. For Ring 2 the pre-test results showed a deviation -4.06˚C for the hot end fluid temperature, 33.23˚C for the intermediate layer inlet fluid temperature, 16.30˚C for the cold end inlet fluid temperature and -7.13˚C for the cold end outlet fluid temperature. Ring 6 average deviation yielded a difference of 2.37˚C for the hot end fluid temperature, 9.97˚C for the intermediate layer inlet fluid temperature, and 8.49˚C for the cold end inlet fluid temperature and -12.43˚C for the cold end outlet metal temperature. As mentioned from the previous pre-

test at 80% MCR, and 99% MCR, these deviations can be caused by ineffective high pressure washing influencing the flow through the perforated areas, and in turn also affecting the heat transfer to an extent where the results was compromised.

C3: Comparison of Measured Results and Simulation Results: Data Set 1

Considering the three different sets of results, three different load conditions had to be simulated using the plant data from the DCS system for verification. Table C2 is a representation of these measured input parameters. Table C3.1 is a representation of the description of each tag used for the profile temperature for each layer's metal and fluid temperatures. This tag configuration was used for all three operating conditions. The tag names are used as reference for the results discussions.

Table C3.1: Tag names for each temperature profile.

Tag name	Description
SIMFITHE	Simulation Fluid Inlet Temperature Hot End
SIMIFIT	Simulation Intermediate Fluid Inlet Temperature
SIMCEIFT	Simulation Cold End Inlet Fluid Temperature
SIMCEOFT	Simulation Cold End Outlet Fluid Temperature
SIMHEIMT	Simulation Hot End Inlet Metal Temperature
SIMIMIMT	Simulation Intermediate Inlet Metal Temperature
SIMCEIMT	Simulation Cold End Inlet Metal Temperature
SIMCEOMT	Simulation Cold End Outlet Metal Temperature
HEIMTR6/R2	Measured Hot End Inlet Metal Temperature Ring 6/Ring2
IMMITR6/R2	Measured Intermediate Inlet Metal Temperature Ring 6/Ring2
CEIMTR6/R2	Measured Cold End Inlet Metal Temperature Ring 6/Ring2
CEMTOR6/R2	Measured Cold End Outlet Metal Temperature Ring 6/Ring2
CEOFTR6/R2	Measured Cold End Outlet Fluid Temperature Ring 6/Ring2
CEIFTR6/R2	Measured Cold End Inlet Fluid Temperature Ring 6/Ring2
IMFITR6/R2	Measured Intermediate Fluid Inlet Temperature Ring 6/Ring2
HEFIR6/R2	Measured Hot End Fluid Inlet Temperature Ring 6/Ring2

C3.1 Air heater performance results vs. VBA RAH simulated results at 670 MW (99% MCR):

For the 99% MCR condition the temperatures were compared to find the deviation between the simulated and measured values. Ring 2 and Ring 6 results were compared. Ring 2 showed a flattened curve in comparison to Ring 6. This was assumed to be caused by the fact that thermocouples were exposed to both the fluid (Flue gas and air streams) region and the metal surface, therefore it measured a combined temperature which showed less fluctuation. This was caused by insufficient thermal insulation of thermocouples. Another possible influence was the

fact that the ash accumulated at the areas where flow was obstructed by wear protection components installed to increase the life expectancy of the thermocouples and compensating cables. The ash could have fouled the open spaces between the metal sheets at Ring 2 to the extent that the thermal inertia was affected. The ash also has a heat capacity with convective and conductive properties; when the thermocouple is in contact with the ash the true temperatures of the streams may not be measured. Figures C3.1 and C3.2 are representations of the difference between the measured and the simulated values for Rings 2 and 6 metal temperatures, and Figures C3.3 and C3.4 show the comparison for simulated and measured flue gas and air temperatures for Rings 2 and 6. These results show that the measurements taken from Ring 6 seem to correlate better to the simulation results. The most important factor in these results is the validation for the metal temperatures. When the metal temperature reaches a minimum, a portion of the flue gas will experience a minimum temperature as well, but because the metal is at a lower temperature, it will be exposed to sulphuric acid dew point conditions for longer periods. This becomes the critical time for sulphuric acid condensation, causing deposition onto the metal surfaces. For the validation of the model the third layer inlet and outlet temperatures are expected to be the most accurate to ensure that the model predicts a correcting fouling range.

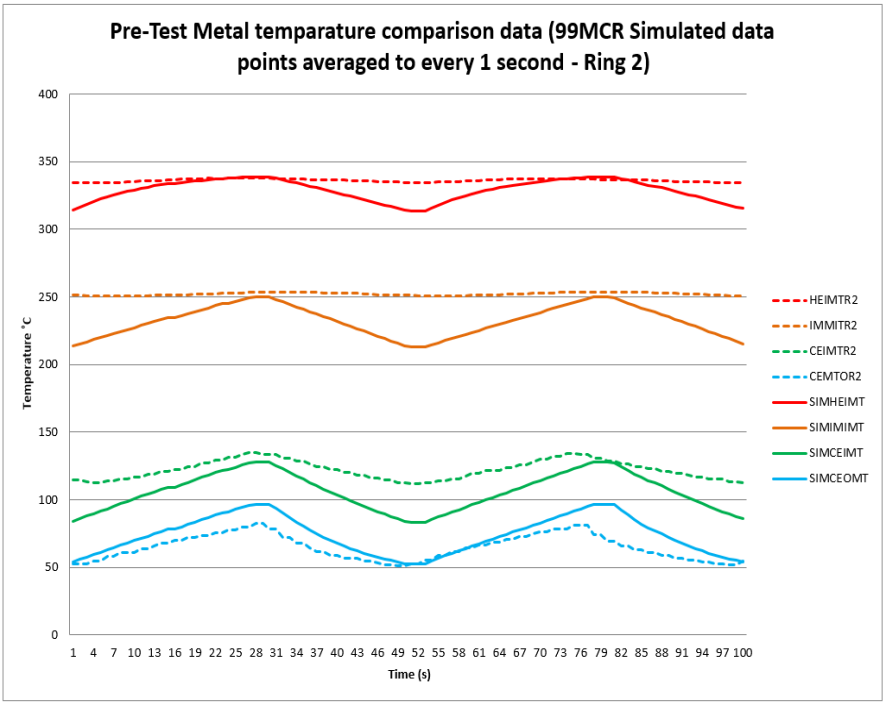

Figure C3.1: Data comparison for Ring 2 Metal temperatures for the 99% MCR pre-test condition.

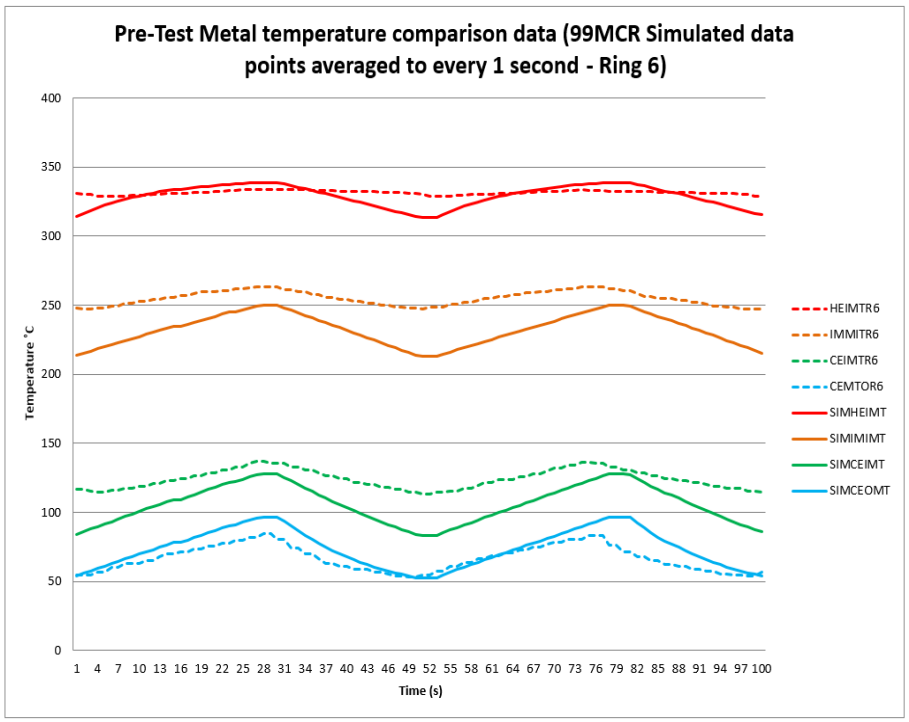

Figure C3.2: Data comparison for ring 6 Metal temperatures for the 99% MCR pre-test condition.

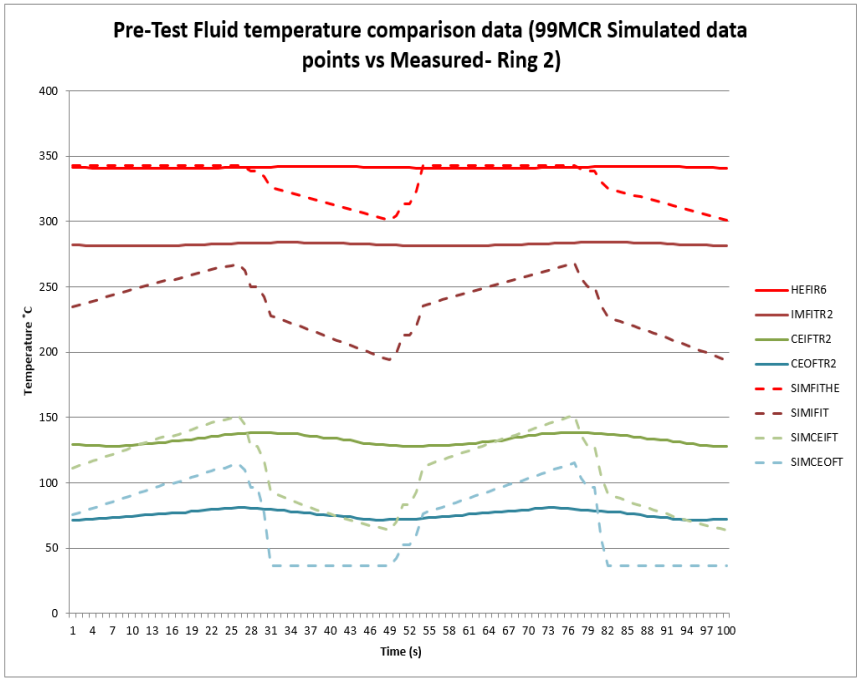

Figure C3.3: Data comparison for Ring 2 fluid temperatures for the 99% MCR pre-test condition.

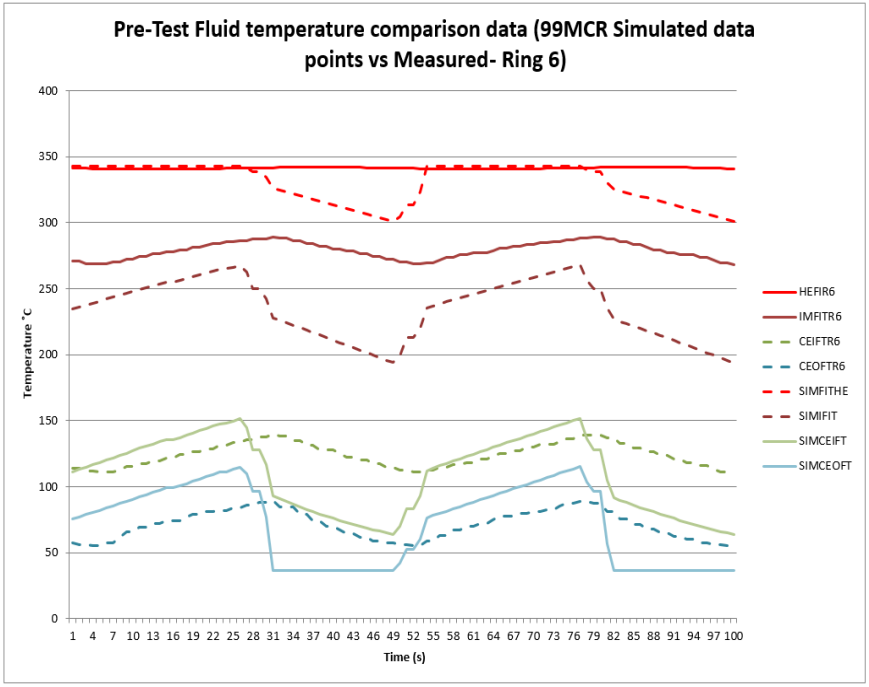

Figure C3.4: Data comparison for Ring 6 fluid temperatures for the 99% MCR pre-test condition.

The Ring 2 and Ring 6 metal temperatures for the simulated results and the measured results were closely matched at the cold end, which was a positive outcome in terms of relying on the VBA RAH model to indicate where dew point related fouling will occur. It is clear that although the temperature levels are fairly similar, the profiles are not the same. The predicted fluid temperatures correlate more with the metal temperature measurements. As mentioned previously this effect could be due to accumulation of ash and also the effects of obstruction in flow and thermocouple wear protection influencing the thermal inertia.

Air heater air outlet temperatures

A 1.8% error occurred between the VBA RAH model and the measured value. This was a difference of 5.8 ˚C at the outlet for the air side. The error between the VBA RAH and the RAH model was 0.5%. This shows that the possible error in flue gas flow used as input parameter to the simulation models could have compromised the simulated results, in this case the outlet flue gas and air temperatures. Section 5.7 elaborates on the effect of the error in flue gas estimation.

Cold end metal temperatures

The comparison between the VBA RAH maximum plate temperatures and the measured maximum plate temperatures indicated a 6.6% error. The minimum VBA RAH metal temperature was found to be 5.2% less than the measured value. Once again the temperatures operated in the same region but the error showed that the measured value was higher in general in comparison to the simulated value. As explained previously, this shows that the thermocouple insulation could have been compromised to give a reading that measured not only metal temperature but also fluid temperature. When the thermocouples were forced into the open spaces between the element-pack metal sheets a form of contact resistance between

the metal surface and the probe were introduced which also affected the readings. A 33.3% deviation in the inlet metal temperature occurred between the results from the VBA RAH and RAH models. When comparing the measured value and the RAH value it is seen that the RAH value is suspicious. It seems that the rate of change in temperature for the metal sheets is higher in comparison with what is seen from the test. The minimum metal temperatures seem to show values that correlate more with the simulated outlet temperature for the diluted flue gas stream (taking leakage into account). The VBA RAH model only deviates by 1.1% which is a promising result when considering the formation of fouling in the cold end region of the air heater.

Differential pressures

The differential pressure across the air heater could only be measured for the air side due to the unavailability of flue gas pressure signals before and after the air heater. The FD fan discharge pressure was used as the inlet pressure and the cross over duct outlet pressure was used as the pressure after the air heater. The difference between these two readings gave an air DP of 1.4kPa. A 37.7% deviation occurred from the VBA RAH model. This shows that the air heater may have experienced fouling during the light-up process when the unit returned to service. An important fact to take into consideration is that the HC11 (profile installed in the air heaters) element profiles were designed to match the thermal properties of the 2.78DU type (profile available in the VBA RAH and RAH model), but the pressure loss component was not taken into account. Since the hydraulic (pressure) performance of the HC11 packs are unavailable, the historic data were analysed with regards to the differential pressures, inlet and outlet temperatures of fluid, and the FD fan motor current before the installation and after the installation of the HC11 profiles. Table C6 in Appendix C is a summary of the results for the inlet and outlet temperatures along with the FD fan current and differential pressure for the condition before the installation and after the installation for each unit. The results showed that the differential pressures increased by 0.26kPa which would change the design differential pressure of 0.702 to 0.962kPa. An average increase in FD fan motor current of 19.1 A. When the air heater experiences fouling the load loss usually starts with increased differential pressures and FD and ID fan capacities. The HC11 packs do not benefit this condition. To compare the effect of both the HC11 and 2.78DU element packs, the OEM (Original Equipment Manufacturer) was requested to simulate the same conditions for verification purposes. These results are discussed in section 5.7.

Fluid Properties

For the Data Set 1 results, no fluid properties were measured. The fluid properties (inlet and outlet density, heat capacity and velocity) of each stream were calculated from both simulation models. The flue gas and air inlet density, and air heat capacity were found to be identical with no error. The heat capacity for the flue gas at the inlet had a discrepancy of 0.4% and the flue gas velocity at the inlet had a discrepancy of 3.6%. The air inlet velocity varied by 0.02%. The outlet velocities had a greater error due to the outlet temperature and pressure being different for the simulations from the two models; flue gas velocity and air velocity had a 12% difference.

Energy Exchange

The result for the VBA RAH model (at 99% MCR) showed a result of +/-47.67 MW energy lost and 47.84 MW energy gained, a difference of less than 1MW on energy exchange. This means the result was found to have good accuracy with regard to the energy balance. The RAH model had an energy exchange of 44.23 MW lost and 44.17 MW gained, which is also an

estimation close to the expected norm of 50 MW and with a difference of less than 1 MW. The discrepancy between the two models is due to the difference in predicted outlet temperatures.

C3.2 Air heater performance results vs. VBA RAH simulated results at 544 MW (80% MCR):

For the simulation of the 80% MCR conditions the input parameters from Appendix C - Table C2 (80% MCR) were used. As expected the inlet gas temperature was lower due to the lower heat energy input for combustion requirement during lower loads. For all the results the same tag descriptions were used as mentioned in Table 5.5. The third layer simulated temperatures were within the range on the measured temperatures, but there is a definite effect of thermal inertia causing the measured temperatures to fluctuate less as seen and explained from the 99% MCR pre-testing phase results. During this phase the measured fluid temperatures also had a similar profile to the metal temperatures. In general the thermocouples installed for the fluid measurements correlated more with the metal temperature curves. Ring 2 showed that the simulated values are estimated in the same temperature regions as the measured temperatures for each layer. This can be seen as a positive outcome showing that the thermal performance is not inaccurate. The simulated trends for the fluid region showed less resistance to changes in temperature during stream change overs from the flue gas stream to the air stream. The same effects occurred for the 99% MCR results. The measured values seemed to give a gradual change in temperature in comparison to the simulated values, which is again an indication that the insulation of the thermocouples was not as successful as expected. Figure C3.5 and C3.6 are representations of the difference between the measured and the simulated values for Ring 2 and six metal temperatures, and Figures C3.7 and C3.8 represents the comparison for Ring 2 and six fluid (Flue gas and air streams) temperatures. From these results the measurements taken from Ring 6 again seems to correlate more to the simulation results. As mentioned previously, causes such as, contact resistance, accumulation of ash in the perforated areas where thermocouples were installed, flow obstruction, poor insulation of thermocouples and contact with thermocouple wear protection influenced the thermal inertial properties influencing the measuring process of the metal and fluid temperatures. The fact that all three layers shows similar results, the assumption can be made that less flow passed through this area therefore the temperature fluctuated less when the streams changed over from flue gas to air.

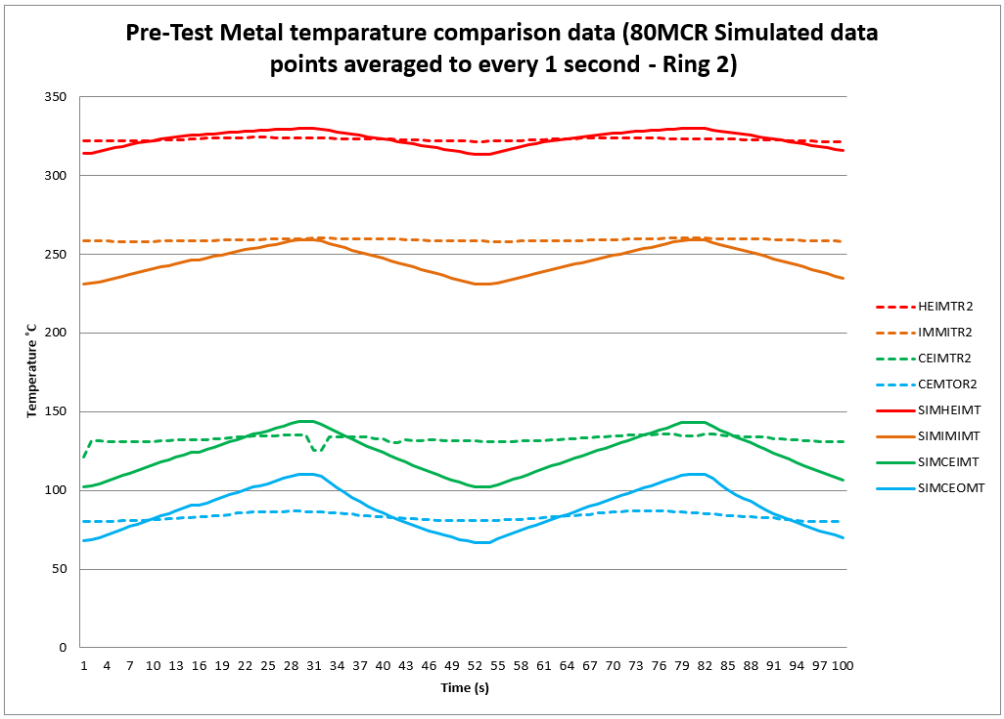

Figure C3.5: Data comparison for ring 2 Metal temperatures for the 80% MCR pre-test condition.

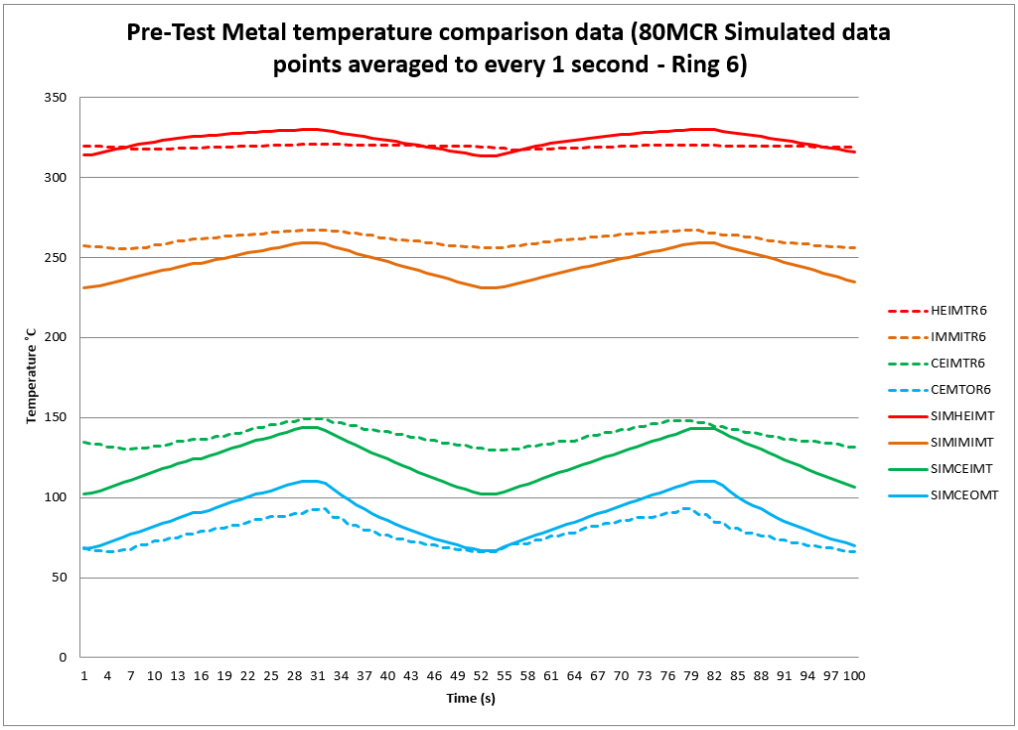

Figure C3.6: Data comparison for ring 6 Metal temperatures for the 80% MCR pre-test condition.

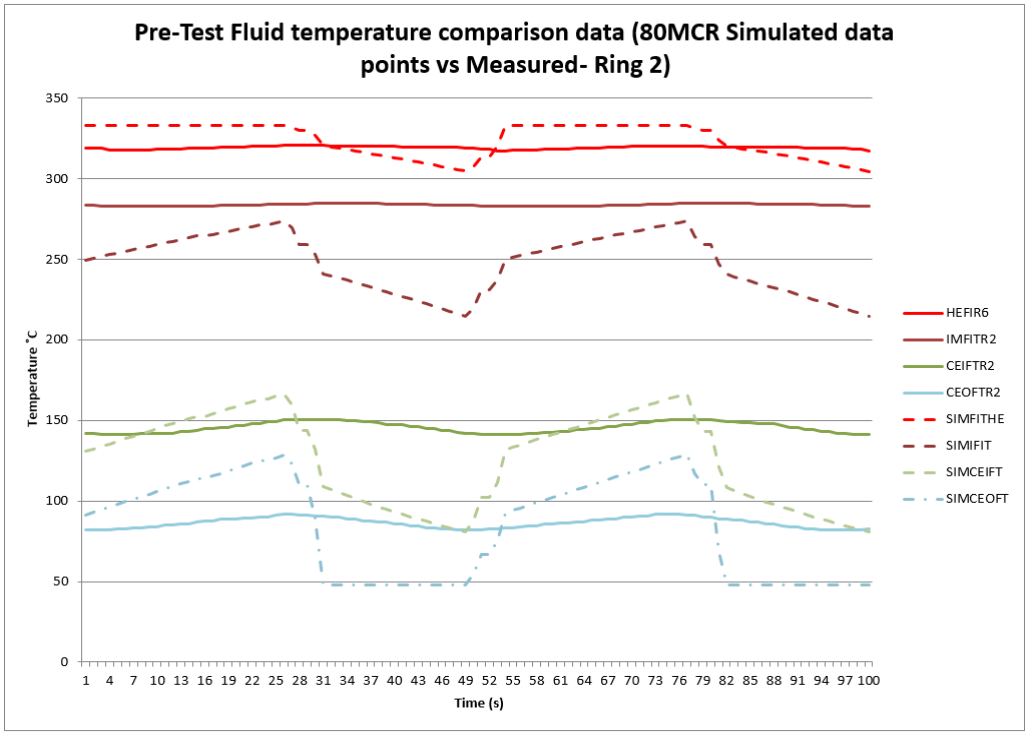

Figure C3.7: Data comparison for ring 2 fluid temperatures for the 80% MCR pre-test condition.

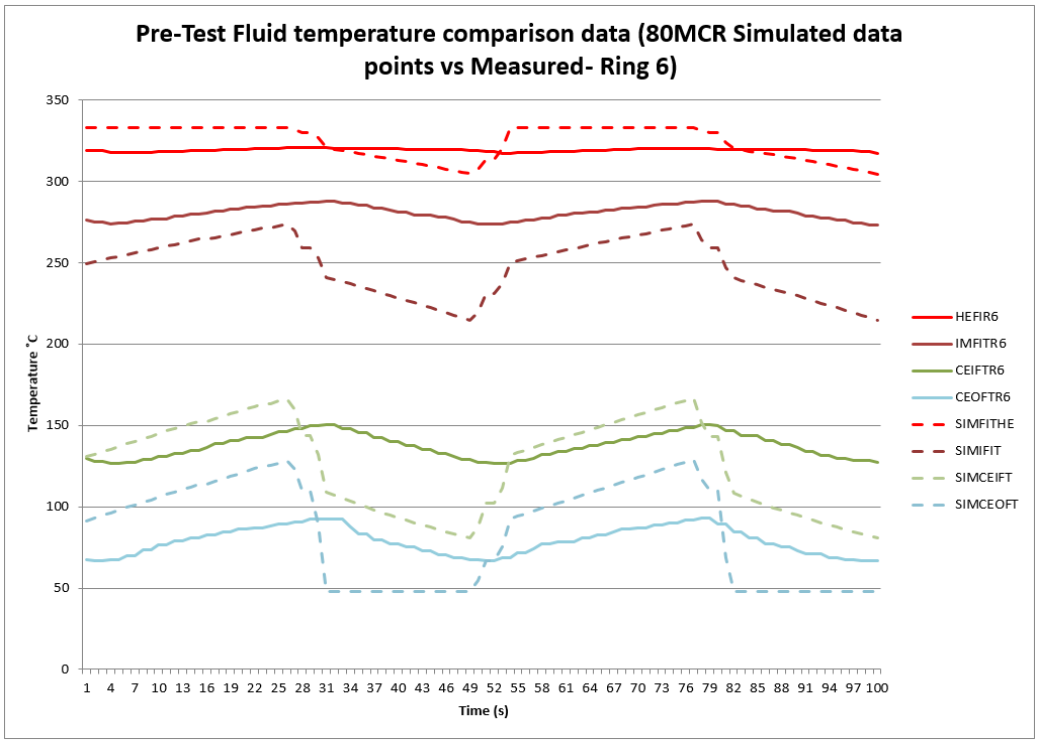

Figure C3.8: Data comparison for ring 6 fluid temperatures for the 80% MCR pre-test condition.

Table C4 in Appendix C – C1 Data Set 1 – Results, is a representation of the results from the 80% MCR load pre-test conducted on 22/12/2019 at 14:27. This time slot was selected due to the matching plant conditions that were planned for actual testing phase in February 2020. The

idea was once again to select a time shortly after the outage. An ideal load condition was reached on this date and therefore pre-test conditions could be recorded for an 80% MCR load. The assumption was again made that the same result for leakage from the 99% MCR condition were used for the pre-test simulations of both the VBA RAH and RAH (GB de Klerk).

Air heater gas outlet temperatures
When comparing the DCS measured value of 130.6˚C to the VBA RAH result of 104.39˚C an error 20.07% exists. This temperature measurement were found to be defective as previously mentioned, therefore the value was measured and not taken from the DCS reading for the actual test. The average cold end outlet fluid temperature measured from the installed test points was 83˚C. This is an average between Ring 2 and Ring 6, and at the pack it is shows that for both readings the actual fluid temperature leaving the pack is low in comparison with the measurement taken at point further back in the downstream condition as seen from the 99% MCR load condition results. The same effects apply in this regards as explained from section 5.2 Figure 5.10. The same input parameters were simulated for the RAH (GB de Klerk) model and an error of 1.76% was found.

Air heater air outlet temperatures
A 0.33% error occurred between the VBA RAH model and the measured value. This was a difference of 1.03˚C at the outlet for the air side. The error between the VBA RAH and the RAH (GB de Klerk) model was 1.56%. The same assumption can be made as the 99% MCR load results, that the possible flue gas flow error could have compromised the simulated results, in this case the outlet temperatures.

Cold end metal temperatures
The comparison between the VBA RAH maximum plate temperatures and the measured maximum plate temperature indicated a 4.22% error. The minimum VBA RAH metal temperature was found to be 1.29% less than the measured value. A 25.04% deviation in the metal temperature occurred between the simulated results from VBA RAH and RAH (GB de Klerk). When comparing the measured value and the RAH value it is seen that the RAH value is suspicious. For the minimum metal temperature, the VBA RAH model only deviates with a 2.8% which shows that the accuracy of identifying a dew point condition at the cold end can still be accomplished through simulated values.

Differential pressures
The FD fan discharge pressure was again used as the inlet pressure and the cross over duct outlet pressure was used as the pressure after the air heater. The difference between these two readings gave an air DP of 1kPa. A 29.6% deviation occurred from the VBA RAH model.

Energy Exchange
For the VBA RAH model an energy loss (at 80% MCR) of 37.67 MW and an energy gain of 38.02 MW were found. A difference of less than 1MW on energy exchange is an indication of good accuracy with regards to the energy balance. The RAH(GB de Klerk) model had an energy exchange of 35.49MW lost and a 35.38MW gained, which is also an estimation close to the expected norm of a difference of less than 1MW. The error between the two models is due to the difference in outlet temperatures by the two simulation models.

C3.3 Air heater performance results vs. VBA RAH simulated results at 465 MW (68% MCR):

For the simulation of the 68% MCR conditions the input parameters from Table C2 in Appendix C – C1 Data Set 1 - Results were used. As expected the inlet gas temperature was lower in comparison to the 80% MCR and 99% MCR, due to the combustion requirement during lower loads requiring a lower heat energy input. Figures C3.9 and C3.10 are representations of the difference between the measured and the simulated values for Ring 2 and six metal temperatures, and Figures C3.11 and C3.12 represents the comparison for Ring 2 and six fluid temperatures.

.

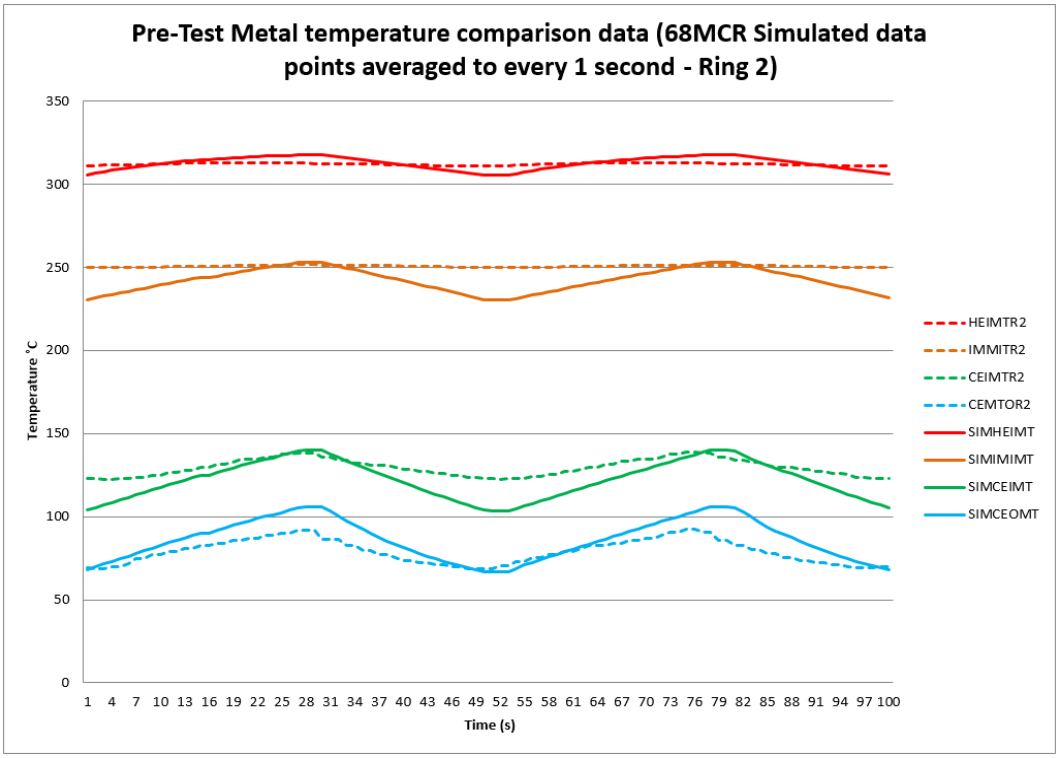

Figure C3.9: Data comparison for ring 2 Metal temperatures for the 68% MCR pre-test condition.

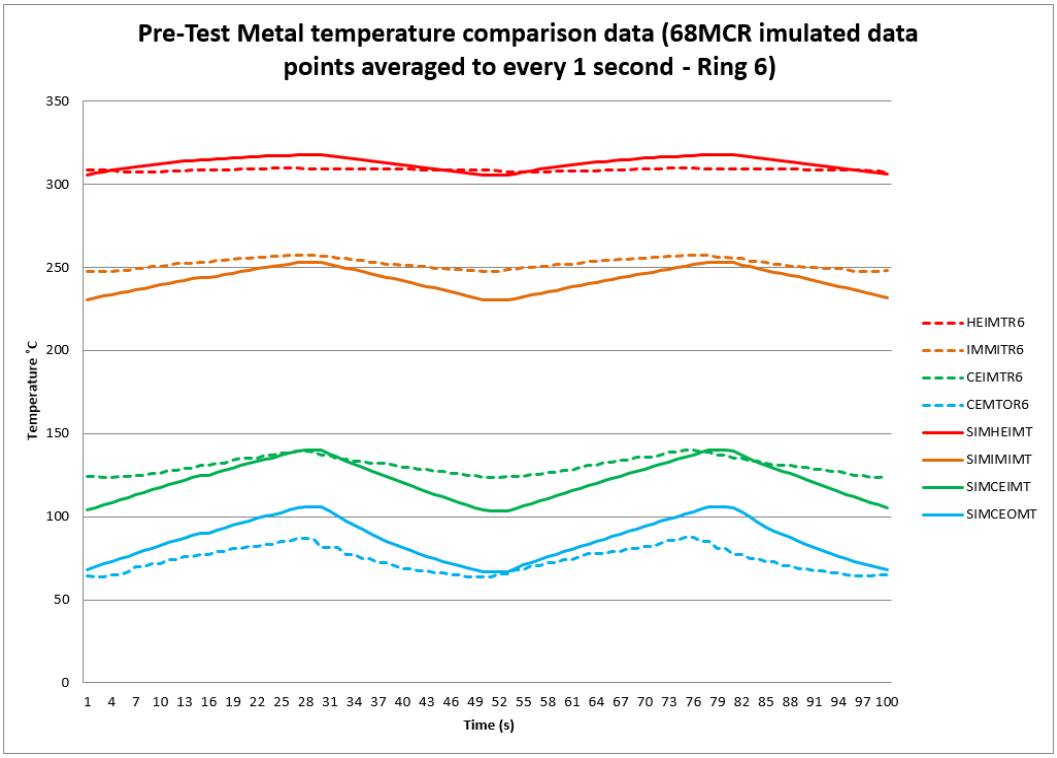

Figure C3.10: Data comparison for ring 6 Metal temperatures for the 68% MCR pre-test condition.

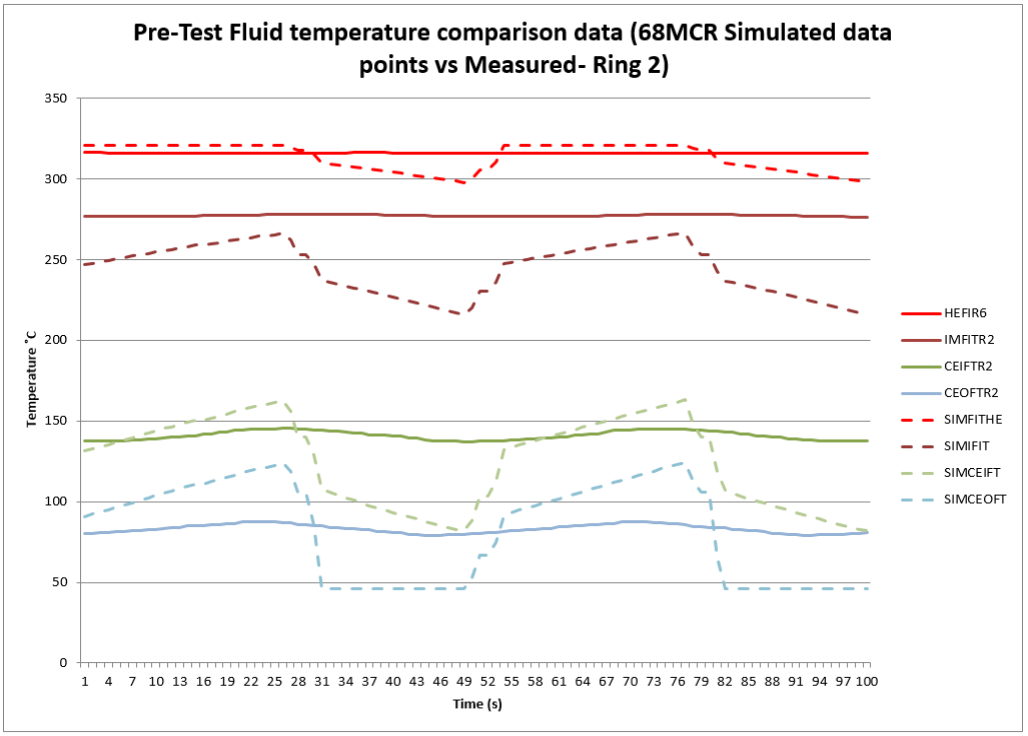

Figure C3.11: Data comparison for ring 2 fluid temperatures for the 68% MCR pre-test condition.

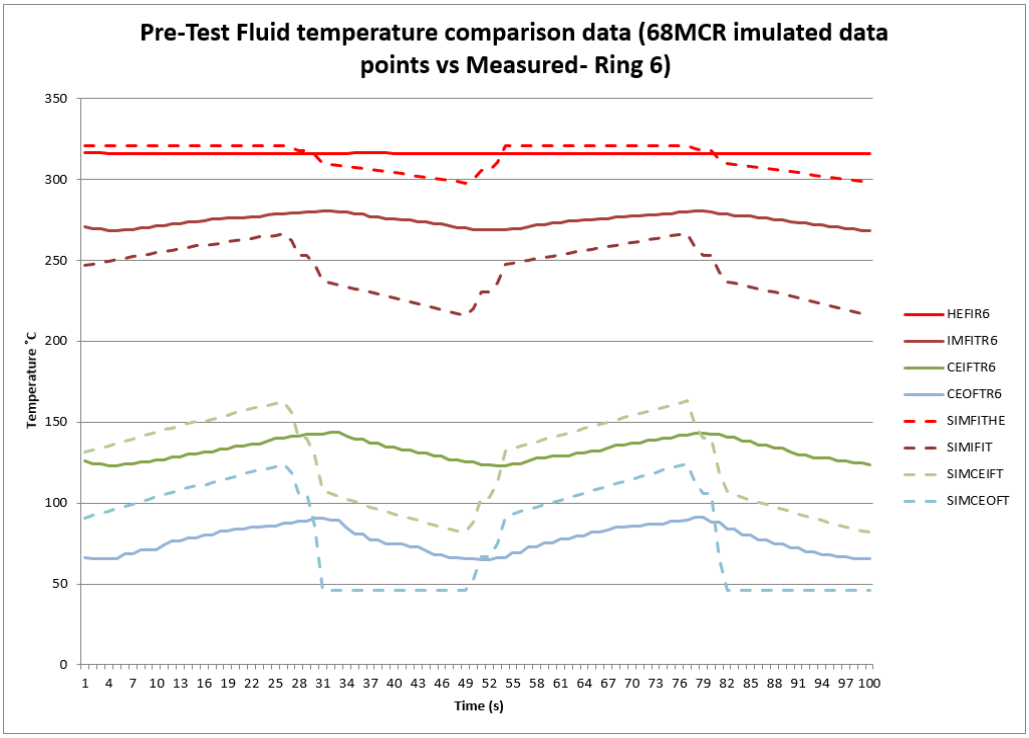

Figure C3.11: Data comparison for ring 6 fluid temperatures for the 68% MCR pre-test condition.

Table C4 (in Appendix C – C1: Data Set 1 - Results) is a representation of the results from the 68% MCR load pre-test conducted on 22/12/2019 at 20:17. This time slot was selected due to the matching plant conditions that were planned for the actual 68% MCR load condition in February 2020.

Air heater gas outlet temperatures

When comparing the DCS measured value of 113.4˚C to the VBA RAH result of 102.07˚C an error 9.99% exists. The average cold end outlet fluid (Flue gas and air stream) temperature measured from the installed test points was 80.2˚C. This is an average between Ring 2 and Ring 6, and at the pack it is shows that for both readings the actual fluid temperature leaving the pack is low in comparison with the measurement taken at point further back in the downstream condition as seen from the 80% and 99% MCR load condition results. Based on the explanation from Figure 5.10, this temperature cannot be compared to the mixed flue gas outlet temperature measured at point C in Figure 5.10. The location of the secondary air heater gas outlet temperature mostly experiences fluid temperatures well above the measured temperature at the element pack outlet. The same input parameters were simulated for the RAH (GB de Klerk) model and an error of 4.95% was found. As experienced from the two previous test results, it does seem that the simulation models tend to overestimate the outlet temperature. An error in flue gas flow measurement also impacted the results negatively as explained in Section 5.7.

Air heater air outlet temperatures

The air outlet temperatures indicated an error of 0.15% for the VBA RAH model and the measured value. This was a difference of 0.45˚C at the outlet for the air side. The error between the VBA RAH and the RAH (GB de Klerk) model was 1.37%. The same assumption can be

made as the 80% MCR and 99% MCR load results, that the possible flue gas flow error could have compromised the simulated results, in this case the outlet temperatures when the actual reading and the simulated values are compared. However the 68% MCR load flue gas flow rate estimation was found to be more accurate compared to the higher load estimations.

Cold end metal temperatures
The comparison between the VBA RAH maximum plate temperatures and the measured maximum plate temperature indicated a 1.15% error. The minimum VBA RAH metal temperature was found to be 0.48% higher than the measured value. Insufficient thermal insulation could have compromised the measured values. A 23.63% deviation in the metal temperature occurred between the simulated results from VBA RAH and RAH (GB de Klerk). The RAH (GB de Klerk) value was again found to be suspicious with regard to the maximum metal temperatures. For the minimum metal temperature, the VBA RAH model only deviates with a 0.48% which, as seen from previous results, shows that the accuracy of identifying a dew point condition at the cold end can be accomplished through simulated values.

Differential pressures
The differential pressure for the air stream across the air heater was measured to be 0.73kPa. The lower differential pressure is expected due to a reduction in coal flow which also then requires less air for combustion, which in turn decreases the operating pressure from the fans. A 25.07% deviation occurred from the VBA RAH model. As mentioned previously from the 99% MCR pre-test, the influence of the use of the 2.78DU profile packs for the simulation could have introduced the great difference in error, in comparison to the HC11 packs installed in the air heater. The OEM (Original Equipment Manufacturer) were requested to simulate the same conditions for verification purposes. These results are discussed in 5.6. The same error existed for the RAH model which was already one of the problems identified for the research conducted by De Klerk (2001).

Fluid Properties
For the pre-test results no fluid properties were measured. But the fluid properties for the inlet and outlet density, heat capacity and velocity of each stream were calculated from both simulation models. The flue gas and air inlet density, and air heat capacity was found to be similar with 0.83 and 0% error respectively. The heat capacity for the flue gas at the inlet had an error 0.47% and the flue gas velocities at the inlet for flue gas had an error 3.97%. The air inlet velocity varied with 0.05%. The outlet velocities had a greater error due to the outlet temperature and pressure being different for the simulations from the two model.

Energy Exchange
For the VBA RAH model the result at 68% MCR showed a 31.04 MW energy loss and 31.66 MW energy gain with a difference of less than 1MW on energy exchange, which can be deemed as an accurate result with regards to conservation of energy. The RAH (GB de Klerk) model had an energy exchange of 29.59 MW lost and a 29.48 MW gained, which is also an estimation less than 1 MW difference. The error between the two models is due to the difference in outlet temperatures by the two simulation models.

C4: Comparison of Measured Results and Simulation Results: Data Set 2 – 80%MCR condition

For the 80% MCR load conditions, the inlet temperature for the flue gas and the metal temperatures were not available due to the failure of the hot end thermocouples. The signals from the cold end element packs were still available and for the verification of identifying dew point related fouling. Ring 6 cold end thermocouples were still reliable (As shown in Figure C8). There was a clear deviation for the metal temperatures measured at the inlet of the third layer in comparison to the simulated values. This deviation was greater than the deviation seen from the 99% MCR results. This effect shows that the model considers ideal conditions, but the plant measurements indicate that the factors mentioned in Figure 5.11 in section 5.2 influenced the data set results. No measurements were available for Ring 2. The simulation once again indicated a higher rate of temperature change in comparison with the measured values.

For Ring 6 both the measured fluid temperatures for the cold end and the simulated temperatures operated below the dew point temperatures for sulphuric acid. Figure C4.1 is a representation of the results for the simulated and measured metal temperatures, and Figure C4.2 shows the results for the simulated and measured fluid temperatures. The measured metal temperature at the outlet of the cold end was higher in comparison with the 99% MCR load conditions due to the fact that flow rates were lower, therefore decreasing the heat transfer rate.

With regard to the dew point related fouling, the graphical representation in Figure C4.1 indicated that sulphuric acid dew point conditions were experienced. For one rotation the simulated metal temperature results yielded that 42.9% of the metal temperatures at the inlet of the cold end layer, operate below the dew point temperature for sulphuric acid condensation at the inlet of the third layer (for 1% conversion of SO_2 to SO_3). For 5% conversion of SO_2 to SO_3, 86.9% of the simulated metal temperatures operated below the sulphuric acid dew point temperatures.

From Figure C4.2 the simulated fluid temperature results showed that for a 1% conversion of SO_2 to SO_3, sulphuric acid condensation will not occur at the inlet of the third layer although with 3% conversion, 6% of the time of flue gas exposure at the inlet of the third layer will experience acid condensation.

The measured values indicated a 100% exposure to sulphuric acid dew point conditions in the third layer, for 1% - 5% conversion of SO2 to SO3.

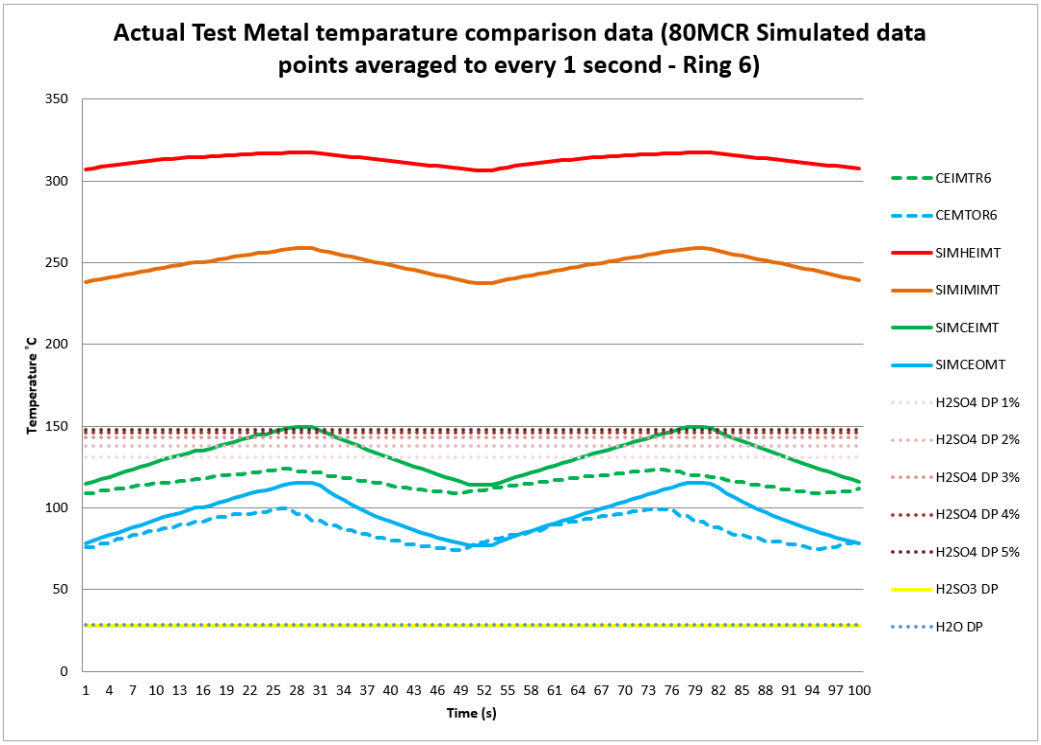

Figure C4.1: Data comparison for Ring 6 Metal temperatures for the 80% MCR pre-test condition.

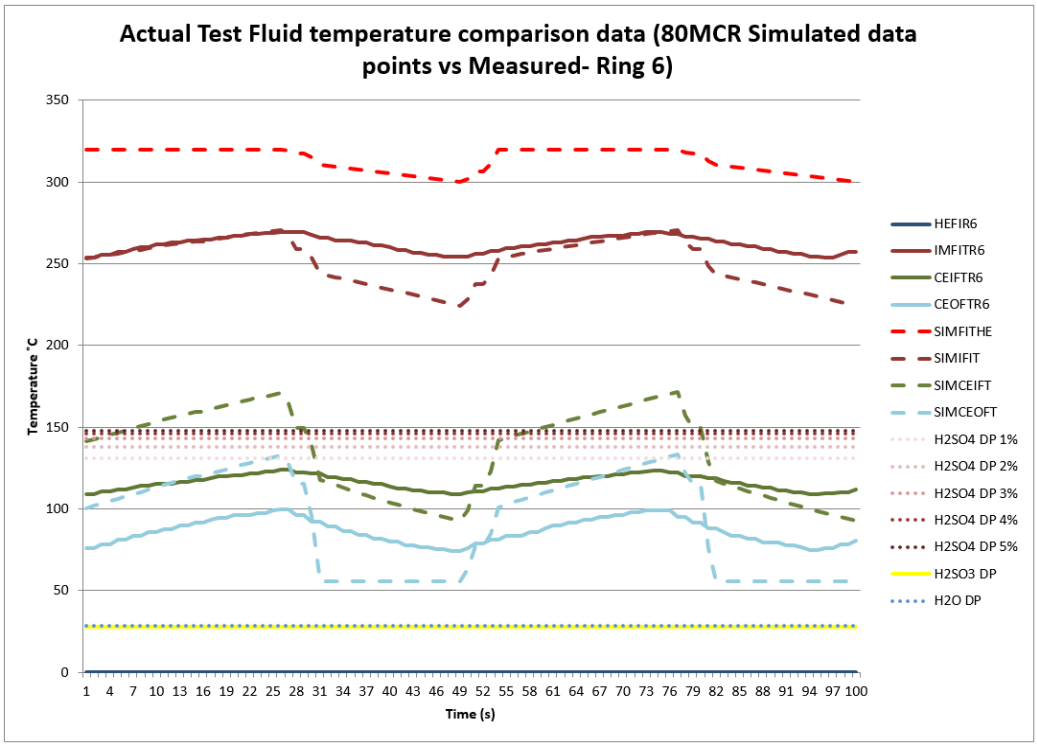

Figure C4.2: Data comparison for Ring 6 fluid temperatures for the 80% MCR pre-test condition.

Considering the measurements for SO_2 and SO_3 at 80% MCR, a value of 0.17% by volume of SO_2 in the flue gas was measured, this value relate to a 10% O_2 normalised measurement. Using the 0.17% of measured SO_2, means that 1% to 5% conversion will give a range of 0.00173% to 0.00865% of SO_3 contained in flue gas, with an estimated excess air of 26.9%. The results from the mass and energy balance indicated a 0.13% volume of SO_2. Following Table 5.7 indicating the results for SO_3 content in flue gas for varying sulphur content of coal concluded by Ganapathy (1989), the amount of SO_3 in the flue gas would be based on a 1.18% (as received) sulphur in coal. According to the table the amount would be 10.71 ppm SO_3 (0.0011%) when using linear interpolation. The amount measured from the 80% MCR Data set 2 test the value was 0,17% (at 10% normalization) for SO_2, which shows the estimated and measured values are still close to each other.

For a 6% O_2 normalised measurement the value was measured to be 0.24% SO_2. If the 6% O_2 normalised value of 0.24% SO_2 was considered it would have given a range of 0.0024 to 0.012% of SO_3 formed in the flue gas.

Based on the table estimation of (0.0011% SO_3) and the measured values (0.017% $SO_{2\ @10\%}$ & 0,0024% $SO_{2\ @\ 6\%}$) result, the assumption that almost 1% of SO_2 converted to SO_3 holds, which further confirms that the cold end was also experiencing dew point related fouling for the 80% MCR conditions.

Figure C4.3 is a representation of the sulphuric acid dew point temperatures from 1% to 5% conversion of SO_2 to SO_3 for the conditions measured during the 80% MCR conditions.

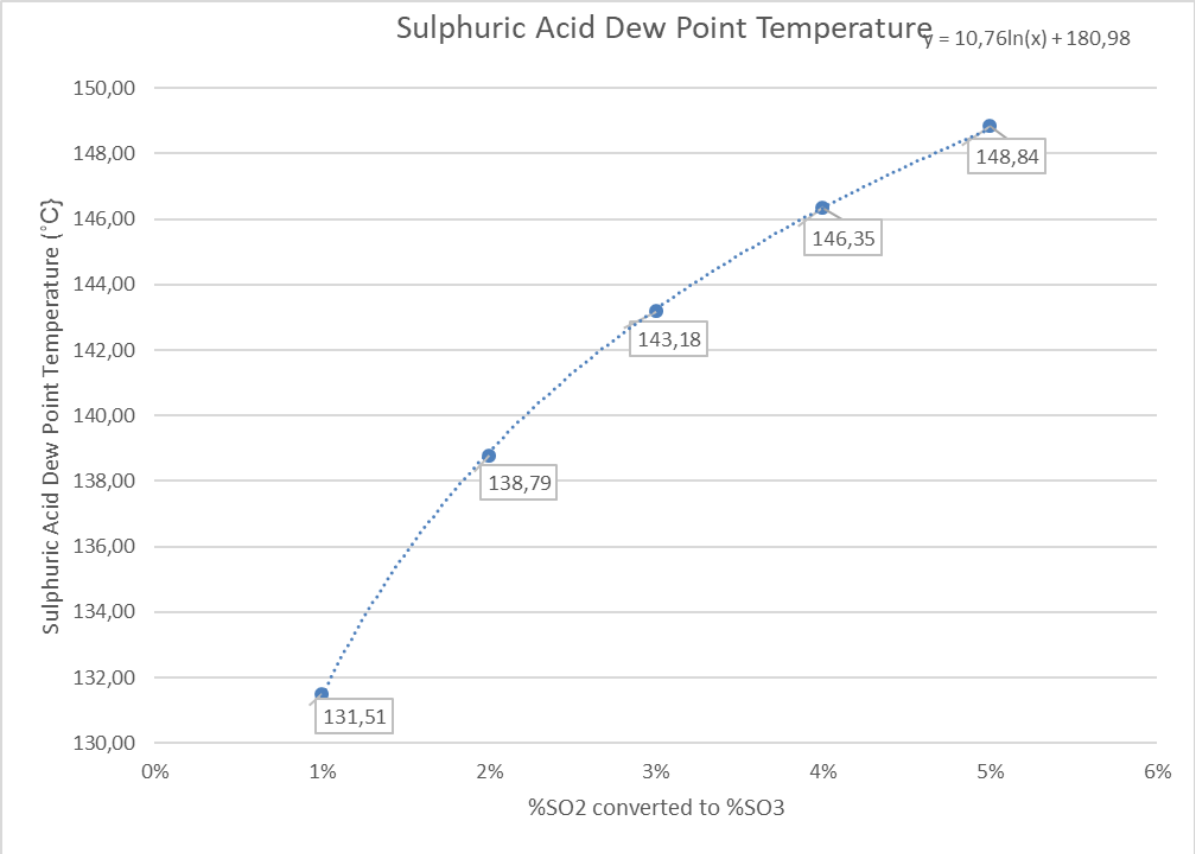

Figure C4.3: Sulphuric acid dew point temperatures for 1% to 5% SO_2 to SO_3 conversion for 80% MCR.

As explained in Figure 5.15 in section 5.3, a 32 x 307 size matrix were generated in the simulation, which contain the final set of cold end layer metal temperatures for the full height of the third layer. This matrix was used to estimate the amount of time dew point related fouling experienced for one gas stream consisting of a sub set of 32 x 84 temperatures of the total matrix. For this sub set the metal temperature will be exposed 81.29% of the length and time step. Due to the fact that this will occur for each annular division of the steel matrix, it can be assumed that the cold end element packs will experience sulphuric acid dew point conditions for 22.2 seconds of the total 27.36 seconds of the flue gas stream for the 80% MCR conditions. This time includes the time when the ash is captured in the seal area directly after the flue gas stream.

The impact of an increase in differential pressure due to fouling was again analysed for the 80% MCR condition. Figure C4.5 is an illustration of the impact of differential pressure increases on dew point temperatures. The same increments were calculated for a differential pressure range of 0kPa to 2kPa as with the 99% MCR condition. The same assumption holds as for the 99% MCR load condition, that a pressure rise from fouling will not deteriorate the sulphurous- and sulphuric acid dew point temperature by a large extent during normal operation. But the moisture dew point can rise with +/-6 ˚C. The air heater still does not operate within these ranges, only during light up and shut down conditions when transient states are experienced.

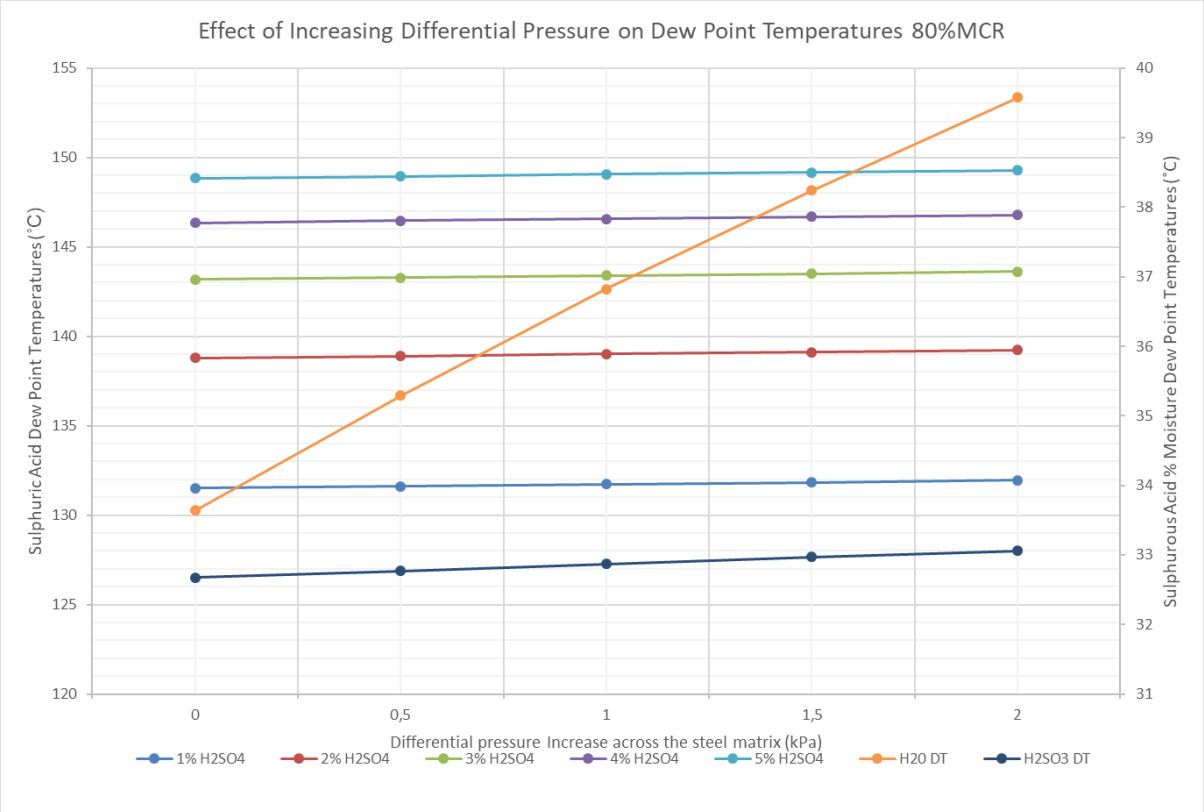

Figure C4.5: Effect of increasing differential pressures on dew point temperatures for 80% MCR.

Table C8 in Appendix C – C2: Data Set 2 - Results is a representation of the results from the 80% MCR load actual test conducted from 00:00 – 04:00 on 25/02/2020.

Air heater gas outlet temperatures
The average of the measured temperature of 117˚C to show an 8.26% deviation from the VBA RAH result of 107.34˚C. The average cold end outlet fluid temperature measured was 88.93˚C. Through considering the maximum simulated outlet temperature at the outlet, a simulated temperature of 134.2˚C is reached within 24 seconds of one revolution. The measured temperature at the pack did not reach the maximum temperature and therefore experiences a lower outlet temperature when compared to the measurement taken after the air heater outlet, as explained in Figure 5.10 in section 5.2. The same input parameters were simulated for the RAH model and an error of 2.43% was evident. As with the previous tests, this result shows that the simulation models tend to overestimate the outlet temperature at higher loads. As mentioned before factors, like the assumption of ideal conditions and the errors incurred by rounded off calculations from an iterative process will introduce a form of error.

Air heater air outlet temperatures
A 2% error occurred between the VBA RAH model and the measured value. This was a difference of 5.9˚C at the outlet for the air side. The error between the VBA RAH and the RAH model was 0.84%. This shows that the possible flue gas flow error (as mentioned in Section 5.7) compromised the simulated results, in this case the outlet temperatures.

Cold end metal temperatures
The comparison between the VBA RAH maximum plate temperature and the measured maximum plate temperature indicated a 0.2% error. The minimum VBA RAH metal temperature was found to be 16.5% less than the measured value. Once again the temperatures operated in the same region but the error showed that the measured value operated at higher ranges in general in comparison to the simulated values. A 20.5% deviation for the inlet metal temperature occurred between the results from VBA RAH and RAH models, with a 4.4% deviation on the outlet metal temperatures. When comparing the measured value and the RAH value the latter again showed unrealistic maximum temperatures. The minimum metal temperatures for the simulated values and for the measured values correlate, which is ideal when the dew point related fouling areas are identified.

Flue gas properties
The estimated oxygen showed a 0.05% (v/v) difference in comparison to the measured oxygen. The measured carbon dioxide was 0.36 % (v/v) higher than the estimated value. The sulphur dioxide showed deviation of 0.11 % (v/v), but when comparing a normalised measurement at 10% oxygen the deviation was 0.04% (v/v). The estimated moisture was 5.7% (v/v), and the measured value was 3.93%. As mentioned previously the accuracy of the moisture measurement at the air heater inlet is affected by the high fly ash content in the flue gas. Ideally the measurements must be taken before the stack.). The emission monitors located in the stack indicated a 5.15% (v/v) measurement, which correlated more with the measured value of 5.7% (v/v). The measured values were used as input parameters and not the simulated values.

Air heater gas flow
A 2.4% error existed between the measured and calculated values for the 80% MCR. The simulation was done using the measured value of 243.15 kg/s. The measured flow proved to be more realistic in comparison with the calculated flow, although an error would still exist as mentioned in Section 5.7.

Differential pressures

The measured differential pressure across the air side was 0.86kPa. The differential pressure calculated by the VBA RAH model had an error of 30%. As mentioned previously, the fact that high differential pressures were measured confirms the condition of fouled element packs. Habbitts (1998) and De Klerk (2001) also experienced similar findings where the estimated differential pressures had a 30% error. The gas side had an error of 1.82% less than the measured value. The fact that high differential pressures were measured at lower loads confirms the condition of fouled element packs.

Fluid Properties

The inlet density for flue gas was measured and in comparison with the simulated value a 3.32% error existed. The flue gas density at the inlet between the VBA RAH and RAH models had a 0.01% difference. As mentioned before, this deviation was caused by the method of estimating the temperature of each condition. The fluid properties for the inlet and outlet heat capacity and velocity of each stream were calculated from both simulation models. The air inlet density, flue gas inlet heat capacity and air inlet heat capacity were identical with no error. The flue gas velocities at the inlet for flue gas had an error of 3.49%. The air inlet velocity varied by 0.04%.

Energy Exchange

The VBA RAH model showed a result of 28.69 MW energy lost and 28.37 MW energy gained. This means the result is accurate with regard to the energy balance. The RAH model gave an energy exchange of 28.55 MW lost and 28.43MW gained, which is also an estimation with a difference of less than 1MW. The error between the two models is due to the slight difference in outlet temperatures by the two simulation models.